Nonlinear transient dynamics of on-board rotors supported by Active Magnetic Bearings

Clément Jarroux

To cite this version:

Clément Jarroux. Nonlinear transient dynamics of on-board rotors supported by Active Magnetic Bearings. Mechanics [physics.med-ph]. Université de Lyon, 2017. English. NNT : 2017LYSEI069 . tel-01999301

HAL Id: tel-01999301
https://theses.hal.science/tel-01999301

Submitted on 30 Jan 2019

N°d'ordre NNT : 2017LYSEI069

THESE de DOCTORAT DE L'UNIVERSITE DE LYON
opérée au sein de
l'INSA LYON

École Doctorale ED 162 MEGA
Mécanique, Énergétique, Génie Civil, Acoustique

Spécialité de doctorat :
GÉNIE MÉCANIQUE

Soutenue publiquement le 19/07/2017, par :
Clément JARROUX

NONLINEAR TRANSIENT DYNAMICS OF ON-BOARD ROTORS SUPPORTED BY ACTIVE MAGNETIC BEARINGS

Devant le jury composé de :

Trébinjac, Isabelle	Professeur	EC Lyon	Présidente
Arghir, Mihaï	Professeur	Université de Poitiers	Rapporteur
Keogh, Patrick S.	Professeur	University of Bath - UK	Rapporteur
Bleuler, Hannes	Professeur	EPFL - CH	Examinateur
Mahfoud, Jarir	Maître de Conférences, HDR	INSA Lyon	Directeur
Dufour, Régis	Professeur	INSA Lyon	Co-Directeur
Alban, Thomas	Ingénieur de recherche	GE Oil & Gas	Invité
Defoy, Benjamin	Ingénieur de recherche	GE Oil & Gas	Invité

Département FEDORA – INSA Lyon - Ecoles Doctorales – Quinquennal 2016-2020

SIGLE	ECOLE DOCTORALE	NOM ET COORDONNEES DU RESPONSABLE
CHIMIE	**CHIMIE DE LYON** **http://www.edchimie-lyon.fr** Sec : Renée EL MELHEM Bat Blaise Pascal 3e etage secretariat@edchimie-lyon.fr Insa : R. GOURDON	M. Stéphane DANIELE Institut de Recherches sur la Catalyse et l'Environnement de Lyon IRCELYON-UMR 5256 Équipe CDFA 2 avenue Albert Einstein 69626 Villeurbanne cedex directeur@edchimie-lyon.fr
E.E.A.	**ELECTRONIQUE, ELECTROTECHNIQUE, AUTOMATIQUE** **http://edeea.ec-lyon.fr** Sec : M.C. HAVGOUDOUKIAN Ecole-Doctorale.eea@ec-lyon.fr	M. Gérard SCORLETTI Ecole Centrale de Lyon 36 avenue Guy de Collongue 69134 ECULLY Tél : 04.72.18 60.97 Fax : 04 78 43 37 17 Gerard.scorletti@ec-lyon.fr
E2M2	**EVOLUTION, ECOSYSTEME, MICROBIOLOGIE, MODELISATION** **http://e2m2.universite-lyon.fr** Sec : Sylvie ROBERJOT Bât Atrium - UCB Lyon 1 04.72.44.83.62 Insa : H. CHARLES secretariat.e2m2@univ-lyon1.fr	M. Fabrice CORDEY CNRS UMR 5276 Lab. de géologie de Lyon Université Claude Bernard Lyon 1 Bât Géode 2 rue Raphaël Dubois 69622 VILLEURBANNE Cédex Tél : 06.07.53.89.13 cordey@univ-lyon1.fr
EDISS	**INTERDISCIPLINAIRE SCIENCES-SANTE** **http://www.ediss-lyon.fr** Sec : Sylvie ROBERJOT Bât Atrium - UCB Lyon 1 04.72.44.83.62 Insa : M. LAGARDE secretariat.ediss@univ-lyon1.fr	Mme Emmanuelle CANET-SOULAS INSERM U1060, CarMeN lab, Univ. Lyon 1 Bâtiment IMBL 11 avenue Jean Capelle INSA de Lyon 696621 Villeurbanne Tél : 04.72.68.49.09 Fax :04 72 68 49 16 Emmanuelle.canet@univ-lyon1.fr
INFOMATHS	**INFORMATIQUE ET MATHEMATIQUES** **http://infomaths.univ-lyon1.fr** Sec :Renée EL MELHEM Bat Blaise Pascal, 3e étage Tél : 04.72. 43. 80. 46 Fax : 04.72.43.16.87 infomaths@univ-lyon1.fr	M. Luca ZAMBONI Bâtiment Braconnier 43 Boulevard du 11 novembre 1918 69622 VILLEURBANNE Cedex Tél :04 26 23 45 52 zamboni@maths.univ-lyon1.fr
Matériaux	**MATERIAUX DE LYON** **http://ed34.universite-lyon.fr** Sec : Marion COMBE Tél:04-72-43-71-70 –Fax : 87.12 Bat. Direction ed.materiaux@insa-lyon.fr	M. Jean-Yves BUFFIERE INSA de Lyon MATEIS Bâtiment Saint Exupéry 7 avenue Jean Capelle 69621 VILLEURBANNE Cedex Tél : 04.72.43 71.70 Fax 04 72 43 85 28 Ed.materiaux@insa-lyon.fr
MEGA	**MECANIQUE, ENERGETIQUE, GENIE CIVIL, ACOUSTIQUE** **http://mega.universite-lyon.fr** Sec : Marion COMBE Tél:04-72-43-71-70 –Fax : 87.12 Bat. Direction mega@insa-lyon.fr	M. Philippe BOISSE INSA de Lyon Laboratoire LAMCOS Bâtiment Jacquard 25 bis avenue Jean Capelle 69621 VILLEURBANNE Cedex Tél : 04.72 .43.71.70 Fax : 04 72 43 72 37 Philippe.boisse@insa-lyon.fr
ScSo	**ScSo*** **http://recherche.univ-lyon2.fr/scso/** Sec : Viviane POLSINELLI Brigitte DUBOIS Insa : J.Y. TOUSSAINT Tél : 04 78 69 72 76 viviane.polsinelli@univ-lyon2.fr	M. Christian MONTES Université Lyon 2 86 rue Pasteur 69365 LYON Cedex 07 Christian.montes@univ-lyon2.fr

*ScSo : Histoire, Géographie, Aménagement, Urbanisme, Archéologie, Science politique, Sociologie, Anthropologie

Abstract

Turbomachinery supported by active magnetic bearings (AMBs) are increasingly used by industrial companies, especially for the absence of direct contact between fixed and rotating parts. The magnetic forces are naturally unstable and the PID (proportional - integral - derivative) controller is the most implemented for its simplicity and robustness. Touchdown bearings (TDBs), which are often ball bearings, support the rotor when the magnetic levitation is no longer provided; when the machine is stopped, during transport, or when an unexpected AMB shut-down occurs. Considering this latter case, the rotor subjected to gravity, undergoes a “landing”, or “drop”, and its behaviour is characterized by transient nonlinear dynamics on its touchdown bearings, which can affect the integrity of the machine. This issue has been intensively discussed since the last twenty years.

Most of the turbomachines are “on-boarded” and are mounted on more or less mobile supports. For example, compressors in floating production storage and offloading (FPSO) units or turbines in nuclear power plants. In some cases of extreme operating conditions, considering their supports fixed may be a too strong assumption. Potential large rotor displacements can cause interactions with touchdown bearings while AMBs still operate. PID controllers used in industrial applications are not designed to withstand the combined loads of base motions and rotor-TDBs interactions. One can then ask what would be the behaviour of the rotor in such a situation.

This thesis is a contribution to the study of the dynamic behaviour of turbomachines supported by AMBs, subject to strong base motions and potential contact nonlinearities. The problem of on-board rotors, active magnetic bearings and touchdown bearings are first addressed individually and then grouped together in order to build the complete model. The contribution of the base motions is considered in the energy formulation of the Timoshenko beam elements for the prediction of bending rotors. The advantage of this method is that any type of bearing model can be implemented; AMBs in our case. The latter are controlled by conventional PID feedback, not particularly tuned to withstand strong base motions and contacts. Rotor-TDB interaction involves analytical modelling of the ball bearing as well as its mechanical link with the housing. The TDB model is validated by drop experiments carried out on an industrial bench. It is shown that quite simple models provide the observed phenomena with sufficient accuracy.

The complete model is validated using tests carried out on an academic rotor-AMB system. A 6-axis shaker makes it possible to impose harmonic and shock to the support. Depending on the acceleration levels generated, the contact between the rotor and the TDBs is triggered. It is shown that AMBs remain globally stable and that no dangerous rubbing vibrations are established. The predicted loads remain far from the maximum TDB load capacity. Considering the academic rotor spinning at full speed, impulse tests up to 3.1 G were carried out. It is shown that loads are shared between AMBs and TDBs. The friction forces remain limited and seem not to be sufficient to ensure instabilities.

KEYWORDS: Rotor-stator interactions, Touchdown bearings, On-board rotors, Active magnetic bearings, Rotordynamics, Nonlinear dynamics

Résumé (en français)

Les turbomachines supportées par des paliers magnétiques actifs (PMAs) sont de plus en plus utilisées par les industriels notamment grâce à l'absence de contact direct entre parties fixes et parties tournantes. Les forces magnétiques sont naturellement instables et le contrôleur PID (proportionnel - intégral - dérivé) reste le plus implémenté pour sa simplicité et sa robustesse. Des paliers atterrisseurs, des roulements à billes pour la plupart, assurent le supportage du rotor lorsque la lévitation des PMAs n'est plus assurée ; lorsque la machine est à l'arrêt, pendant le transport, ou lorsqu'une coupure inattendue des PMAs survient. Considérant ce dernier cas, le rotor soumis à la gravité, subit un "atterrissage" et son comportement se caractérise par une dynamique transitoire et non-linéaire sur ses paliers atterrisseurs, pouvant porter atteinte à l'intégrité de la machine. Cette problématique a été largement étudiée ces vingt dernières années.

La majorité des turbomachines sont "embarquées" et reposent sur des supports plus ou moins mobiles. C'est le cas notamment pour les compresseurs montés sur les unités flottantes de production, de stockage et de déchargement (FPSO en anglais), ou encore pour les turbines de centrale nucléaire. Dans certains cas de fonctionnement critique, considérer leurs supports fixes peut être une hypothèse trop forte. Les forts déplacements potentiels du rotor peuvent engendrer des intéractions avec les paliers atterrisseurs alors que les PMAs sont toujours opérationnels. Les contrôleurs PID utilisés dans les applications industrielles ne sont pas conçus pour supporter les charges combinées des mouvements de la base et des interactions rotor-palier atterrisseurs. On peut alors se demander quel serait le comportement du rotor dans une telle situation.

Cette thèse est une contribution à l'étude du comportement dynamique des turbomachines supportées par des PMAs, sujettes à de fortes sollicitations extérieures et des non-linéarités de contact potentielles. Les problématiques des rotors embarqués, des paliers magnétiques actifs et des paliers atterrisseurs sont traitées individuellement puis regroupées afin de bâtir le modèle complet. L'apport des mouvements de la base est considéré dans la formulation énergétique des éléments de poutre Timoshenko pour la prévision des rotors en flexion. L'avantage de cette méthode est qu'elle permet d'implémenter n'importe quel modèle de palier, dans notre cas des PMAs. Ces derniers sont contrôlés par des PID conventionnels, pas particulièrement conçus pour supporter de forts mouvements de la base et des contacts. L'interaction avec les paliers atterrisseurs comprend la modélisation analytique du roulement à billes ainsi que celle de la liaison au support. Le modèle de palier atterrisseur est validé grâce à des expériences d'atterrissage réalisées sur un banc de type industriel. Il est montré qu'un modèle relativement simple est capable de retranscrire les phénomènes observés avec une précision suffisante.

Le modèle complet est validé à l'aide d'essais réalisés sur un banc académique rotor-PMA. Un excitateur 6-axes permet d'imposer des mouvements de type harmoniques et chocs, représentatifs de conditions réelles de fonctionnement. En fonction des niveaux d'accélération générés, le contact avec les paliers atterrisseurs est déclenché. Il est montré que les PMAs restent globalement stables et qu'aucune vibration dangereuse de frottement est mise en place. Les charges calculées au niveau des paliers restent loin de leurs capacités maximales. Considérant le rotor académique tournant à vitesse maximale, des essais de choc jusqu'à 3.1 G ont été réalisés. Il est montré que les charges sont partagées entre les PMAs et les paliers atterrisseurs. Les efforts de frottement restent limités et ne semblent pas être suffisants pour générer des instabilités.

MOTS CLÉS: Contact rotor-stator, Paliers atterrisseurs, Rotors embarqués, Paliers magnétiques actifs, Dynamique des rotors, Dynamique non-linéaire

Remerciements

Voilà maintenant dix ans, depuis mon entrée à l'IUT d'Évry, que je cultive intérêt et curiosité à l'égard de la mécanique et de la dynamique des structures. S'il est vrai que le travail de thèse est un défi que l'on se lance à soi-même, il n'en reste pas moins une expérience partagée. De nombreuses personnes ont contribué, de près ou de loin, à l'élaboration de ce mémoire. Je souhaite ici les en remercier.

J'exprime d'abord toute ma reconnaissance à mes directeurs de thèse, Monsieur Jarir Mahfoud, maitre de conférence, HDR et Monsieur le professeur Régis Dufour pour leurs conseils avisés et leur très grande disponibilité. Nos nombreuses discussions scientifiques ont enrichi mes réflexions et ont contribué à l'aboutissement de ce projet scientifique. J'adresse également mes vifs remerciements à Thomas Alban et Benjamin Defoy, de la société Thermodyn GE Oil & Gas, pour leurs compétences et l'intérêt qu'ils ont porté à mes travaux de recherche.

Toute ma gratitude va aux professeurs Mihaï Arghir, de l'Université de Poitiers et Patrick S. Keogh, de l'Université de Bath en Angleterre, pour avoir accepté d'être les rapporteurs de ce travail, ainsi qu'aux professeurs Isabelle Trébinjac, de l'École Centrale de Lyon et Hannes Bleuler, de l'École Polytechnique Fédérale de Lausanne en Suisse, pour avoir accepté d'en être les examinateurs.

La thèse CIFRE a été menée au Laboratoire de Mécanique des Contacts et des Structures (LaMCoS) de l'INSA Lyon en collaboration avec l'entreprise Thermodyn GE Oil & Gas localisée au Creusot. Je tiens donc à remercier Messieurs les professeurs Alain Combescure et Daniel Nelias, directeurs successifs du LaMCoS ainsi que Messieurs Corso Balboni et Florent Boche, directeurs successifs de Thermodyn GE Oil & Gas, pour leur accueil et les conditions de travail optimales qui m'ont été offertes.

Ma thèse a débuté dans les locaux de Thermodyn. Je remercie ici Pascal Gaudez et Matthieu Gerbet pour leur précieuse aide, ainsi que Pascale Pierre pour sa bonne humeur et son efficacité.

J'ai passé un peu plus de trois ans au sein de l'équipe de dynamique et contrôle des structures. Je tiens à remercier chaleureusement ses membres permanents. Je pense notamment à Simon Chesné et Sébastien Baguet, qui m'ont apporté leur aide et leur regard d'expert sur certaines de mes problématiques, aux membres de l'Equipex PHARE, Éric Châtelet mais également Franck Legrand, sans qui une grande partie des expériences présentées dans cette thèse n'auraient pu être réalisées. Je remercie également Zahia Achoui pour sa disponibilité et sa gentillesse. Aux docteurs, doctorants et étudiants du LaMCoS avec qui j'ai passé le plus clair de mon temps : Marion, Marc-André, Zaki, Sophie, José, Giovanna, Lihan, Wenfeng, Elena, Seb, Clément, Carlos, Matthias, Aroua, Emna, Shaoyi, Étienne, Lodovico et Kevin. Une pensée toute particulière à mon cher partenaire et ami Guillaume, avec qui j'ai partagé bien plus que mon bureau. Je lui souhaite le meilleur.

Qu'auraient été ces trois années sans mes amis lyonnais ? Merci à eux d'avoir été présents et de m'avoir permis de souffler dans ces nombreux moments de doute que traverse tout doctorant.

Je me tourne désormais vers mes proches de toujours. À mes parents, du plus profond de mon coeur, à mon frère et mes soeurs, à mes grands-parents, à ma Famille, pour leur amour, leur bienveillance et leur soutien sans faille. À mes meilleurs amis, mes frères et soeurs de coeur, pour leurs encouragements depuis le berceau. La liste est longue et je remercie spécialement ici ceux qui sont venus assister à ma soutenance : à Dilshan le photographe, Bérenger l'espagnol, et Anthony l'artiste.

Enfin et surtout, à Diaraye, pour avoir partagé ma vie, mes joies et mes peines. Pour ton amour, ton attention, ta confiance et ta joie de vivre. Que ces mots te parviennent.

Contents

Résumé étendu

Contexte

D'une manière générale, les turbomachines jouent un rôle clef dans la transformation, l'extraction ou le transport de l'énergie. Selon les applications ciblées, ces dernières sont sujettes à des environnements plus ou moins sévères. Par exemple, les turbomachines utilisées pour la production électrique dans une centrale nucléaire peuvent faire face à des tremblements de terre. Les événements récents de Fukushima au Japon, où la station a été profondément endommagée, l'attestent. Un autre exemple concerne la production offshore d'énergie fossile. Les unités flottantes de production, de stockage et de déchargement (FPSO en anglais) sont des navires utilisés pour la production et le stockage off-shore du pétrole et du gaz. Des turbomachines sont nécessaires dans ces bateaux pour le traitement des hydrocarbures. Lors de fortes tempêtes, de grandes vagues s'écrasant sur la coque du bateau peuvent provoquer d'importantes vibrations de la structure, perturbant le processus de production. Dans ces deux cas, l'opérabilité des turbomachines, définie comme la capacité d'une machine à fonctionner de manière sûre et fiable en toutes circonstances, peut être affectée. Au-dessus d'un certain seuil de vibrations, une procédure d'arrêt d'urgence stoppe la machine afin d'éviter des comportements souvent mal maîtrisés et des dommages structurels couteux. D'autre part, les spécialistes des questions énergétiques ont besoin de machines dotées d'une efficacité maximale pour répondre aux besoins énergétiques croissants. La question des fabricants de turbomachines est alors de savoir comment améliorer l'opérabilité de leurs produits face aux environnements externes potentiellement critiques.

Ce projet de recherche, réalisé en collaboration avec la société Thermodyn GE Oil & Gas et le laboratoire LaMCoS de l'INSA Lyon, contribue à l'amélioration des connaissances concernant le comportement dynamique des turbomachines soumises à des évènements extérieurs plus ou moins critiques.

Introduction

Une turbomachine est le lieu d'un échange d'énergie entre un fluide et une partie mécanique tournante, appelé rotor. C'est par le biais de la rotation que l'énergie est transférée (compresseur) ou extraite (turbine) du fluide. Cette rotation est donc l'élément clef de ces machines. Le guidage du rotor dans le stator est assuré par les paliers et le choix de la technologie employée est important. Il existe une grande variété de paliers adaptés pour différentes applications. Les paliers à éléments roulants (billes, rouleaux, aiguilles, etc.), les paliers à fluide (huile, air, eau, etc.) ou bien encore les paliers magnétiques passifs ou actifs. Ces derniers sont considérés dans cette thèse. Ce type de technologie est présent dans un nombre croissant d'applications telles que les volants d'inertie, les pompes turbomoléculaires, les compresseurs centrifuges, les broches de machines-outils pour usinage à grande vitesse, etc. Contrairement aux paliers conventionnels, le contact direct entre le rotor et le stator est évité grâce à la lévitation magnétique. Les paliers magnétiques actifs (PMAs) présentent de nombreux avantages par rapport aux paliers conventionnels. L'absence de contact direct est sans aucun doute le principal avantage ; la consommation de lubrifiant est inexistante et l'empreinte environnementale s'en trouve fortement réduite. De plus, les pertes énergétiques sont limitées et les turbomachines plus efficaces. De manière générale, l'utilisation des paliers conventionnels nécessite souvent une boîte de transmission afin de moduler la puissance générée, par un moteur électrique par exemple, tandis que la technologie PMA permet un couplage direct pour des vitesses de fonctionnement plus élevées. La lévitation du rotor est obtenue grâce à des forces magnétiques attractives induites par un courant appliqué aux bornes d'un électroaimant. Ce dernier est composé d'un aimant ferromagnétique sur lequel est enroulée une bobine. La nature de la force rend le système rotor-PMA instable et ceci doit être compensé par une boucle de contrôle appropriée. Les systèmes rotor-PMA sont systématiquement équipés de paliers atterrisseurs supportant l'arbre lorsque la lévitation magnétique n'est plus présente. Cela peut se produire lorsque la machine est arrêtée, lors du transport ou lors d'une coupure inattendue des PMAs. Dans ce cas, le rotor a un comportement dynamique transitoire et non-linéaire caractérisé par des rebonds suivis de mouvements pendulaires, inoffensifs pour l'intégrité de la structure. Dans certains cas particuliers, le rotor peut cependant développer des instabilités générées par le frottement sec à l'interface entre le rotor et le palier atterrisseur, menant à un comportement du rotor en contact permanent en précession indirecte appelé “dry whip”. Les déplacements du rotor et les efforts de contact générés sont alors de grande amplitude. Prendre en compte ce type de comportement est d'une importance majeure pour la conception du système rotor-PMA et en particulier, des paliers atterrisseurs. De manière générale, les turbomachines sont sollicitées par un grand nombre de phénomènes physiques liés à leur fonctionnement ou leur environnement. Le balourd est certainement la source d'excitation la plus connue concernant les machines tournantes. D'autres excitations existent, comme les vibrations basses fréquences dues aux échanges d'énergie entre fluide et rotor ou bien encore, les excitations relatives au mouvement du support de la machine. De ce fait, la majorité des turbomachines peuvent être considérées comme étant embarquées, ce qui signifie que leurs supports ne sont pas fixes par rapport au sol. C'est le cas pour les turbocompresseurs automobiles, les moteurs d'avions, les turbines à vapeur dans les centrales nucléaires ou les compresseurs centrifuges montées sur FPSO. Les mouvements de la base génèrent une dynamique de rotor complexe qui dépend du type d'excitation appliquée. D'autre part, la technologie PMA est de plus en plus utilisée dans les applications industrielles et le PID (proportionnel - intégral - dérivé) reste la stratégie de contrôle la plus utilisée. Différentes études ont été effectuées sur les systèmes rotor-PMA soumis à un mouvement de leur support. Certains travaux traitent de l'utilisation des forces magnétiques pour éliminer ou détériorer les zones d'instabilité. D'autres travaux traitent spécifiquement du contrôle des mouvements du support par l'ajout de compensateurs (boucle feedforward) en parallèle d'une boucle de contrôle plus conventionnelle. Cependant, la plupart des stratégies de contrôle mise en place dans les machines industrielles ne sont pas faites pour contrer les mouvements de la base. Ainsi, lorsqu'un fort mouvement du support se produit alors que les PMAs fonctionnent toujours, il est possible que le rotor, tournant à une vitesse de rotation élevée, entre en contact avec les paliers atterrisseurs. Ce dernier subit donc les excitations de son support combinées aux interactions rotor-palier atterrisseur. Les forces tangentielles induites par le frottement sec pourraient déclencher des comportements de rotor complexes, voir dangereux. Dans le but d'améliorer la conception des turbomachines équipées de PMA et d'éliminer un point bloquant concernant la pénétration de ce type de technologie dans des applications embarquées, ce projet propose une approche globale pour la modélisation et la prévision du comportement dynamique d'un système rotor-PMA soumis à la fois aux effets classiques de la dynamique des rotors (balourd et effets gyroscopiques) et aux excitations de mouvement de base. Le contact avec les paliers atterrisseurs ainsi que les non-linéarités provenant des PMA sont également considérés. Ainsi, la modélisation comprend un modèle de rotor embarqué, de PMA et de palier atterrisseur. Dans ce qui suit, chaque élément est présenté et les différentes hypothèses associées sont évoquées.

Approche de modélisation

Rotor embarqué

Dans cette étude, la flexibilité du support n'est pas prise en compte. Au regard des designs de machines industrielles actuelles, cette hypothèse semble adaptée à la problématique de ce sujet. De plus, la modélisation des structures de supportage, souvent par le biais de méthodes, type éléments finis, génère un grand nombre de degrés de liberté, alourdissant le modèle pour un apport scientifique faible dans notre cas. L'étude se focalise sur la dynamique des rotors en flexion (4 degrés de liberté par noeud) et l'approche Lagrangienne classique est employée pour la mise en place des équations du mouvement. Habituellement, deux repères sont nécessaires pour établir la formulation des différentes énergies des éléments composant un rotor en flexion ; un repère local et un repère associé au support fixe, supposé Galiléen. Dans le cas des rotor embarqués, ce dernier n'est plus Galiléen et peut bouger selon les six directions de l'espace. Un troisième repère, Galiléen donc, est mis en place. L'écriture des différentes énergies par rapport à ce repère fixe fait apparaitre l'apport des mouvements rigides du support. Seules les énergies cinétiques des éléments de disques, d'arbre et de balourd sont modifiées. Par la suite, les équations de Lagrange permettent l'obtention des équations du mouvement grâce à la discrétisation spatiale du rotor en éléments de poutre de Timoshenko. L'expression des équations du mouvement est faite dans le repère non-inertiel associé à la base mobile. De ce fait, les effets d'inertie relatifs à un repère en constante accélération ou en constante rotation (effet de Coriolis) apparaissent sous la forme d'efforts extérieurs. Des matrices de raideur (effets centrifuges) et de gyroscopie à coefficients paramétriques dépendant des différentes rotations du support sont également générées. Des instabilités dues à ces excitations paramétriques peuvent apparaître pour certaines amplitudes et fréquences d'excitation, proches des fréquences naturelles du système et de ses combinaisons. Les forces de balourd sont également modifiées et la combinaison avec les mouvements de rotation du support génèrent des excitations multi-harmoniques. En définitive, le modèle de rotor embarqué permet de prendre en compte n'importe quel type de mouvement du support dans les six directions de l'espace. Ces mouvements peuvent être quelconques ; harmonique, choc, séisme, bruit blanc, etc. De plus, les équations du mouvement étant écrites dans le repère non-inertiel du support mobile, n'importe quel modèle de palier peut être implémenté. Dans le cas de cette étude, les PMAs génèrent des forces magnétiques par le biais du contrôle actif.

Paliers magnétiques actifs

Les PMAs permettent la sustentation des rotors, sans contact direct avec le stator, par le biais de forces attractives magnétiques. Le système PMA comprend de nombreux éléments électroniques qui ne sont pas détaillés dans ce travail. Seuls les éléments ayant un effet direct sur les forces de restitutions des PMA sont considérés. Le contrôleur, générant un courant de consigne, et l'actionneur transformant cette consigne en effort mécanique appliqué sur le rotor.

Actionneur

Les PMAs utilisés sont composés de deux lignes d'actions, chacune d'entre elles comprenant une paire d'actionneur. Ce dernier comprend un amplificateur et un électroaimant, combinaison d'un aimant en acier ferromagnétique à forte perméabilité et d'une bobine de cuivre enroulée autour. La circulation d'un courant dans la bobine induit un champ magnétique guidé par l'aimant vers le rotor générant ainsi une force d'attraction. La formulation de cette force est non-linéaire par nature : elle est proportionnelle au carré du courant appliqué et inversement proportionnelle au carré du déplacement du rotor dans sa ligne d'action. Lorsque le cas d'étude implique de faible déplacement du rotor, il est d'usage de linéariser ces efforts autour d'une position d'équilibre en déplacement et en courant. Une raideur en courant et une raideur négative déstabilisatrice, relative au déplacement, sont alors générées. L'investigation porte ici sur le cas de potentiels forts déplacements du rotor dans ses lignes d'action. La linéarité des PMAs peut donc être remise en cause. Un outil développé au cours de ce travail permet l'évaluation de l'hypothèse de linéarité. Il est possible, en fonction des déplacements du rotor et du courant appliqué dans l'électroaimant, de déterminer si la formulation linéaire ou non-linéaire doit être utilisée. L'électroaimant est contrôlé en courant par l'amplificateur et ce dernier limite les capacités des PMAs. Le courant et la tension maximale limitent respectivement l'amplitude et la variation de la force magnétique. Si le courant requis dépasse un certain seuil, l'amplificateur est saturé et la force magnétique est écrêtée. Cette non-linéarité peut se produire dans le cas de fort mouvements de la base et est considérée dans cette étude. Si le taux de variation de cette force dépasse une certaine limite, un retard en temps, équivalent à un retard de phase, entraîne une diminution de l'amortissement généré par les PMAs. Par conséquent, les capacités dynamiques d'un actionneur sont limitées en fréquence et sont modélisées par un filtre passe-bas.

Contrôleur

La demande en courant de l'amplificateur est fournie par le contrôleur qui génère une instruction en fonction des déplacements du rotor. De nombreux types de contrôleurs existent mais le PID reste le plus utilisé dans les applications industrielles pour sa simplicité et sa robustesse. Le PID est considéré dans ce travail. Il génère une action proportionnelle à une erreur, mais aussi à sa dérivée et à son intégrale dans le temps. Pour le cas particulier des systèmes rotor-PMA, cette erreur est la distance du rotor par rapport à la position zéro, c'est-à-dire, le déplacement relatif du rotor par rapport au centre des PMA. Le gain proportionnel est équivalent à la raideur et est choisi afin de contrecarrer la raideur négative inhérente aux PMA. Le gain intégral, ou intégrateur, est une caractéristique spécifique des PMA. Il permet de centrer le rotor dans le palier ; lorsque le temps tend vers l'infini, l'erreur tend vers zéro. Lorsque le gain intégral est trop élevé, le rotor atteint rapidement le centre des PMAs et des instabilités peuvent être générées. Le gain dérivé apporte l'amortissement au système et dissipe l'énergie. Plusieurs filtres sont ajoutés à la formulation du simple PID. Ces derniers ont pour but la limitation de l'amortissement sur la plage de fonctionnement du rotor, ou bien encore l'amortissement des modes hautes fréquences présent dans la bande passante du contrôleur.

Peu importe la stratégie de contrôle, lorsque le rotor dépasse un certain jeu, ce dernier entre en contact avec les paliers atterrisseurs.

Palier atterrisseur

Les paliers atterrisseurs ont deux fonctions principales. Le premier est de protéger les PMAs contre des charges transitoires importantes et inattendues dépassant la capacité des PMAs. Le second est d'assurer le supportage du rotor lorsque les PMAs ne fonctionnent plus. C'est le cas lorsque la machine est à l'arrêt ou lorsqu'une coupure inattendue des PMAs survient. Dans ce cas, le rotor tombe sur ses paliers atterrisseurs sous l'effet de la gravité induisant une dynamique transitoire caractérisée par des rebonds suivis d'une oscillation pendulaire, dans la majorité des cas. L'étude bibliographique montre que ces comportements dépendent entre autre du type de montage de la machine, vertical ou horizontal. L'étude se focalise sur des montages horizontaux. Deux principaux types de paliers atterrisseurs existent : les paliers lisses et les paliers à éléments roulants. Ces derniers peuvent supporter des atterrissages radiaux, axiaux ou combinés. Dans ce projet, l'étude se focalise sur l'analyse des paliers atterrisseurs de type roulements à bille dans le cas des atterrissages radiaux, la dynamique axiale n'étant pas considérée. Les roulements à billes sont largement utilisés pour les applications d'atterrissage des rotors. Cette technologie limite les comportements dangereux du rotor induits par le frottement ; les paliers atterrisseurs atteignent habituellement la vitesse du rotor en un temps très courts, réduisant fortement les forces de frottement. Les cages, habituellement utilisées pour éviter l'interaction des éléments roulants, sont rarement utilisées dans ce type d'application ; un palier atterrisseur subit de fortes accélérations angulaires et la cage peut ne pas être capable de l'endurer. Les billes sont généralement faites de matériaux céramiques utilisés pour leur résistance mécanique élevée, leur faible coefficient de frottement à l'acier et conductivité thermique. Les arrangements modernes sont souvent de types axial-radial, comme par exemple les roulements à billes à contact angulaire à deux rangées pouvant supporter des atterrissages axiaux et radiaux. Cependant, dans d'autres applications telles que les pompes à vide, le palier atterrisseur peut être un roulement à billes à gorge profonde. Quel que ce soit le type de palier atterrisseur, les éléments souples sont utilisés pour limiter les charges transmises au stator et apporter une stabilité lors des interactions avec le rotor. Ce type de composants est monté serré entre le stator et la bague extérieure du roulement atterrisseur.

L'étude bibliographique montre que le degré de détail de la modélisation des paliers atterrisseurs dépend de l'application visée. Lorsque l'intérêt porte sur le comportement dynamique de la ligne d'arbre, la modélisation se révèle relativement simple. Il n'est donc pas nécessaire de modéliser l'interaction de chaque élément roulant avec les bagues et le nombre de degrés de liberté reste limité. Le modèle de palier atterrisseur doit générer une force normale de restitution lorsque le rotor dépasse un certain jeu. Cette modélisation doit prendre en compte l'élément souple liant le palier atterrisseur au stator. Lorsque le rotor entre en contact avec le palier, les effets de frottement induits par les vitesses relatives rotor-bague intérieure doivent pris en compte par une force tangentielle. Cette dernière entraîne la mise en rotation du palier et une modélisation rotationnelle doit être considérée. L'interaction entre le rotor et la bague intérieure est traité avec la méthode des pénalités. Cette dernière autorise la pénétration du rotor afin d'appliquer un effort de contact proportionnel à cette même pénétration. Le modèle de Hunt and Crossley comporte un amortisseur non-linéaire et permet d'annuler les discontinuités des lois de contact linéaire. La modélisation du roulement à bille est une loi analytique effort-déflection bien connues basée sur la théorie de Hertz. Le processus consiste en la détermination d'une rigidité de contact pour un élément roulant puis en la généralisation de cette loi pour l'ensemble du roulement. Cette méthode est comparée avec une méthode élément finis et donne des résultats satisfaisants. La mise en rotation est basée sur une inertie polaire équivalente, mise en place grâce à l'hypothèse de roulement sans glissement. Un couple résistant basé sur les travaux de Palmgren ainsi qu'un amortissement polaire sont ajoutés à la modélisation. Le ruban amortisseur est l'élément souple, placé entre la bague intérieure et le stator, considéré dans cette thèse. Il s'agit d'une feuille d'acier ondulé apportant l'amortissement lors de contact rotor-palier atterrisseur, il est donc primordial pour la stabilité et la limitation des charges générées. Ainsi, cet élément a fait l'objet d'essais durant cette thèse afin de caractériser son comportement dynamique réel. De manière générale, cet élément est modélisé comme un ressort en parallèle avec un amortisseur de type visqueux. Il a été montré par des essais harmoniques que le comportement est plutôt de type frottement sec. Les dents du ruban en contact avec les parois sont d'abords en état collées puis glissantes, lorsque l'effort appliqué dépasse le seuil de glissement. L'alternance d'états collés et glissants produits l'amortissement par le phénomène de "stick-slip" associé au frottement sec. Les boucles d'hystérésis sont anguleuses et ces dernières dépendent très peu de la fréquence d'excitation, confirmant l'hypothèse de frottement sec. Le modèle de Dahl généralisé reproduit fidèlement les phénomènes observés.

Investigation sur la dynamique d'atterrissage

Cette étape permet entre autre de s'assurer que les différents éléments composants les paliers atterrisseurs sont modélisés de manière satisfaisante avant d'analyser le comportement dynamique d'un système rotor-PMA embarqué soumis à des excitations de sa base. Ce dernier doit fournir des prévisions, en termes de dynamique de rotor et de charges générées, suffisamment précises. Les essais d'atterrissage utilisés pour la validation du modèle proviennent d'un banc d'essais de taille industrielle. Trois modèles de paliers atterrisseurs sont utilisés. Le premier est une loi de contact bilinéaire. Les interactions rotor-bague intérieure et bague extérieure-housing sont supposées infimement rigide. La dynamique des bagues est négligée et les seuls contributeurs à la force de contact sont le ruban (principalement) et le roulement. Les deux autres modèles comportent quatre degrés de liberté. Les interactions des bagues avec le rotor et le housing sont donc considérées ; l'un d'eux comprend le nouveau modèle de ruban, basé sur l'hypothèse d'amortissement par frottement sec. Les calculs sont comparés aux mesures, en termes de déplacements et de charges. L'objectif est d'analyser le degré de détails requis pour simuler correctement la dynamique d'atterrissage. Deux tests d'atterrissages sont effectués pour deux objectifs différents :

- Les essais d'atterrissage avec un rotor à l'arrêt permettent d'analyser uniquement les effets des forces de contact générées par les paliers atterrisseurs. En effet, la dynamique d'atterrissage est sensible à la distribution de balourd et à la vitesse de rotation. Ces tests permettent la sélection et la validation du modèle de palier atterrisseur, parmi les trois testés, répondant aux besoins de l'étude.

- Considérer un rotor tournant à une vitesse de rotation de 6 500 tr/min permet d'identifier le temps nécessaire pour que les paliers atterrisseurs atteignent la vitesse du rotor. Les forces de frottement générées pendant le contact entraînent les roulements à billes en rotation. Lorsque ces derniers atteignent la vitesse du rotor, les forces de frottement sont annulées ce qui entraîne un changement dans le comportement dynamique du rotor : ce dernier se recentre dans le palier. Ces tests permettent donc de valider la modélisation rotationnelle du palier.

Le banc de type industriel est équipé d'un rotor de 200 kg et d'1.2 m de long. Ce dernier est rigide pour des vitesses de rotation inférieures à 25 000 tr/min. Les PMAs ont 5 axes et supportent le rotor avec un courant de biais de 6 A. Des capteurs inductifs permettent de mesurer les déplacements du rotor. Des cellules de forces fournissent les efforts transmis du housing vers le stator lorsque le rotor entre en contact avec les paliers atterrisseurs. Ces derniers sont des roulements à billes à contact oblique à deux rangées. L'atterrissage consiste en la coupure des PMAs puis en l'analyse de la dynamique transitoire qui en résulte.

Les essais d'atterrissage à l'arrêt montrent que le comportement du ruban est différent quand ce dernier est soumis à des excitations de type transitoire. En effet, les résultats de calculs montrent des rebonds très aplatis impliquant un fort amortissement généré par le ruban, cependant, ce comportement n'est pas observé dans les essais. Il semble donc que l'amortissement généré par frottement sec soit plus élevé pour des excitations de type harmonique que transitoire. En abaissant le seuil de glissement du modèle de Dahl généralisé, il apparaît alors des résultats plus en adéquation avec les observations. En effet, diminuer le seuil de glissement diminue la surface de l'hystérésis et donc l'amortissement. L'hypothèse est donc que le caractère transitoire du choc abaisse le seuil de glissement des dents du ruban. Pour les besoins de l'étude, il apparait cependant que le modèle de contact bilinéaire permet d'obtenir des résultats satisfaisant en termes de dynamique du rotor et de charges au palier. Les essais d'atterrissage à 6500 tr/min montrent le comportement pendulaire associé à la dynamique des rotors. Le modèle rotationnel permet une estimation satisfaisante du temps de mise en rotation. La prédiction du changement de la dynamique latérale du rotor associée à la mise en rotation du roulement est en effet observé à des temps très proche des mesures. L'hypothèse cinématique de roulement sans glissement semble donc satisfaisante. Cette étape a donc permis la validation du modèle de palier atterrisseur, notamment en termes de charge dynamique. Malgré certains écarts, les résultats sont satisfaisants pour le besoin de l'étude et cette modélisation est conservée pour l'étape suivante.

Investigation sur la dynamique non-linéaire des rotors embarqués

Dans cette partie, le modèle numérique comprenant les modèles de rotor embarqué, de PMA et de palier atterrisseur est validé grâce à un banc rotor-PMA de type académique. Le rotor est conçu pour avoir les caractéristiques dynamiques des turbomachines industrielles. Un excitateur six axes est utilisé pour effectuer des tests harmoniques et impulsionnels représentant respectivement des tremblements de terre et des chocs, induits par exemple par de grandes vagues générées lors de violente tempêtes. Le but est de valider le modèle numérique complet, mais aussi de répondre à la problématique initiale de cette thèse qui est : quel serait le comportement dynamique d'un rotor supporté par des PMAs, contrôlé avec une stratégie de contrôle conventionnelle de type PID, soumis à des charges classiques de dynamique des rotors (gravité et distribution de balourd), mais aussi aux mouvements de sa base et aux non-linéarités de contact ?

Les turbomachines industrielles ne sont généralement pas conçues pour fonctionner lors de conditions critiques impliquant de grands déplacements du rotor. Lorsque ce dernier dépasse un certain seuil, une procédure d'arrêt d'urgence est lancée et la machine est progressivement arrêtée ; le rotor décélère, suivi par une coupure des PMAs. Ici, ce seuil n'est pas pris en compte et le système est autorisé à fonctionner même lorsque le contact rotor-palier atterrisseur se produit. Il est alors possible d'analyser le comportement du système et sa capacité à gérer ce type d'événements.

Le banc de type académique est équipé d'un rotor de 6.5 kg et de 0.6 m de long. Ce dernier est rigide pour des vitesses d'opération inférieures à 10 000 tr/min. Les PMAs ont 4 axes et supportent le rotor avec un courant de biais de 1 A. Ces derniers sont équipés de roulements à billes à gorge profonde à simple rangée. Des capteurs inductifs permettent de mesurer les déplacements du rotor. Les courants de contrôle sont également enregistrés.

Tout d'abord, le modèle numérique est évalué à l'aide de réponses au balourd et d'atterrissages à l'arrêt. Les résultats obtenus sont en accord avec les mesures. Les paramètres estimés des paliers atterrisseurs sont considérés comme valides. Ensuite, des investigations numériques et expérimentales considérant des essais harmoniques et impulsionnels dans la direction verticale sont menées. Les tests ont été choisis pour être représentatifs de conditions réelles de fonctionnement des turbomachines. Les essais harmoniques sont réalisés à basse fréquence, spécifiquement à 20 Hz, une gamme fréquentielle où l'énergie générée par les séismes est la plus grande. Le niveau d'accélération est choisi proche des niveaux associés aux tremblements de terre, jusqu'à 1.1 G. Considérant les essais harmoniques avec de faible niveau d'accélérations (aucun contact avec les paliers atterrisseurs jusqu'à 0.7 g), le contrôleur supporte les effets combinés du mouvement du support avec les forces de balourd générant des orbites périodiques ou quasi périodiques dépendant du rapport de la fréquence du support sur la vitesse de rotation. Ceci est bien reproduit par le modèle. D'une manière générale, le contact avec les paliers atterrisseurs limite les déplacements du rotor. Un contenu fréquentiel riche comprenant de nombreuses harmoniques de la fréquence fondamentale du mouvement du support peut être observé. Les modes du système rotor-PMA sont excités puisque les contacts agissent sur les structures comme des tests modaux. Les forces magnétiques générées par les actionneurs restent dans une gamme linéaire acceptable. Aucune saturation d'amplificateur n'est observée. Les modes couplés rotor-palier atterrisseur sont excités pendant la durée du contact. Même si le contrôleur PID est réglé sans tenir compte de ces fréquences particulières, il reste globalement stable. Ni la saturation de l'amplificateur, ni la non-linéarité des forces magnétiques ne sont observées numériquement et expérimentalement. Cela s'explique principalement par le fait que les contacts avec les paliers atterrisseurs limitent fortement les déplacements du rotor et empêchent l'émergence des non-linéarités des actionneurs : le ratio de jeu rotor-palier atterrisseur et rotor-PMA est proche de 0,25, ce qui est inférieur aux valeurs industrielles, plus proche de 0,5. Considérant un arbre en rotation, aucune instabilité établie, de type précession inverse, n'est déclenchée durant les tests harmoniques et impulsionnels. Lors des essais harmoniques, il semble que les paliers atterrisseurs soient entraînés en rotation, atteignant la vitesse du rotor et par conséquent, limitant les effets de frottement. De plus, les niveaux d'accélération testés n'ont pas généré d'efforts de contact importants. Considérant les tests de choc, les effets sont plus visibles. D'une part, car les niveaux d'accélération testés sont plus élevés et d'autre part, car les paliers atterrisseurs ne sont pas entraînés en rotation jusqu'à la vitesse du rotor. Les effets de frottement sont plus élevés que pour les essais harmoniques. De plus, certaines instabilités fugaces ont été observées expérimentalement. Cependant, ces dernières n'ont jamais été établies et le rotor a toujours été rapidement centré par les PMAs. Ces instabilités sont susceptibles d'être déclenchées par les PMAs. Une analyse plus détaillée montre que ces derniers apportent de l'amortissement négatif pendant un court instant, suffisamment pour pousser le rotor vers l'instabilité. Rapidement après cela, le contrôleur recentre le rotor et génère de nouveau de l'amortissement.

Conclusions

Dans le but d'améliorer constamment la conception et l'exploitation des machines, cette thèse contribue à l'amélioration des connaissances concernant le comportement dynamique des turbomachines lorsqu'elles sont soumises à des événements externes critiques. Les problematiques des rotors embarqués, des paliers magnétiques actifs et des paliers atterrisseurs sont d'abord analysées individuellement puis combinées. Le modèle éléments finis du rotor embarqué est basé sur l'approche Lagrangienne intégrant les trois translations et rotations d'une base rigide. Tous types de mouvement (harmonique, choc, etc.) peuvent être implémentés. La formulation énergétique de chaque élément composant le rotor est modifiée : des vecteurs des forces extérieures et des matrices à coefficients paramétriques sont ajoutés aux équations du mouvement conventionnelles des éléments de poutre de Timoshenko. Un avantage majeur de cette méthode réside dans le fait que tout type de palier peut être utilisé. Les PMAs génèrent des forces actives modulées par un contrôleur de type PID augmenté. Plusieurs filtres sont ajoutés afin d'amortir les modes hautes fréquences et d'assurer la stabilité du système. Lorsque le déplacement du rotor dépasse le jeu palier atterrisseur, le contact se produit. Une grande partie du travail concerne la description et la modélisation des différents éléments composant les paliers atterrisseurs et sa liaison avec le stator. Parmi les différents types de paliers atterrisseurs, le roulement à billes est exclusivement étudié. Une loi analytique classique est utilisée pour décrire la relation non-linéaire effort-déflection du roulement et une inertie de rotation équivalente basée sur des conditions cinématiques de roulement sans glissement est établie pour la dynamique angulaire du palier. Les propriétés dynamiques du joint mécanique situé entre la bague extérieure du palier et le stator, appelé ruban amortisseur, ont un rôle majeur. Cet élément a été testé expérimentalement et génère un amortissement par frottement sec lorsqu'il est soumis à des excitations harmoniques. Le modèle de Dahl généralisé est une équation différentielle non-linéaire du premier ordre adaptée pour reproduire fidèlement le phénomène observé sous forçage harmonique. La validation expérimentale du modèle de palier atterrisseur s'effectue à l'aide d'un système rotor-PMA d'échelle industrielle. L'idée était d'obtenir un modèle suffisamment détaillé capable de générer les phénomènes observés. Des investigations numériques et expérimentales ont été menées pour des essais d'atterrissage à l'arrêt et à 6 500 tr/min. Les modèles développés permettent d'obtenir des résultats satisfaisant.

Il est observé que :

- Une simple loi de contact bilinéaire semble être assez précise pour décrire adéquatement la dynamique du rotor et les charges d'atterrissage.
- Le temps de mise en rotation du palier atterrisseur est correctement estimé à l'aide d'une seule équation du mouvement. La condition cinématique de roulement sans glissement semble être valide.
- Le ruban a un comportement différent lorsqu'il est soumis à des excitations transitoires plutôt que des excitations harmoniques.

Par la suite, des investigations expérimentales et numériques ont été menées en considérant un système rotor-PMA de type académique soumis à des mouvements de son support. Le rotor possède les caractéristiques dynamiques des turbomachines réelles et le contrôleur PID implémenté a été réglé pour des effortss dynamiques conventionnels (balourd, effets gyroscopiques). Des essais harmoniques et impulsionnels ont été réalisés. Les conclusions générales, qui peuvent être valables pour tout type de design de turbomachines, sont listées comme suit :

- Lorsque les mouvements de support dépassent la capacité dynamique des PMAs, les charges sont partagées avec les PMAs limitant ainsi les charges aux paliers atterrisseurs.
- Les modes couplés rotor-palier atterrisseurs sont excités tout au long de la durée de contact.
- La mise en rotation du palier atterrisseur réduit les effets de frottement pendant les tests harmoniques et ces derniers sont plus visibles sur les essais de choc.

Les conclusions, au moins valables dans le cadre de cette thèse, sont listées comme suit :

- Le contrôleur PID est capable de supporter les efforts classiques associés à la dynamique des rotors, les effets du mouvement de la base et les efforts non-linéaires de contact, sans développer d'instabilités établies.
- Aucune saturation d'amplificateur ni de forte non-linéarité magnétique ont été révélées ; ceci est principalement dû au fait que le ratio des jeux rotor-palier atterrisseur, rotor-PMA est de 0,25 dans le système testé, limitant ainsi l'apparition de ces non-linéarités de PMAs.
- Les charges de contact prédites pour tous les cas testés étaient loin de la capacité de charge maximale des paliers atterrisseurs.

D'une manière générale, le modèle produit des résultats fiables. La validation du modèle numérique développé avec un banc rotor-PMA de type universitaire donne confiance quant à la capacité du modèle à reproduire les phénomènes physiques observés en considérant des designs de turbomachines réelles. D'un point de vue industriel, il est encore difficile de réaliser des essais de mouvement de la base sur des machines pour des problèmes évident de masse. Le modèle pourrait avoir une grande utilitée lors des phases avant-projets pour la conception et le dimensionnement des turbomachines industrielles embarquées sujettes à leurs environnements extérieurs.

Perspectives

Un certain nombre de perspectives peuvent être envisagées pour la suite de ce projet. Tout d'abord, la conception du PID conventionnel pourrait être améliorée en considérant au moins le premier mode couplé rotor-palier atterrisseur. Le fait d'amortir cette fréquence pourrait empêcher les instabilités fugaces du contrôleur observées lors des essais de chocs. Plusieurs stratégies de contrôle pourraient être utilisées pour limiter séparément les effets du mouvement de base et du contact. Tout d'abord, l'effet du support pourrait être réduit en mettant en place une boucle de contrôle type feedforward, en utilisant l'accélération de support comme entrée.

Si le contact se produit, la stratégie de contrôle floue utilisant des quantités polaires pourrait être améliorée pour traiter les problèmes de contact. L'effet du contact est clairement visible sur le déplacement normal tandis que la vitesse tangentielle du rotor donne des informations utiles sur les effets de frottement. L'augmentation de l'amortissement tangentiel pourrait probablement limiter ces effets. Compte tenu des rotations du support (tangage ou pontage), il pourrait être intéressant de déterminer l'effet d'un contrôleur PID simple sur les zones d'instabilité produites par les excitations paramétriques. Le modèle du ruban amortisseur basé sur des tests d'excitation harmoniques a donné des résultats précis. Cependant, son comportement en transitoire semble être différent. Il pourrait être intéressant de mettre en place un seuil de glissement dépendant de la vitesse de la bague extérieure du palier atterrisseur. Des tests d'impact devraient être effectués sur le ruban pour analyser l'évolution du seuil de glissement en fonction de la vitesse d'impact. Des modèles discrets de ruban pourraient également être envisagés. La validation de la modélisation rotationnelle pourrait être effectuée en mesurant la vitesse de rotation du palier atterrisseur d'un banc d'essai à la suite d'un atterrissage. En parallèle, une simulation utilisant des éléments roulants avec plusieurs degrés de liberté pourrait être effectuée pour analyser les limites de la modélisation considérant une seule équation du mouvement pour la mise en rotation du roulement.

List of Figures

List of Tables

List of Symbols

Symbols

As the problem is multi-physic, several letters are used for different meanings and the major part of symbols is defined locally. The main symbols (used in different sections) are defined below.

M, K^e, C^g	Conventional rotor mass, stiffness and gyroscopic matrices	–
K^*_{bm}, C^*_{bm}	Rotor stiffness and gyroscopic matrices associated with base motions (rotations)	–
F_{bm}	External force vector associated with base motions (rotations, translations)	–
$F_{mu,bm}$	Mass unbalance force vector associated with base motions (rotations)	–
F_{mu}	Conventional mass unbalance force vector	–
F_g	Gravity force vector	–
ψ	Modal matrix	–
δ	Generalised rotor coordinates vector	–
δ_0	Nominal rotor-stator clearance	$[m]$
δ_{rs}	Rotor-stator clearance	$[m]$
R_{rotor}	Rotor radius	$[m]$
x_0, y_0, z_0	Support translations	$[m]$
Ω	Rotor rotational speed	$[rpm]$
$\omega^x, \omega^y, \omega^z$	Support angular speeds	$[rad.s^{-1}]$

F_{amb}	Magnetic bearing force vector	–
$f_{amb,l}$	Linear magnetic bearing force	$[N]$
$f_{amb,nl}$	Nonlinear magnetic bearing force	$[N]$
k_i	Magnetic bearing current stiffness	$[N.A^{-1}]$
k_x	Magnetic bearing negative stiffness	$[N.m^{-1}]$
g	Magnetic air gap	$[m]$
g_0	Nominal magnetic air gap	$[m]$
i	Current in coil	$[A]$
i_c	Control current	$[A]$
I_0	Bias current	$[A]$
I_W	Static control current	$[A]$
N	Number of turn in coil	–
μ_r	Relative magnetic permeability of steel	–
μ_0	Magnetic permeability of vacuum space	$[H.m^{-1}]$
S	Active surface (cross-section area)	$[m^2]$
α	Angle between the action line and the line linking the rotor centre to the pole centre	[deg]

Z	Number of rolling elements	–
ξ_{ir}, ξ_{or}	Inner and outer race conformity parameters	–
Γ	Curvature difference	–
α_c	Ball bearing contact angle	[deg]
D	Ball diameter	$[mm]$
d_{ir}, d_{or}	Inner and outer race contact diameters	$[mm]$
d_m	Pitch diameter	$[mm]$
$\Re$	Equivalent radius	$[mm]$
δ_r	Overall ball bearing radial deflection	$[mm]$
F_r	Overall ball bearing radial load	$[N]$
k_{brg}	Ball bearing stiffness	$[N.m^{-1}]$
c_{brg}	Ball bearing damping	$[N.s.m^{-1}]$
ω_{ir}	Inner race angular speed	$[rad.s^{-1}]$
J_{eq}	Equivalent ball bearing rotational inertia	$[kg.m^2]$
M_1	Ball bearing resistance torque due to external loads	$[N.m]$
Ω_{tdb}	Ball bearing rotational speed	$[rpm]$
Φ	Ball bearing rotational damping	$[N.m.s.rad^{-1}]$

F_c	Contact force vector	–
μ	Sliding friction coefficient	–
f_n	Normal contact force	$[N]$
f_t	Tangential contact force	$[N]$

Abbreviations

ADC	Analog to digital converter
AMB	Active magnetic bearing
DAC	Digital to analog converter
FE	Finite element
FF	Feedforward loop
FPSO	Floating production storage and offloading
FRF	Frequency response function
FXLMS	Filtered-x least mean square
GE	General electric company
ICL	Integrated compressor line
IIR	Infinite impulse response
MIMO	Multiple input multiple output
PID	Proportional integral derivative
PWM	Pulse width modulation
SISO	Single input single output
TDB	Touchdown bearing
TDC	Top dead centre

Chapter 1

General introduction

Contents

1.1 Motivations

1.1.1 Context

Since the second industrial revolution a hundred years ago, global energy consumption has never stopped growing and is now a major challenge for our modern societies. The increasing population drives industrial firms, specialists of energetic production, in developing new technologies to meet this challenge. Usually, the manipulation of energy is realised by machines. Generally speaking, turbomachinery play a key role in the transformation, extraction or transport of the different types of available energies. An example of these machines is presented in Figure 1.1. Turbomachinery is a generic term for rotating machines that interact with a fluid in any kind of manner.

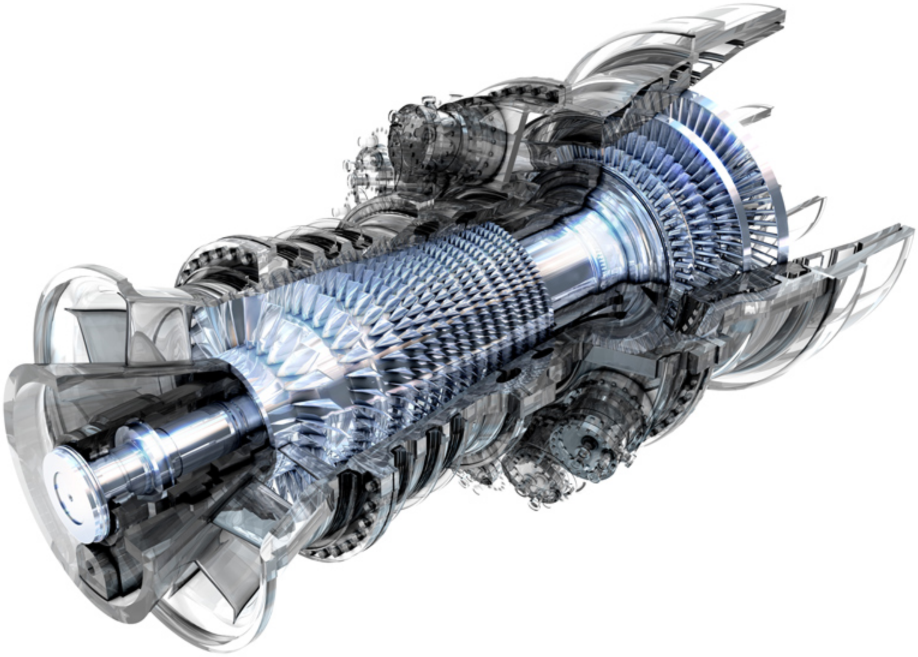

Figure 1.1: GE turbomachinery

The working principle of these machine will be further detailed. They are employed in many industrial applications such as nuclear power plant, aircraft, automotive, oil platforms, etc.

Depending on the targeted applications, these machines may have to face more or less severe environmental conditions. For example, turbomachinery used for the electrical production in nuclear plant may deal with earthquake such as the recent events of Fukushima in Japan where the station, see Figure 1.2(a), was deeply damaged. Another example concerns the off-shore production of oil. Floating production storage and offloading (FPSO) units, see Figure 1.2(b), are floating vessels used for the off-shore production and storage of oil. Turbomachinery are needed in these boats for oil and gas processing. During storms, large waves crashing on the hull of the boat can cause large structural vibrations.

(a) Nuclear power plant (b) Floating production storage and offloading

Figure 1.2: Applications for turbomachinery

In both these cases, the operability of turbomachinery, defined as the capacity of a machine to operate safely and reliably in any circumstances, may be affected. Above a certain magnitude threshold, an emergency shut-down procedure stops the machine to avoid non-mastered behaviours and structural damages. Considering large turbomachinery such as those in nuclear plants, the time to restart and recover nominal operating conditions can be very long. If some structural damages occurred, maintenance implies non negligible costs.

On the other hand, industrial companies, specialising in energetic production, need machines with a maximal operability to respond to the growing energy needs. The question of turbomachinery manufacturers is then how to enhance the operability of their products facing external environments ? One response to that particular point could be an optimal conception and design able to handle these events. However, this is possible only if the effects of these events are well-understood, which can be done with experiences or reliable predictions. It is often accepted that simulation is the most efficient solution for industrial companies since numerical tools are widely spread and powerful computers permit realizing highly detailed simulations.

This research project, performed in collaboration with the GE Oil & Gas company and the LaMCoS laboratory of INSA Lyon, contributes to the improvement of knowledge concerning the dynamic behaviour of turbomachinery when subjected to external events.

In what follows, a brief introduction on turbomachinery principles and on the concept of active magnetic bearings (AMBs) is given. Unexpected events such as AMB shut-down and the case of an "on-board" machine are defined. The positioning of the study introduces the literature review on the different phenomena involved in this research project. Finally, the objectives and the approaches of this study are presented.

1.1.2 About turbomachinery

Turbomachinery manages fluid-mechanical transfer energy thanks to the interaction of a rotor placed in a stream of fluid. Depending on the path of that energy transfer, the machine will be called a compressor or a turbine. Basically, compressors use mechanical energy to compress fluid while turbines convert kinetic energy from fluid expansion into the spin-up of wheels. The term “compressor” is usually employed when the fluid is a gas while “pump” is used for liquid. Gas turbines, see Figure 1.1, combine both an upstream compressor and a downstream turbine separated by a combustion chamber where fuel is burned. It is then a type of internal combustion engine which is employed in aircraft application for example. Turbomachinery can be open or closed. Wind turbines or propellers are example of open turbomachines, not considered in this research project. They can be classified according to the fluid flow direction with respect to the rotor shaft line. The latter can be axial, radial or mixed. The fluid-transfer energy is based on well-known physical laws in thermodynamics and fluid dynamics, not detailed here, but also mechanics. A consequence of Newton’s second law is the conservation of angular momentum relating the sum of external moments to the change of angular momentum. This is of fundamental importance for all turbomachinery since it drives the required and generated torques respectively for compressors and turbines.

Compressors

Often, compressors are driven by electrical motors or turbines. The machine category and the requested power are chosen according to the flow rate and pressure requirements, which depend on the targeted application. Axial compressors are designed for high volume and relatively low pressure output while centrifugal compressors, see Figure 1.3, cover a large range of volume and pressure ratio. Impellers use the centrifugal effect to push the fluid in small channels progressively increasing its pressure. Several stages of compression are often needed to provide the requirements. For centrifugal compressors, this value can reach several hundreds of bars. Mixed axial centrifugal configurations are often found in industrial applications.

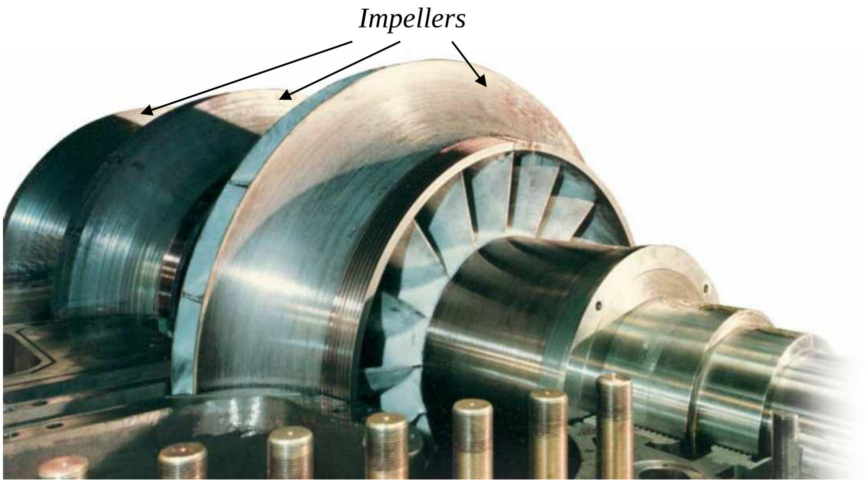

Figure 1.3: Horizontally split centrifugal compressor

Turbines

Turbines drive alternators, compressors, power gear transmissions, etc. Different types exist but the two mainly used in industrial applications are either impulse or reaction turbines, depending on the type of forces involved in the spin-up of turbine wheels. Considering impulse design, a high velocity jet is created by a nozzle where the fluid pressure is expanded. This jet is projected onto concave blades where a large change of its direction creates an impulsive force. Usually, this type of machine is employed for high pressure applications. The Pelton wheel is an example of impulse turbine used in hydraulic power station. Considering reaction turbines, no nozzles are employed; the blades profile at the rotor and stator side are designed to behave like airplane wings in a fluid flow. The latter streams smoothly and the decrease of pressure is done progressively. This type of turbine is employed for low to medium pressure applications. Usually, several stages are needed to better exploit the fluid pressure drop. Nowadays, turbine conception often combine both these designs.

To sum up, in any type of turbomachinery whether compressors and turbines, the rotating shaft is the key part of their working principles. Sustaining its rotation is then of major importance and this task is carried out by bearings providing a rotor-stator mechanical link. Three main types of bearings exist:

- Rolling element bearings: the most commonly used bearings. Many different types of rolling elements may be employed such as balls, cylindrical and tapered rollers, etc. which are placed between the inner and outer races. These bearings carry loads without significant rolling resistance. Usually, lubrication systems improve the tribological aspects limiting the direct steel-steel contact between the different components.

- Fluid bearings: a thin fluid layer separates component surfaces avoiding direct contacts. Oil, air or even water may be employed. Pressurised fluid is used in hydrostatic bearings while the rotating surfaces of hydrodynamic bearings suck the fluid into the bearing. Start-up phases can be delicate and rotor instabilities as well as complex nonlinear phenomena may be exhibited.

- Magnetic bearings: they can be passive or active and only the latter is considered in this project. Active magnetic bearings provide a non-contacting pivot linkage thanks to magnetic levitation. It is a purely mechatronic product supporting high speed rotors for medium power applications. Inherently unstable, this technology needs a feedback control loop.

1.1.3 Positioning of the study

AMBs are employed in the rotor-bearing system investigated in this research project. This type of technology is present in a large number of applications such as flywheels, turbomolecular pumps, compressors, high speed milling spindles, etc. In contrast with conventional bearings, AMBs avoid direct contacts between the rotor and the stator thanks to magnetic levitation. They have many advantages over conventional bearing systems. No direct contact is obviously the main advantage, but the energetic losses are also strongly limited and the turbomachinery is therefore more efficient. Using conventional bearing needs the use of a gearbox to manage power coming from electrical motor while AMB technology allows a direct coupling for higher operating speeds. Wear or oil contamination are no more considered and lubrication systems are no longer relevant. The footprint is also strongly reduced and AMB-equipped turbomachinery can be used for subsea applications. Since 2007, GE Oil & Gas has manufactured centrifugal compressors supported by active magnetic bearings. The integrated compressor line (ICL) obtains the same performance than a conventional 6 MW unit while reducing the size (length) by two, as shown in Figure 1.4. The ICL saves almost 30 metre cube of lubricant, per year and per unit, while avoiding the emission of 600 tons of CO2.

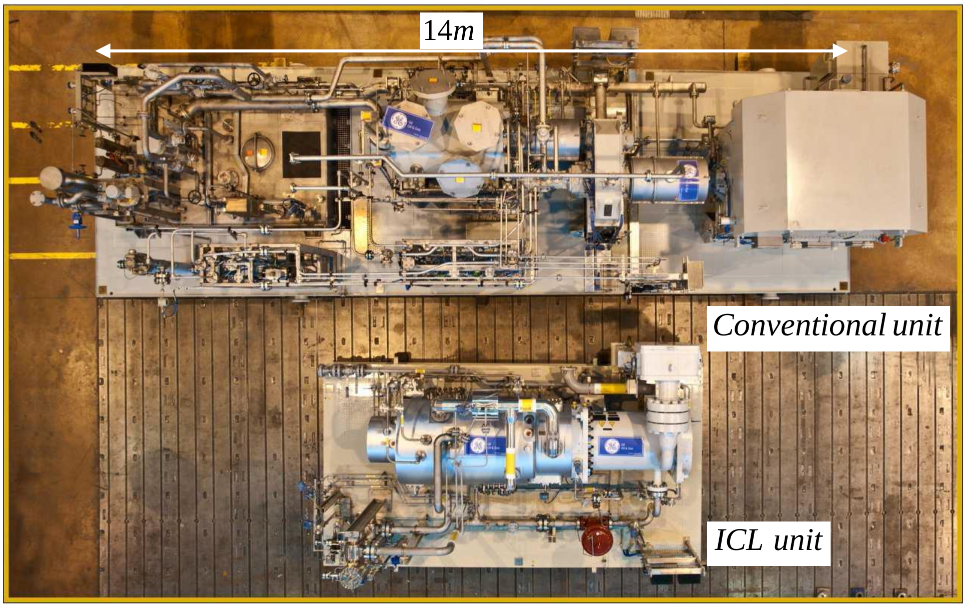

Figure 1.4: Integrated compressor line - GE Oil & Gas

The rotor levitation is achieved by attractive magnetic forces induced by a current applied in a coil wounded around a magnet, see Figure 1.5. This attractive force is nonlinear since it is relative to the square of the applied current in the coil and reversely proportional to the square of the rotor position. The nature of the force makes the rotor-AMB system unstable and this must be compensated by a proper control loop. Proportional-integral-derivative (PID) feedback is the most employed control strategy in industrial applications. Optimal control, μ-synthesis or fuzzy logic are other types of strategies which are not detailed in this research project. If not well designed, the controller may produce instabilities. Rotor-AMB systems are systematically equipped with touchdown bearings (TDBs) supporting the shaft when magnetic levitation is

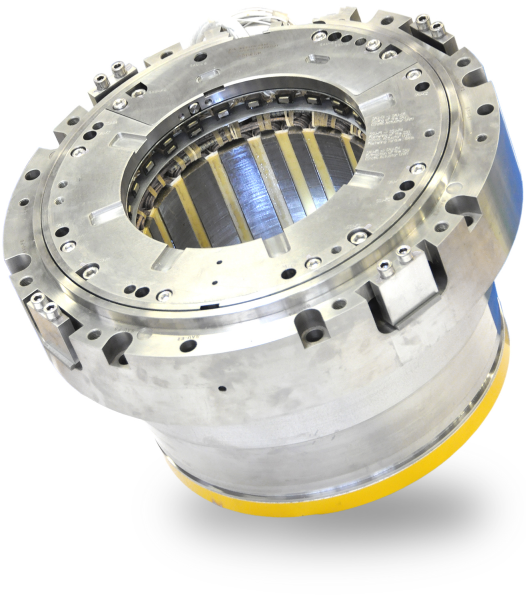

Figure 1.5: Active magnetic bearing - SKF®

no more provided. This can happen when the machine is stopped, during transport or when unexpected AMB shut down occurs. In this case, the rotor usually ensures a transient dynamic behaviour characterized by harmless rebounds followed by pendulum motions. In some particular cases however, the rotor may develop dangerous dry friction self-induced instabilities, called “dry whip”. Considering this type of behaviour is of major importance for the design of rotor-AMB systems and especially TDBs. Most of the turbomachinery can be considered as “on-board” machines, which means that their supports are not fixed with respect to the ground. This is the case for automotive turbochargers, aircraft engines, emergency steam turbines in nuclear plants or centrifugal compressors mounted on FPSO.

The improvement of technologies requires one to consider all the possible disturbances encountered during the product lifetime. When examining on-board turbomachinery, the rotor has to face external disturbances coming from the frame motions. Considering rotor-AMB systems, this could lead the rotor to contact with the TDBs while operating, creating complex nonlinear vibrations and potential instabilities. Two main consequences of these critical conditions are important to avoid:

- Controller instabilities
- Rotor-TDB dangerous rubbing vibrations

The following literature review provides insights into the phenomena involved in this study such as on-board rotor dynamics and rotor-TDB interactions. The phenomenological aspects are highlighted.

1.2 Literature review

When structures are subjected to dynamic loads, vibration analysis becomes necessary for optimal design of products. Lalanne *et al.* [28] gave an extended overview of vibration phenomena, such as resonances, damping effects, forced vibrations, etc. using a single degree of freedom mass-spring-damper system. Rotors in turbomachinery are also subjected to dynamic loads. A detailed and practical overview on rotordynamics is given by Swanson *et al.* [29]. Basic phenomena associated with rotating machines are explained such as gyroscopic and mass unbalance effects, rotor forward or backward whirl, etc. A complete procedure for the modelling and the prediction of bending rotors is given by Lalanne and Ferraris [30]. For more insights about rotordynamics phenomena, readers can refer to the work of Genta [31].

Most rotating machinery can be considered as on-board machines. On the other hand, active magnetic beatings are increasingly being employed to sustain rotors in industrial applications for their different advantages. In the case of extreme external events, rotor-AMB systems may deal with nonlinear TDBs interactions generating a wide variety of regimes and complex dynamics. The problematic of this project is multiphysics and an appropriate literature must bring insights and understandings onto the involved phenomena. A non-exhaustive literature survey is given in the next section on the different problematics listed hereafter:

1. Rotor-bearing and rotor-AMB systems subjected to base motions.
2. Rotor-stator interactions and the related phenomena. The rotor drop, occurring when no more magnetic levitation is provided, is investigated further.

1.2.1 Base motion phenomena

Considering a simple non-rotating system such as a composite pendulum attached to a harmonically base excited mass-spring subsystem, Berlioz *et al.* [1] showed all the complexity of parametric excitations related to base motions. Nonlinear equations of motion of the pendulum fixed on a translation mass are considered and the experimental set-up is sketched in Figure 1.6(a).

Considering a base frequency fixed at 3.5 Hz, increasing the amplitude parameter leads to a period-doubling bifurcation at around 4.7 mm, see Figure 1.6(b). The points A, C and D represent respectively periodic, quasi-periodic and chaotic motions. The stability of solutions are found with symbolic computation of the Floquet transition matrix based on Chebyshev polynomial expansions. The same kind of equations of motion with parametric coefficient were developed by Doughty [32] for a single degree of freedom system such as simple slider-crank mechanism.

Generally, industrial turbomachinery supports are very stiff. The transmissibility to the rotor is then high and the dynamic contributions of the foundation may be neglected. In what

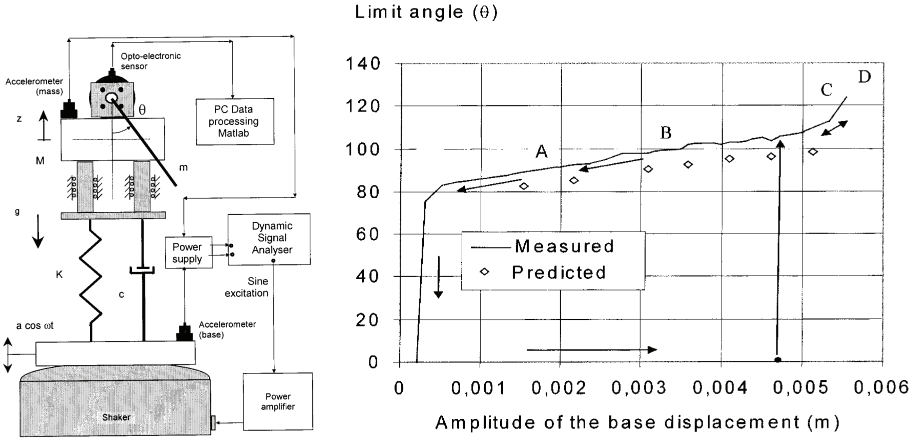

(a) Experimental set-up

(b) Bifurcation diagram

Figure 1.6: Experimental vs predicted results - Berlioz *et al.* [1]

follows, the base is always considered rigid and movable. However, some works consider flexible supports, and readers can refer to the works of Edwards *et al.* [33], Bonello and Brennan [34], Feng and Hahn [35], Cavalca *et al.* [36] or Lees *et al.* [37].

For the rest of this section, Figure 1.7 will be the reference for the analysis of base motion considering a rigid, but movable base. The three translations of the base are described by x_0, y_0, z_0. The base rotations, the pitching, the rolling and the yawing are represented by $\omega^x, \omega^y, \omega^z$, respectively. The parameters ω and Ω refer to the base motion frequency and the rotor rotational speed respectively.

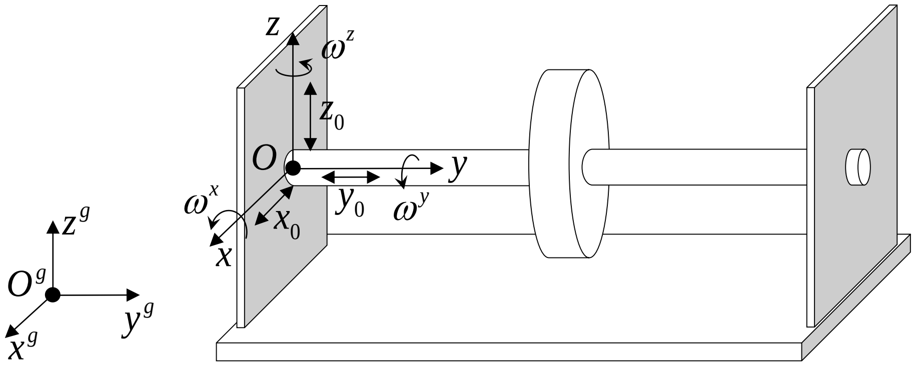

Figure 1.7: On-board rotor on a rigid but movable frame

The effects of constant base motions on the rotor behaviour are explained by Dakel *et al.* [38, 39]; a constant acceleration $\ddot{z}_0$, along the z-axis for example, results in a rotor static deflection acting like the gravity. A constant rotation of the base along the x-axis, $\omega^x \neq 0$, generates rotor-bearing system anisotropy while a constant rotation of the base along the y-axis, $\omega^y \neq 0$, modifies the rotor natural frequencies and the backward/forward whirl modes may be reversed.

1.2.1.1 Sinusoidal motion of the base

On-board turbomachinery may be subjected to harmonic base motions. This can be the result of the dynamic response of their supporting structures for example. For the machine, this response implies rotational and/or translational motions. Hereafter is presented the different effects of sinusoidal base motions on the dynamic behaviour of on-board rotors.

Parametric instabilities

Taking into account sinusoidal base rotations raises the issue of the system stability. Indeed, base motions generate parametric excitations that depend on rotation terms. Considering simple models, like a Rayleigh rotor, the multiple scales method enables to analyse the system stability, as realised by Driot *et al.* [4] and Duchemin *et al.* [2] At certain angular frequencies ω combined with the rotor natural frequencies, instabilities are exhibited, in the sense of an indefinitely increase of amplitude. The determined instability zones depend on the angular magnitude, as shown in Figure 1.8. These zones are reduced by adding damping.

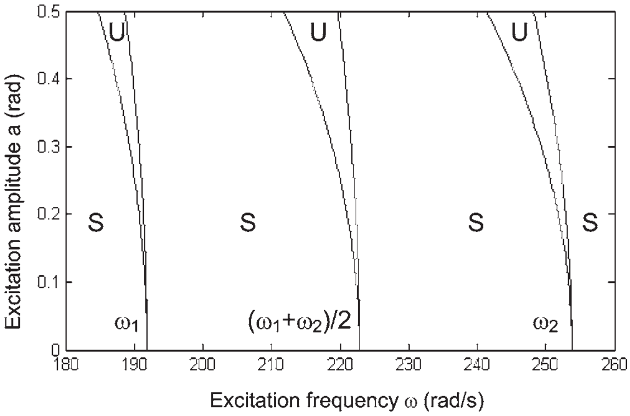

Figure 1.8: Instability zones (u) and stable zones (s) vs angular frequency and amplitude considering a sinusoidal rotation ω^x - Duchemin *et al.* [2]

The same kind of study was realised by Dakel *et al.* [39] while considering a Finite Element (FE) rotor model. Several combinations of base rotations, such as $\omega^x \neq 0$ and $\omega^z \neq 0$, are analysed by Han and Chu [40]. Instability regions are more extended in the case of base rotations along the rotor spin axis, $\omega^y \neq 0$. The phase angle between the different excitations is fundamental for the stability of the rotor.

Particular combinations

Particular combinations of rotating effects (unbalance forces and gyroscopic moments) and base motions can be exhibited. In case of a vertical sine translation z_0, Duchemin [3] showed the gyroscopic coupling effects using a simple Rayleigh rotor with a decentred disc, see Figure 1.9(a). The rotor deflection was pushed orthogonally with respect to the translation direction. This effect was proportional to the rotational speed. In case of base rotations along the x-axis,

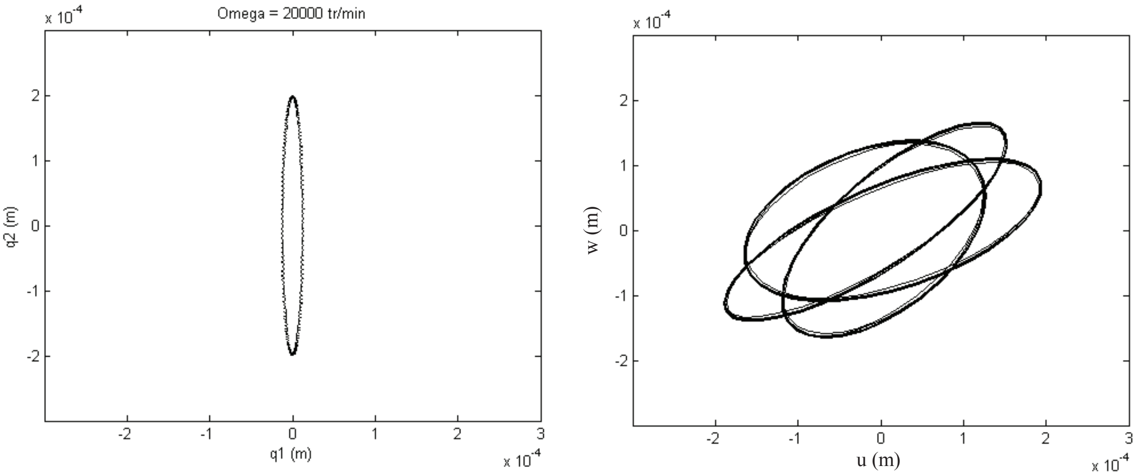

(a) Translational combination - Ω=333 Hz and ω=2 Hz (b) Rotational combination - Ω=20 Hz and ω=30 Hz

Figure 1.9: Effects of the base motion on the dynamic behaviour of a spinning shaft - translation (a) see Duchemin [3], and rotation (b) see Driot *et al.* [4]

$\omega^x \neq 0$, combinations with unbalance forces are generated, resulting in a multiple harmonic response. According to Driot *et al.* [4], when the ratio of the support rotational frequency over the shaft rotational speed is a natural number, the rotor orbits are fixed and perfectly periodic, as shown in Figure 1.9(b). It was noticed that when the same ratio is a rational number, orbits are periodic with more complex shapes. Bouziani and Ouella [41] studied the dynamic behaviour of a rotor subjected to different kind of base motions and a variable rotor spin speed. No particular coupling was identified between the stiffening effect of the variable spin speed and base motions.

Nonlinear effects

When on-board rotors are supported by nonlinear bearings, complex dynamics are expected. El-Saeidy and Sticher [42] studied the effects of harmonic base motions on a rigid rotor considering linear and cubic nonlinear force-deflection characteristics for a ball bearing. In Dakel *et al.* [38, 5], a FE rotor model supported by nonlinear hydrodynamics bearings was studied. Depending on the amplitude of the applied sinusoidal base motion (translation z_0 or rotation ω^x), the rotor-bearing system exhibits periodic, quasi-periodic or even chaotic motions, as shown with the simple pendulum system of Berlioz *et al.* [1]. These nonlinear behaviours are analysed by means of bifurcation diagrams, see Figure 1.10, using the amplitude of the base motion as control parameter. These diagrams reveal the type and the change of dynamic regimes. The stability of dynamic solutions (in the sense of the change of dynamic regime) is studied through the "Floquet transition matrix" and its eigen values. When the latter remain in the unit circle, the solution is stable.

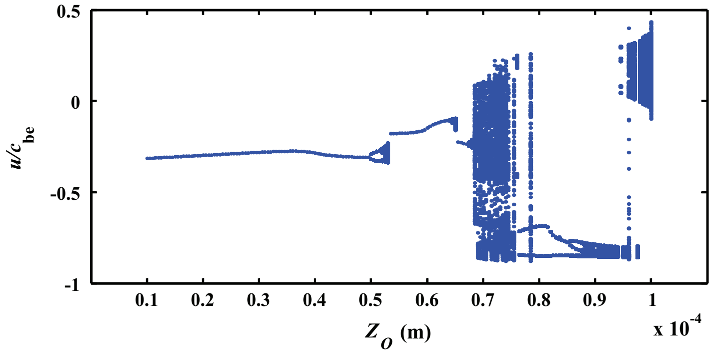

Figure 1.10: Bifurcation diagram of a rotor supported by nonlinear hydrodynamic bearings subjected to sinusoidal translation motion z_0 from its base at different amplitude Z_0 - Dakel *et al.* [5]

1.2.1.2 Shock and earthquake

Real turbomachinery may be subjected to earthquakes or shocks. The dynamic behaviour of a 17 kg rotor mounted on ball bearings subjected to vertical shock z_0 was analysed numerically and experimentally by Lee *et al.* [6]. The importance of the duration of the shock on the rotor response was highlighted. When the frequency of the shock is close to a rotor-bearing system natural frequency, a significant vibration amplification is observed. Gyroscopic coupling effects just after the shock were also exhibited. An energy transfer between directions was observed; the amplitudes along the loading direction decrease while those in the perpendicular direction progressively increase, as shown in Figure 1.11.

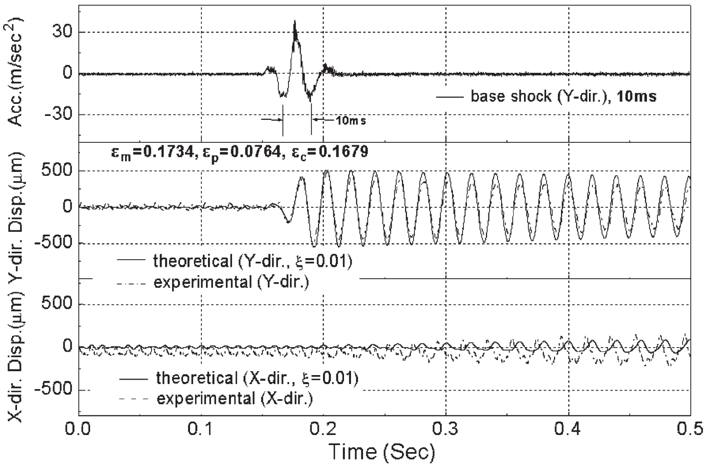

Figure 1.11: Base shock response of a rotor in bending along z-axis - Lee *et al.* [6]

The dynamic behaviour of a rigid rotor mounted on linearised hydrodynamic bearings subject to earthquake was investigated by Samali *et al.* [43]. The translations of the base z_0 describe the earthquake with a non-stationary random process like Monte Carlo. The rotational components are related to the translation jerks (time derivative of acceleration) following the approach proposed by Newmark further developed by Ghafory-Ashtiany and Singh [44]. Once the base motions are determined, they are used as input in the rotor-bearing system. These steps are repeated many times to obtain mean values, standard deviations, etc. The authors noticed that the rotational components influence significantly the rotor rotational-type response while the effect on the rotor-bearing relative displacements and force is limited. It was also mentioned that the rotor-bearing system natural frequencies are much higher than the representative frequency of the earthquake, therefore, no large rotor deflections are expected. The analysis of the transient dynamic behaviour of a FE rotor under seismic excitations supported by fluid-film bearings was done by Suarez *et al.* [45]. The translational acceleration time histories $\ddot{z}_0$ are generated thanks to a spectral density function combined with a random phase process. Rotational acceleration inputs are obtained by time-derivation of translations. Even for large base rotations, matrices with parametric coefficients as well as nonlinear terms (product of input velocities) can be ignored without changing the dynamic behaviour of the rotor. However, the second member base rotation terms have a strong influence. The major conclusion of the study was that the analysis of a rotor under seismic excitation can be made by a classical modal approach without using parametric terms. The rotations mainly contribute in the external force vector. It was shown by Hori and Kato [46] that a rotor supported by oil-film bearings can become unstable after a shock or seismic waves.

1.2.1.3 Base motion and AMB

Some studies were dedicated to the dynamic behaviour of rotor-AMB system subjected to base motion for different types of applications. By the end of the 80s, Murai *et al.* [47] were one of the first groups to study the effect of earthquake on a rotor-AMB system. Since that, some works were dedicated to the implementation of different control strategies to limit these base motions and avoid TDBs interactions. Other works showed the effect of base disturbances when the control strategy was not specifically tuned for that purpose.

Conventional controllers

Hawkins *et al.* [48] tested a vertical flywheel-AMB system subjected to translational (z_0) and rotational (ω^x, ω^y) shocks for transit bus applications. Even if the controller was not specifically tuned for base disturbance rejections, it was able to maintain the rotor and no TDB contacts occurred. The use of a shock isolator allowed to reduce the transmitted axial shock by 65 %, corresponding with the work of Leilei *et al.* [49]; using flexible supporting conditions, base disturbance rejection of rotor-AMB system can be improved. Latter, Hawkins *et al.* [50] focused on the same type of AMBs. The authors presented an experimental and numerical comparison of a rotor-AMB system subjected to sinusoidal translation z_0 up to 1.5 G. The target application was a direct drive shipboard compressor for the US Navy using vibration requirements in accordance with MIL-STD-167 standards. AMBs remained in their linear range during these tests. This was not the case in the work of Kasarda *et al.* [51] where a non-rotating mass mounted on magnetic bearings controlled by PID feedback and subjected to a sinusoidal base motion z_0 was analysed numerically and experimentally. The response, depending on the base amplitude, was linear expect in the case of extremely low damping. A nonlinear stiffening or softening response depending on the displacement was observed; the linear assumption of the magnetic bearing force was no more valid. Considering rotor-AMB system subjected to large base motions, the rotor can interact with its TDBs generating complex nonlinear dynamics. Hawkins [52] studied numerically the transient dynamic behaviour of a rotor supported by homopolar, permanent magnet bias magnetic bearings subject to vertical shocks z_0 for US Navy applications. Nonlinearities such as saturation, rotor-stator interactions, clearance effects were taken into consideration. The shock generates an acceleration around 40 G, leading the rotor to contact with the TDBs with a high impact force exceeding its load capacity. Even if some saturation effect appears, the rotor quickly recovered its centred position.

Base disturbance rejections

Several control strategies were developed to limit the base motion effects. The latter concern specifically vertical translation motions z_0, either impulse or harmonic. Matsushita *et al.* [7] investigated numerically and experimentally the dynamic behaviour of a flexible rotor supported by AMBs controlled with conventional proportional-derivative (PD) feedback and subjected to the Kobe earthquake. The accelerograms multiplied by the rotor mass matrix are used as input in the numerical model. A feedforward (FF) compensator generating an action proportional to the external acceleration was implemented to control the base motion; 60 % reduction of vibration amplitude was obtained, as shown in Figure 1.12. In parallel, a design guideline to avoid resonance and rubbing vibrations (rotor-stator contact) was to set the rotor rigid modes above 20-30 Hz, since most of the energy delivered by the seism is contained on that particular bandwidth.

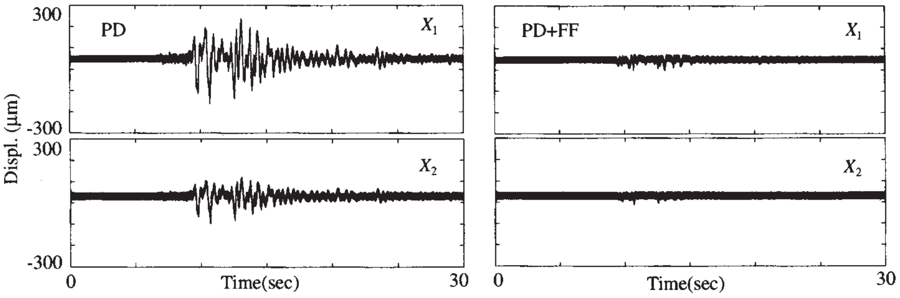

Figure 1.12: Dynamic response of a rotor-AMB system subject to seism (without and with FF control loop) - Matsushita *et al.* [7]

The infinite impulse response (IIR) filter in a feedforward control loop was used by Suzuki [53] to limit the base motion effects on a flexible rotor supported by AMBs controlled by PID feedback. Harmonic and random translation motions are generated by the base. The rotor response, using the feedforward control loop, can be reduced about the half of the response only using PID. Moreover, this amplitude reduction was achieved using less control current. A rigid rotor supported by nonlinear AMBs are considered in the study of Marx and Nataraj [54]. A conventional PD controller was used as feedback loop. The developed feedforward control loop was based on the observation that nonlinear systems generate sub and super harmonics when subjected to harmonic excitations. Therefore, the correction current was set to be a sum of multiples and fractions of the base motion frequency, allowing to effectively reduce the effect of the harmonic translation motion of the base. The acceleration feedforward compensation appears to be also effective in Kang and Yoon [55] to limit harmonic base motions for applications such as electro-optical sight mounted on a moving vehicle. The compensator was designed experimentally thanks to the filtered-x least mean square (FXLMS) algorithm, which was also used by Kim *et al.* [56]. Later, considering the same application, Kang *et al.* [57] used the sliding mode control, which was able to achieve high performance robust control against parameter uncertainties and external disturbances. The case of shock was also treated by Cole *et al.* [58] where an horizontal impact was applied on the base as an external force. Three control strategies are developed to reduce the direct forcing as well as the motions of the support. If the controller was not suitable, the movement of the base may generate contacts between the rotor and the auxiliary bearings. Some control strategies, however, can limit or even prevent the rotor-stator interaction such as the H_∞ controller according to Keogh *et al.* [59]. The combined $wavelet - H_\infty$ controller gives the best performance in terms of transmitted forces and vibration limitations. The wavelet transform decomposes the base excitation signal to allocate the proportion of hard and soft of the H_∞ controller and to obtain benefits from the both of them.

The case of base rotations was investigated by Maruyama *et al.* [60] where the stator motions, integrated as rotation disturbances, act on the rotor-stator relatives angles. The control system is based on a PD controller. An efficient observer allows to estimate the stator disturbances and to cancel it. Finally, the use of magnetic forces can also limit instabilities zones inherent to rotor-bearing system subjected to harmonic pitching motions. This was done numerically by Das *et al.* [61]. A FE rotor supported by conventional bearings is subjected to base pitching motion ω^x. It is shown that a magnetic actuator controlled by a PD feedforward makes the system more rigid deteriorating the areas of instability.

In most of these studies, the rotor response due to base motions remained small, either because a specific control strategy was applied to reject external disturbances (PD feedforward loop, $wavelet - H_\infty$, etc.) or because the acceleration levels tested remained quite small. Even if the nonlinearity of magnetic forces was exhibited in some cases, few studies have considered rotor-TDB interaction while AMBs still operate. This was numerically investigated by Hawkins [52]. In most cases, the rotor-TDB interaction is treated in the context of magnetic levitation losses, called the rotor drop. This is a part of the rotor-stator interaction field which belongs to the more general nonlinear dynamics. As an introduction, readers can refer to the work of Thompson and Ghaffari [62], Shaw and Holmes [63], Mahfouz and Badrakhan [64, 65], Natsiavas [66], Choi and Noah [67], Narimani *et al.* [68], Deshpande *et al.* [69], where simple dynamic systems develop complex behaviours with contact nonlinearties. In the following part, a non-exhaustive literature survey on the rotor-stator interaction is given. Then the particular case of the rotor-drop dynamics, associated with rotor-AMB system and the loss of magnetic levitation is treated.

1.2.2 Rotor stator interaction

Contact represents a large change of the global stiffness of dynamic systems. It is then a strong nonlinearity able to generate asynchronous, quasi-periodic or even chaotic behaviours. A good description of the different rotor steady-state responses under stator interactions as well as their conditions of appearance was done by Jiang *et al.* [70, 71, 72] and Shang *et al.* [73] using a the Jeffcott rotor. Jacquet *et al.* [74] and Alber and Markert [75] summarized the current research on the rotor-stator interaction. Two main categories of rotor contact modes exist:

1. Partial contact, where the rotor motion is characterized by rebounds on the stator. It can be either forward (forward partial rub) or backward direction (backward partial rub). Chaotic motions also exist.
2. Continuous contact, where the rotor can move in forward (full annular rub) or in backward direction (dry whirl, dry whip) in permanent contact with its stator.

1.2.2.1 Continuous contact (forward, backward whirl)

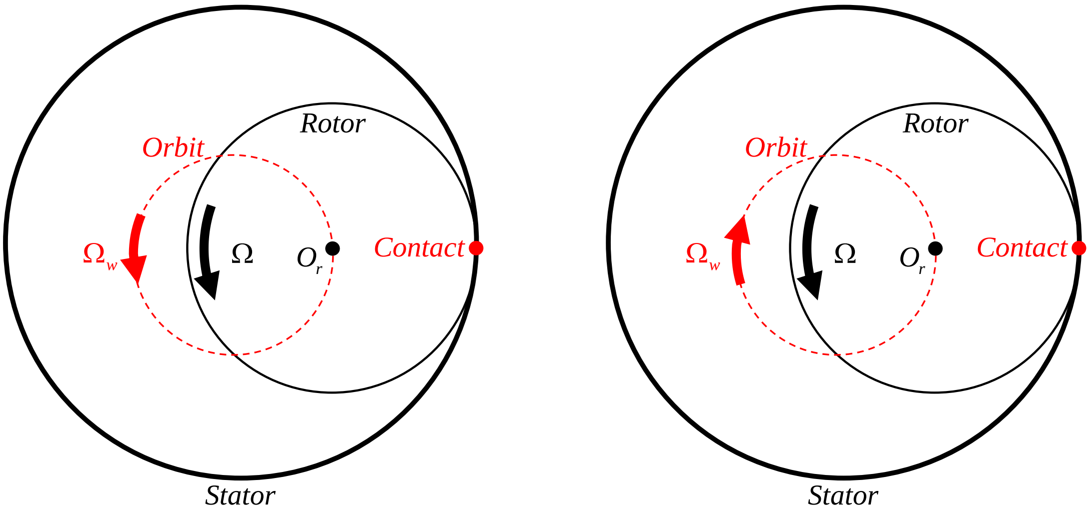

(a) Full-annular rub (b) Dry whirl/whip

Figure 1.13: Continuous contact of a rotor interacting with its stator

The full-annular rub motion, see Figure 1.13(a), is the less dangerous for the turbomachinery integrity. It is generally induced by large unbalance levels. The rotor is in continuous rubbing motion on the stator at a synchronous frequency, the contact loads remaining limited. The backward whirl, see Figure 1.13(b), can be more dangerous. This motion is induced by rotor-stator dry friction that progressively transforms the rotor rotational speed energy into lateral vibrations. When the kinematic rolling-without-slipping condition is satisfied, the regime is called dry whirl. The resulting whirling frequency depends on the shaft spin speed and the ratio of the rotor radius over the rotor-stator clearance, as shown in Figure 1.14. Reaching the coupled rotor-stator natural frequency, the dry whirl ends and the rolling-without-slipping kinematic condition is no longer guarantee. The dry whip regime, which is generally considered as the dry whirl instability, is established, see Figure 1.14. At this point, the rotor whirling speed is close to the circumferential speed and friction forces oscillate around zero. The generated contact loads can be large.

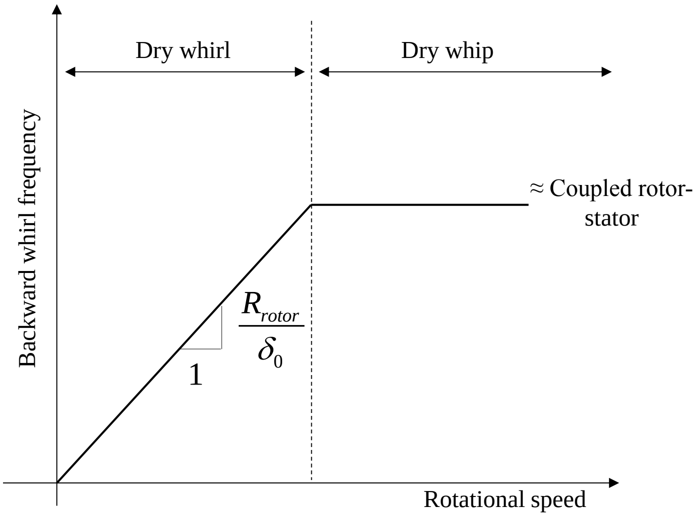

Figure 1.14: Campbell diagram showing the dry whirl to dry whip transition

In 1968, Black [76] used the rotor and stator polar receptances to derive the rotor frequency response in synchronous permanent contact (full-annular rub) with its stator. The nonlinear modes generated seems to be frequency limited by the coupled rotor-stator modes. Establishing rolling-without-slipping kinematic conditions defines zone, called “U-shaped plot”, see Figure 1.15, where the dry whirl motion is possible depending on the rotor spin speed and a “necessary” friction coefficient.

Lingener [77] showed that the dynamic behaviour of the shaft in contact situation was depending on the condition of triggering. Only synchronous vibrations were found when contact was generated with mass unbalance forces. An impulse on the rotor at very low rotational speed generated backward whirl. An asynchronous component, which depends on the rotational speed and the ratio of the rotor radius over the rotor-stator clearance appeared in the spectrum. This phenomenon was later called dry whirl. As shown by Black [76], the latter was frequency limited; the coupled rotor-stator resonates on its first mode and the frequency was no longer dependent on the rotational speed. This phenomenon was later called dry whip. Lingener [77] concluded that the coupled rotor-stator mode represents an impassable limit for a rotor in a per-

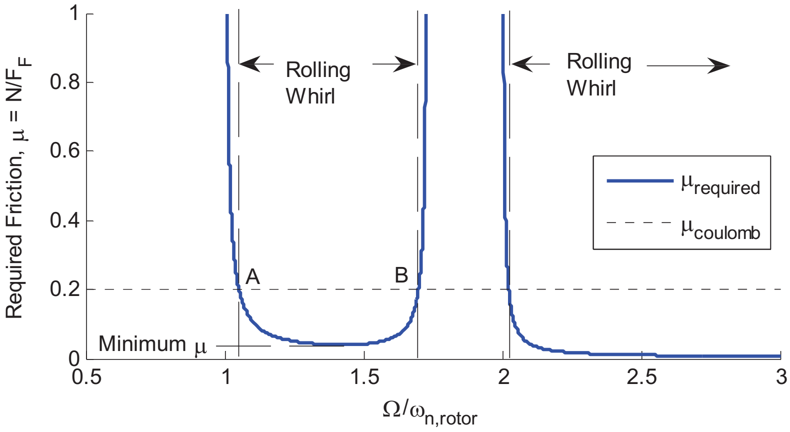

Figure 1.15: U-shaped plot - Wilkes *et al.* [8]

manent contact situation with its stator. Jiang and Ulbrich [70] derived the natural frequency of the coupled nonlinear rotor-stator system considering a Jeffcott rotor. The latter is negative which corresponds to a backward whirl motion. The value of that frequency is smaller but really close to the coupled linear rotor-stator natural frequency.

During his PhD, Bartha [9] especially dealt with the onset mechanisms of the backward whirl motion of rotors. The rotor-stator contact is generated by impacting the rotor with a hammer. The critical radial impact velocity is defined as the velocity from which the backward whirl regime exists, as seen in Figure 1.16(a). The greater the friction coefficient is, the less the critical radial impact velocity must be large to trigger backward whirl. The rotor-stator angle of impact, see Figure 1.16(b), seems to have also a major importance. Indeed, an impact velocity in the direction of forward whirl may be ten times less dangerous than an impact velocity normal to the contact. Jiang [71] built the same kind of map, see Figure 1.16(a), but used the rotor rotational speed instead of the radial impact velocity. It appears that backward whirling may exist at very low rotational speed.

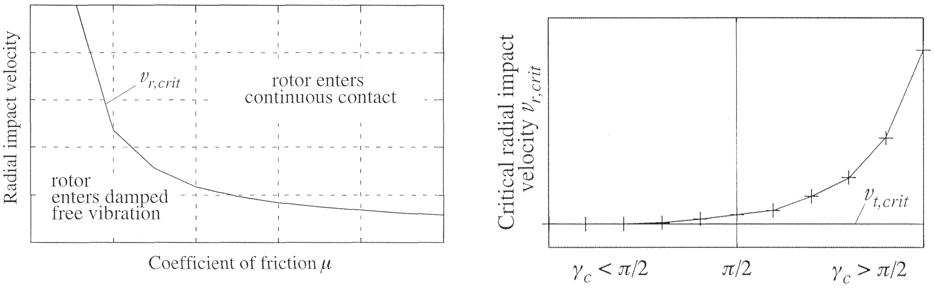

(a) Critical radial impact velocity vs friction coefficient

(b) Critical radial impact velocity vs contact angle

Figure 1.16: Critical radial impact velocity vs friction coefficient (a) and contact angle (b) - Bartha [9]

Choi [10] showed experimentally that the dynamic behaviour of a rotor in contact situation can jump from a dry whip to another dry whirl regime while the shaft speed increases, contrary to the conclusion given by Lingener [77]. These jumps in frequency are followed by jumps in amplitude, the dry whip generating the largest amplitudes. Moreover, the rotor regimes are different whether the rotor runs-up or coasts-down highlighting hysteretic behaviours related to the nonlinear dynamics, as shown in Figure 1.17.

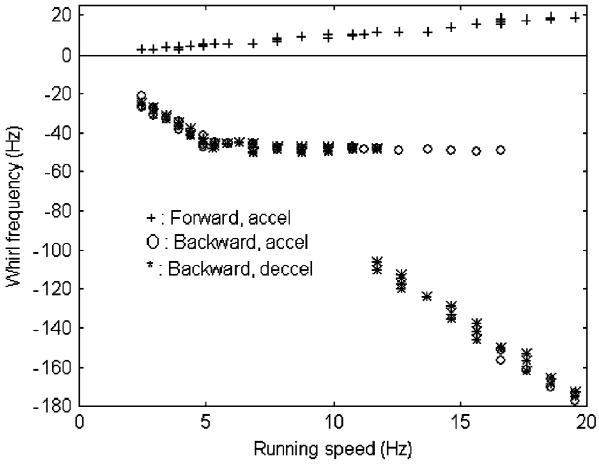

Figure 1.17: Hysteretic behaviour in a Campbell diagram showing dry whip to dry whirl regime jumps - Choi [10]

The computed U-shaped plot fits well with experimental results even if some discrepancies are noticed. Childs and Bhattacharya [78] generalized the solution derived by Black [76] by adding up to seven modes to determine the analytical solutions of the U-shaped plots. The authors used the previous works of Yu *et al.* [13] and Bartha [9]. It is shown that adding modes and shifting the rotor-stator contact location along the shaft line modify the U-shaped plots. Several zones, where backward whirl is possible, were found. Wilkes *et al.* [8, 79] used FE software to determine dry whip and whirl regimes. The numerical results were close to experiments and multiple whip and whirl regimes were exhibited, as previously shown by Ismeurt [80]. The generated sidebands could be the cause of the jumps between different dry whip and dry whirl regimes.

These jumps phenomena were also observed by Bently *et al.* [11, 12] and Yu *et al.* [13] by analysing the dynamic behaviour of an unbalanced rotor in contact with different types of seals. During run-up, the contact is triggered by mass unbalance forces close to the frequency of the first bending mode. In the case of a low friction coefficient using Teflon seals lubricated with oil, the rotor remains in synchronous contact until a jump phenomenon occurs, see Figure 1.18(a). When running-down, the hysteresis phenomena associated with the nonlinear dynamics appear very clearly. With a higher friction coefficient (no lubrication at rotor-seal interface), the synchronous contact mode gradually transforms into backward whirl via partial rub during run-up, see Figure 1.18(b). This was shown analytically by Jiang and Ulbrich [70] where the condition of existence of dry whip was defined to be the rotational speed where the partial rub

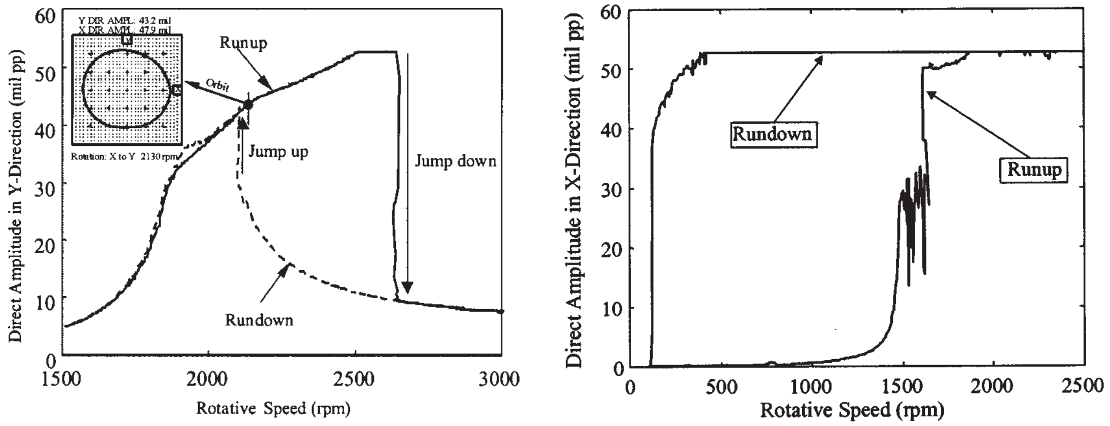

(a) Low friction coefficient (b) High friction coefficient

Figure 1.18: Nonlinear hysteresis phenomenon related to rotor-stator interaction - Bently *et al.* [11, 12] and Yu *et al.* [13]

motion becomes unstable. Once in place, dry whip only disengages at a very low rotational speed since it is a self-sustaining phenomenon. During run-down, the kinematic condition of rolling-without-slipping is reached below 500 rpm. Braut *et al.* [81] analysed numerically and experimentally the dynamic behaviour of a Jeffcott rotor in contact situation due to a sudden unbalance created by a blade loss. After such an event, the rotor is decelerated by the contact forces and an aerodynamic torque. During coast-down, they observed the following behaviours: synchronous contact, intermittent contact phase (partial rub) and a backward whirl regime until the natural frequency of the coupled system was reached. In this case, the rotor is strongly decelerated by the friction forces. The same scenario was investigated by Duran *et al.* [82, 83] who analyse numerically the dynamic behaviour of a helicopter turbine in a multiple contact situation due to blade loss. When coasting-down, predominant forward whirl behaviours are found contrary to Braut *et al.* [81]. Different contact laws are used according to their nature (rotor in contact with seals or blades with abradable materials). The fan blade out scenario is also studied by Wang *et al.* [84] and Sinha [85] for high bypass ratio turbofan engine applications. Some works of Lahriri *et al.* [86] and Fonseca *et al.* [87] investigated unconventional containment bearing to avoid these dangerous dry whip regimes. Several pins, distributed along the circumference, are able to stop continuous contact.

1.2.2.2 Partial contact (forward, backward whirl)

In some of the previous works cited, partial rub motions are transition modes appearing before reaching a dry whirl or whip regime, such as in Bently *et al.* [11, 12], Yu *et al.* [13] or Braut *et al.* [81]. The forward partial rub, see Figure 1.19, is characterized by rebounds mainly in forward direction. Generally, contacts occur more than one time per revolution and these rebounds are characterised by superharmonic components in the frequency domain. The contact force at the interface is larger than the one generated in permanent contact. The whirl direction is forward even if some components are backward.

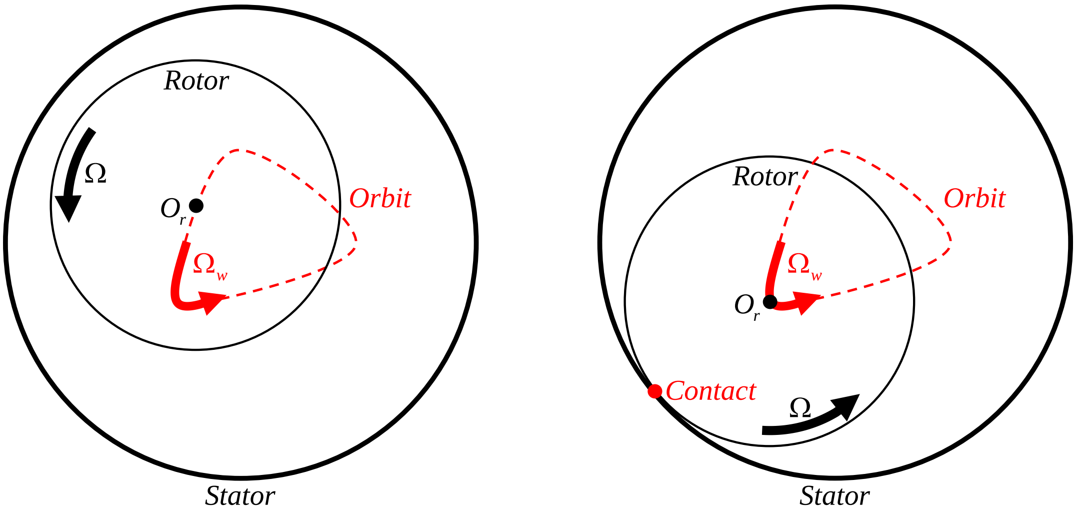

(a) Partial forward whirl - before contact (b) Partial forward whirl - during contact

Figure 1.19: Forward partial rub of a rotor interacting with its stator

The backward partial rub, see Figure 1.20, is also characterized by rebounds but they are generally more violent than those generated in forward direction. These rebounds are generally characterised by subharmonic components in the frequency domain. Rotor-stator interactions appear after several revolutions and the related contact forces are large. The whirl direction is mainly backward even if forward components still exist.

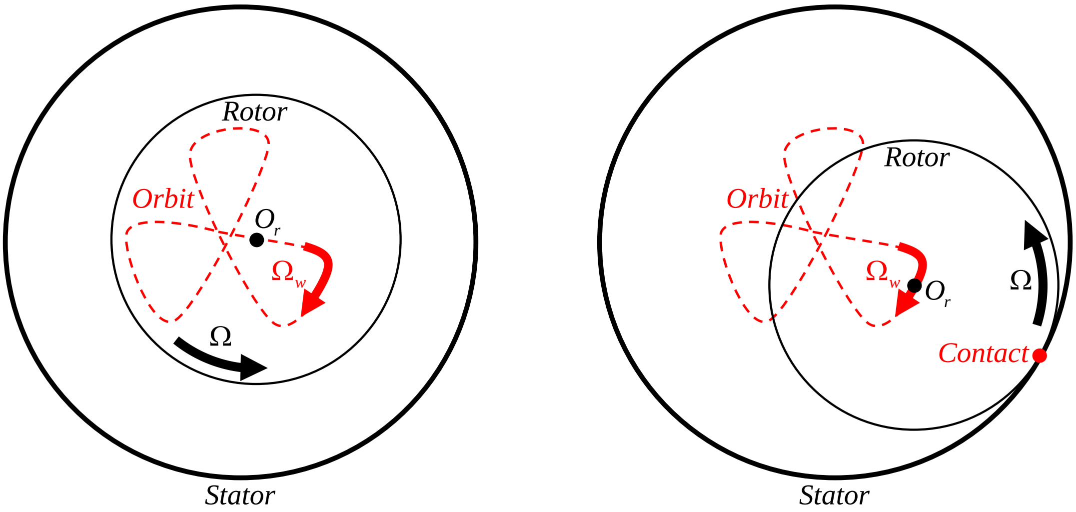

(a) Partial backward whirl - before contact (b) Partial backward whirl - during contact

Figure 1.20: Backward partial rub of a rotor interacting with its stator

The contact generates complex vibrations characterised by periodic, quasi-periodic or even chaotic regimes. Dedicated tools are then used to perform relevant analysis of these complex vibrations such as bifurcation diagrams or Poincaré sections. Muszynska and Goldman [88] showed, using the bifurcation diagram, the various dynamic regimes appearing when the rotational speed increases considering a rotor either in rubbing contact with its stator or after a pedestal loss. The order of the harmonics decreases (1/2, 1/3, 1/6 etc.) when shaft rotational speed increases. The transition zones between the different dynamic regime exhibit chaotic behaviour. Chu and Zhang [89] focused on the type of bifurcation of a Jeffcott rotor in contact with stator. According to them, the roots to chaos are period doubling, grazing-type bifurcation but also sudden transitions from a periodic regime to chaos. Chu and Lu [90] confirmed experimentally these results, where several configurations of rotors and discs were analysed. It appears that the more severe the contact is, the more the spectra are rich and complex to interpret. Popprath and Ecker [91] used the rotor-to-stator mass ratio as control parameter in bifurcation diagrams. A Jeffcott rotor and a 2-Dof stator are used. It is shown that rotor orbits can be influenced strongly by the stator motions. Varney and Green [92] analysed a rotating mass in contact situation with an isotropic stator. The influence of the support cross-coupling stiffness and anisotropy as well as the gravity are analysed. A wide variety of periodic, quasi-periodic and chaotic responses are possible. It appears that the effect of the support cross-coupling stiffness can be neglected while direct stiffness asymmetry has a strong influence. Period-doubling and sudden bifurcations are the primary roots to chaos, which is close to the conclusion of Chu and Zhang [89].

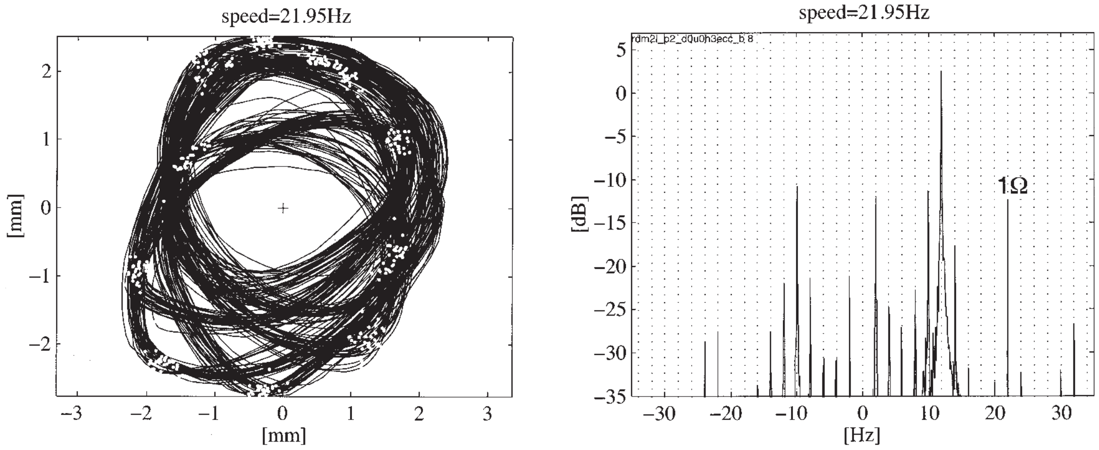

Figure 1.21: Periodic orbits and the related frequency content - Von Groll and Ewins [14]

Von Groll and Ewins [14] analysed experimentally the dynamic behaviour of an aircraft engine during windmilling. After a blade loss, the rotor under heavy mass unbalance decelerates in rubbing contact with the casing. Once this transient regime damped, periodic or quasi-periodic regimes appear characterized by intermittent contacts; an example is provided in Figure 1.21. The authors noted the appearance of superharmonics and subharmonics, related to larger rotor displacements. Their conclusion was that the orders of the harmonics depend on the ratio between the frequency of the coupled system and the rotational speed of the rotor. Abuzzaid *et al.*

[93] suggested another interpretation. They studied the quasi-periodic phenomena of a rotor in rubbing contact with a stator. Slight contact results in the occurrence of orders greater than the rotational speed (superharmonics), indicating several contacts per revolution while severe contacts produce harmonics of lower order where several revolutions are required before contact occurs again (subharmonics). This assumption is also proposed by Duran [83]. A frequency of order n of the rotational speed appearing during a contact situation means that the rotor is in contact n+1 times per revolutions. Superharmonics of integer-order were also found by Pennacchi *et al.* [94] considering real rotating machinery designs where the seals over rotor stiffness ratio is often small, generating rather forward short arc rubs.

The level of mass unbalance is used to generate light, medium and heavy rotor-stator contacts in Torkhani *et al.* [95]. The unbalance procedure is realized in order to contact only during rotor coast-down thanks to the ice block melting. This procedure is close to the fan blade out scenario investigated by Braut *et al.* [81], Duran *et al.* [82] and Wang *et al.* [84]. The contact model is based on Lagrange multipliers and is further detailed by Roques *et al.* [96]. Partial rub is numerically and experimentally exhibited and no dangerous permanent contact is triggered. The rotor deceleration due to rubbing at the interface is also investigated. Often, partial contact is treated as a transient phenomenon. However, some studies were dedicated to the steady-state responses of this type of contact modes. Cole and Keogh [15] used a rotating frame to determine the asynchronous contact modes of a rotor-bearing system, as shown in Figure 1.22.

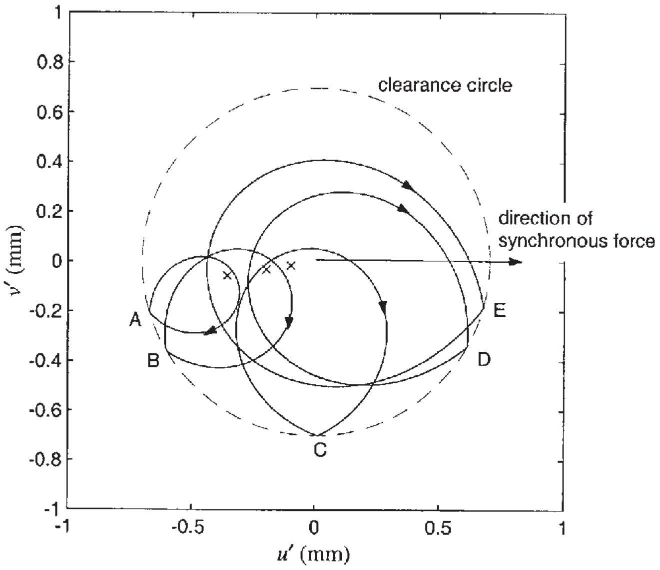

Figure 1.22: Rotor motions in the rotating frame - Cole and Keogh [15]

Some particular numerical methods, such as the harmonic balance method, can be used to determine the quasi-periodic response in a rotor-stator system. This was performed by Kim and Noah [97] where a good agreement was found with direct integration. This method was also employed in Peletan *et al.* [98, 99] and in Xie *et al.* [100].

1.2.3 Drop dynamics

The study of classical rotor-stator interactions considers bearing restoring forces often without considering the gravity. Rotor-AMB horizontally split systems are generally levitated by one axial thrust bearing and two radial bearings. At both rotor ends are positioned the touchdown bearings as shown in Figure 1.23. When the magnetic levitation is no longer provided by the AMBs, the rotor is forced to drop on TDBs, often ball bearings or in some cases bush bearings with low friction coefficient. Since the restoring forces of the bearings no longer exist, the normal critical velocity in the sense of Bartha [9] should be zero, enabling in theory, dangerous backward whirl behaviours. Two types of rotor drop exist:

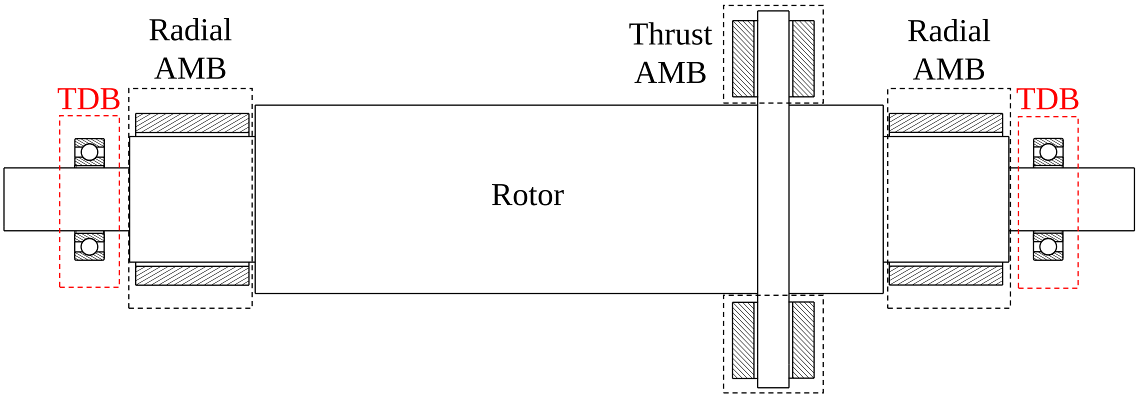

Figure 1.23: Typical rotor-AMB system equipped with TDBs

- Vertical drop: the rotor axis is parallel to the direction of the gravity.
- Horizontal drop: the rotor axis is perpendicular to the direction of the gravity.

In case of horizontal drops, gravity tends to stabilize the rotor at the bottom of its TDBs, compensating for the loss of the bearing restoring forces. Gravity counteracts friction force generated by the contact. In case of vertical drops, gravity acts more like a destabilizing force.

1.2.3.1 Vertical drop

Generally speaking and from experimental studies, the vertical landing can be described by three distinct phases as explained by Yang *et al.* [16]:

1. Free-fall phase: once the AMBs are switched off, the rotor falls under the effect of gravity.
2. Rebound phase: when impact occurs, the rotor undergoes a transient phase marked by rebounds and sometimes, backward whirls.
3. Forward whirl phase: the rotor evolves in permanent contact at a synchronous or usually subsynchronous frequency, as shown in Figure 1.24.

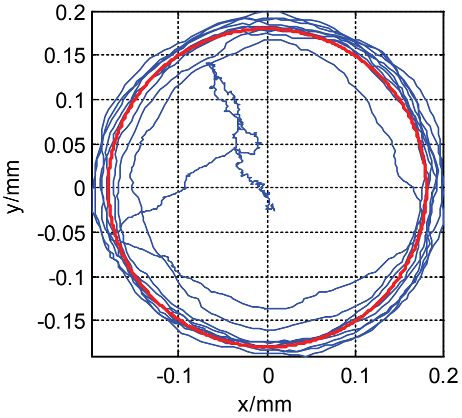

Figure 1.24: Forward whirl after a vertical drop - Yang *et al.* [16]

Forward whirl explanation

Sun [22, 101], and Sun *et al.* [23], carried out numerous studies on the vertical drop of an inertia wheel with a detailed touchdown bearing model. They used a rigid rotor model with 16 degrees of freedom including gyroscopic effects. The vertical dynamics are included in the simulation. Thermal losses in the TDBs were also taken into account. They analysed the influence of a large number of parameters thanks to “performance” indices. They emphasized once again the fundamental importance of the friction coefficient and recommended determining a threshold from which the backward whirl is triggered. However, in many experimental studies, forward whirl behaviours appeared, see references [16, 17, 18, 102]. Schmied and Pradetto [17] carried out a numerical and experimental study on the vertical drop of a one-ton compressor. Only the lateral vibrations were considered. Their simulations revealed that tangential damping is able to stop a backward whirl motion in just a few cycles, as shown in Figure 1.25.

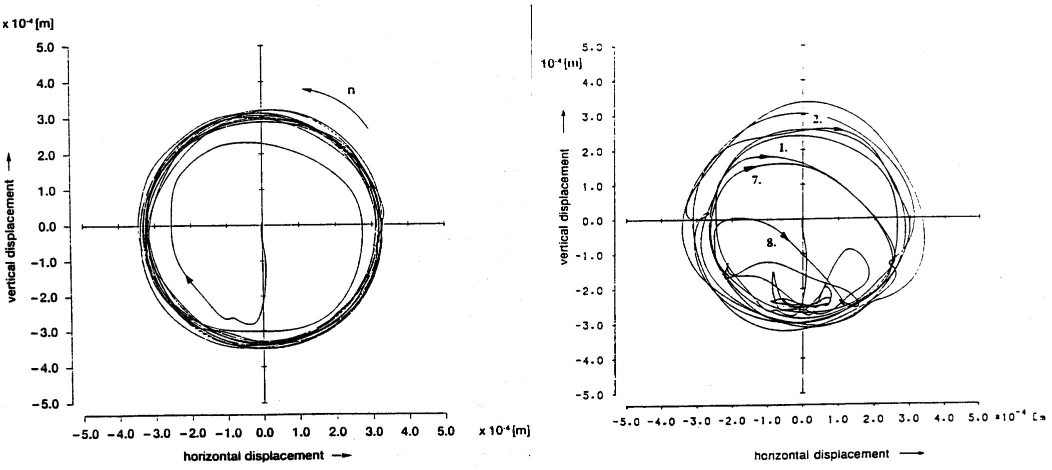

(a) Without circumferential damping (b) With circumferential damping

Figure 1.25: Influence of the circumferential damping on the rotor drop dynamics - Schmied and Pradetto [17]

However, their experiments indicated forward whirl orbits. The authors concluded that some phenomena were not modelled, such as possible electromagnetic effects appearing during AMBs shut-down, forcing the rotor in its direct precession. Ransom *et al.* [103, 104] introduced a cross-coupled stiffness in their TDB model forcing the rotor whirl in forward direction. Although the nature of this cross-stiffness was not clearly identified, it gave simulations consistent with the tests performed by GE Oil & Gas. Wilkes *et al.* [105] explained that the misaligned vertical axis of the rotor in the TDBs generates a load, equivalent to a cross-coupled stiffness which forces the rotor whirl in forward direction. Caprio *et al.* [18] observed that from a certain rotor spin speed at the moment of drop, the steady state whirling frequency as well as the whirl orbit radius no longer evolve and seem to be blocked at a frequency close to 25 Hz, as shown in Figure 1.26.

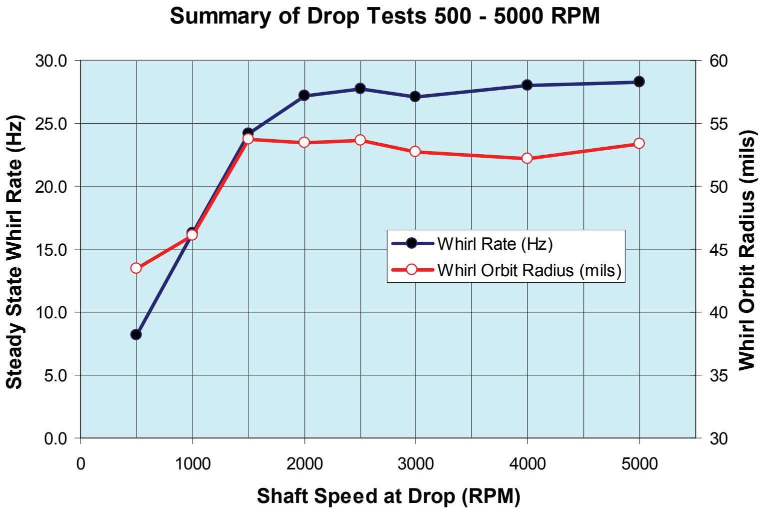

Figure 1.26: Vertical drop followed by forward whirl limited frequency - Caprio *et al.* [18]

The forward whirl motion is frequency-limited by the conical coupled rotor-stator mode. This is consistent with many of the previous studies concerning the rotor-stator interaction, see references [10, 76, 77, 78].

Miscellaneous optimisations

Hawkins *et al.* [102] studied the vertical landing of a flywheel rotating in vacuum. They showed the advantage of the flexible assemblies of the touchdown bearings in reducing the forward whirl frequency and therefore the centrifugal forces transmitted to the support. The use of electromagnetic forces to limit dangerous behaviour was numerically analysed by Sun [22, 101]. Leaving active an AMB stabilizes the drop dynamics and prevents backward whirl motion. This was experimentally showed by Caprio *et al.* [18] where only one side of an AMB was activated and led the forward whirl motion to stop after some orbiting cycles. Then, the rotor stabilizes at a position slightly offset with respect to the direction of the magnetic forces.

1.2.3.2 Horizontal drop

Generally speaking, and according to experimental investigations, the typical horizontal drop is composed of three distinct phases, the last phase containing either stable oscillations or backward whirl motions:

1. Free-fall phase: once the AMBs are switched off, the rotor falls under the effect of gravity.

2. Rebound phase: at the moment of the first impact, the rotor enters in a transient phase marked by rebounds on the stator. In some experimental studies such as those of Hawkins *et al.* [106], a short period of forward whirl is observed before the pendulum oscillation movement.

3. Oscillation phase at the bottom of the TDBs: once the transient phase ends, the rotor performs a pendulum motion at the bottom of the bearings. This motion corresponds to a dynamic equilibrium between the friction forces which tend to push the rotor in backward whirl and the forces of gravity which tend to bring the rotor back to the bottom of the bearings, as shown in Figure 1.27. The oscillation frequency is close to the pendulum natural frequency, given in Hertz in equation (1.1):

$$f = \frac{1}{2\pi}\sqrt{\frac{g}{\delta_0}} \tag{1.1}$$

with g the gravity, δ_0 the rotor-stator clearance.

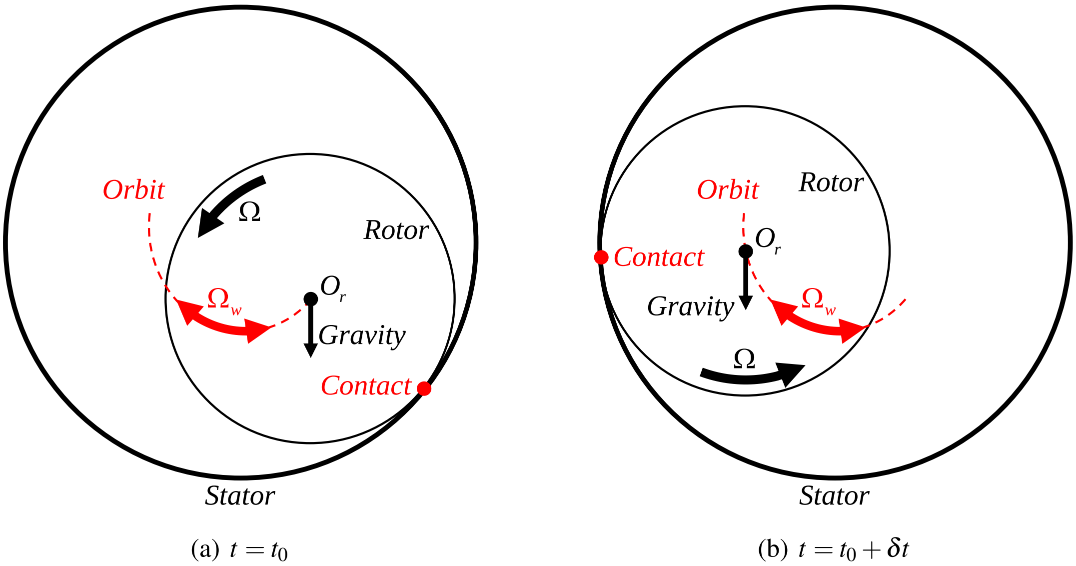

(a) $t = t_0$ (b) $t = t_0 + \delta t$

Figure 1.27: Pendulum motion of a horizontal dropped rotor

However, the rotor can perform backward whirl motion if the energy brought by the friction, partially dissipated in the TDBs, exceeds the potential energy of gravity. In some cases, such as a high friction coefficient, stiff support, very low damping or misalignment, the rotor may describe this type of behaviour which can affect the integrity of the machine.

Effects of support

The dynamic parameters of the support have a fundamental influence of rotor drop dynamics. Ishii and Kirk [107] and Kirk [108] used an extended Jeffcott rotor to perform transient drop simulations. In particular, they determined the optimal range of damping for the support to limit the TDBs loads, the displacement of the disc placed in the centre of the rotor, but also to cancel backward whirl motions. This was latter questioned by Zeng *et al.* [109] who showed that considering the rotor-seal contact, it was not possible to determine any optimal damping support. Zeng *et al.* [110] analysed experimentally and numerically the transient response of a rotor during a drop event. Hard and soft support as well as inner race constraint device are tested. During the drop of a rotor at rest, the authors showed that the effect of the decaying of magnetic force of the failed AMBs can be ignored, thus answering to the previous assumption emitted by Schmied and Pradetto [17]. With lubricated surfaces, regardless of the type of TDB, no whirling motions appeared while the unlubricated and hard mounted case generated full backward whirl up to 145 Hz.

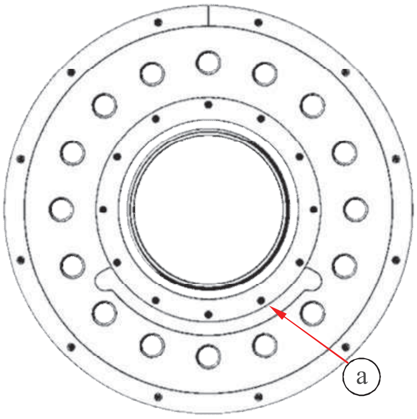

Figure 1.28: TDB support with a “smiley design” - Siebkea *et al.* [19]

The compromise between the reduction of the impact forces and whirling frequencies by softening the support and the contact with the seals is discussed. The softening of the drop structure is also discussed by Siebkea *et al.* [19]. They propose a new bushing-type TDB design to provide vertical flexibility when landing a 9-ton rotor. The design called “smiley design”, see Figure 1.28, limits the impact loads transmitted to the support.

Coast-down

The effects of the mass unbalance during rotor coast-down has been treated in many studies. Ishii and Kirk[107] and Kirk[108] pointed out the need to have a well-balanced rotor and an operating speed far away from the first flexible mode to avoid dangerous behaviours. Fang

[111] confirmed this assertion. According to him, passing through the first bending mode during a rotor drop followed by a coast down can seriously damage the structure. This was also highlighted by Kirk *et al.* [112] where the author analysed the dynamic behaviour of several flexible rotor geometries in drop situations and their dynamic behaviour during coast-down using the FE software DyRoBes. The descent through the first free-bending mode of the rotor may be dangerous. This effect diminishes as the rate of deceleration increases. Kärkkäinen *et al.* [113] designed a detailed ball bearing model to describe the landing behaviour of a supercritical flexible rotor. This bearing takes into account the thickness of the oil film, the inertia effects of the rolling elements as well as the friction between the rings and the balls. On this aspect, the authors concluded that it is not necessary to model the precise interaction between races and rolling elements to correctly predict the behaviour of the rotor. The Coulomb and Stribeck friction models are used and the resulting dynamic rotor responses obtained are comparable. As the dropped rotor is supercritical, they raised once again the potential danger of passing through the first free-free bending mode. Siegl *et al.* [114] investigated experimentally and numerically the drop of a 9-ton supercritical rotor followed by a coast-down. The TDBs are mounted in a housing with the same asymmetric compliance. Unlike previous studies on this particular aspect, it is shown that no particular dangerous behaviours were triggered.

Stable pendulum motion

For most of the case, industrial turbomachinery dropped quickly reach a stabilized equilibrium at the bottom of their TDBs. Gelin *et al.* [115, 116] were one of the first groups to describe numerically and experimentally the transient dynamic behaviour of a FE rotor onto TDBs. The rotor behaves globally rigidly with a stable motion at the bottom of its TDBs. Spectral analysis reveals the appearance of rigid modes (especially cylindrical), the rotor rotational speed as well as frequency combinations. Fumagalli [117] analysed the interactions between a rotor and its TDBs. The author focused in particular on the energy transfer from the rotor rotational speed to its backward whirl motion considering different bearing types (bushing or ball bearing), different types of materials etc. He emphasized the generally stable behaviour of the heavy rotors horizontally dropped onto their TDBs and specified that in order for the rotor to establish a circular movement, the input energy must be at least equivalent to the potential energy of the rotor in the highest position of the bearing. Drop tests on ball bearings were performed and only rotor pendulum oscillations were observed. Hawkins *et al.* [106] also found this type of behaviour for the drop of a cryogenic turbo-expander even if a short period of forward whirl appeared in his tests just after the landing.

Misalignments

Kärkkäinen *et al.* [118] and Halminen *et al.* [20], highlighted the influence of horizontal misalignment of TDBs on the behaviour of a flexible rotor during landing. The misalignment of the TDB axis generates a contact angle and therefore pushes the rotor into backward whirl, as shown in Figure 1.29. It is noteworthy that these effects appear for relatively large misalign-

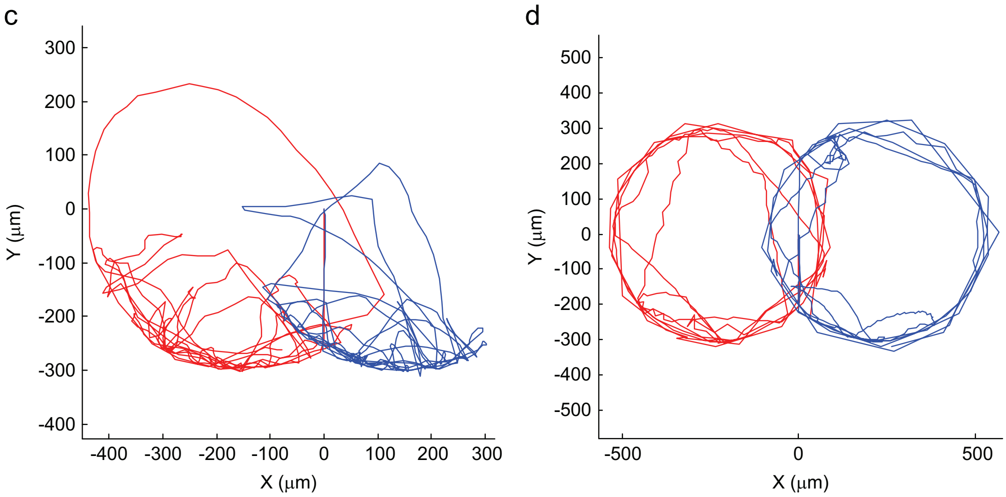

Figure 1.29: Effect of an increasing horizontal misalignment from c to d - Halminen *et al.* [20]

ments. This finding about the major importance of the contact angle corresponds to the studies of Bartha [9]. The vertical misalignment does not modify a priori the direction of the forces at the impact, but modifies the height of drop and therefore the resulting drop load.

Steady-state behaviours

Even if rotor drop dynamics is often treated as a transient phenomenon, it is interesting to determine the steady-state solutions of this kind of systems, especially the type of nonlinear regimes appearing during coast-down after a drop event. Maslen *et al.* [119] studied the permanent solutions of a rotor in an isotropic TDB. They considered that the transient behaviour of the rotor during the landing is less damaging to the machine than a behaviour in steady state backward whirl. Thus, they analytically predicted the feasibility of a backward whirl motion depending on the deviation from a nominal friction coefficient and damping present in the TDB. The well-known U-shaped plot is generated. This study is comparable to those made by Black [76], Choi [10] or Wilkes [79]. The shooting method is used by Wang *et al.* [120] to determine the whirling frequency response of a rotor subjected to gravity, mass unbalance forces, cross-coupling fluid forces and contact forces with TDBs. Jumps, periodic, quasi-periodic and chaotic motions are found. Modal coordinates and the harmonic balance method were used by Xie *et al.* [21] to determine the synchronous response of a rotor subjected to gravity, mass unbalance and contact forces. It appeared that gravity has the same effect than asymmetric support since the linear first critical speed is split in two. Depending on the value of the rotor-stator clearance, the frequency response exhibits nonlinear phenomena such as jumps. It appeared that a large clearance means a low apparent stiffness and then, the first critical speed is shifted in lowest frequencies as shown in Figure 1.30. Bifurcation diagrams were generated using TDB stiffness, damping as well as the rotor-stator clearance as bifurcation parameters. Generally, high stiffness support combined with a low support damping and high mass unbalance level are more able to generate multi-frequency responses and chaotic motions. Ishida and Inoue [121] inves-

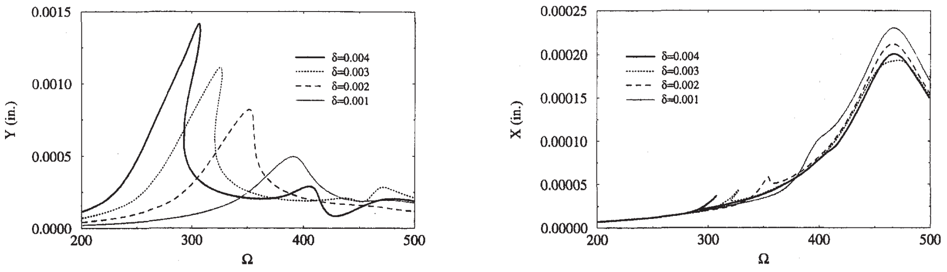

(a) Vertical response (b) Horizontal response

Figure 1.30: Unbalance response of a rotor subjected to gravity and in contact with auxiliary bearings - Xie *et al.* [21]

tigated the dynamic response for four kinds of AMBs failures numerically and experimentally. For example, the case where all the electromagnet failed exhibited subharmonic resonances.

TDB lifetime

For the TDB design and lifetime, it can be useful to focus on the interactions between races and rolling elements. Cole *et al.* [122] modelled with a flexible inner ring mounted in series with the nonlinear Hertz type stiffness of the balls. The rigidity of the inner ring is fundamental for the load distribution on balls and for the limitation of the temperature gradients. At the same time, the smaller is the inner race polar inertia (generally linked with low stiffness), the faster it reaches the rotor speed; which greatly limits the friction at the rotor interface and therefore the dangerous behaviours and heat losses. The thermal assessment of rotor-auxiliary bearing contact is done by Keogh and Yong [123]. Lee and Palazzolo [124] study the TDB lifetime using the “rainflow couting alogrithm”. It is concluded that the TDB lifetime could be extended by decreasing the rotor-inner race clearance, applying a static load to the rotor during landing, reducing the rotor rotational speed, reducing the stiffness of the support, increasing its damping and finally reducing the friction coefficient.

1.2.3.3 Contact and AMB

Some works were also dedicated to the case of rotor-TDB contact while AMBs are still operating. An overview of contact phenomena including active considerations are given by Keogh [125]. Lawen and Flowers [126] employed the synchronous interaction methodology used by Black [76], using rotor and stator polar receptances modelled with modal coordinates. The AMBs are considered as simple spring / damper without considering any type of control. Inayat [127, 128] considered the nonlinear restoring force of AMBs and nonlinear contact with TDBs to derive bifurcations diagrams. Keogh and Cole [129] first analysed the behaviour of an unbalanced rotor in a contact situation with its auxiliary bearings while considering AMBs as simple spring / damper elements. Conventional controls for synchronous whirl appeared to be ineffective due to the large changes of phase associated with contact situations. Since these strategies only act on the synchronous components, the backward contact modes cannot be avoided but can be prevented by increasing the damping. Keogh *et al.* [130] derived a modified controller where the phase shift and amplitude of the synchronous component induced by the contact were taken into consideration. Keogh and Cole [131] proposed an alternative for the generation of contact which is usually induced by mass unbalance forces close to bending modes. Magnetic forces are used here instead to generate rotor whirl and TDB contact. Some works investigated active TDBs allowing the rotor to recover a non-contacting situation such as in Cole [132] and Cade *et al.* [133] or to limit or cancel rubbing vibrations such as Jiang *et al.* [134] using an optimal and PD controller.

1.3 Objectives and approaches

Base motions generate complex rotor dynamics which depends on the type of excitation applied. Harmonic rotational motions are able to provide parametric excitations and therefore instability zones which depend on their forcing frequencies and amplitudes. These zones are reduced by the rotor-bearing system damping. The multiple frequency response of the rotor is due to the rotational speed and to the base forcing frequency making the periodic orbits non elliptic. Second member vectors are provided by base translations combined or not with rotations. In the case of nonlinear bearings and an increasing base amplitude, the on-board rotor dynamics follows a route to chaos comprising nT periodic or quasi-periodic behaviours. On the other hand, AMB technology is more and more utilized in industrial applications where the PID remains the most commonly used controller. Different studies were performed on rotor-AMB systems subjected to base motion. In some previous works, magnetic forces are used to remove or deteriorate instability zones. Other works focused on the control of the base motion, often concerning sinusoidal translations, by adding a compensator (feedforward loop) besides a more conventional feedback control loop. The influence of the shock on rotor-AMB systems has also been treated. In most of the previous works, a feedforward control loop is added to the conventional feedback control loop to specifically limit the effect of the foundation on the rotor dynamics. In rotor-AMB systems, touchdown bearings are used to protect AMBs and to ensure a back-up pivot linkage when magnetic forces are no more present. In case of AMB shutdown, the rotating shaft dropping onto its TDBs is subjected to gravity, mass unbalance and contact forces. In horizontal industrial applications, the rotor behaviour often stabilizes after few rebounds, oscillating at the bottom of its TDBs. A well balanced rotor combined with a soft and damped support may help to avoid dangerous behaviours during drop.

When severe base motion occurs while AMBs still operate, rotor may contact TDBs. The rotor-AMB system has to deal with conventional unbalance forces, external base motions and rotor-TDB interactions. The contact can trigger complex nonlinear rotordynamics such as periodic, quasi-periodic or chaotic regimes, in forward or backward direction. The dry friction tangential forces are responsible for partial backward whirl contact modes, often characterized by rebounds and subharmonic responses. These modes can progressively evolve into continuous dry whirl or even dry whip instability, where large contact loads are expected affecting the TDB lifetime.

In the aim of enhancing the design of AMB-equipped turbomachinery and eliminating blocking points to the penetration of this kind of technology in on-board applications, this project proposes a complete approach for modelling and predicting the dynamic behaviour of a rotor-AMB system subjected to both the conventional rotordynamics effects (mass unbalance, gyroscopic) and base motion excitations. The nonlinear contact with TDBs as well as nonlinearities coming from AMBs are considered. As very few studies give insights into rotor-TDB interactions while AMBs still operate, the context of unexpected AMBs shut-down is investigated. To the best of author's knowledge, very few studies were dedicated to this particular issue. In 1997, Hawkins [52] conducted this kind of study considering a rotor-AMB system subjected to very large shocks causing high TDB forces. The main conclusions were that the TDB load capacity could be exceeded and that the rotor quickly recovered its centred position. However, these results were not confirmed experimentally. Here, the developed approach is numerical and experimental. The degree of details of the required models has to be sufficiently representative. Indeed, the whole turbomachinery dynamics is targeted and located phenomena cannot be considered.

To this end, the thesis is composed of 4 chapters:

- Chapter 2 describes the numerical model and the related assumptions. In the first part, the FE model of on-board rotors, based on a Lagrangian approach, is detailed. The base motion energy intakes on the conventional Timoshenko beam element formulation is described and the related equations of motion are set-up. This model is based on previous investigations where it appeared to be effective. Then, the AMB model and the related assumptions are described. A brief introduction to magnetic force is given as well as the elements taken into account in each action line. The PID, which is the strategy employed in this work to control AMBs, is further investigated. A detailed approach for the modelling of the components of a TDB is then proposed. Several TDB designs exist, but the ball bearing is particularly investigated in this work for its numerous benefits. Well-known analytical methods are derived to obtain a representative ball bearing model. The rotational aspects are also treated with energetic methods. The numerical treatment of rotor-inner race interaction is detailed carefully and the different modelling techniques are reviewed.

- Chapter 3 proposes an experimental and a numerical approach in the particular problematic of AMB losses, called rotor drop dynamics. Even if it is not the main purpose of this research project, this chapter permits the experimental validation of the TDB model. This step was important since it brought useful informations concerning the degree of details required to predict with sufficient accuracy the dynamic behaviour of dropping rotors. The first part of this chapter deals with the description of a key component for the stability of rotors during these unexpected events, called ribbon damper. A mathematical model, based on experimental results, is able to accurately reproduce the observed non-linear dynamic behaviour of that component. The second part of this chapter focuses on numerical and experimental comparisons of an industrial test bench rotor in drop situation. Two TDB models are used. The elements detailed in Chapter 2 are implemented in a very simple TDB model, used as reference and in a more complex model, where the newly developed ribbon damper is included.

- Chapter 4 combines the different models developed throughout this PhD to investigate numerically and experimentally the dynamic behaviour of on-board rotors subjected to critical external excitations. To achieve this, an academic rotor test bench having the characteristics of industrial turbomachinery is mounted on a 6-axis shaker. The first part of this chapter describes the rotor-AMB system characteristics and the experimental set-up. Then, preliminary tests are performed to validate the model for simple cases, such as unbalance response and rotor drop at standstill. The third subsection describes the base motion test configurations comprising harmonic and impulse tests, representative of real operating conditions. Depending on the acceleration level applied, the rotor contacts the TDBs. Several speeds of rotation are tested. The last subsections describe the numerical and experimental results for these cases. The system stability and the effects of contact are assessed numerically and experimentally, in terms of rotordynamics, control currents and spectral contents. The nonlinearity of magnetic forces is also analysed. This chapter permits the validation of the complete numerical model.

Table 1.1 summarizes the three experimental tests validating the proposed models.

Table 1.1: Description and objectives of the tests

	Description	**Goal**
Test 1	Harmonic characterization of the ribbon damper	Giving insight on the dynamic behaviour of that key component providing rotor stability during drop and contact events. Enhancing rotor drop predictions
Test 2	Rotor drop dynamics	Validating the rotor drop model and the newly developed ribbon damper model in transient simulations. Discuss on the capability of simple TDB models to catch the observed phenomena
Test 3	On-board rotor-AMB system subjected to more or less severe base motions	Validating the complete numerical model. Investigate the dynamic behaviour of on-board rotor-AMB system during critical events. Discuss the capability of the controller to sustain these events, the on-set of the particularly feared rotor behaviours, the linearity of AMBs, etc.

Chapter 2

Theory and models

The first part of this chapter describes briefly the model assumptions concerning all the components of a rotor-bearing system when the movement of its rigid base is considered. The equations of motion are set-up using a classical Lagrangian approach. The related vectors and matrices are implemented into a finite element mesh generator. Then, the description of each elements composing the active magnetic bearing action line is detailed. The formulations of the magnetic force and transfer functions related to the implemented controller are detailed. A general introduction of touchdown bearings, detailing their different designs and arrangements found in industrial applications, is provided. An analytical method is used to set-up the force-deflection relationship of a rolling element touchdown bearing. The results are compared with finite elements predictions. A rotational equivalent model is set-up with energetic methods. Finally, the numerical methods and modellings to treat the rotor inner race interactions are investigated. The more general case of rotor-stator contact is discussed.

Contents

The aim of this chapter is to provide the description of all the different models needed to perform transient simulations considering a rotor-AMB system subjected to external disturbances and potential TDB contacts. The on-board rotor, the AMBs and the touchdown bearing models are described separately; the modelling approach is modular and each model can be either employed or not in simulations. For example, it is possible to perform a mass unbalance response or rotor drop predictions without considering any base disturbance effects. The common feature of all these presented models is that they describe the global characteristics of systems.

The study focuses on horizontally split systems, which are generally levitated by one axial thrust AMB and two radial AMBs. At both rotor ends are positioned the TDBs, as shown in Figure 2.1. The lateral dynamics are considered and the axial one is assumed to be decoupled from bending vibrations. The modelling of the thrust bearing and the axial TDBs are thus not provided.

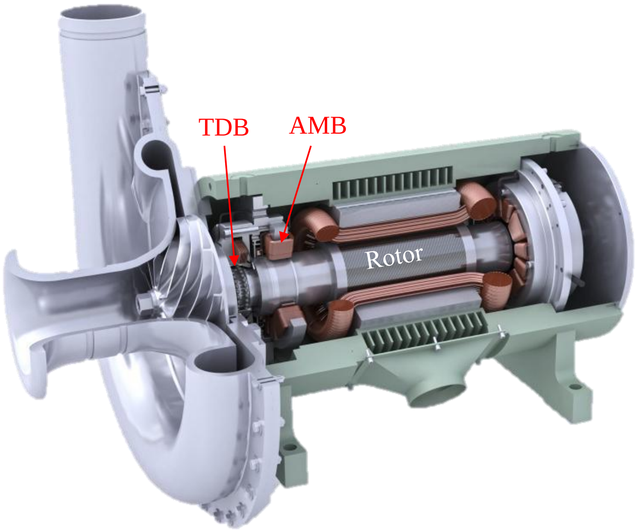

Figure 2.1: Horizontally split rotor-AMB system and its TDBs (ball type bearing)

Industrial turbomachinery supports are stiff and assuming them rigid seems not to be a strong assumption. Modelling a flexible support leading to an avoidable increase of degrees of freedom would have little relevance in the context studied. The on-board rotor model includes the support motions in the energetic formulation of conventional Timoshenko beam elements; dot not increase the system degrees of freedom. The possibility to implement any type of bearings makes this model modular and easy to use. AMBs are active restoring forces and the description of the action line is done according to elements that have a significant influence on rotordynamics such as actuators and controller. TDBs are ball bearings exclusively. The chosen approach is global; when rotor exceeds the rotor inner race clearance, the deflected TDBs generate restoring forces and are driven in rotation. For this purpose, an analytical force-deflection relationship and rotational modelling are incorporated, respectively. The rotor inner race interaction is a contact problem and the different modellings are presented. A third component is needed to complete the TDB modelling and the latter is numerically and experimentally assessed in the next chapter.

2.1 On-board rotor

2.1.1 Assumptions

Conventionally, the rotor is composed of a shaft, bearings, discs, and unbalance distribution. To study the dynamic behaviour of an on-board rotor, the support component is added. The major assumptions of this modelling are:

- The shaft is flexible and modelled by beam elements for lateral analysis.
- The discs are rigid and symmetric.
- The unbalance distribution is modelled by discrete masses.
- The support is rigid but mobile.

The method chosen in this study is a Lagrangian method based on Duchemin *et al.* [2, 3], Dakel *et al.* [5, 38, 39] and Bouziani and Ouella [41]. It consists in describing the motion of the rotor with respect to the rigid support R, as usually done in conventional rotor dynamics studies, and the support motion with respect to the ground R^g, which is a Galilean frame. An intermediate frame is set-up to take into account the base motion energy intake and to investigate the deflection of the rotor neutral line in the frame attached to the rigid support, see Figure 2.2.

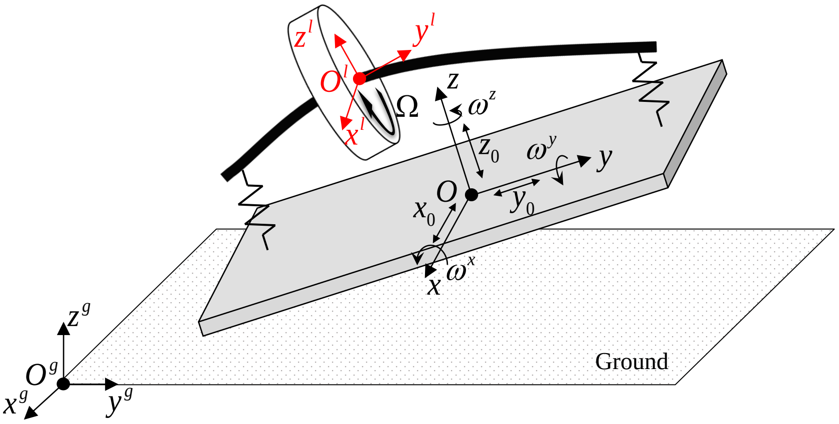

Figure 2.2: On-board rotor - set-up of the different frames

- $R^g\left(x^g, y^g, z^g\right)$ is the Galilean frame of centre O^g, fixed and attached to the ground.
- $R\left(x, y, z\right)$ is the non-inertial frame of centre O, attached to the rigid base.

- $R^l\left(x^l, y^l, z^l\right)$ is the local non-inertial frame of centre O^l, attached to the deflection line of the rotor (centre of mass disc or shaft element).

The method to obtain the equations of motion is identical to the one proposed by Lalanne and Ferraris [30]. The frames of reference are first established and then vectors describing the different motions between each others are calculated. To derive the different energies of each components of the rotor, the instantaneous angular velocity vector $\overrightarrow{\omega}_R^{R^g}$ and the position vector $\overrightarrow{O^gO}$ are needed. These vectors are expressed with respect to the Galilean frame R^g in the rigid support frame R.

$$\overrightarrow{O^gO} = \begin{Bmatrix} x_0 \\ y_0 \\ z_0 \end{Bmatrix}_R ; \overrightarrow{\omega}_R^{R^g} = \begin{Bmatrix} \omega^x \\ \omega^y \\ \omega^z \end{Bmatrix}_R \tag{2.1}$$

The detailed formulations of these vectors can be found in Dakel *et al.* [39]. Thus, it is possible to compute the energetic contribution and the virtual work of each components of the rotor:

- The kinetic and strain energies of the flexible shaft,
- The kinetic energy of the discs,
- The kinetic energy of the discrete mass unbalances,
- The virtual work of the bearing restoring forces.

The different contributions of the base are expressed in the frame associated with the rigid base R in motion with respect to the Galilean frame R_g. Only the kinetic energies are modified by the base motions. The strain energy of the shaft and the virtual work of the bearing restoring forces are not affected since they depend on the relative motions between the rotor and the base; this means that any type of bearing can be used. This is due to the fact that support motions are expressed in the rigid support non-inertial frame R, see Figure 2.2, as relative effects. The details of the different energies provided by each rotor components as well as the derivation of these energies in the Lagrange's equations are not provided and readers can refer to references [38, 39, 41] for more details.

Once the energies are set-up, they are derived using the Lagrange's equations and the equations of motion are obtained:

$$\frac{d}{dt}\left(\frac{\partial T}{\partial \dot{q}_i}\right) - \frac{\partial T}{\partial q_i} + \frac{\partial U}{\partial q_i} = F_{q_i} \tag{2.2}$$

with:

- q_i a degree of freedom of the system,
- T and U, the kinetic and strain energies, respectively,
- F_{q_i} the external force applied to the degree of freedom q_i.

2.1.2 Finite element model

The finite element method is used to predict the rotor lateral deflections. The disc and shaft are assumed to be symmetric, the disc rigid and the rotational speed variable. The shaft is modelled with Timoshenko elements in bending made of circular and constant sections with two nodes and four degrees of freedom per node, see Figure 2.3. The nodal displacement vector $\{\delta_i\}$ of a shaft finite element associated with the i-th degree of freedom and expressed in the reference frame R is:

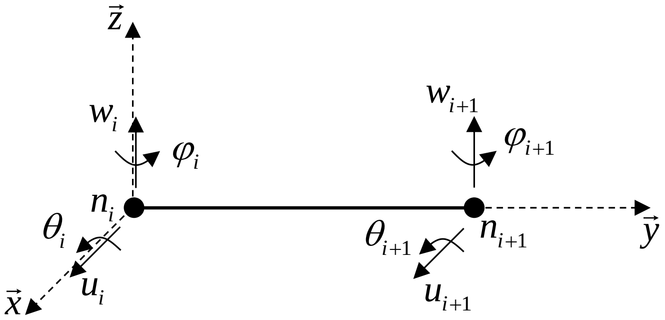

Figure 2.3: Timoshenko beam element

$$\{\delta_i\} = \langle u_i, w_i, \theta_i, \varphi_i, u_{i+1}, w_{i+1}, \theta_{i+1}, \varphi_{i+1}\rangle^T \tag{2.3}$$

Finally, the equations of motion have the following form:

$$\begin{aligned} &M\ddot{\delta} + \left(\Omega C^g + \omega^y C_{bm}^{\omega^y}\right)\dot{\delta} + \left(K^e + \dot{\Omega} K^{\dot{\Omega}} + \dot{\omega}^y K_{bm}^{\dot{\omega}^y} + \Omega\omega^y K_{bm}^{\Omega\omega^y} + \omega^{x2} K_{bm}^{\omega^{x2}}\right. \\ &\left. + \omega^{y2} K_{bm}^{\omega^{y2}} + \omega^{z2} K_{bm}^{\omega^{z2}} + \omega^x\omega^z K_{bm}^{\omega^x\omega^z}\right)\delta = F_{mu} + F_{mu,bm} + F_{bm} + F_{amb} + F_c + F_g \end{aligned} \tag{2.4}$$

where M, K^e and C^g are respectively the mass, the structural stiffness and the gyroscopic matrices. Matrices and external force vectors come from the sum of the contribution of shaft and/or discs elements. The subscript *bm* stands for the base motions effects. For more details about the elementary formulation, readers can refer to Appendix A.

When taking into consideration a variable rotational speed, the matrix and $K^{\dot{\Omega}}$ is added to the equations of motion according to Lalanne and Ferraris [30] and Bouziani and Ouella [41] for the particular case of on-board rotors. F_{mu} is the mass unbalance force vector taking into account the normal centrifugal and tangential centripetal forces respectively associated with constant and variable rotational speed of the rotor. All the other matrices with the subscript *bm* are related to base motions: the second gyroscopic matrix C^{ω^y} on the rotational speed ω^y of the support along the direction of the shaft line, the stiffness matrix $K^{\dot{\omega}^y}$ on the angular acceleration $\dot{\omega}^y$, the other stiffness matrices depend on the square of the angular velocities of the support or on particular combinations. They can be seen as centrifugal effect matrices where the associated geometric stiffening effect is considered. Consequently, the support rotations introduce time-varying parametric excitations that could generate lateral instabilities. The support motion also modifies the classical mass unbalance contribution and another vector $F_{mu,bm}$ is created. The external force vector F_{bm} contains all the contribution of the translations of the support combined with its rotations that does not depend on the degrees of freedom of the shaft. The influences of the different base motion effects are studied in Dakel [38, 39] and Bouziani and Ouella [41] for the case of transient rotational speed. The effect of gravity is also considered in the force vector F_g. F_{amb} and F_c represent the magnetic and the TDBs contact force vectors respectively. The related modellings are described in the next sections.

Analysis in the time domain is required to catch the transient behaviour of an on-board rotor-AMB system subjected to critical external events. The modal method is used to reduce the system of equations size providing an efficient model with low computational time while maintaining high reliability. It is a well-known method that uses a modal matrix ψ to project the equations of motions from the physical coordinate into the modal basis. A modal truncation limits the modal variable and the first ten mode shapes compose the matrix ψ. It permits the introduction of the modal ratio α_ψ. Finally, the equations of motion (2.5) are expressed in the modal basis where q is the modal variable vector. For practical reasons, the time dependent and parametric matrices are considered as external forces and placed in the second member:

$$\begin{aligned} M_\psi \ddot{q} + C_\psi \dot{q} + K_\psi q = &- \left(\Omega C_\psi^g + \omega^y C_{bm,\psi}^{\omega^y}\right)\dot{q} - \left(\,\dot{\Omega} K_\psi^{\dot{\Omega}} + \dot{\omega}^y K_{bm,\psi}^{\dot{\omega}^y} + \Omega\omega^y K_{bm,\psi}^{\Omega\omega^y} + \omega^{x2} K_{bm,\psi}^{\omega^{x2}} \right.\\ &\left. + \,\omega^{y2} K_{bm,\psi}^{\omega^{y2}} + \omega^{z2} K_{bm,\psi}^{\omega^{z2}} + \omega^x\omega^z K_{bm,\psi}^{\omega^x\omega^z}\right) q + \psi^t \left(F_{mu} + F_{mu,bm} + F_{bm} + F_{amb} + F_c + F_g\right) \end{aligned} \tag{2.5}$$

with $C_\psi = 2\alpha_\psi\sqrt{K_\psi M_\psi}$. Equation (2.5) is rewritten in state space form:

$$\begin{cases} \dot{X} = AX + BU \\ Y = CX + DU \end{cases} \tag{2.6}$$

with the variable of state:

$$X = \begin{Bmatrix} q \\ \dot{q} \end{Bmatrix} \tag{2.7}$$

$$A = \begin{bmatrix} 0 & I \\ -M_\psi^{-1} K_\psi & -M_\psi^{-1} C_\psi \end{bmatrix} \tag{2.8}$$

$$B = \begin{bmatrix} 0 \\ M_\psi^{-1} \end{bmatrix} \tag{2.9}$$

$$\begin{aligned} U = &- \left(\Omega C_\psi^g + \omega^y C_{bm,\psi}^{\omega^y}\right)\dot{q} - \left(\,\dot{\Omega} K_\psi^{\dot{\Omega}} + \dot{\omega}^y K_{bm,\psi}^{\dot{\omega}^y} + \Omega\omega^y K_{bm,\psi}^{\Omega\omega^y} + \omega^{x2} K_{bm,\psi}^{\omega^{x2}} \right.\\ &\left. + \,\omega^{y2} K_{bm,\psi}^{\omega^{y2}} + \omega^{z2} K_{bm,\psi}^{\omega^{z2}} + \omega^x\omega^z K_{bm,\psi}^{\omega^x\omega^z}\right) q + \psi^t \left(F_{mu} + F_{mu,bm} + F_{bm} + F_{amb} + F_c + F_g\right) \end{aligned} \tag{2.10}$$

C is the output matrix from where the degrees of freedom of interest are extracted. The matrix D is the feedforward matrix and is zero in this study. In Jarroux *et al.* [135], the dynamic behaviour of on-board rotor-AMB system was numerically investigated during rotational and translational motions of the base. In order to validate the model, experimental results coming from a previous study were used. Angular shocks were applied to a flexible rotor with high gyroscopic effects supported by conventional ball bearings. It is shown that the model is able to describe with a fair degree of accuracy the dynamic behaviour of the rotor during transient pitching motions.

2.2 Active magnetic bearings

Active magnetic bearings allow frictionless rotations thanks to magnetic forces. They are inherently unstable and need a control loop to work. The aim of this section is to give sufficient informations concerning AMBs for the purpose of that work. For more details about AMB theory and design, readers can refer to Schweitzer and Maslen [136]. In rotor-AMB systems, the rotor displacements are used as inputs to a dedicated controller, the latter produces an output instruction providing a corrective action force on the rotor. To this aim, several components are needed in a control line or action line, see Figure 2.4. Detailed definitions of each of these components are given in Defoy [137]. Sensors respond to the displacements of the rotor rotating surface. They produce a voltage depending on the rotor motion and the variation of the magnetic flux (inductive sensors). The digital controller is composed of the analog-to-digital converter (ADC in Figure 2.4), the microprocessor and the digital-to-analog concert (DAC in Figure 2.4). The ADC samples the continuous signal at the sampling frequency while DAC carries out the reverse procedure. The microprocessor computes the controller response and

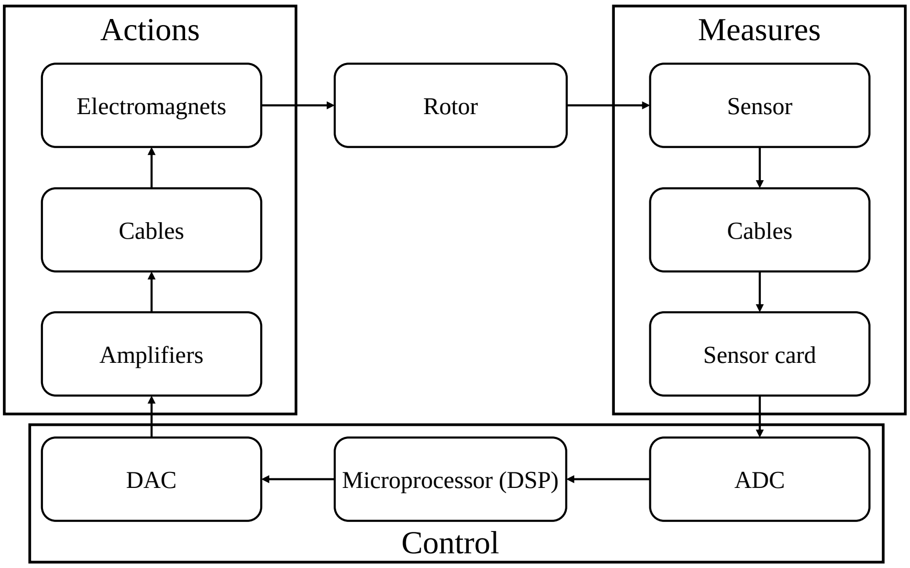

Figure 2.4: Action line and its components

a time delay is generated. These components, important for the design of the AMBs, are not considered in this thesis. The AMB restoring forces have a major importance. The latter are generated by two key components of the action line; the controller provides a request current sent to actuators while the latter converts this electrical energy into mechanical one.

2.2.1 Magnetic force and actuator

An electromagnet has usually two poles (sometimes more) and is made of a coil wrapped around an iron core made of laminated steel sheets stacked together. A laminated steel sheet ring is also mounted of the rotor side. It is assumed that the lines of the magnetic induction follow the path imposed by the iron core shape, as shown in Figure 2.5. Therefore, no magnetic losses are considered. To derive the magnetic force applied on the rotor, the reluctance network model, schemed in Figure 2.6, is employed. The reluctance of a magnetic circuit is analogous to resistance in electrical circuits. It is then the capacity of a material to be opposed to the magnetic field. The different reluctances of the magnetic circuit are given in Figure 2.6(b). It is composed of the rotor R_r, the stator R_s and the air gap R_g reluctances and the magnetic scalar potential Θ_1 and Θ_2 generated by each coil.

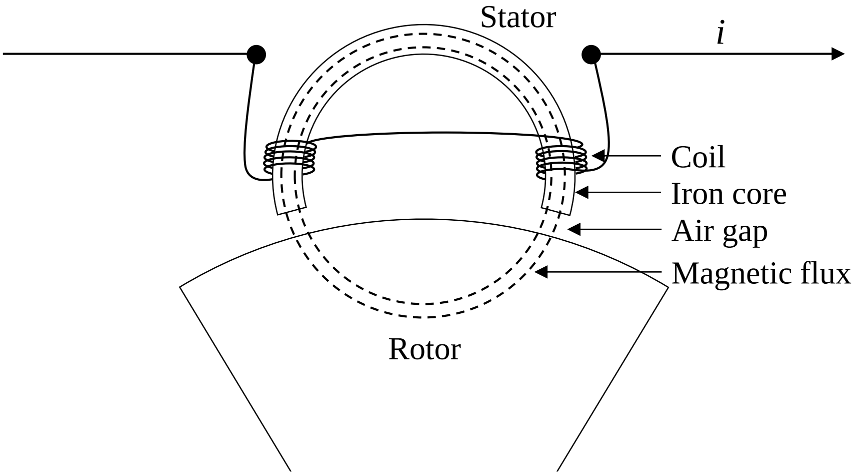

Figure 2.5: Actuator components

The equivalent circuit is schemed in Figure 2.6(b). The equivalent magnetic scalar potential Θ_{eq} is expressed as:

$$\Theta_{eq} = 2Ni \tag{2.11}$$

where N is the number of turns in the coil and i is the current travelling through the coil. The reluctance is defined as the ratio of the circuit length L over the magnetic permeability of material μ times the cross-section area S. The equivalent reluctance R_{eq} has the following

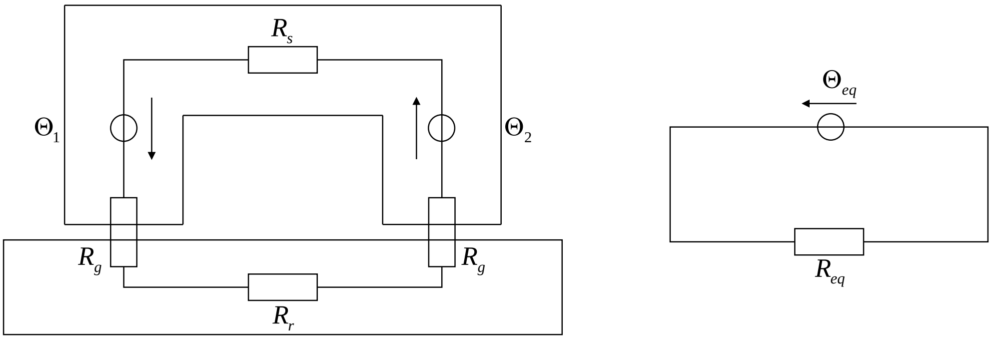

(a) Magnetic circuit (b) Equivalent magnetic circuit

Figure 2.6: Reluctance network model

formula:

$$R_{eq} = R_s + R_r + 2R_g = \frac{\frac{L}{\mu_r} + 2g}{\mu_0 S} \tag{2.12}$$

where L is the sum of the average length L_s and L_r of the magnetic field line in the stator and in the rotor respectively. The cross-section area S is supposed identical for the rotor, the stator and the air gap. The degree of magnetization of a material when subjected to a given magnetic field is called permeability. μ_0 and μ_r are the magnetic permeabilities of vacuum space and steel respectively. It is the coefficient linking the magnetic field H ($A.m^{-1}$) and the magnetic induction B (T), illustrated by the well-known B-H curve in Figure 2.7. The larger the permeability the more the material is sensitive to a magnetic field. Therefore, a high permeability is targeted for iron core while the permeability of air is close to zero. As shown

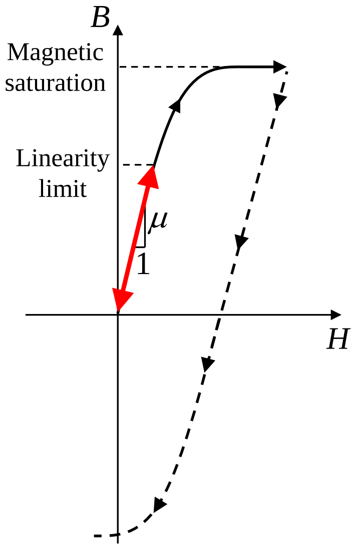

Figure 2.7: B-H curve - linear (red) and hysteretic behaviours (dotted lines)

in Figure 2.7, the B-H curve is linear until the so-called magnetic saturation. From there, the relationship becomes nonlinear and hysteresis phenomenon appears: an increasing magnetic field H gives a path different than a path created by a decreasing H. This effect makes difficult the behaviours prediction. In rotor-AMB system, the operating point of the electromagnet is supposed to be placed far from magnetic saturation and the B-H relationship is assumed to be linear. The flux density B is described as a function of the previously defined equivalent magnetic scalar potential Θ_{eq} and reluctance R_{eq}:

$$B = \frac{\Theta_{eq}}{SR_{eq}} \tag{2.13}$$

Considering that the normal to the surface S is x which is also the direction of motion of the rotor, the magnetic flux in the air gaps in the x-direction is H_x such as:

$$H_x = \frac{1}{\mu_0}B \tag{2.14}$$

The Maxwell stress tensor T is then used to determine the applied force $F_{electromag}$ by one electromagnet. Using only T_{xx} the component along the x-direction:

$$T_{xx} = \frac{1}{2}\mu_0 H_x^2 \tag{2.15}$$

The magnetic force $F_{electromag}$ formula is:

$$F_{electromag} = 2T_{xx}S = \frac{4\mu_0 SN^2 i^2}{\left(\frac{L}{\mu_r} + 2g_0\right)^2} \tag{2.16}$$

with μ_0 the magnetic permeability of the vacuum, S the pole area and N the number of turns in one coil, g_0 the nominal air gap, x the rotor position, μ_r the relative permeability of iron core and L the average length of the magnetic flux lines. The attractive magnetic force $F_{electromag}$ generated by one electromagnet is proportional to the square of applied current i but inversely proportional to the square of the magnetic air gap g_0. This means that the force tends to infinity when the rotor tends to contact the stator. Each action lines are composed of two electromagnets and are controlled in differential driving mode. This means that the current i applied to the electromagnet coils is a sum of a constant bias current I_0 and a control current i_c, provided by a controller. The latter is added to one electromagnet coil and subtracted to the opposite one. This is schemed in Figure 2.8.

The magnetic force produces by one action line, see equation (2.17), is then the sum of the

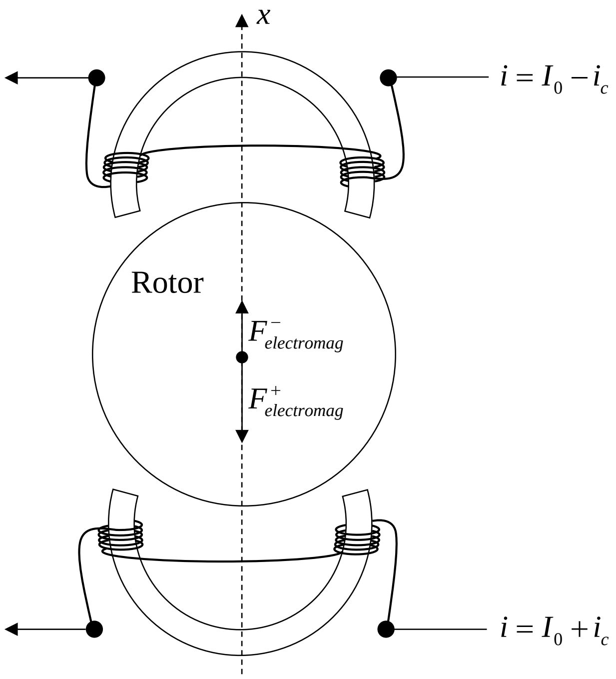

Figure 2.8: Magnetic force produced by a pair of two electromagnets

force applied by both the two electromagnets:

$$f_{amb,nl} = 4\cos\alpha\mu_0 SN^2 \left[\frac{(I_0 - i_c)^2}{\left(\frac{L}{\mu_r} + 2g_0 - 2x\cos\alpha\right)^2} - \frac{(I_0 + i_c)^2}{\left(\frac{L}{\mu_r} + 2g_0 + 2x\cos\alpha\right)^2} \right] \tag{2.17}$$

The constant angle α is between the action line and the line joining the pole and the rotor centres respectively. This force is represented by the surface plot, see Figure 2.9(a). The numerical values employed to build this plot come from the academic scale test rig used in this work. The boundaries are respectively the control current range and the TDB clearance. The current stiffening effect is more significant than the negative softening effect and the surface plot is asymmetric due to the bias current. In case of small rotor displacements and currents, equation (2.17) can be linearised. The linear magnetic force becomes:

$$f_{amb,l} = k_i i_c + k_x x \tag{2.18}$$

where k_i and k_x respectively the current and the negative stiffness:

$$k_i = \left.\frac{\partial f_{amb}}{\partial i_c}\right|_{i_c = I_W; x=0} = \frac{-16\cos\alpha\mu_0 SN^2}{\left(\frac{L}{\mu_r} + 2g_0\right)^2} I_0 \tag{2.19}$$

$$k_x = \left.\frac{\partial f_{amb}}{\partial x}\right|_{i_c = I_W; x=0} = \frac{32\cos^2\alpha\mu_0 SN^2}{\left(\frac{L}{\mu_r} + 2g_0\right)^3} \left(I_0^2 + I_W^2\right) \tag{2.20}$$

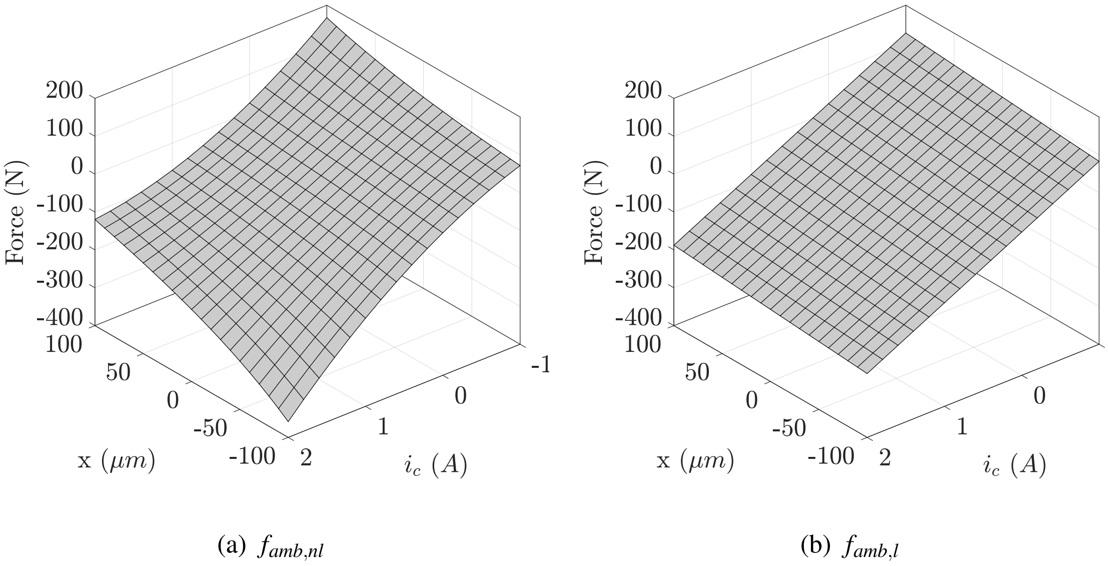

(a) $f_{amb,nl}$ (b) $f_{amb,l}$

Figure 2.9: Nonlinear (a) and linear (b) magnetic forces vs the displacement and the control current considering one action line

where I_W is the static control current provided to sustain the rotor weight.

The surface plot of the linear magnetic force is given in Figure 2.9(b). To compensate for base motions, the controller may have to generate large currents to counteract large rotor displacements. The question then arises whether the AMBs can be assumed linear or not. A first approach is to consider AMBs linear when the relative deviation between the linearised (2.18) and the nonlinear (2.17) equations, plotted in Figure 2.10(a), does not exceed the absolute value

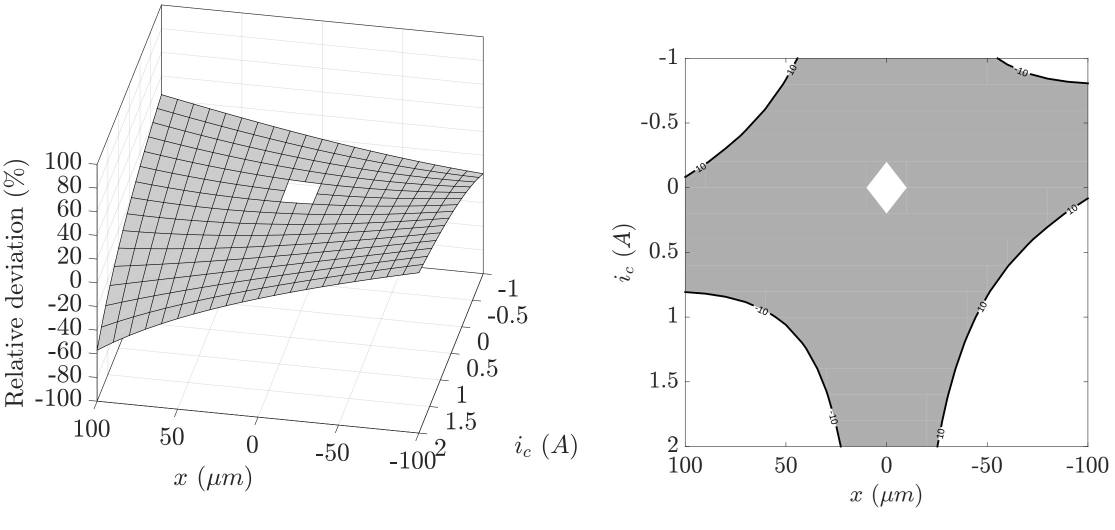

(a) Relative deviation (b) Linearity zone until 10% of deviation (grey)

Figure 2.10: Relative deviation and limits for 10%

of 10%. This is represented by Figure 2.10(b) where the linear (grey) and nonlinear zones are represented. Therefore, according to the operating points of the magnetic forces, in terms of rotor displacement and control current, it is possible to determine which of these formulations should be employed.

The amplifiers, see the action line sketched in Figure 2.11, control the electromagnets by applying a voltage u_p over the coil. The PWM (pulse width modulation) amplifiers using a current feedback permits the control current to follow the controller instruction; by applying a positive or negative voltage u_p over the coil, the control current i_c either increases or decreases, as shown in Figure 2.12.

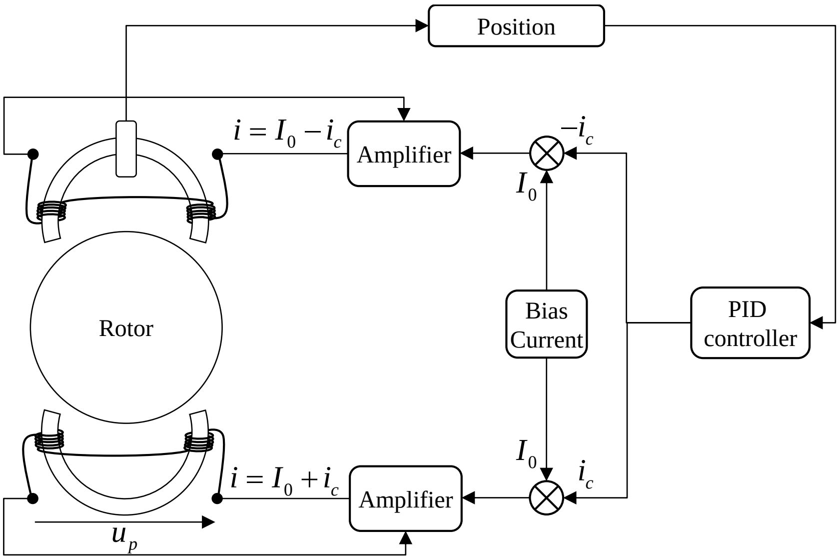

Figure 2.11: Complete action line

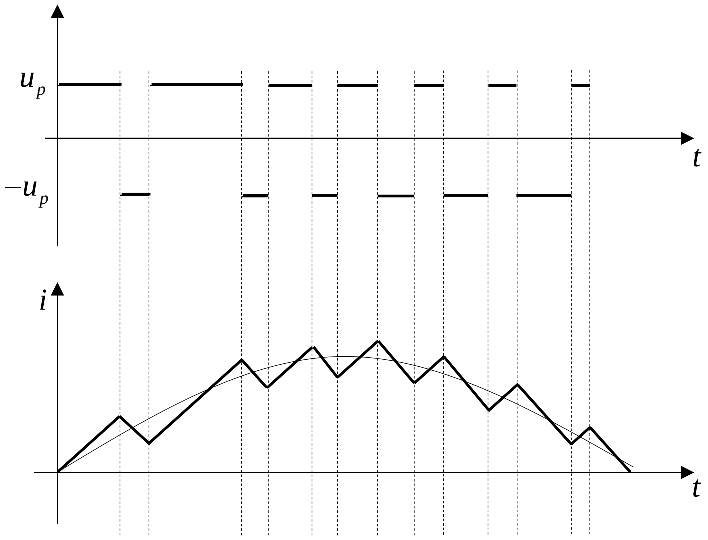

Figure 2.12: Coil current i_c (in bold) vs request current according to the applied voltage u_p

The actuator limits the capacity of the AMBs. The maximum current and voltage limits the maximal amplitude and variation (its time derivative) of the magnetic force respectively. If the requested current exceeds a threshold, the amplifier is saturated and the magnetic force is clipped. This nonlinearity may be considered in the case of strong base motions. If the force variation exceeds a certain limit, a time delay, and therefore a phase lag appears, decreasing the damping generated by the AMBs. Consequently, the dynamic capabilities of an actuator is frequency limited and is modelled by a low pass filter.

2.2.2 PID controller

The amplifier current request is provided by the controller which determines an instruction according to the measured rotor displacements. Many types of controller exist in the literature but the PID remains the most employed in industrial application for its simplicity and robustness. The PID is considered in this work. It generates a proportional action to an error, but also to its derivative and integral over time. For the particular case of rotor-AMB system, the error is the distance of the rotor from the zero position, in other words, the rotor relative displacement with respect to the centre of AMBs. The simplest way to formulate a PID transfer function in the Laplace domain is expressed in equation (2.21):

$$G(s) = \frac{K_I}{s} + K_P + K_D s \tag{2.21}$$

The gain K_P is equivalent to the stiffness and is chosen to counteract the inherent negative stiffness of AMBs. K_I is the integral gain and is a specific feature of AMB systems. It permits centering the rotor in the bearing: when time tends to infinity, the errors tend to be nil. For high integral gain, the rotor quickly reaches the centre of AMBs. If too large, instabilities can be exhibited. The integral gain is responsible for a time delay of the magnetic restoring force which represents negative damping. However, its influence is located in very low frequencies where no rotor modes are present. K_D, the derivative gain, brings damping to the system and dissipate energy. Using conventional bearings such as ball or hydrodynamic bearings, it is possible to directly select stiffness and damping parameters. In AMB system, the stiffness and damping parameters come from the real and imaginary parts of the bearing transfer function respectively in the case of a whole action line. For the design process of a PID, it is then more convenient to use transfer function expressed in terms of gain and phase. The latter determines completely the proportion of stiffness and damping from the gain as detailed by Figure 2.13.

A phase equals to 0° indicates a pure stiffness while a phase equals to 90° implies a pure damping. An appropriate phase for a rotor-AMB system would be comprised between 0 and 90°. Otherwise, either the damping or the stiffness would be negative. Several filters are often added to the simple PID formulation expressed by equation (2.21). First order lag filters can be used to limit the increase of damping generated by the derivative gain. Indeed, a too large increase of phase on the operating speed range may imply a low stiffness and difficulty to

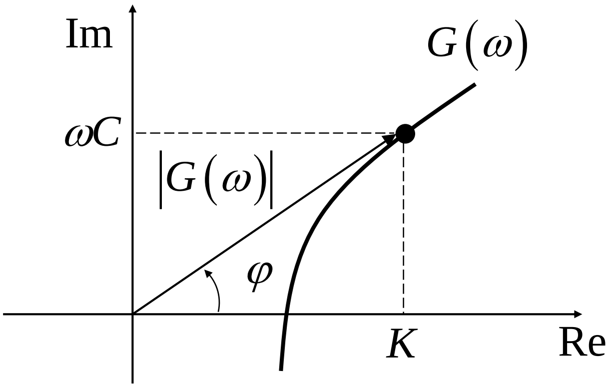

Figure 2.13: Transfer function - stiffness and damping relationship

limit the gain in higher frequency. For shaft having one or more bending modes in their operating speed ranges, second order lead-lag compensators are used to bring damping on narrow bandwidth. The high frequency modes, outside the operating speed ranges, comprised in the controller bandwidth should be damped to avoid spillover effect (high frequency instability). Second order lead-lag compensators are also used to this end. For robustness purpose, the gyroscopic effects on the different rotor modes should be taken into account for the application of phase. The combination of these filters with a simple PID is an augmented PID, which is considered in this research work.

Usually, each action line has its own PID operating independently from the others. A rotor-AMB system with two radial and one thrust AMBs has five SISO PID working separately. A single input single output (SISO) system uses only one sensor and one actuator in contrast with multi input multi output (MIMO) systems which are able to generate cross-coupled stiffness for example. Other configurations such as SIMO or MISO are also possible.

Table 2.1 gathers the components considered in the action line and the related assumptions.

Table 2.1: Modelling of the elements of the action line

Elements of the action line	**Modelling**
Cables	Not considered
Inductive sensors	Not considered
Converters (ADC - DAC)	Not considered
Amplifiers	Low pass filter (0 - 2kHz) - current saturation (for large rotor displacement)
Electromagnets	Linear force (current and negative stiffness) - nonlinear force (for large rotor displacement)
Controller	SISO augmented PID

2.3 About touchdown bearings

2.3.1 Functions and arrangements

TDBs have two main functions. The first one is to protect the AMBs from large unexpected transient loads that exceed the design capacity of AMBs. Sudden increases of pressure in a compressor, blade loss or even earthquake can appear on real industrial turbomachines while operating. The second is to ensure a back-up support when AMBs are no longer available. This is obviously the case when the machine is stopped, in storage or during transport but also when the AMBs fail. There may be several reasons for this; an electrical failure, for example. In this case, the rotor forced by gravity drops onto its TDBs and the previous literature survey has shown the wide variety of induced rotor behaviours. The latter depend, among others, on whether the rotor-AMB system assembly is vertical or horizontal. The choice of the type of assembly is guided by the type of applications targeted. Vertical assemblies are interesting when the available surface to fix the turbomachinery is limited. This research project focuses especially on the horizontal assembly and the targeted applications concern compressors mounted on FPSO or turbines in nuclear plants. The TDBs have atypical operating conditions compared to conventional bearings. They have to sustain highly transient loads during a short-period of time. Usually, the TDB design includes the following features:

- No fluid lubrication systems; one of the main advantages of rotor-AMB system is the absence of lubrication. To maintain these advantages, the TDBs should run without any lubrication devices. Dry-lubricated materials or sometimes greases can be employed.

- Materials with low thermal conductivity and high mechanical strength, like ceramics are used.

- A rotor-TDB clearance about the half of the rotor-AMB clearance to carry out its protecting role.

- A compliant supporting housing: it is now well-established that soft and damped supports can limit dangerous rotor behaviours during rotor-stator interactions.

- A hard-stop to limit the motion of the TDB relative to its housing, to avoid large deflections and potential damages on seals.

- No cages avoiding direct contact between rolling elements.

Two main types of arrangement can be found in industrial applications. A typical radial arrangement, as shown in Figure 2.14, is able to handle only radial drops while the axial and radial arrangement, as shown in Figure 2.15, can handle a combined rotor drops (in the case of thrust and radial AMB failures).

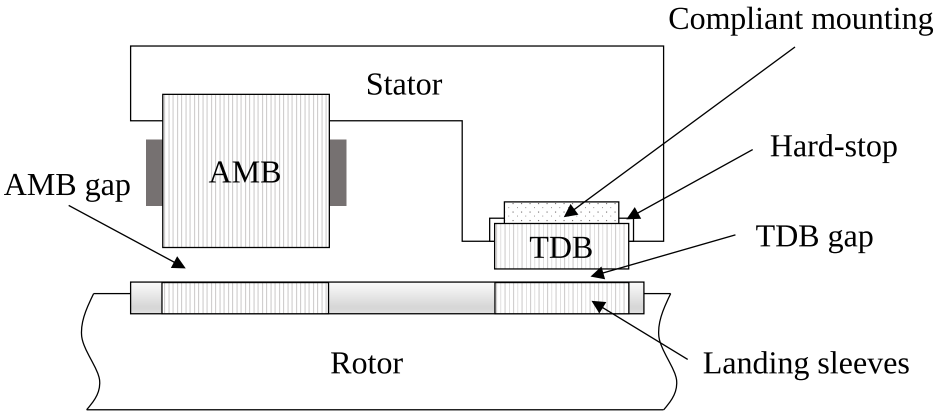

Figure 2.14: Typical radial TDB arrangement

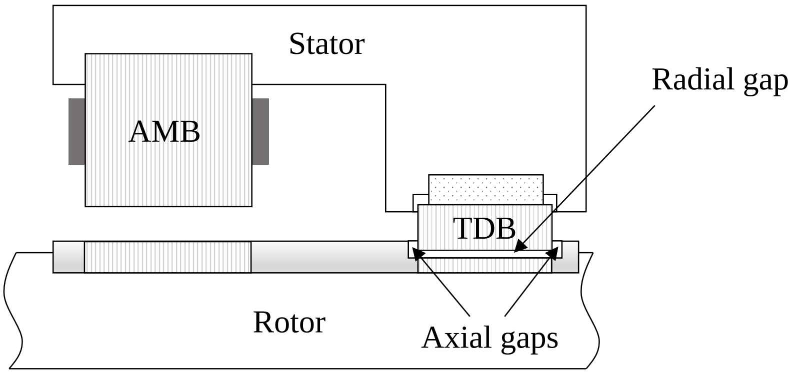

Figure 2.15: Typical axial-radial TDB arrangement

2.3.2 Typical design

Two main types of TDBs can be found: ball bearings and bushing type bearings. Hybrid types also exist but are not treated in this research work. The bushing type bearing, see Figure 2.16(a), generally consists in a fixed stator part made of bearing pads mounted in a supporting housing. When dropping, the rotor landing sleeves contact the bearing pads. As no rotating parts are available in this design, the friction effects have to be considerably low to avoid as much as possible dangerous rotordynamics. Therefore, dry-self lubricated materials are often used to meet that criterion. A major focus of research concerning this type of bearing is dedicated to tribological aspects and materials to obtain reduced friction coefficients. Bushing type bearings are reliable thanks to their design simplicity. It is generally adapted for heavy machines where gravity effects are large enough to stabilize the rotor in its TDBs. This technology is not employed in this research project and for more details, readers can refer to the work of Fumagalli [117] or Collins *et al.* [138]. For the rest of this work, touchdown bearings refer to ball bearings.

Ball bearings are widely employed in the rotor drop dynamics field. This type of technology limits dangerous rotor behaviours induced by sliding friction; the TDBs usually reach the rotor

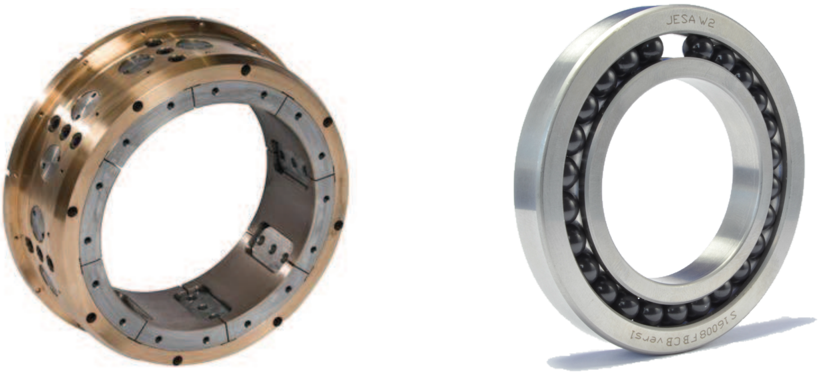

(a) Bushing type (b) Ball bearing type

Figure 2.16: Different type of touchdown bearings

speed in very short times while cancelling the friction forces. Cages, classically used to avoid rolling element interactions, are not often present in this type of application. A TDB has to carry out strong rotational accelerations and the cage may not be able to sustain it. Balls are usually made of ceramic materials employed for their high mechanical resistances, low friction coefficients with steel and low thermal conductivities. Modern arrangements are often axial-radial types; double-row angular contact ball bearings are able to sustain both axial and radial drops. However, in other applications such as vacuum pumps, the TDB may be a simple deep groove ball bearing, see Figure 2.16(b).

Whether the type of TDB employed, compliant mountings are often used to limit transmitted loads and bring stability when interactions with the rotor occur. Considering ball bearing, this type of components are fitted between the housing and the outer race as shown in Figure 2.17.

2.3.3 Assumptions and requirements

TDBs are still the subject of intensive research. In the literature, various models are available depending on the need of the study. Bearings manufacturers, involved in improving TDB designs, may need detailed models where interactions between races and each rolling elements are considered; it allows the estimation of the TDB life time for example. This is the case in references [22, 23, 114, 122, 124].

The main interrogation for the TDB modelling concerns the need to model all the rolling elements. Helfert *et al.* [139] analysed with a rapid camera the rotation of the balls of a cageless TDB during a rotor drop. They observed that the balls as well as the inner race reached the shaft rotational speed almost at the same time: the sliding between the rolling elements has few influence on the time needed for the TDB to reach the rotor spin speed. As explained by Kärkkäinen *et al.* [113], focusing on the reliable prediction of the overall dynamic behaviour of a turbomachinery, such a detailed model, where each rolling element has several degrees of freedom, seems not to be necessary. On the other hand, Sun *et al.* [22, 23] emphasized that if

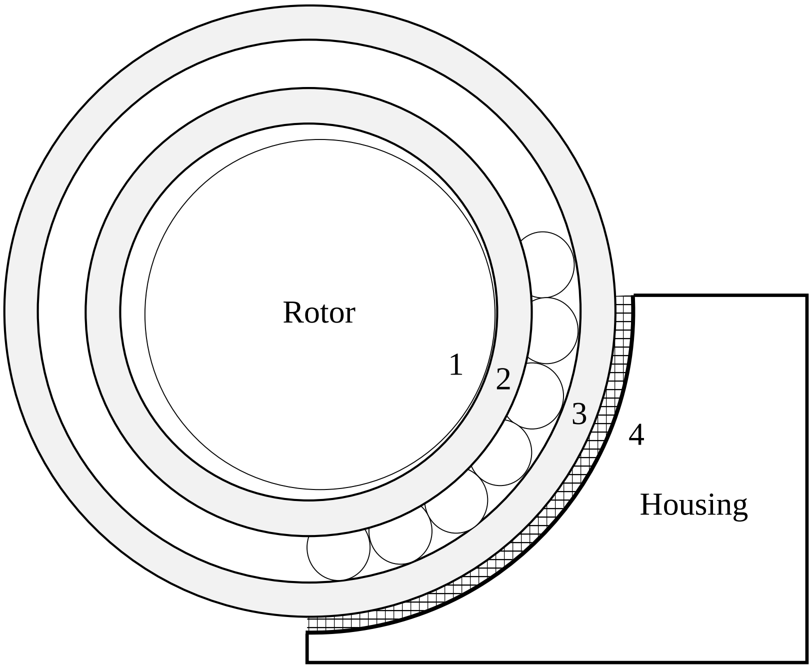

Figure 2.17: TDB-housing assembly

well assessed, the required axial-preload avoids the radial stiffness decrease of angular contact ball bearing with respect to rotational speed, as shown in Figure 2.18.

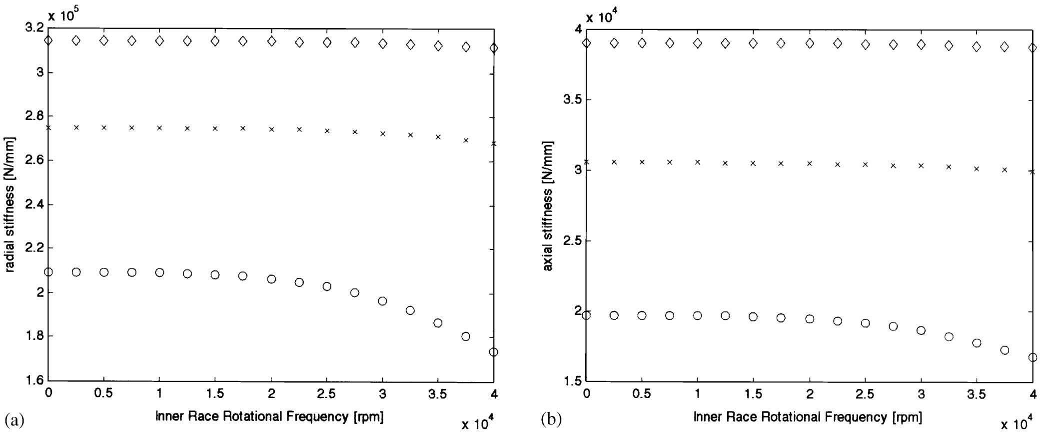

Figure 2.18: Influence of different axial pre-load cases ($\circ$ $89N$, $\times$ $222N$, $\diamond$ $356N$) on the radial (a) and axial (b) stiffnesses of the TDB vs the rotational speed - Sun *et al.* [22, 23]

In the light of these conclusions, the modelling of each rolling elements seems not to be relevant for the targeted application in this study and the related assumptions concerning the TDB model are given hereafter:

- The bearing dynamic properties do not change with its rotational speed (no softening effects).

- The rolling-without-slipping kinematic conditions are satisfied (no sliding of rolling elements).

The TDB model requirements are then:

- The interaction between the rotor (1) and inner race (2), see Figure 3.2. The different types of contact models are presented in the Section 2.5.
- The ball bearing model, linking the motion of the inner race (2) and the outer race (3), see Figure 3.2, as well as the ball bearing rotational speed. A complete procedure is described in the Section 2.4 for this particular purpose.
- The interaction between the outer race (3) and the housing (4), see Figure 3.2. The dynamic characterisation of the considered compliant component is provided in the Chapter 3. Numerical models are developed accordingly.

As the compliant device is not presented in this chapter, it is preferred to present the complete TDB models in Chapter 3. The following sections deal with the two first point of the TDB requirements.

2.4 Ball bearing modelling

The ball bearing can be modelled by a radial force-deflection relationship which may come from experimental, finite element or analytical results. The latter is employed in this project for its simplicity and efficiency. The rotational modelling is also considered.

2.4.1 Force-deflection relationship

Palmgren [140] was one on the first to derive empirically a simple bearing load-deflection relationship. The main assumptions lie in the fact that the ball bearing has no internal clearance, the races are completely rigid and mounted in a rigid housing. This well-known model is used as reference here. Other models enable to produce more precise results. The work of Brewe and Hamrock [141], Hamrock and Anderson [142] or Harris [143] gave deep insights into the modelling of rolling-element bearings. Sopanen and Mikkola [144, 145] also developed a complete 6 degrees of freedom ball bearing model for dynamic analysis including localized effects. In radial direction, their work is based among other on Brewe and Hamrock [141] concerning the approximation of ellipticity parameter. Kramer [146] used more simple formula not adapted for angular-contact ball bearing. Recently, Guay [147] summarized the procedure to set-up the load-deflection relationship of a ball bearing, based on geometrical and material characteristics.

Generally speaking, this procedure requires:

- The bearing geometric parameters such as radii of element in contact, materials, type of contact etc. Equivalent radii and curvature differences can be set-up to describe the races rolling-elements interactions.

- The derivation of the contact stress and the approximation of elliptic integrals to obtain the load-deflection relationship for one rolling element in contact with both the inner and outer races.

- Considering the bearing static equilibrium when subjected to an external load in order to determine the global load-deflection relationship.

This procedure is briefly described hereafter and readers can refer to Harris [143] or Guay [147] for more informations.

2.4.1.1 Geometric contact parameters

The geometric contact parameters are determined after having extracted basic dimensions of the ball bearing. D is the ball diameter and the pitch diameter d_m is the mean of the inner d_{ir} and outer d_{or} raceway contact diameters, as shown in Figure 2.19. The conformity parameter, given by equation (2.22), is the ratio of the raceway groove curvature radius r_j over the ball diameter D. The subscript j can represents whether the inner or outer race. In terms of load capacity, the perfect conformity value would be 0.5, meaning that the ball and the raceway groove have the same radii. However, this would lead to large rolling friction losses resulting in a significant global resistant torque and a reduced lifetime. In modern ball bearing designs, the conformity

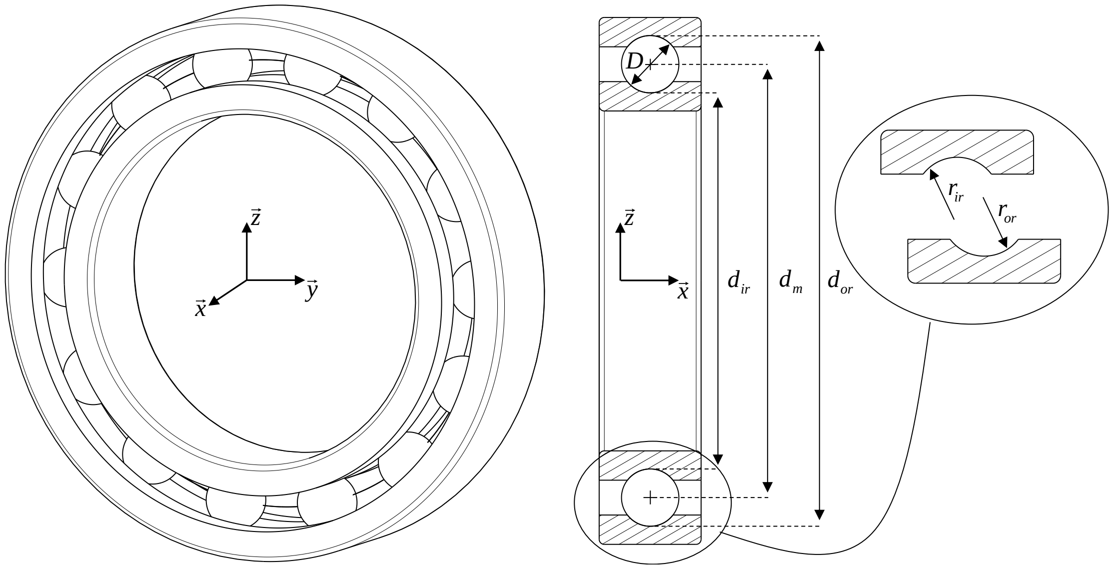

(a) Overview (b) Cross-section in the z-x plane

Figure 2.19: Deep groove ball bearing geometry

between races and rolling elements lies between 0.51 to 0.54, 0.52 being the reference value.

$$\xi_j = \frac{r_j}{D} \tag{2.22}$$

As explained by Harris [143] and detailed in Figure 2.20, two bodies having different radii of curvature, in a pair of principal planes passing through the contact between the bodies may contact each other at a single point under the condition of no applied load. Therefore, each ball-race contact can be reduced to ellipsoids in contact.

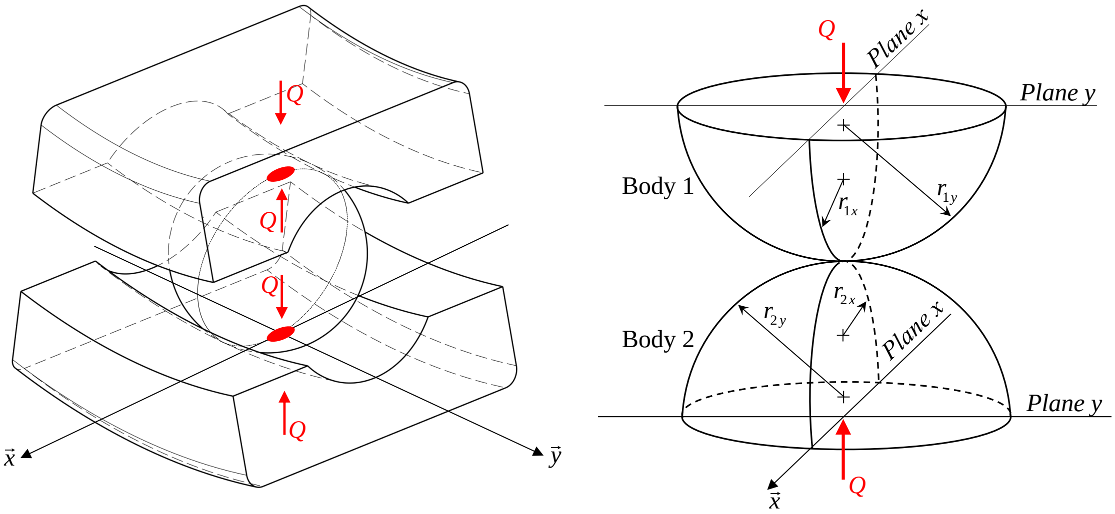

(a) One rolling element contact case

(b) Ellipsoids in contact

Figure 2.20: Geometry of a race rolling element contact

In Figure 2.20(b), the upper and lower bodies are denoted by 1 and 2 respectively while the principal planes are denoted by x and y.

For example, the radius of curvature of body 1 in plane y is r_{1y} and the related curvature is $\frac{1}{r_{1y}}$. Although the radius of curvature is always positive, the curvature may be negative or positive; convex surfaces, or non-conformal, (the centre of curvature is located inside the solid) being positive while concave surfaces, or conformal, negative. To define the contact between body 1 and 2, the equivalent radius $\Re$ and the curvature difference Γ are defined as:

$$\Re = \left(\frac{1}{\Re_x} + \frac{1}{\Re_y}\right)^{-1} \tag{2.23}$$

$$\Gamma = \Re\left(\frac{1}{\Re_x} - \frac{1}{\Re_y}\right) \tag{2.24}$$

where $\Re_x$ and $\Re_y$ are the radii of curvature of each principal planes defined as:

$$\Re_x = \left(\frac{1}{r_{1x}} + \frac{1}{r_{2x}}\right)^{-1} \tag{2.25}$$

$$\Re_y = \left(\frac{1}{r_{1y}} + \frac{1}{r_{2y}}\right)^{-1} \tag{2.26}$$

Let the body 1 and 2, see Figure 2.20(b), be respectively the ball and the inner or outer race. The contact properties are provided in Table 2.2.

Table 2.2: Contact properties

	Inner race-ball contact	**Outer race-ball contact**
r_{1x}	$\frac{D}{2}$	$\frac{D}{2}$
r_{1y}	$\frac{D}{2}$	$\frac{D}{2}$
r_{2x}	$-\xi_{ir}D$	$-\xi_{or}D$
r_{2y}	$\frac{D(1-\gamma)}{2\gamma}$	$-\frac{D(1+\gamma)}{2\gamma}$
Radii of curvature $\Re_y$	$\frac{D\xi_{ir}}{2\xi_{ir}-1}$	$\frac{D\xi_{or}}{2\xi_{or}-1}$
Radii of curvature $\Re_y$	$\frac{D(1-\gamma)}{2}$	$\frac{D(1+\gamma)}{2}$
Equivalent radii $\Re$	$\frac{D}{4+\frac{2\gamma}{1-\gamma}-\frac{1}{\xi_{ir}}}$	$\frac{D}{4-\frac{2\gamma}{1+\gamma}-\frac{1}{\xi_{or}}}$
Curvature difference Γ	$\frac{\frac{2\gamma}{1-\gamma}+\frac{1}{\xi_{ir}}}{4+\frac{2\gamma}{1-\gamma}-\frac{1}{\xi_{ir}}}$	$\frac{\frac{-2\gamma}{1+\gamma}+\frac{1}{\xi_{or}}}{4-\frac{2\gamma}{1+\gamma}-\frac{1}{\xi_{or}}}$

The parameter γ is defined as:

$$\gamma = \frac{D}{d_m}\cos\alpha_c \tag{2.27}$$

where α_c is the contact angle for angular contact ball bearing.

2.4.1.2 Contact stress and deformation

The load-deflection relationship is extracted from the Hertz contact theory and is achieved for both the ball inner race and ball outer race contact cases. In 1882, Hertz [148] developed in his work, *On the contact of elastic solids*, the force-deflection relationships adapted for point contact cases, like sphere-sphere contact. It was shown that the contact area increases with the load and becomes elliptical, making the relationship nonlinear. The normal stress σ, see Figure 2.21, within the contact area is expressed in equation (2.28).

In order to calculate the stress σ at any location in the contact area, the ellipticity parameter κ which depends on the a and b ellipse axes has to be sought:

$$\kappa = \frac{a}{b} \tag{2.30}$$

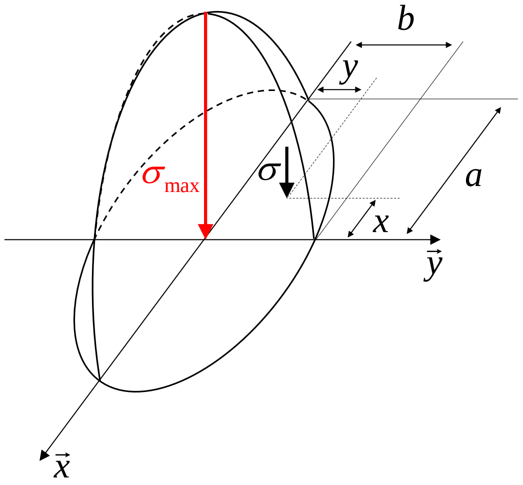

Figure 2.21: Normal stress and elliptical area

$$\sigma = \frac{3Q}{2\pi ab}\left[1-\left(\frac{x}{a}\right)^2-\left(\frac{y}{b}\right)^2\right]^{\frac{1}{2}} \tag{2.28}$$

where Q is the normal load applied to the rolling element, a and b are the semi-major and semi-minor axes of the projected elliptical area of contact. The maximal compressive stress is located at the geometrical centre of the contact:

$$\sigma_{max} = \frac{3Q}{2\pi ab} \tag{2.29}$$

It can be shown that κ depends on the curvature difference Γ of the two bodies in contact, but also on the elliptic integrals of the first $F(\kappa)$ and second $S(\kappa)$ kinds. κ is determined by solving the following equation:

$$1-\frac{2}{\kappa^2-1}\left[\frac{F(\kappa)}{S(\kappa)}-1\right]-\Gamma=0 \tag{2.31}$$

where the elliptic integrals of the first $F(\kappa)$ and second $S(\kappa)$ are expressed as:

$$F(\kappa)=\int_0^{\frac{\pi}{2}}\left[1-\left(1-\frac{1}{\kappa^2}\right)\sin^2\phi\right]^{-\frac{1}{2}}d\phi \tag{2.32}$$

$$S(\kappa)=\int_0^{\frac{\pi}{2}}\left[1-\left(1-\frac{1}{\kappa^2}\right)\sin^2\phi\right]^{\frac{1}{2}}d\phi \tag{2.33}$$

No analytical solution exists for these elliptic integrals and an iterative procedure is required. Approximate solutions were given by Brewe and Hamrock [141] and Hamrock and Anderson [142] using a least squares method of linear regression with an induced error of less than 4 %. These solutions were also employed by Harris [143]. Guay [147] proposed a solution with less than 1 % of error:

$$\kappa \approx 1.18\left(\frac{\Re_x}{\Re_y}\right)^{0.598}-0.19 \tag{2.34}$$

The elliptic integrals have the following approximate values:

$$F(\kappa)\approx 1+q\left(1+\ln\left(\frac{\Re_x}{\Re_y}\right)\right) \tag{2.35}$$

$$S(\kappa)\approx 1+\frac{q}{\left(\frac{\Re_x}{\Re_y}\right)} \tag{2.36}$$

with $q = \frac{\pi}{2} - 1$. The semi-major axis a of the elliptical contact can be expressed as:

$$a = \left[\frac{6\kappa^2 S(\kappa) Q \mathfrak{R}}{\pi E}\right]^{\frac{1}{3}} \tag{2.37}$$

where E the effective modulus of elasticity defined as:

$$E = \frac{2}{\frac{1-\nu_1^2}{E_1} + \frac{1-\nu_2^2}{E_2}} \tag{2.38}$$

where E_i the Young's modulus and ν_i the Poisson ratio of the i body in contact. The equation of the semi-minor axis b is given by:

$$b = \frac{a}{\kappa} \tag{2.39}$$

It is then possible to determine the maximum normal contact stress σ_{max} depending on the applied normal load Q, by introducing equation (2.37) in equation (2.29):

$$\sigma_{max} = \frac{3Q}{2\pi ab} = \frac{3Q}{2\pi \frac{a^2}{\kappa}} = \left(\frac{E}{S(\kappa)\mathfrak{R}}\right)^{\frac{2}{3}} \left(\frac{3Q}{32\pi\kappa}\right)^{\frac{1}{3}} \tag{2.40}$$

One can also define relation between the deformation of the contact δ (race + rolling element) and the applied normal load Q:

$$\delta = \frac{F(\kappa)}{[2S(\kappa)\mathfrak{R}]^{\frac{1}{3}}} \left(\frac{3Q}{\pi\kappa E}\right)^{\frac{2}{3}} \tag{2.41}$$

This deformation is maximal inside the bodies in contact. By rearranging equation (2.41), the contact stiffness K_j appears in equation (2.42), where the subscript j can represents whether the inner *ir* or outer *or* race. The contact stiffness K_j is normal to the contact and nonlinear. It increases with the load since the elliptic contact surface increases too.

$$K_j = \frac{\pi\kappa_j E}{3} \left[\frac{2S_j(\kappa_j)\mathfrak{R}_j}{F_j(\kappa_j)^3}\right]^{\frac{1}{2}} \tag{2.42}$$

Finally, equation (2.41) can be rewritten as equation (2.43).

$$Q = K_{ir}\delta_{ir}^{\frac{3}{2}} = K_{or}\delta_{or}^{\frac{3}{2}} \tag{2.43}$$

The coupled normal stiffness K_n takes into account the normal deformation between the rolling element and the inner δ_{ir} / outer δ_{or} races. This will give the coupled normal deformation δ_n

associated with one ball in contact with the races:

$$Q = K_n \delta_n^{\frac{3}{2}} \tag{2.44}$$

where the coupled normal stiffness K_n is defined as:

$$K_n = \left(\frac{1}{K_{ir}^{\frac{2}{3}}} + \frac{1}{K_{or}^{\frac{2}{3}}} \right)^{-\frac{3}{2}} \tag{2.45}$$

Palmgren gave a much more simple load-deflection relationship for one rolling element, see equation (2.46), where only the ball diameter D and the applied load Q are involved. All parameters concerning materials or ellipticity are supposed to be contained in the coefficient 0.002 which depends on the type of bearing employed:

$$\delta_n = 0.002 \left(\frac{Q^2}{D} \right)^{\frac{1}{3}} \tag{2.46}$$

2.4.1.3 Bearing under radial load

Once the load-deflection relationship for one ball in contact with two races has been set-up, the overall bearing force-deflection relationship can be determined. Depending on the initial clearance and the preloading, the distribution of an external load (radial, axial or combined) on each balls is different as shown in Figure 2.22, where ε is the load distribution factor. If well assessed, the preload avoids overloaded rolling elements. External loads imply a relative displacement between the inner and the outer races. More details are given in Guay [147]. Assuming that the outer race is fixed, the static equilibrium of the inner race for an angular contact ball bearing when an external load F (combination of an axial and a radial component)

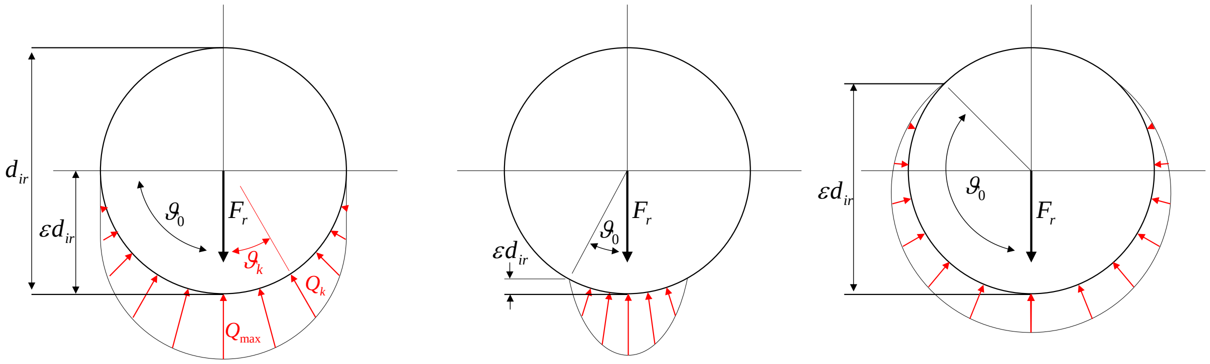

(a) $\varepsilon = 0.5$ - without clearance (b) $0 < \varepsilon < 0.5$ - with clearance (c) $0.5 < \varepsilon < 1$ - with preload

Figure 2.22: Clearance effect on the radial load distribution

is applied can be set-up as:

$$F + \sum Q_k = 0 \tag{2.47}$$

with Q_k, the load on the k-th ball expressed in equation (2.44). Projecting equation (2.47) in the axial and radial directions gives:

$$\begin{aligned} F_a &= \sum Q_k \sin \alpha_c \\ F_r &= \cos \alpha_c \sum Q_k \cos \vartheta_k \end{aligned} \tag{2.48}$$

with ϑ_k, the azimuth angle. Finally, equation (2.48) can be written in the integral form as:

$$\begin{aligned} F_a &= \frac{ZK_n}{2\pi} \sin \alpha_c \left(2\varepsilon \delta_r \cos \alpha_c\right)^{\frac{3}{2}} \int_{-\vartheta_0}^{+\vartheta_0} \left(1 - \frac{1}{2\varepsilon}\left(1 - \cos \vartheta\right)\right)^{\frac{3}{2}} d\vartheta \\ F_r &= \frac{ZK_n}{2\pi} \cos \alpha_c \left(2\varepsilon \delta_r \cos \alpha_c\right)^{\frac{3}{2}} \int_{-\vartheta_0}^{+\vartheta_0} \left(1 - \frac{1}{2\varepsilon}\left(1 - \cos \vartheta\right)\right)^{\frac{3}{2}} \cos \vartheta d\vartheta \end{aligned} \tag{2.49}$$

with Z, the total number of balls. The equation (2.49) gives the final relationship between external axial F_a and radial F_r loads and the overall radial deflection δ_r of the bearing. According to Palmgren, the global radial deflection δ_r is mainly due to the highest loaded rolling element. Determining the maximal load seen by the most charged rolling element, given in equation (2.50), the load-deflection relationship, see equation (2.51), is then found by combining equation (2.50) and (2.46).

$$Q_{max} = \frac{5F_r}{Z \cos \alpha_c} \tag{2.50}$$

$$F_r = \frac{Z\sqrt{D} \cos \alpha_c}{5} \left(\frac{\delta_r}{0.002}\right)^{\frac{3}{2}} \tag{2.51}$$

These analytical methods (Guay and Palmgren) are used and compared with the FE methods: a mesh where balls and races are modelled with 3D elements was obtained. The outer race was clamped and a distributed radial load was applied on the inner race surface. The relative inner-outer race radial deflection was recorded. This was done for the case of a double-row angular contact ball bearing where races were made of nitrogen steel with ceramic balls. The results are reported in Figure 2.23. It appears that the analytical and the FE methods give close results. As a first attempt, the Palmgren model gives rather good predictions and could be used when only few informations on the ball bearing are available. The method proposed by Guay [147] is used finally for its more accurate results.

Due to their nonlinearity, these load-deflection relationships are not convenient to determine the solution of the eigenvalue problem and realised modal analysis of a rotor-bearing system. For this purpose, the linearisation is often performed to obtain conventional stiffness and damping parameters, easily implementable in FE codes. The tangential stiffness is obtained by deriving the force-deflection relationship F_r of the bearing around an operating point.

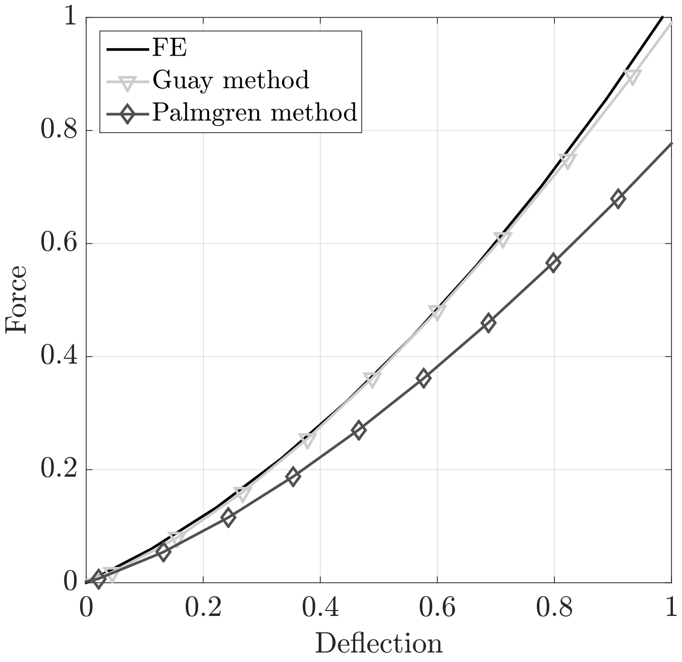

Figure 2.23: FE - analytical results comparison

2.4.1.4 Damping in bearing

Damping in a ball bearing is rather small and complex to determine. According to Dietl *et al.* [149], the major sources of damping in a ball bearing are due to lubricant, Hertzian hysteresis due to rolling deformations and friction between the outer race and the support. For our application, no lubricant is present and the outer race housing interaction is treated in another section. Kramer [146] gives the following range of reasonable values for the damping:

$$\frac{c_{brg}}{k_{brg}} \times 10^5 \in [0.25, 2.5] \tag{2.52}$$

where k_{brg} is the linearised stiffness value of the ball bearing. As the bearing damping is very small, this raw estimation is sufficient for our model.

2.4.2 Rotational dynamics

The spin-up is one of the key feature of the ball bearing type TDB. It has been previously seen that the detailed modelling of each rolling element was not necessary to describe the whole rotor behaviour during drops. In this context, a global modelling is appropriate. The employed method consists in calculating an equivalent rotational inertia of the TDB by taking into account the different kinetic energy contributions of each bearing component, as in Kärkkäinen *et al.* [113] and Cole *et al.* [122]. An internal resistance torque has to be identified. The main advantage of this modelling is its simplicity of resolution since it is represented by only one equation of motion. The major uncertainties lie in the assumptions made about the kinematic conditions of the bearing elements and in the internal resistance modelling used.

2.4.2.1 Equivalent inertia

To determine the equivalent rotational inertia J_{eq} of the ball bearing, the equivalent rotational energy T_{eq} has to be determined and derived in the Lagrange's equations. Three components must be defined:

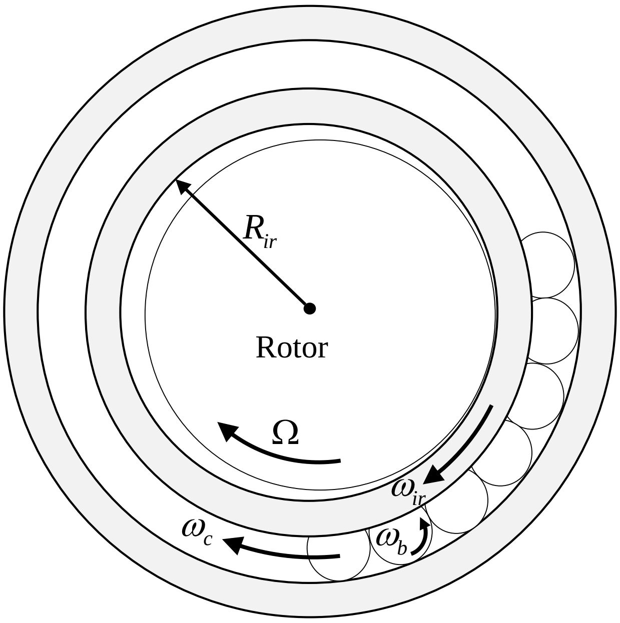

Figure 2.24: TDB components driven by the rotor after a drop event

- The rotational kinetic energy T_{ir} of the inner race,

$$T_{ir} = \frac{1}{2} J_{ir} {\omega_{ir}}^2 \tag{2.53}$$

  where ω_{ir} is the inner race rotational speed, see Figure 2.24. Considering the inner race as a simple ring, the rotational inertia J_{ir} is defined as:

$$J_{ir} = \frac{1}{2} m_{ir} \left(\left(\frac{d_{ir}}{2} \right)^2 + R_{ir}^2 \right) \tag{2.54}$$

  with m_{ir}, d_{ir} and R_{ir} the mass, the groove diameter and the radius of the inner race, respectively.

- The kinetic energy of the k-th ball in rotation around its own axis T_b^k,

$$T_b^k = \frac{1}{2} J_b {\omega_b}^2 \tag{2.55}$$

where ω_b and J_b are respectively the ball rotational speed and inertia defined as:

$$J_b = \frac{2}{5} m_b \left(\frac{D}{2}\right)^2 \tag{2.56}$$

- And the kinetic energy of the k-th ball in a circumferential motion at a distance d_m from the centre of the ball bearing T_c^k,

$$T_c^k = \frac{1}{2} J_c {\omega_c}^2 \tag{2.57}$$

where ω_c and J_c are respectively the circumferential rotational speed and inertia defined as:

$$J_c = m_b d_m^2 \tag{2.58}$$

Assuming a perfect rolling-without-slipping kinematic condition between balls and races, the ball rotational ω_b and circumferential ω_c speeds are expressed as a function of ω_{ir}:

$$\omega_b = \frac{1}{2} \frac{d_m}{D} \left(1 - \gamma^2\right) \omega_{ir} \tag{2.59}$$

$$\omega_c = \frac{1}{2} (1 - \gamma) \omega_{ir} \tag{2.60}$$

The equivalent rotational kinetic energy T_{eq} of the ball bearing can be written as:

$$T_{eq} = T_{ir} + \sum_{k=1}^{Z} \left(T_b^k + T_c^k\right) \tag{2.61}$$

The expression of this energy is then derived using the Lagrange's equations (2.2) where the equivalent rotational inertia J_{eq} is defined as:

$$J_{eq} = J_{ir} + Z \left(\frac{1}{4} J_c (1 - \gamma)^2 + \frac{1}{4} J_b \frac{d_m^2}{D^2} \left(1 - \gamma^2\right)^2 \right) \tag{2.62}$$

Z being the total number of balls contained in the TDB and γ being the previously defined ratio of the ball and pitch diameters. This energy gives an equivalent TDB rotational inertia considering rolling-without-slipping kinematic conditions.

2.4.2.2 Internal resistance torque

The internal resistance torque in a ball bearing is generated by various and complex physical phenomena. It is still difficult today to obtain reliable models describing well the rolling internal resistance since the involved phenomena are complex: the external loads, the hydrodynamic resistance of the lubricant, the sliding of the balls in the contact zone, the gyroscopic effects due to the rotation of the balls on themselves, the losses due to the permanent local deformations and hysteresis phenomena. In conventional applications, ball bearings are lubricated and must withstand rather constant loads and speeds over time. Most of the analytical models have been developed empirically based on these operating conditions, such as those of Lundberg and Palmgren [150], Palmgren [151] where it is considered that the global resistance torque M is the sum of M_1, due to external forces, M_2 due to the lubricant and M_3 due to seal frictions. In case of rotor drop, the bearing must carry out transient loads and high accelerations. Such conditions differ completely from conventional ball bearings. However, the semi-empirical models are often used for rotor drop analysis due to a lack of knowledge. Considering the TDB design involved in this research work, no lubricant nor seals are present, therefore M_2 and M_3 are not considered. The detailed formulations of these torques are given in Lundberg and Palmgren [150], Palmgren [151] but also in Harris [143].

The resistance torque M_1 due to external loads can be defined as:

$$M_1 = f_1 F_\beta d_m \tag{2.63}$$

where d_m is the pitch diameter and F_β depends on the magnitude and the direction of the applied loads:

$$F_\beta = 0.9 F_a \cot\alpha_c - 0.1 F_r \tag{2.64}$$

or

$$F_\beta = F_r \tag{2.65}$$

The largest value of F_β is taken. The factor f_1, depending on bearing design and loads, is defined as:

$$f_1 = z \left(\frac{F_s}{C_s} \right)^y \tag{2.66}$$

C_s is the static load capacity, F_s the equivalent static load, z and y coefficients that depend on bearing geometry. Some degrees of strain plasticity are unavoidable in rolling bearings. Previous experiences have shown that permanent deformations smaller than one ten thousandth of the ball diameter are not harmful for the bearing. C_s represent this limit and is determined as:

$$C_s = f_s Z D^2 \cos\alpha_c \tag{2.67}$$

with Z the number of rolling elements, D the ball diameter and f_s a coefficient depending on the type of bearing. The equivalent static load F_s is defined as:

$$F_s = X_s F_r + Y_s F_a \tag{2.68}$$

with F_r and F_a the radial and the axial external load respectively, X_s and Y_s the coefficients that depend on the type of bearing. For a deep groove ball bearing, $X_s = 0.6$ and $Y_s = 0.5$. In the context of this research work, alternative rotor-TDB contact and non-contact situations may be found while the resistance torque M_1 appears only when an external load is applied to the bearing. This means that no resistance torque is able to decelerate the ball bearing without any external load. To this end, a rotational damping Φ coefficient is added to the bearing system as previously done in references [21, 109, 110, 111]. The final equation of motion is given in equation (2.69). For clarity, ω_{ir} is recalled Ω_{tdb} and refers to the global TDB rotational speed.

$$J_{eq}\dot{\Omega}_{tdb} + \Phi\Omega_{tdb} = f_t R_{ir} - M_1 \tag{2.69}$$

where f_t is the driven friction force produced by rotor inner race interactions.

The ball bearing modelling has been completely described. It consists of a radial force-deflection relationship based on well-known analytical works. The rotational dynamics is considered with a single equation of motion using an equivalent rotational inertia and a resistance torque.

2.5 Contact modelling

When the rotor exceeds the TDB clearance, interactions with inner race are generated. This section provides insights into the contact modelling and presents the selected models to be implement in the TDB model.

Contact is a complex phenomenon occurring when several bodies collide. A fairly complete census of the different modellings is done in the publication of Gilardi *et al.* [24] for the case of contact dynamics. Pereira *et al.* [152] give a good overview for the particular case of cylindrical contacts. Experimental and numerical contact dynamics concerning the particular case of rotor-stator interaction is investigated by Lahriri and Santos [153, 154, 155]. Readers can also refer to the work of Popov [156] for the treatment of contact problems. There is a large number of contact models used in the literature for a wide variety of applications. However, the procedure for setting-up these models in numerical simulations is identical:

- Define the contact characteristics: the coordinate system, the contact surfaces and their related normals and clearances,
- Identify a method to treat contacts numerically,
- Use a contact model to compute normal and tangential contact forces.

For clarity purposes, stator is employed as a generic term instead of inner race.

2.5.1 Contact definition

The surfaces in contact are defined by the degrees of freedom of the rotor where contacts may happen. It is therefore necessary to define the relative rotor-stator motions to generate a co-ordinate system in which the contact forces are calculated. Thus, the vector of the relative rotor-stator centre motion defines the normal of contact, as shown by Figure 2.25 and equation (2.70):

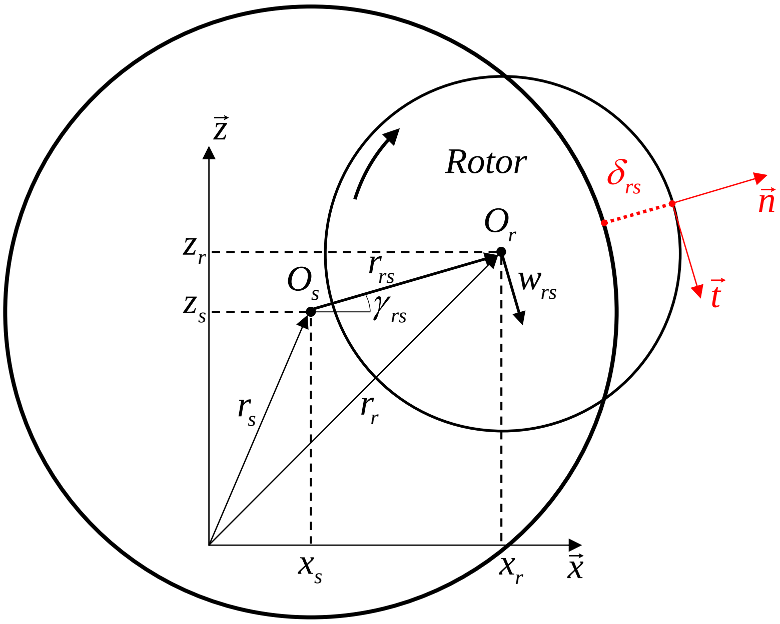

Figure 2.25: System of coordinate for contact force computation

$$\vec{n} = \frac{1}{\sqrt{(x_r - x_s)^2 + (z_r - z_s)^2}} \begin{Bmatrix} x_r - x_s \\ 0 \\ z_r - z_s \end{Bmatrix} \tag{2.70}$$

In the presence of friction, tangential forces at the interface are generated and the tangential contact direction is given by equation (2.71).

$$\vec{t} = \frac{1}{\sqrt{(x_r - x_s)^2 + (z_r - z_s)^2}} \begin{Bmatrix} z_r - z_s \\ 0 \\ -(x_r - x_s) \end{Bmatrix} \tag{2.71}$$

The numerical forces between two bodies in contact result from the evaluation of the clearances between the structure surfaces, which depend on the initial clearance and the relative motions. Beam theory gives only access to the displacement of the neutral line. Assuming a perfectly circular contact surface, the displacement of the node in the contact plane is equivalent to the surface one. Thus, considering Figure 2.25, the rotor-stator clearance δ_{rs} is defined as follows:

$$\begin{cases} \delta_{rs} = \left(\overrightarrow{O_r O_s} - \delta_0 \vec{n}\right) \vec{n} \\ \delta_{rs} = r_{rs} - \delta_0 \end{cases} \tag{2.72}$$

where δ_0 is the initial rotor-stator clearance. The normal relative displacement between the rotor and the stator r_{rs} is defined as:

$$r_{rs} = \sqrt{(x_r - x_s)^2 + (z_r - z_s)^2} \tag{2.73}$$

Other parameters can be employed to compute contact forces. The normal relative velocity $\dot{\delta}_{rs}$, defined by equation (2.74), is used to introduce damping in the contact. The relative whirling speed w_{rs}, defined by equation (2.75), is used to analyse the condition of friction at the rotor-stator interface and to determine the relative sliding velocity but also to implement tangential damping.

$$\dot{\delta}_{rs} = \frac{d\delta_{rs}}{dt} = \frac{(x_r - x_s)(\dot{x}_r - \dot{x}_s) + (z_r - z_s)(\dot{z}_r - \dot{z}_s)}{\sqrt{(x_r - x_s)^2 + (z_r - z_s)^2}} \tag{2.74}$$

$$w_{rs} = r_{rs}\dot{\gamma}_{rs} = \frac{(\dot{x}_r - \dot{x}_s)(z_r - z_s) - (\dot{z}_r - \dot{z}_s)(x_r - x_s)}{\sqrt{(x_r - x_s)^2 + (z_r - z_s)^2}} \tag{2.75}$$

where γ_{rs} is the relative angle defined as:

$$\gamma_{rs} = \arctan\left(\frac{z_r - z_s}{x_r - x_s}\right) \tag{2.76}$$

Once the coordinate system and the variables needed determined, a method to compute the contact loads should be chosen. There are two main approaches to numerically treat contact issues: the penalty method, widely used, authorizing solids penetrations, the Lagrange multiplier method, respecting the integrity of deformable solids by forbidding penetration and finally Hybrid methods, combining both of these methods, not treated in this work.

2.5.2 Lagrange multipliers method

The Lagrange multiplier method confers several advantages over the penalty method such as not requiring the contact parameters like stiffness or damping and avoiding the penetration of solids in contact. This method is equivalent to the imposed displacement resolution in static analysis. Hereafter is given an example of this method for the case of a unique contact point, constraining only the radial displacement of the rotor. No stator degrees of freedom are considered. The holonomic equation, provided in equation (2.77), represents the radial constraint to be satisfied.

$$h_r = x_r^2 + y_r^2 - \delta_0 = 0 \tag{2.77}$$

This equation is then incorporated into a rotor-bearing equations of motion through the Lagrange multiplier λ_r as follows:

$$M_r\ddot{q}_r + J^T\lambda_r = f_{ext} - C_r\dot{q}_r - K_r q_r \tag{2.78}$$

where M_r, C_r and K_r are the structural rotor matrices, f_{ext} is any external force vector and J is the Jacobian row vector (a matrix when several contact points exist) of the constraint equation (2.77). The components of J are the partial derivatives with respect to the rotor degrees of freedom. The Lagrange multiplier method adds another unknown to the overall system and equation (2.79) is added by time derivating equation (2.77) twice:

$$\ddot{h}_r = 2x_r\ddot{x}_r + 2y_r\ddot{y}_r + 2\dot{x}_r^2 + 2\dot{y}_r^2 = 0 \tag{2.79}$$

The constraint equation (2.77) and its time derivative equation (2.79) as well as the related Jacobian vector J are then included in the following differential equation system:

$$\begin{bmatrix} M_r & J^T \\ J & 0 \end{bmatrix} \begin{Bmatrix} \ddot{q}_r \\ \lambda_r \end{Bmatrix} = \begin{bmatrix} f_{ext} - C_r\dot{q}_r - K_r q_r \\ D(q_r, \dot{q}_r) \end{bmatrix} \tag{2.80}$$

where:

$$D = 2\dot{x}_r^2 + 2\dot{y}_r^2 \tag{2.81}$$

Thus, the displacement correction prevents the rotor penetration and the resulting Lagrange multiplier is related to the normal contact force applied on the rotor, written as:

$$f_n = -J^T\lambda_r \tag{2.82}$$

This non-penetrability makes contact infinitely stiff and does not take into account any damping. The implementation of this method increases the computing time since unknowns are added to the system. This method is no more detailed in this study since the penalty method was chosen to treat contact issues due to the ease of implementation and the good representativity of the results. However, for more details about the Lagrange multiplier method, readers can refer to Legrand [157], Legrand *et al.* [158], Abulrub [159], Sahinkaya *et al.* [160, 161], Roques [162], Roques *et al.* [96] and Torkhani *et al.* [95].

2.5.3 Penalty method

This method is used in most of the rotor-stator interaction problems. It permits the interpenetration of bodies in contact, which is not physically observable. However, it is representative of the phenomena observed in real turbomachinery and provides satisfactory overall dynamics. There are many variants for the penalty method but the principle remains the same: "penalize" the relative displacement between the structures in contact using dynamic parameters. Many type of laws can be implemented to represent a wide variety of contact types. The major drawback could be the difficulty to select these dynamic parameters, in particular the stiffness and damping values.

Linear normal contact laws

The most simple way to compute a contact force is to multiply the rotor-stator normal relative clearance by a stiffness. It is widely recognised that structures in contact absorb shocks by different phenomena such as plastic micro-deformations or wave propagation. Thus, this dissipated energy inherent to the contact can be represented by viscous linear damping, relative to the normal velocity of impact. This model is usually called the Kelvin-Voigt model. The related mathematical expression of the contact force is given by equation (2.83). This type of model is

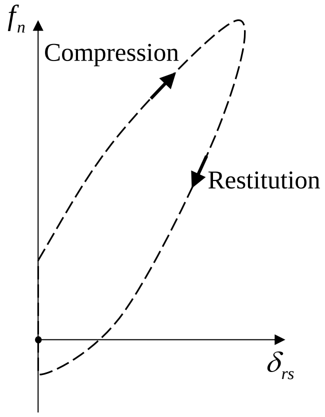

$$f_n = \begin{cases} \delta_{rs} k_n + \dot{\delta}_{rs} c_n & ; \delta_{rs} > 0 \\ 0 & ; \delta_{rs} \leq 0 \end{cases} \tag{2.83}$$

Figure 2.26: Kelvin-Voigt force-deflection loop

widely employed by using simple rotor models such as the well-know Jeffcott rotor. It permits exhibiting the wide complexity of rotor-stator phenomena, see references [70, 71, 72, 73, 89]. This linear modelling, however, has some drawbacks, such as discontinuities and the appearance of traction forces. In the exit phase, see Figure 2.26, in the vicinity of $\delta_{rs} = 0$ the sign of the contact forces is inverted, resulting in a traction load which is not physically observable. In the compression phase, in the vicinity of $\delta_{rs} = 0$, the damping force is predominant since solids in contact have their maximum relative velocity at the moment of impact; a jump discontinuity of the contact force amplitude is created. Its time derivative is not continuous and this represents a difficulty for numerical schemes, especially if the viscous damping is high. Obviously, the contact force should grow progressively and this jump in amplitude is not physically observable. A solution to solve this problem is to smooth the contact stiffness and damping, as done by Duran *et al.* [82]. The contact parameters depends on the normal relative clearance δ_{rs} according to an arctangent law. The resulting contact force is expressed by equation (2.84):

This method limits the discontinuity brought by the linear viscous damping in the vicinity of $\delta_{rs} = 0$ and avoids traction loads in the restoring phase, see Figure 2.27. Arctangent laws

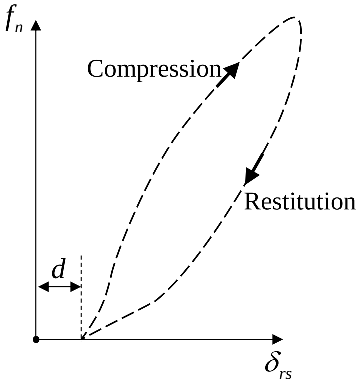

$$f_n = \begin{cases} \delta_{rs} k_n\left(\delta_{rs}\right) + \dot{\delta}_{rs} c_n\left(\delta_{rs}\right) & ;\delta_{rs} > 0 \\ 0 & ;\delta_{rs} \leq 0 \end{cases} \tag{2.84}$$

with:

$$\begin{cases} k_n\left(\delta_{rs}\right) = \frac{k}{2}\left(\frac{2}{\pi}\arctan\left(\pi\lambda\left(\delta_{rs} - d\right) + 1\right)\right) \\ c_n\left(\delta_{rs}\right) = \frac{c}{2}\left(\frac{2}{\pi}\arctan\left(\pi\lambda\left(\delta_{rs} - d\right) + 1\right)\right) \end{cases} \tag{2.85}$$

Figure 2.27: Smoothed Kelvin-Voigt force-deflection loop

are controlled by the λ and d parameters, respectively corresponding to the slope and shift. In Duran *et al.* [82], this smoothed Kelvin-Voigt model avoids an iterative process, such as the Newton-Raphson method, to handle the strong nonlinearities.

Nonlinear normal contact laws

As explained previously for the ball bearing modelling, Hertz [148] can be seen as one of the major contributor to the research in the contact mechanics field. His work has been often applied in the context of rotor-stator interaction. The mathematical expression of the force-deflection relationship considering a non-conformal contact is usually given as:

$$f_n = \begin{cases} k_n \delta_{rs} & ;\delta_{rs} > 0 \\ 0 & ;\delta_{rs} \leq 0 \end{cases} \tag{2.86}$$

The power n is related to the contact type and k_n represents a normal stiffness that depends on material and geometrical properties of both contacting bodies. Nowadays, most works are based on the Hertz theory like the study of Lankarani *et al.* [163] who used equation (2.86) and a normal stiffness k_n to model sphere-sphere interactions, see equation (2.87). The power n is set to $\frac{3}{2}$ for punctual contact type.

$$k_n = \frac{4}{3}\pi E^* \sqrt{R^*} \tag{2.87}$$

where the E^* and R^* are the equivalent Young's modulus E^* and radius of curvature of the two bodies in contact, respectively. In the case of cylinder-cylinder interactions, the contact is stiffer and the force-deflection relationship is more linear (the power is close to one) than for the punctual case. Gummer and Sauer [164] determined the local friction energy and the stiffness of a revolute joint using different types of line contact. Liu *et al.* [165] were particularly interested in setting up laws for very conformal cylindrical contacts which is typically the case in the context of rotor-stator interactions. They modelled a cylinder in contact with a bore in a pivot connection with very close diameters using volumic FE. The authors obtained a law explicitly dependent on the indentation, the geometry and the material, matching well the numerical results. The contact length is no longer employed and the resulting force is given by:

$$f_n = \begin{cases} \frac{1}{2}\pi\delta_{rs}E^*\sqrt{\dfrac{\delta_{rs}}{2\left((R_2-R_1)+\delta_{rs}\right)}} & ;\delta_{rs} > 0 \\ 0 & ;\delta_{rs} \leq 0 \end{cases} \tag{2.88}$$

where R_1 and R_2 being respectively the stator and the rotor radii. Many other laws for conformal contacts exist, however, the latter is practical since being an explicit function of indentation, no iterative loop is necessary.

As explained previously, impacts generate damping and the linear modelling of this phenomenon is responsible for discontinuities. Based on the Hertz theory, Hunt and Crossley [166] introduced a nonlinear damper, characterized by the parameter α_{nl} in equation (2.89). The force-deflection loop generated is plotted in Figure 2.28.

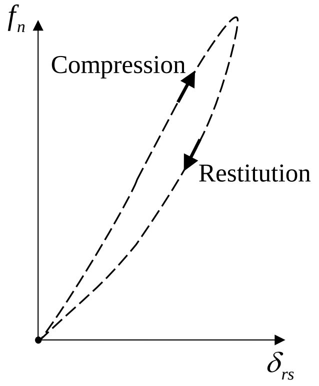

$$f_n = \begin{cases} k_n\delta_{rs}\left(1+\frac{3}{2}\alpha_{nl}\dot{\delta}_{rs}\right) & ;\delta_{rs} > 0 \\ 0 & ;\delta_{rs} \leq 0 \end{cases} \tag{2.89}$$

Figure 2.28: Hunt and Crossley force-deflection loop

The nonlinear damper α_{nl} is related to the coefficient of restitution e and the impact velocity C_0 via equation (2.90). This relationship is valid for hard materials and small impact velocities $\left(< 500 mm.s^{-1}\right)$, which is true for rotor drops. According to Hunt and Crossley [166], the coefficient α_{nl} lies from 0.08 to $0.32 s.m^{-1}$ for standard steels.

This type of model, continuous and differentiable at $\delta_{rs} = \delta_0$ thanks to the nonlinear damper, was first used by Bartha [9] and Fumagalli [117] for rotor-stator interaction and rotor drop dynamics respectively. Nonlinear damper model is still the subject of further researches, such as in Zhang and Sharf [167] and Jacobs *et al.* [168] where it is shown that the Hunt and Crossley model is very efficient for low speed impact.

Tangential contact laws

Any rotor interacting with its stator generates a friction force at the interface which is controlled by the relative sliding velocity, named v_s. When the latter reaches zero, it is usually

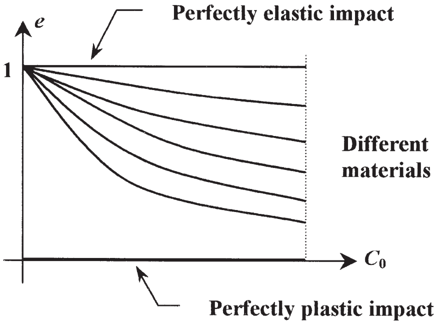

$$e = 1 - \alpha_{nl} C_0 \tag{2.90}$$

Figure 2.29: Coefficient of restitution for different material, depending on the impact speed - Gilardi [24]

admitted that no more friction is generated. The models developed are based mostly on the well-known Coulomb theory, which consists in the calculation of a tangential component f_t using the normal contact force f_n and a friction coefficient μ. The direction of the generated load is opposed to the relative sliding velocity v_s. The classical Coulomb model, see Figure 2.30, is highly nonlinear in the vicinity of zero and can be responsible for numerical issues.

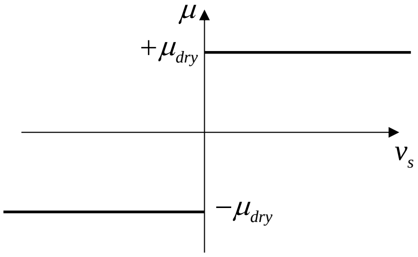

$$\begin{cases} f_t = sign\left(v_s\right) \mu_{dry} f_n \ \leftrightarrow \ v_s \neq 0 \\ \quad \left|f_t\right| < \left|\mu_{dry} f_n\right| \ \leftrightarrow \ v_s = 0 \end{cases} \tag{2.91}$$

Figure 2.30: Classical Coulomb friction model

One way to regularize the Coulomb model is to implement an arctangent law, see Figure 2.31, as done by Wilkes *et al.* [105]. The latter provides numerical stability in the vicinity of the zero and solves the problem of the tangential forces sign changing. The parameter v_{ref} controls the inversion of the friction coefficient in the vicinity of zero.

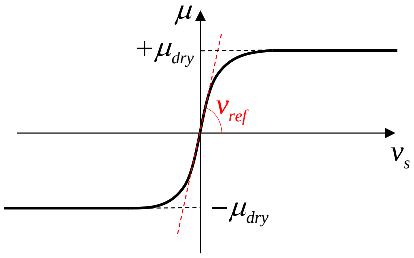

$$f_t = \mu_{dry} \left(\frac{2}{\pi} \tan^{-1}\left(v_{ref} v_s\right) \right) f_n \tag{2.92}$$

Figure 2.31: Smoothed Coulomb friction model

Other models, such as the Stribeck model, see Figure 2.32, take into account the dynamic nature of contact and consider that when the rotor-stator sliding velocity is large, the friction coefficient is reduced, resulting in smaller tangential forces. Duran *et al.* [82] described the

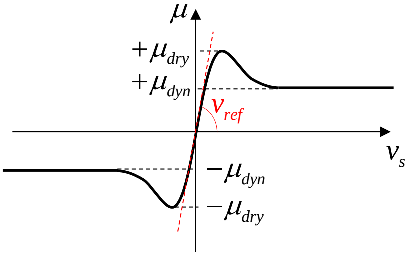

Figure 2.32: Stribeck friction model

Stribeck model as a polynomial sum:

$$f_t = \frac{v_s}{2v_{ref}} \left(\frac{1-\sqrt{1-\frac{\mu_{dyn}}{\mu_{dry}}}}{1+\frac{|v_s|}{2v_{ref}\mu_{dyn}}\left(1-\sqrt{1-\frac{\mu_{dyn}}{\mu_{dry}}}\right)} + \frac{1+\sqrt{1-\frac{\mu_{dyn}}{\mu_{dry}}}}{\left(1+\frac{|v_s|}{2v_{ref}\mu_{dyn}}\left(1-\sqrt{1-\frac{\mu_{dyn}}{\mu_{dry}}}\right)\right)^2} \right) f_n \qquad (2.93)$$

2.6 Conclusions

Taking into account base motion effects permits the prediction of the dynamic behaviour of on-board turbomachinery. A classical Lagrangian method based on previous works is used to derive the equations of motion when rigid support motions are considered. The base rotations modify deeply the elementary kinetic energies generating equations with parametric terms able to cause lateral instabilities, and with external force vectors which also include the base translations. The classical contributions of rotor dynamics such as unbalance are also considered. The AMB modelling has been described: the magnetic restoring forces depend on electromagnet properties (number of turn in the coil, iron core material, etc.), but also on the applied control current in the coil. The latter is generated by an augmented SISO PID controller, widely employed in industry. An integral gain centres the shaft, the damping is provided by the derivative gain on the operating speed range and high frequency stability is guaranty.

When large rotor displacement occurs, contact with touchdown bearings may happen. Focus is on the overall rotor dynamic behaviour and a TDB model is developed according to this particular need. Three different part are needed to set-up the complete TDB model and two of them have been presented in this chapter. A complete procedure to determine the ball bearings stiffness and damping characteristics as well as a rotational modelling, comprising an equivalent rotational inertia and a resistance torque, have been described. A detailed description of the different contact laws employed in case of rotor-stator interactions has been realised. The penalty method is chosen to numerically treat the contact between the rotor and the TDBs.

In the next chapter, the third component needed for establishing the TDB model is experimentally and numerically investigated. The complete touchdown bearing models are then described. An experimental validation is provided using industrial scale test rig results.

Chapter 3

Rotor drop dynamics - TDB model validation

The aim of this chapter is to validate the rotor-drop system model. A first test rig is used to identify the dynamic characteristics of a corrugated ribbon damper, which is the considered compliant device. The second experimental set-up is devoted to the rotordynamic response during drop tests on an industrial scale rotor-AMB system equipped with touchdown bearings. Rotor drop simulations are performed with the TDB models including the newly developed ribbon damper model. The results are compared with tests performed on the rotor industrial test bench. The level of detail of the touchdown bearing models needed for sufficiently accurate rotor drop predictions is discussed.

Contents

This step ensures that all the different elements of the touchdown bearings are modelled satisfactorily before analysing the dynamic behaviour of an on-board rotor-AMB system subjected to strong base motions, in the next chapter. Drop tests coming from an industrial scale test rig are used for the validation of the TDB model. The latter must provide sufficiently accurate predictions in terms of drop dynamics and loads. The industrial scale test rig is equipped with TDBs, mounted in the housing through a ribbon damper which is a key component for system stability when rotor-TDB interactions occur. The ribbon damper has been tested. The related experimental set-up is first presented and a model is developed according to measurements. Then, three TDB models are presented, one of them includes the new ribbon model. The aim is to analyse the degree of details required to correctly represent the drop dynamics. Predictions are compared with measures, in terms of rotor displacements and loads. Two particular drop tests are performed for two different objectives:

- Rotor drop dynamics at a given speed is very sensitive to the unbalance distribution; therefore, drop tests considering a standstill rotor should allow to analyse only the effects of the lateral restoring forces provided by the TDBs.
- Drop tests considering a 6 500 rpm spinning rotor should permit the identification of the time needed for the TDBs to reach the rotor speed. The sliding friction forces generated during contact drives the ball bearings in rotation. When the latter reach full speed, sliding friction forces are cancelled and this should be visible by analysing the rotor displacements.

This chapter provides insights onto the drop dynamics considering horizontally split systems, which has been a significant part of this research.

3.1 Ribbon damper characterisation

3.1.1 About ribbon dampers

Soft and damped elements are crucial for rotor stability during drop, as recalled by Kirk [108]. Flexible support connections are used for limiting the impact forces but also for reducing the rotor whirling frequencies (forward or backward), as explained by Hawkins *et al.* [102, 106]. In Sun *et al.* [22, 101], the use of squeeze film dampers decouples the relative rotor-support motions during a drop. The use of pressurized oil brings damping to the overall system. This kind of technology is widely used in the aeronautics industry. As the main drawback of the squeeze film dampers is the need of a lubrication system, cancelling one of the main advantages of AMB technology, ribbon dampers, sketched in Figure 3.1, equip most of modern touchdown bearing designs. The TDBs mounted on the industrial scale test rig are equipped with ribbon dampers. This device, made of a corrugated steel foil, is simple and brings no lubrication to the

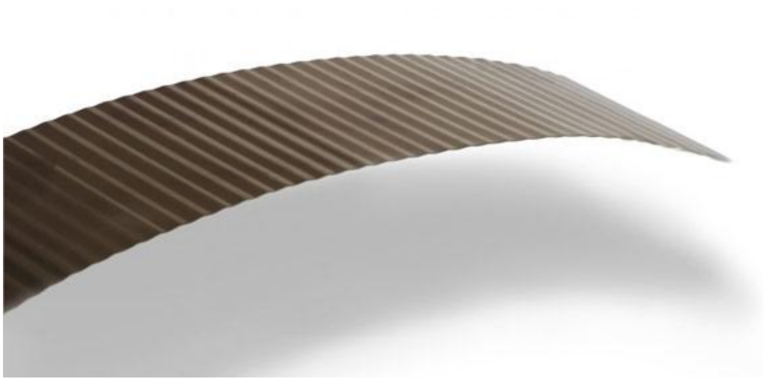

Figure 3.1: Corrugated ribbon damper

rotor-AMB system. It is fitted between the TDB outer race and the housing, as shown in Figure 3.2.

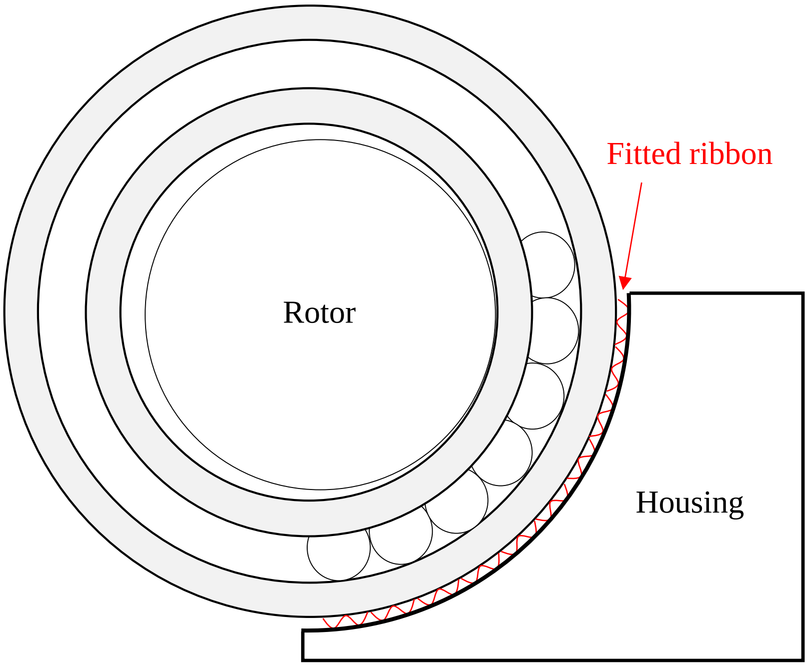

Figure 3.2: TDB-housing assembly

The ribbon damper is a key parameter for rotor drop dynamics as shown by Jarroux *et al.* [169, 170, 171]. For this reason, dynamic characterization tests were carried out by the GE global research center (GRC) in Niskayuna, NY, USA. The corrugated foil and the multiple contacts of its bumps with the outer race of the ball bearing and the stator makes its modelling difficult. The chosen approach focuses on the restoring force extracted from experimental force-deflection loops. Gas supported rotors are also equipped of corrugated foils having designs close to ribbon dampers. Complex foil models are developed by Le Lez *et al.* [25, 26], considering discrete modelling of bumps, as shown in Figure 3.3. Elementary stiffness matrices are obtained and a complete mesh describes finely the bumps deflections and displacements. Dry friction is considered in contact points. Further informations concerning analytical methods or experimentations are given in Iordanoff *et al.* [172], Bou-Saïd *et al.* [173], and Balducchi *et al.* [174], Andrés *et al.* [175], respectively.

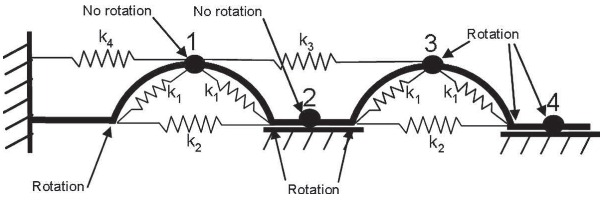

Figure 3.3: Discrete bump modelling - Le Lez *et al.* [25, 26]

The aim of these tests is to extract the ribbon restoring force when subjected to harmonic excitations, with different forcing amplitudes and frequencies. The test rig, see Figure 3.4, was developed for that particular purpose and the operating conditions of the industrial scale test rig were reproduced.

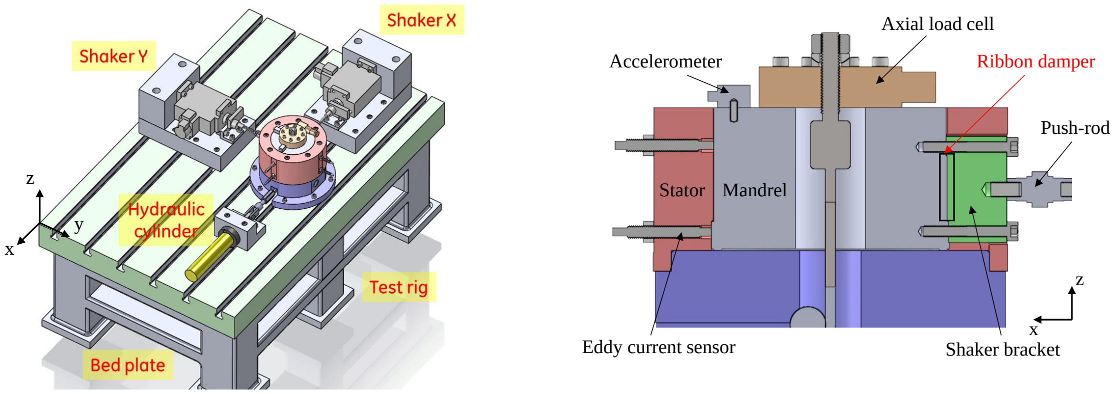

(a) Test rig frame

(b) Mandrel housing

Figure 3.4: Ribbon test set-up

Two 8 900 N electro-hydraulic shakers, see Figure 3.4(a), fixed on the test rig frame, force the mandrel, see Figure 3.4(b), with a sinusoidal translation by the way of brackets rigidly screwed. The wrapped ribbon is fitted between the mandrel and the stator; it is only deflected by the mandrel. Two piezoelectric cells record the forces transmitted to the mandrel using push-rods while two eddy current sensors (bottom and top) placed into the stator measure the displacements of the mandrel. An accelerometer is screwed into the mandrel. As the tests are not only quasi-static, the ribbon force can be recovered by subtracting the inertia force to the measured external force, assuming that the ribbon is only subject to these two forces. The sampling frequency is 8 192 Hz and the tests are harmonic and unidirectional for different imposed displacements and frequencies.

In the following section, the experimental results as well as the numerical models developed are presented.

3.1.2 Dry friction phenomena

A 29 test series was carried out at different frequencies for several imposed sinusoidal displacements. For each of these test cases, the signals are recorded during 0.5 s when the steady-state motion is reached. Figure 3.5 presents the force-deflection loops for the 20 Hz test case where f_{rd} and u are, respectively, the ribbon restoring force and the mandrel displacement.

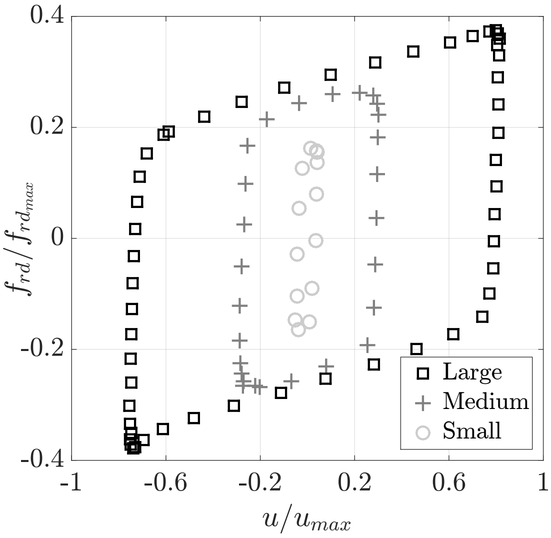

Figure 3.5: Normalized ribbon force-deflection loop

The force-deflection loop is a hysteretic and quasi-symmetric regarding the zero origin denoting that the compression and traction phases are rather similar. The angular corners at the change of the velocity sign confirm a dry friction behaviour inducing a stick-slip phenomenon. Since the ribbon multiple contacts provide dry friction, the behaviour does not depend on the forcing frequency. The force-deflection loop exhibits an hysteretic behaviour with two slopes change.

When the mandrel deflects the ribbon, see Figure 3.6(b), the bumps are first all stuck on the mandrel and stator surfaces due to dry friction which results in a global high stiffness, known as contact stiffness, see Figure 3.6(c). Then, passing above the slipping threshold force μF_N (F_N being the normal contact force and μ the friction coefficient), all of these bumps slip, see Figure 3.6(d), resulting in a global smaller stiffness, known as residual stiffness or slipping stiffness, see Figure 3.6(e). Dry friction is a well-known phenomenon which is often used to reduce vibrations of mechanical structures; see for example the camera isolation presented by Gjika and Dufour [176]. In a turbojet engine, dry friction devices are integrated under platforms, which are the fan blade supports, providing a nonlinear dynamic behaviour flattening the frequency response, as studied in Ciğeroğlu *et al.* [177]. Macroslip and microslip models are the two main categories of friction models and the choice may be important, as explained by Chatelet *et al.* [178]. Considering macroslip models, the dynamic behaviour is homogeneous, meaning that everything slips or sticks at the same time while in microslip, mixed configurations

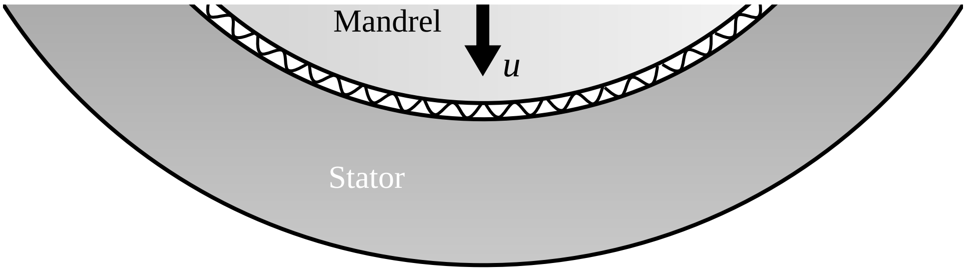

(a) Test rig frame

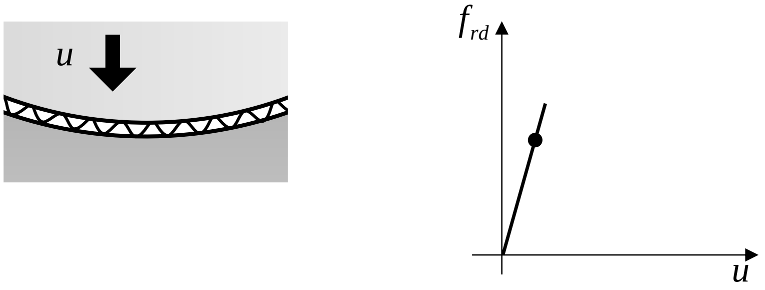

(b) Stuck bumps (c) Resulting ribbon restoring force

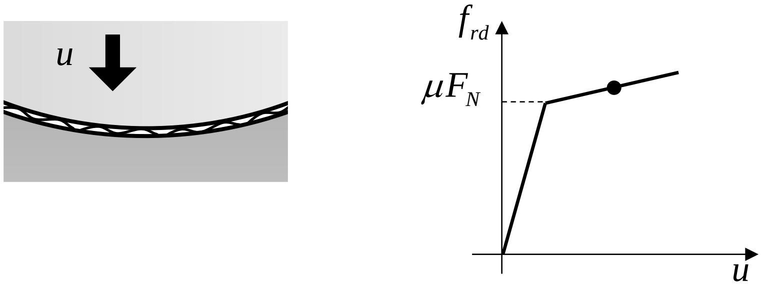

(d) Slipping bumps (e) Resulting ribbon restoring force

Figure 3.6: Stick-slip phenomenon in the ribbon damper

appear. In the case of multiple contacts, the stick-slip transition can be either in the same time, permitting the use of macroslip models or during an interval of time, permitting the use of microslip models. The microslip behaviour makes the force-deflection loop corners smoothed.

Regardless of the selected model, dry friction is responsible for the peak flattening in frequency responses. Al Sayed *et al.* [27] used the Masing macroslip model to characterize the stick-slip effects on the frequency response function (FRF) of a S-Dof model, see Figure 3.7. When the normal force is much greater than the external force, implying a high slipping threshold, the FRF is linear because the system remains in stuck motion and a 21 Hz resonance peak is exhibited. When this normal force decreases, implying a smaller slipping threshold, alternating stick and slip over one period may appear. The FRF is then no longer linear and the resonant peak is reduced to between 19 and 21 Hz. Depending on the proportion of stick and slip, one can find optimum parameters to obtain the smallest peak at resonance. Finally, when the normal load is small, the FRF is once again linear and remains in slip motion exhibiting a 19 Hz resonance peak. Two main approaches are employed to explain this peak flattening. Energy-based

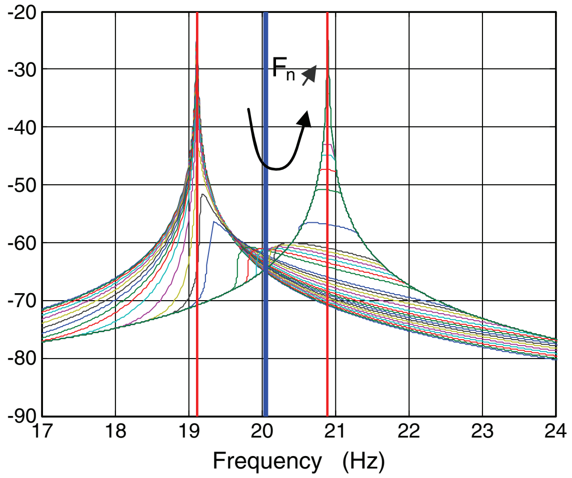

Figure 3.7: Frequency response (dB) depending on the applied normal load - Al Sayed *et al.* [27]

approaches state that this nonlinear behaviour is related to the energy dissipated in hysteresis loops; the more the area is large the more energy is dissipated, therefore, the more the resonant peak is flattened. On the other hand, this could be explained by the change of the boundary conditions generated by friction. More precisely, the out-of-phase between the friction force and the displacement would be the cause of this peak flattening, conclusion of Al Sayed *et al.* [27]. These explanations could be extended for the ribbon case; the damping provided by the ribbon when a rotor drops onto its TDBs would come mainly from the stick-slip alternating states of each ribbon bump, rubbing along the outer race and housing surfaces, generating this force-displacement out-of-phase.

3.1.3 Models and results

The aim of this section is to assess the capability of two damper models to reproduce the previously observed phenomena. Thus, the ribbon damper is modelled successively by the generalized Dahl and the Kelvin-Voigt models. The latter is used here as reference for comparisons since it is usually employed in rotor drop dynamics investigations such as in Sun *et al.* [23], Kärkkäinen *et al.* [113, 118], Lee *et al.* [124] or Halminen *et al.* [20].

3.1.3.1 The generalized Dahl model

The Dahl model, generalized by Al Majid and Dufour [179, 180], used by Michon *et al.* [181] and Bastien *et al.* [182], is based on a nonlinear first order differential equation, given in equation (3.1). Any shape of force-deflection can be adopted in order to model the ribbon restoring force f_{rd}.

$$\frac{df_{rd}}{dt} = \beta \frac{du}{dt} \left(h - f_{rd} sign \left(\frac{du}{dt} \right) \right) \tag{3.1}$$

$$h = \frac{1}{2}\left((h_u + h_l) + sign\left(\frac{du}{dt}\right)(h_u - h_l)\right) \tag{3.2}$$

The β term is the only parameter that controls the transition between slip and stick states. Implementing a high value of β leads to a close macroslip behaviour. The envelop h depends on the sign of the deflection velocity to become either h_u or h_l, which are respectively the upper and the lower asymptotic envelops of the measured hysteretic loop plotted in Figure 3.8.

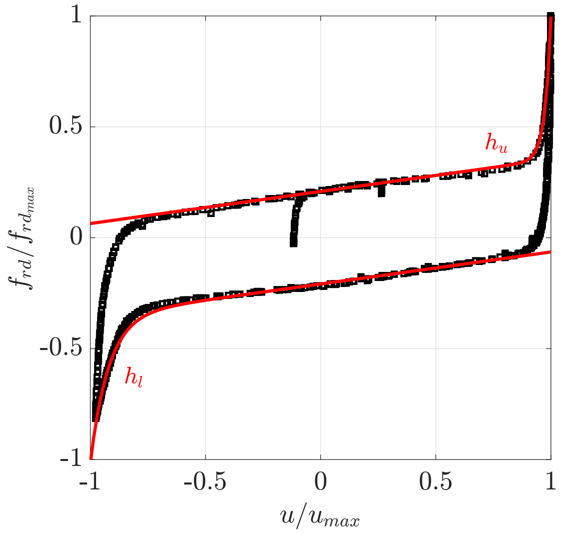

$$\begin{cases} h_u = \mu F_N + k_{slip} u + a e^{bu} \\ h_l = -\mu F_N + k_{slip} u - c e^{-du} \end{cases} \tag{3.3}$$

Figure 3.8: Normalized measured quasi-static force-deflection loop (black square) and the upper h_u - lower h_l envelops (red lines)

As these envelops are curved fitted, see equation (3.3), the hysteretic behaviour is characterized by a force-deflection relationship where μF_N is the slipping threshold, k_{slip} is the slipping stiffness (residual stiffness). Due to the double stopped-ends (actually the mandrel and stator), the ribbon exhibits a hardening-hardening nonlinear behaviour for the higher deflections and a, b, c, d are the exponential parameters of the envelop curves. The main assumption lies in the fact that the dynamic behaviour of the ribbon when subjected to harmonic or transient loads is assumed to be identical. Indeed, the experiences used for the set-up of the generalized Dahl model comes from harmonic tests while the application targeted concerns rotor drop and transient dynamics. However, this assumption seems to be reasonable according to previous experiences conducted by Al Majid and Dufour [179], Gjika *et al.* [183].

3.1.3.2 The Kelvin-Voigt model

Classically employed in rotor drop investigations, the so-called Kelvin-Voigt model, which is a linear spring-damper system, is described in equation (3.4). It is then characterised by its stiffness and damping but also by its "crushing capacity"; the larger the crushing, the larger the provided damping. When the latter is flattened, the outer race reaches the housing and the TDB faces higher loads. The stiffness k_{rd} is provided by the manufacturer and the damping c_{rd}, measured with logarithmic decrement technique, is set to 0.16.

$$f_{rd} = c_{rd}\frac{du}{dt} + k_{rd}u \tag{3.4}$$

Sometimes a cross-coupled stiffness term opposed to the outer race whirling motion is applied to counteract rotor whirl, see references [103, 105, 169].

3.1.3.3 Results

The displacements measured with the eddy-current sensors as well as their time derivatives are the input for the two developed models described by equations (3.1) and (3.4).

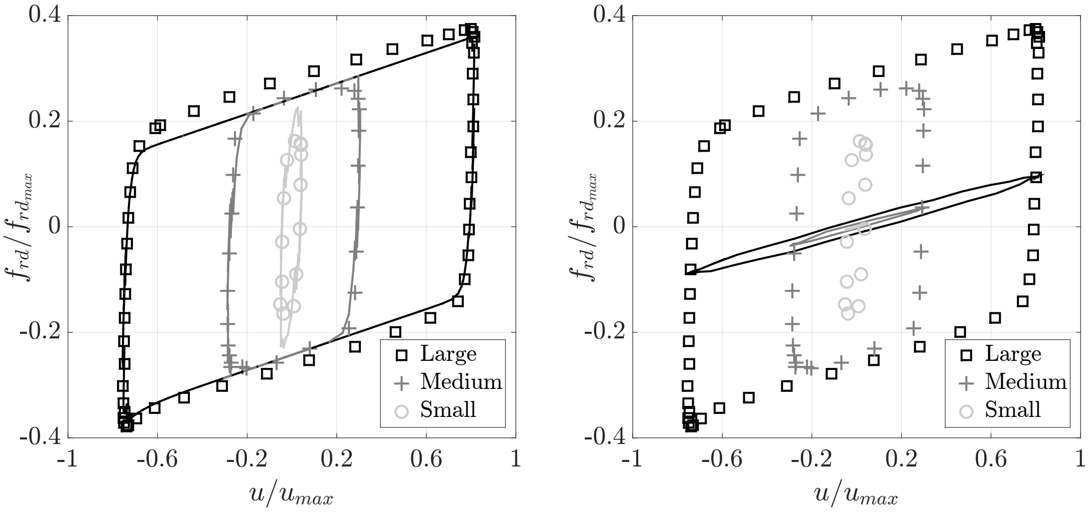

(a) Generalized Dahl model

(b) Kelvin-Voigt model

Figure 3.9: Normalized predicted (solid lines) vs measured (dotted lines) force-deflection loop with the generalized Dahl (a) and the Kelvin-Voigt (b) models

Figure 3.9 compares the force-deflection loops predicted and measured with a 20 Hz forcing frequency. The generalized Dahl model, see Figure 3.9(a), is accurate enough for all ranges of imposed displacement whether the stiffness parameter β is well assessed. On the other hand, the Kelvin-Voigt model using manufacturer parameters, see Figure 3.9(b), represents the slip stiffness without considering any stick-slip phenomenon. Even if the amount of damping is related to the out-of-phase generated by stick-slip phenomenon rather than the dissipated energy, the area of hysteretic loop remains a good indicator for the purpose of this work. The Kelvin-Voigt model seems to underpredict the damping significantly. The two developed models are then implemented successively in a TDB model.

3.2 Touchdown bearing models

The TDBs mounted in the industrial scale test rig are double-row angular contact ball bearings equipped with ceramic balls providing dry lubrication. They are modelled with the four Dof model, see Figure 3.10(b), and a contact law based on the work of Schmied and Pradetto [17], see Figure 3.10(a).

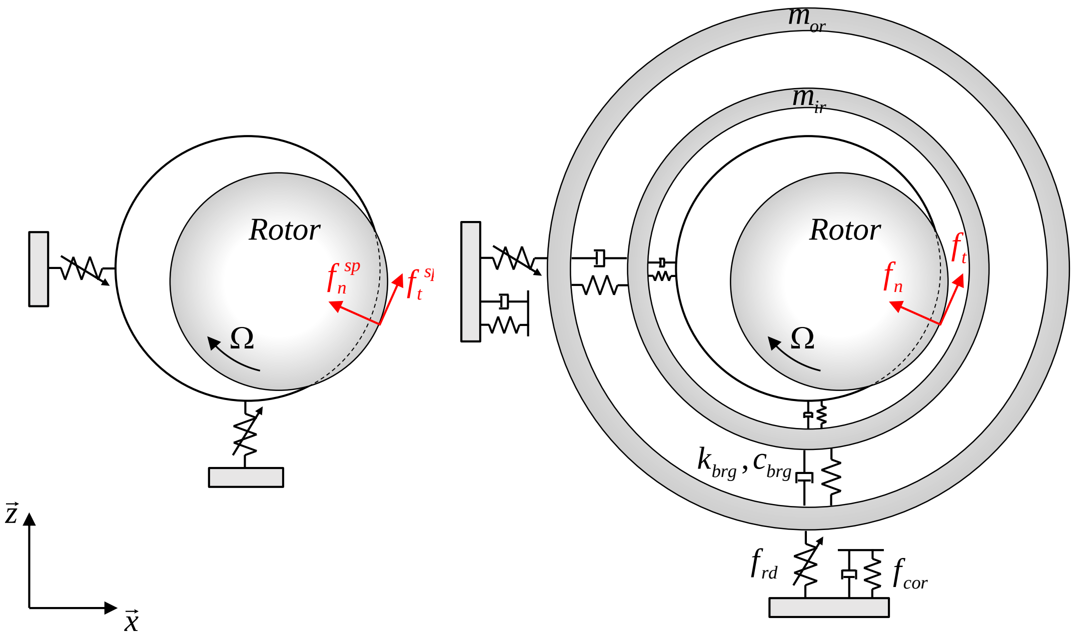

(a) Contact law

(b) Four Dof model

Figure 3.10: TDB models employed

These models are used for two specific objectives:

- Determining the degree of detail required for TDB models to represent with sufficient accuracy the whole rotordynamics during drop events.
- Verifying the previous assumption concerning the identical dynamic behaviour of the ribbon damper subjected either to transient or harmonic loads.

Both the models consider the same rotational equation of motion, previously described in equation (2.69). The stator is rigid and has no modal contributions. The main differences between these two TDB models lie on the consideration of the TDB lateral dynamics or not. Both the models consider vertical and horizontal misalignments which can influence significantly the rotor dynamic behaviour, as shown in references [20, 118, 131].

The assumptions of the models are provided in Table 3.1.

Table 3.1: TDB models assumptions

	Contact law	**Four Dof model**
Rotor inner race interaction	Rigid	Flexible
Ball bearing	Flexible	Flexible
Ribbon damper	Flexible	Flexible
Housing outer race interaction	Rigid	Flexible
Races dynamics	Not considered	Considered

3.2.1 Four Dof model

This model is interesting since a wide variety of laws, modelling different components, can be easily implemented. In particular, having the outer race degree of freedom permits the implementation of the previously developed generalized Dahl model.

The Hunt and Crossley model, described by equation (2.89), is used to compute the normal force f_n when rotor inner race interactions occur. The nonlinear damper avoids discontinuities and its explicit mathematical formulation makes it easy to handle. Moreover, this model has been used intensively in the literature and has proved its effectiveness. The outer race housing interaction is also computed with the Hunt and Crossley contact law giving the force f_{cor}. The tangential load f_t is derived by using the regularized Coulomb model, see equation (2.92). It was shown by Kärkkäinen *et al.* [113] that the model of friction chosen in the context of rotor drop did not have a significant influence. The relative speed between the rotor and the TDB drives the value of the friction coefficient, especially around the zero relative speed. The maximal value of the coefficient is set to 0.2.

The ball bearing model integrates the force-deflection relationship, see equation (2.49), giving, after linearisation, the dynamic parameters k_{brg}, c_{brg}. Finally, the ribbon damper represented by the force f_{rd} successively includes the previously developed generalized Dahl, see equation (3.1), and the Kelvin-Voigt, see equation (3.4), models. It is possible to analyse the effect of the newly developed dry friction model on the drop dynamics.

3.2.2 Contact law model

The contact law states that the race dynamics are negligible. The ribbon damper comprises the dynamic parameters of the Kelvin-Voigt model in equation (3.4), and the dynamic parameters k_{brg}, c_{brg} of the ball bearing coming from the previous analytical results, in equation (2.49), as for the four Dof model. The related mathematical expression is given by equation (3.5) and a typical force-deflection loop is plotted in Figure 3.11; δ_{rs} is the rotor-TDB relative clearance and δ_{rd} is the ribbon crushing capacity.

$$f_n^{sp}\left(\delta_{rs}\right) = \begin{cases} k_{brg}\left(\delta_{rs}-\delta_{rd}\right)+c_{brg}\dot{\delta}_{rs}+k_{eq}\delta_{rd} & ;\delta_{rs}\geq\delta_{rd} \\ k_{eq}\delta_{rs}+c_{eq}\dot{\delta}_{rs} & ;\delta_{rd}>\delta_{rs}\geq 0 \\ 0 & ;\delta_{rs}<0 \end{cases} \tag{3.5}$$

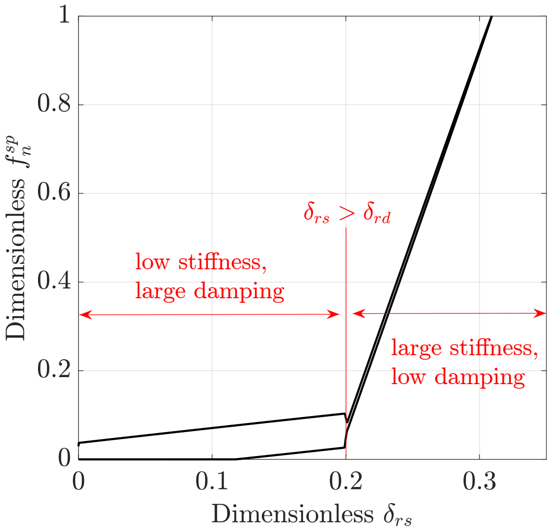

Figure 3.11: Normalized contact law force-deflection loop

The related drop scenario is detailed in what follows: when the rotor drops, it first contacts the coupled ball bearing ribbon damper system, considered in series mode. The related contact force is composed of the equivalent stiffness k_{eq} and damping c_{eq}. Once the ribbon is fully crushed, meaning that $\delta_{rs} \geq \delta_{rd}$, the ribbon only has a static contribution and the rotor faces the ball bearing stiffness. This model is characterized by softness and large damping when the ribbon is not crushed, then by a high stiffness and a low damping, as shown in Figure 3.11. As this contact law comprises viscous damping, discontinuities appear as shown in Figure 3.11. Therefore, the regularized arctangent law, described in equation (2.85), is used to smooth the restoring force.

The tangential force f_t^{sp} provides the sliding friction force using the regularized Coulomb model, in equation (2.92), as for the four Dof model, and a viscous force, which depends on the rotor tangential speed, counteracting the rotor whirl motions.

Table 3.2 summarizes features of each TDB models. Two versions of the four Dof model are used to test the Kelvin-Voigt and the generalized Dahl models.

Table 3.2: Tested TDB models

	MODEL 1	MODEL 2	MODEL 3
TDB model	**Contact law**	**Four Dof**	
		Version 1	Version 2
Rotor inner race interaction	Rigid	Hunt and Crossley f_n in eq. (2.89)	
Ball bearing	Force-deflection k_{brg}, c_{brg} in eq. (2.49)		
Ribbon damper	Kelvin-Voigt f_{rd} in eq. (3.4)		Generalized Dahl f_{rd} in eq. (3.1)
Housing outer race interaction	Rigid	Hunt and Crossley f_n in eq. (2.89)	

3.3 Experimental validation of the TDB model

3.3.1 Industrial scale test rig

Rotor drop tests were performed by GE Oil & Gas Thermodyn at Le Creusot, France. The industrial scale test rig, see Figure 3.12, is equipped with a 5-axis AMB system.

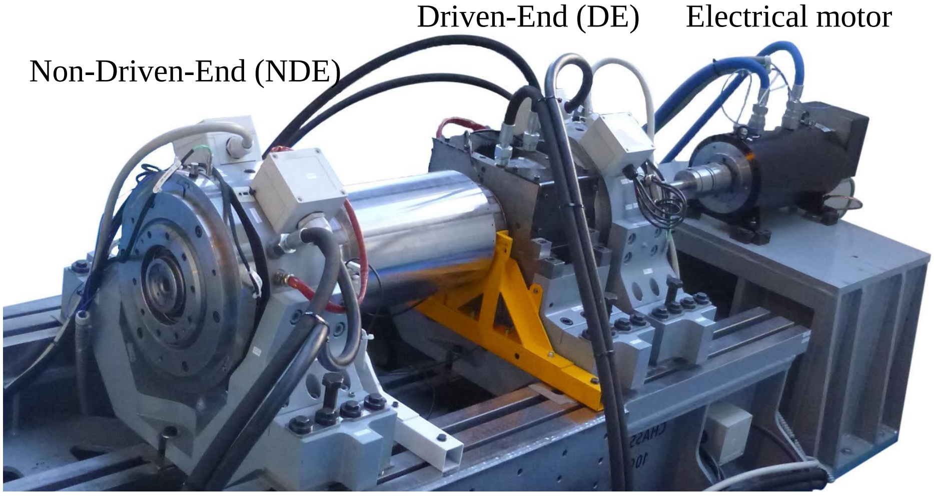

Figure 3.12: Industrial test bench

The test platform is modular and can be used with different rotor configurations. The heteropolar AMBs are powered in differential driving mode with a 6 A bias current. Forced air cooling is used to evacuate bearing losses mainly due to windage. The rotor employed is sized to be rigid for rotational speeds below 25 000 rpm. The rotor has a total length of 1 150 mm and the driven-end (DE) and non-driven-end (NDE) actuators span is 787 mm. The large central part has a diameter of 230 mm. It is driven by an electrical motor through a flexible coupling.

Inductive sensors measured the rotor displacements at AMB DE and NDE and are not collocated with actuators. No measures of the TDB rotational speed were available. The sampling

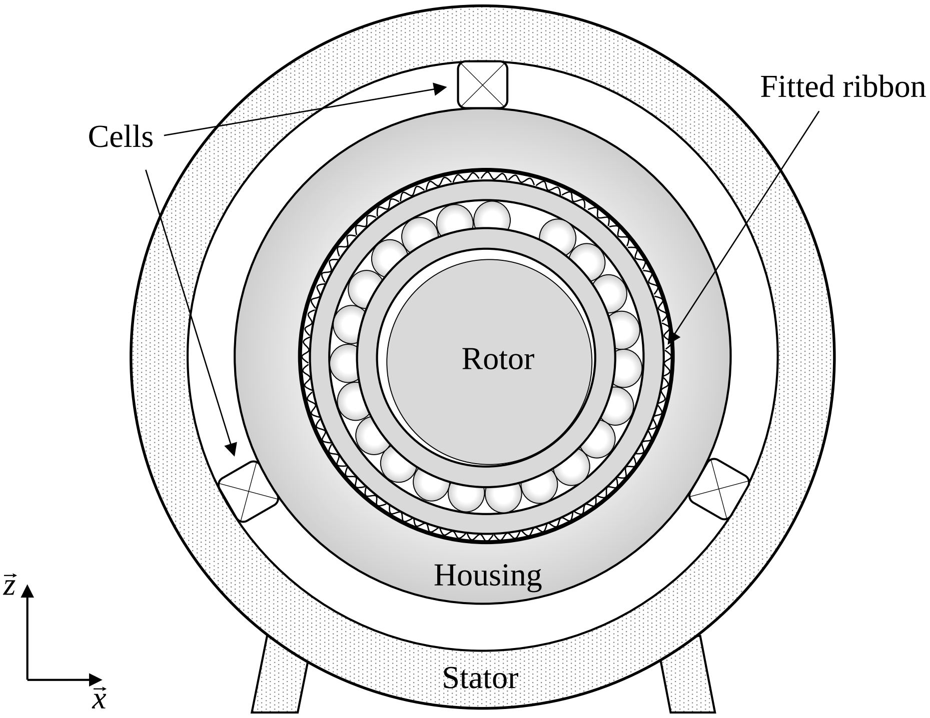

Figure 3.13: Scheme of the force cells positions

frequency is 20 kHz which is sufficient to analyse nonlinear dynamics phenomena. TDBs are monitored with three axis accelerometers and pre-loaded force cells. The latter measured only radial forces and are placed between the TDB housing and the stator. Therefore, the drops loads are entirely transmitted to the stator through these cells, as shown in Figure 3.13.

The rotor FE model is based on the beam theory of on-board rotors presented in Chapter 2. For rotor drop analysis, the support is considered fixed, therefore base motions are not taken into account and all the related components, vectors or matrices do not appear in the equations of motion. The rotor is modelled with 41 Timoshenko beam elements for a total mass of 168 Dof for the lateral analysis, see Figure 3.14.

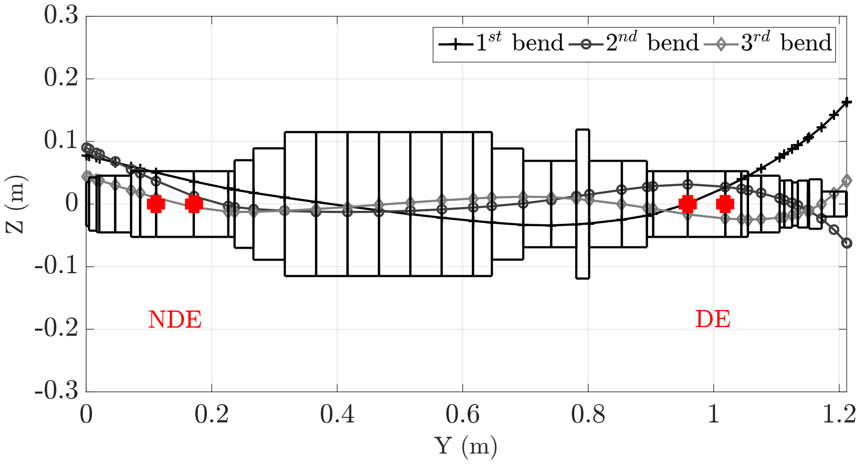

Figure 3.14: Industrial test bench shaft FE model and the first three FE in-plane mode shapes

Pseudo-modal method is used to reduce the model size. Only the first 12 modes are kept and the first three bending modes are plotted in Figure 3.14. The coupling is supposed completely flexible with no damping and is represented by a rigid disc (inertia and mass) at DE. The rotor is supported by linearised AMBs, which are therefore considered as simple spring-dampers. No control loop is activated; the stiffness and damping parameters are provided by the AMB transfer function for a given shaft rotational speed.

These experimental and numerical comparisons should lead to the validation of the TDB model. The study focuses on rotor drop at rest and at 6 500 rpm. At rest, the effect of the TDB model in lateral direction is observed since the rotor is only subjected to gravity and contact. No unbalance nor gyroscopic forces are present. The results are compared in terms of overall dynamics, maximal vertical rebound heights and drop loads. This experimental and numerical comparison should lead to the selection of the model 1, 2 or 3. No measured TDB rotational speed is available and the modelling could not be validated by comparing the measured and the predicted rotational speeds. Analysing the rotor horizontal dynamics after the drop at 6 500 rpm gives useful informations concerning the time needed for the TDBs to reach full speed. Then, the rotor inner race friction forces are suddenly cancelled and the shaft is usually recentred with respect to its TDBs, moving down to its bottom level. This experimental and numerical comparison should lead to the validation of the rotational modelling.

Numerical simulations of 1 s are performed using the 5th order Runge-Kutta explicit scheme with a typical time step for nonlinear analysis of 5 μs. At 0.2 s, AMBs restoring forces are shut down. Rotor displacement and TDB load results have been normalized respectively according to the rotor-TDB clearance and to the maximal load observed during the ribbon experimental characterisation, see Figure 3.8. Models 1, 2 and 3 are implemented in the simulation successively.

3.3.2 TDB model selection - drop at rest

The rotor drop simulations predicted by using the three TDB models, see Table 3.2, are compared with the test in Figures 3.15, 3.16 and 3.17, respectively. In particular, the rotor displacements / orbits and contact forces along the z-axis at both NDE and DE positions are presented.

In the case of the contact law, vertical predicted and measured displacements as well as orbits are close, especially at the DE side, see Figure 3.15. At the NDE side, the predicted rebounds and the depth of penetration are higher than measured results. The predicted DE side loads are close in amplitude, but not in duration while at the NDE side, loads are partially well described up to 0.017 s.

The four Dof model using the Kelvin-Voigt law, see Figure 3.16, and the contact law, see Figure 3.15, results are close; the rotor inner race and the outer race housing interactions imply high contact stiffness, much greater than the ribbon outer race interaction.

The results predicted with the generalized Dahl model are plotted in Figure 3.17. For both

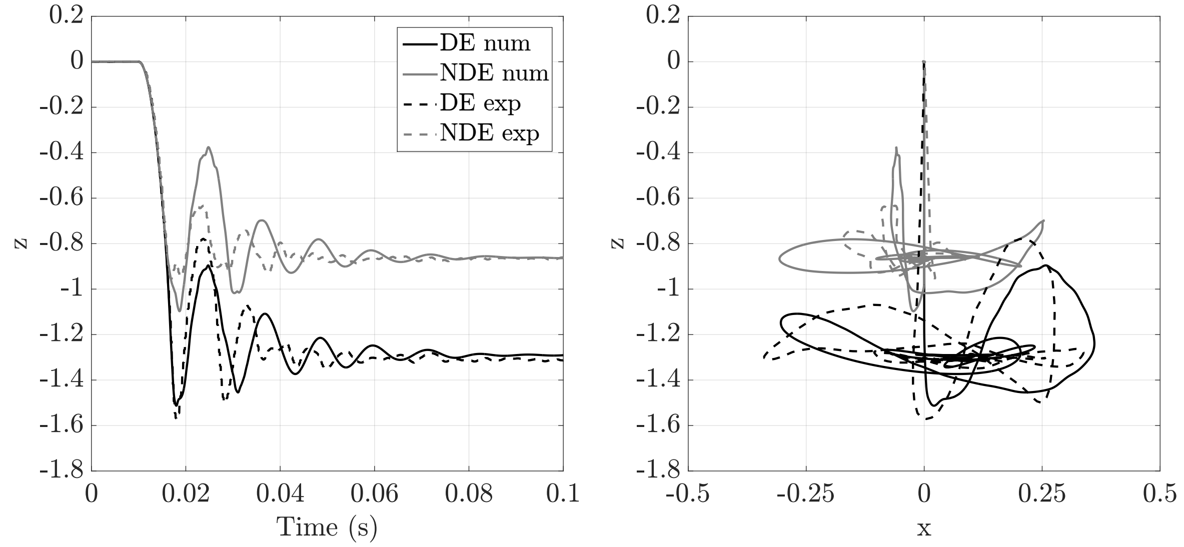

(a) Vertical drop

(b) Orbits

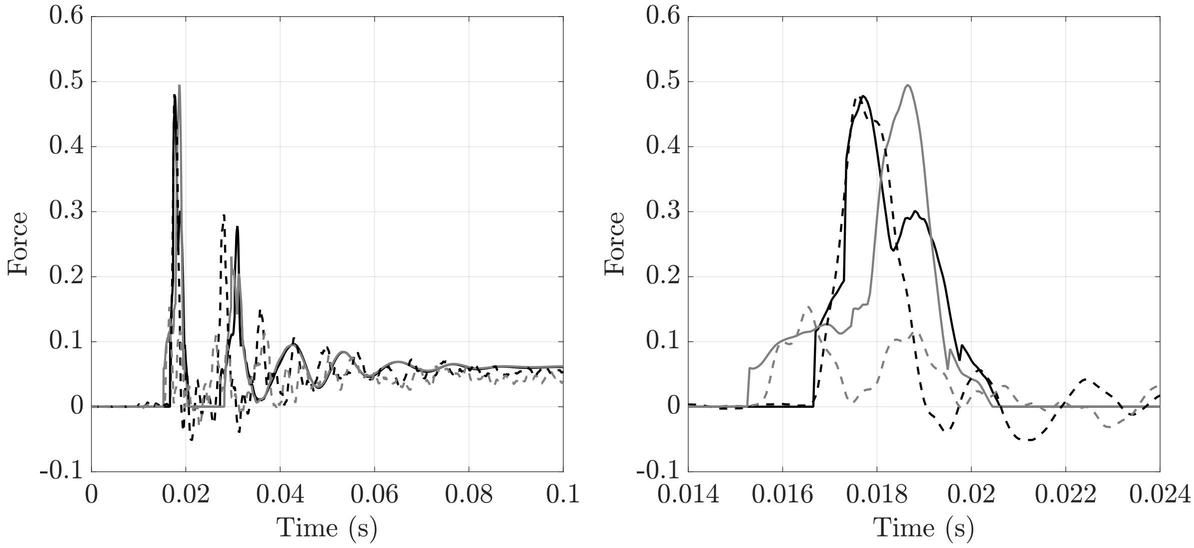

(c) Drop loads

(d) Drop loads zoom

Figure 3.15: Normalized predicted (solid lines) vs measured (dotted lines) results - Model 1, see Table 3.2

NDE and DE sides, the predicted rebounds are flattened; this is due to the high level of damping brought by the dry friction generated in the ribbon damper model. The final static positions of the rotor at the bottom of its TDBs are not identical. The loads are better predicted than those coming from the Kelvin-Voigt model even if stick-slip transitions are much more visible than in experiments: the two slopes are clearly visible at the DE side, see Figure 3.17(d).

The previously developed generalized Dahl model, established on harmonic tests performed on the ribbon damper, gives mixed results in terms of rotor drop dynamics; it generates too much damping and drop rebounds are flattened. In order to enhance the numerical simulation, the slipping threshold μF_N of the generalized Dahl model contained in the upper and lower

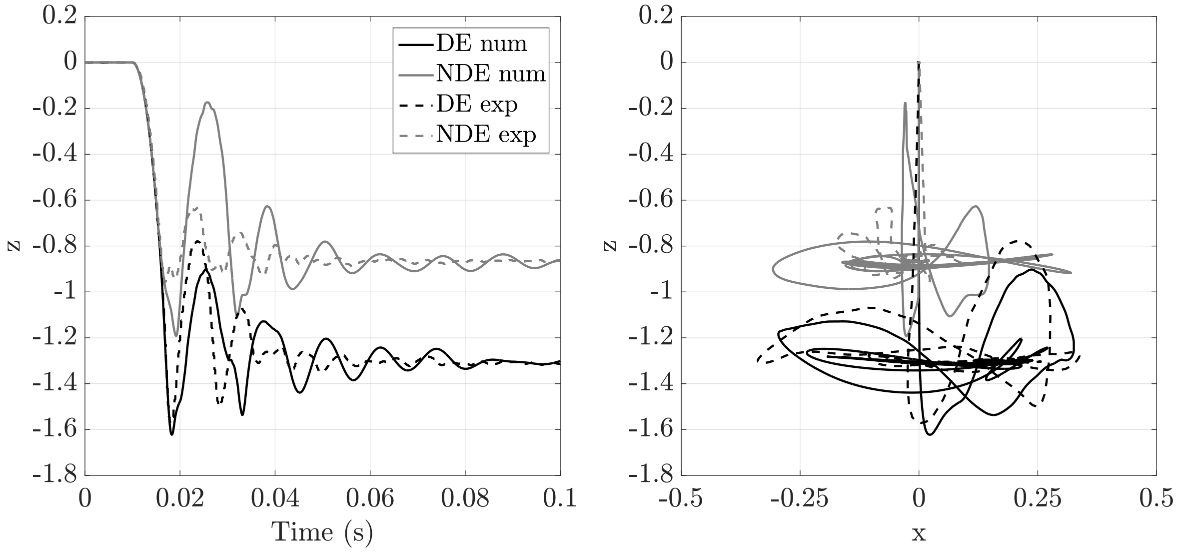

(a) Vertical drop

(b) Orbits

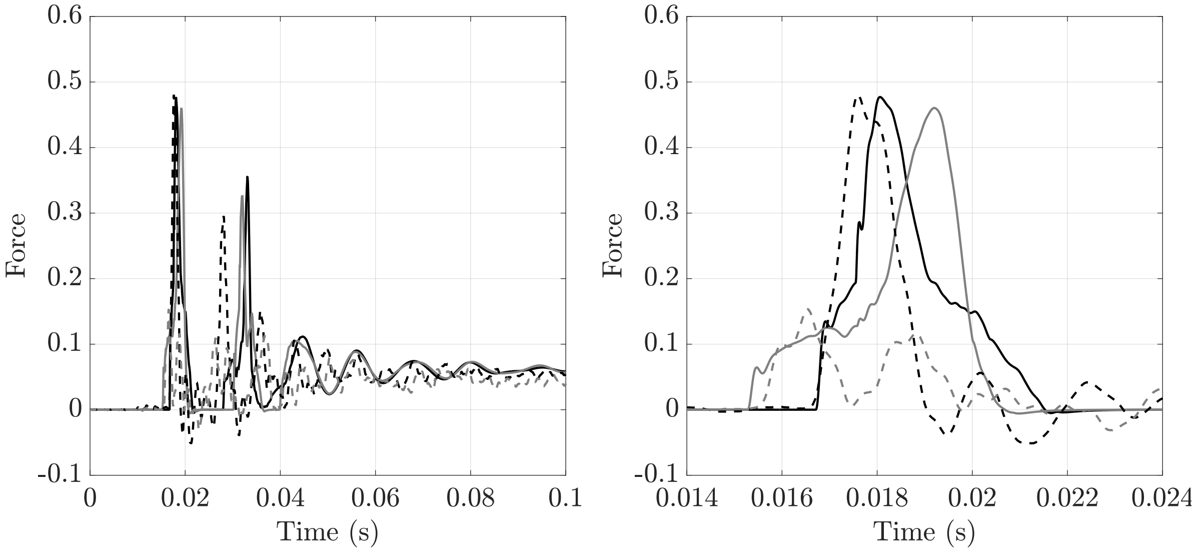

(c) Drop loads

(d) Drop loads zoom

Figure 3.16: Normalized predicted (solid lines) vs measured (dotted lines) results - Model 2, see Table 3.2

envelops, see equation (3.3), is decreased at both DE and NDE sides.

Figure 3.18 shows the effect of decreasing the slipping threshold on the rotor drop dynamics in terms of orbits and hysteresis loops. Drop rebounds are closer to experimentations, especially at the DE side. The parameter μF_N was adapted to better describe the drop experiments; it was reduced by a factor of 30 and 4 at the DE and NDE sides respectively. The ribbon hysteresis loop surfaces are then reduced implying a global reduction of the dissipated energy and the related damping. The modification of the ribbon parameters enables to obtain a satisfactory correlation between predicted and measured results. The dynamic behaviour of the ribbon is probably different when subject to shocks rather than harmonic excitations.

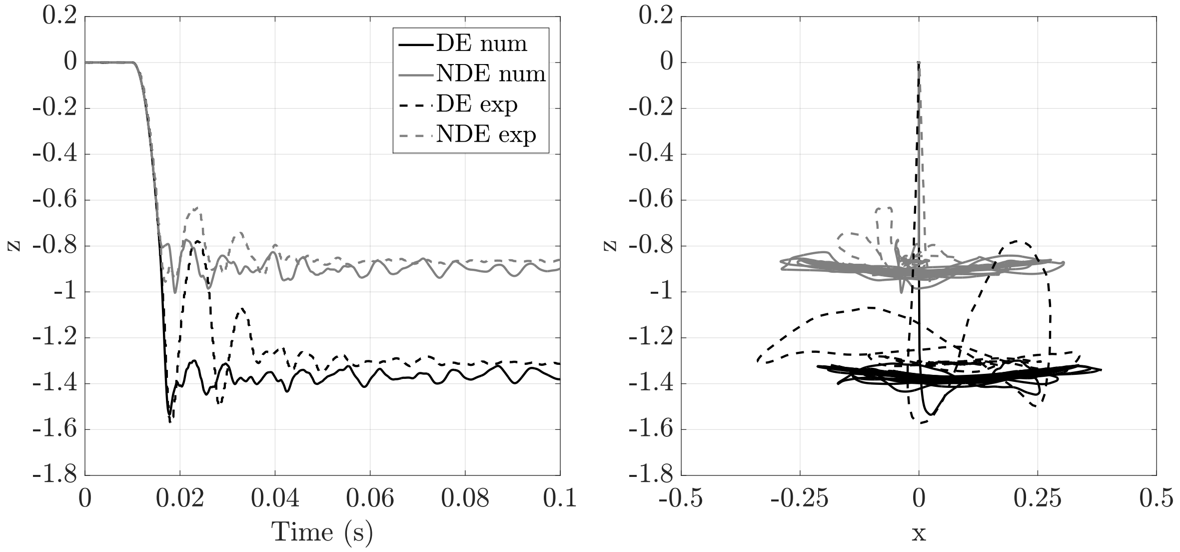

(a) Vertical drop (b) Orbits

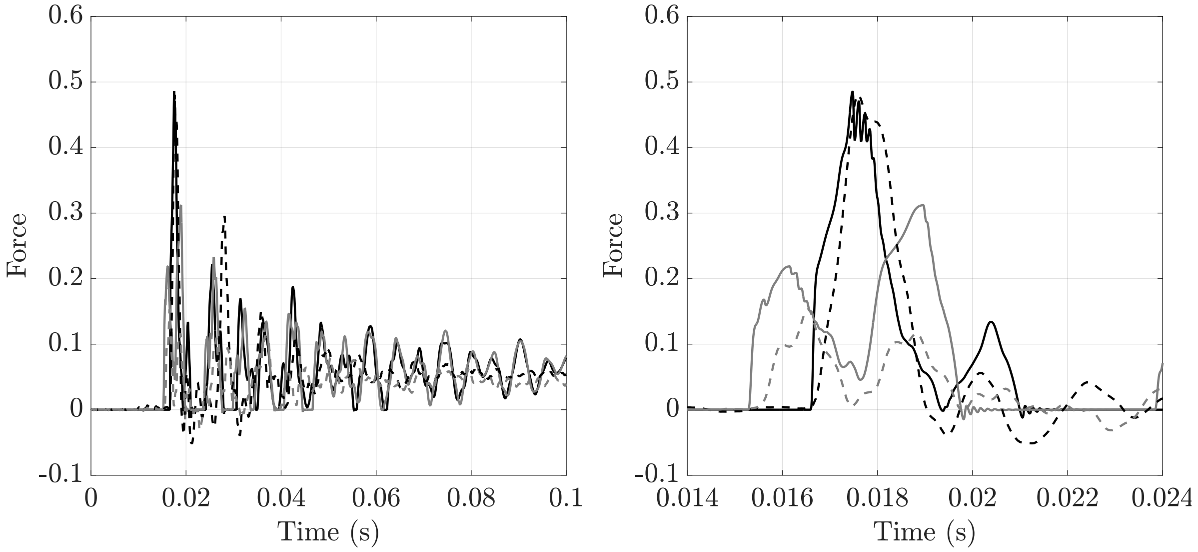

(c) Drop loads (d) Drop loads zoom

Figure 3.17: Normalized predicted (solid lines) vs measured (dotted lines) results - Model 3, see Table 3.2

Shocks could generate waves able to easily unstick the ribbon bumps leading to a global decrease of the slipping threshold μ_{FN}, in equation (3.2), and to a diminution of the damping in the system drop. This theory is sustained by the fact that slipping threshold is significantly smaller on the DE side where the rotor drops from 50% higher. The generalized Dahl model could be certainly improved by an adaptive model where the slipping threshold would be dependant on the impact velocity. These investigations were not treated in this work and it could be the subject of further research. As the slipping threshold seems to be completely reduced, viscous damping instead of dry friction seems to be able to describe the transient drop events.

To sum-up these comparisons, Tables 3.3 and 3.4 gather the maximal measured and pre-

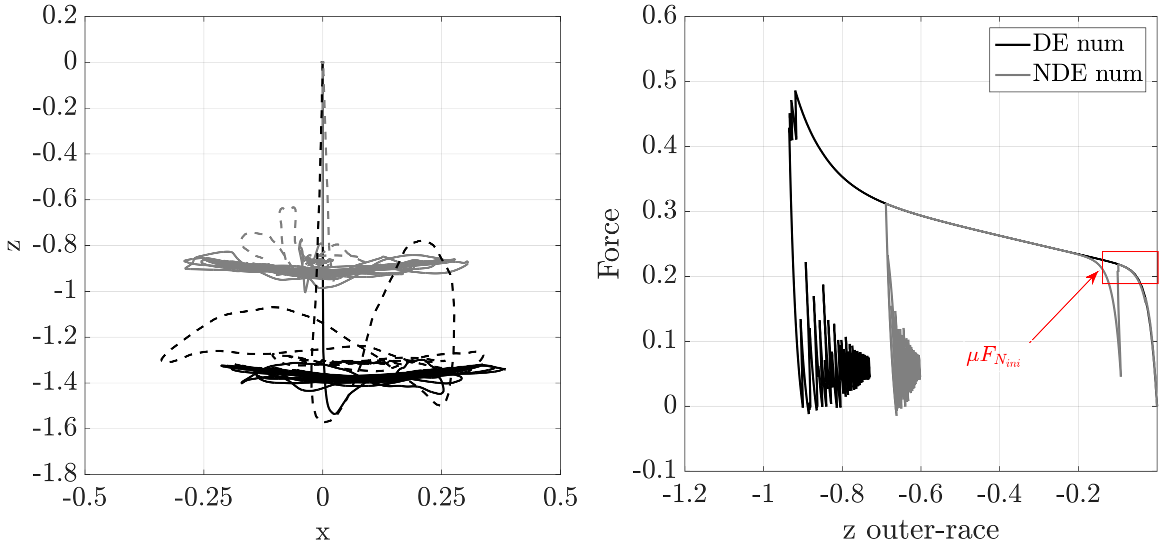

(a) Orbit - $\mu F_{N_{ini}}$ (b) Hysteresis loops - $\mu F_{N_{ini}}$

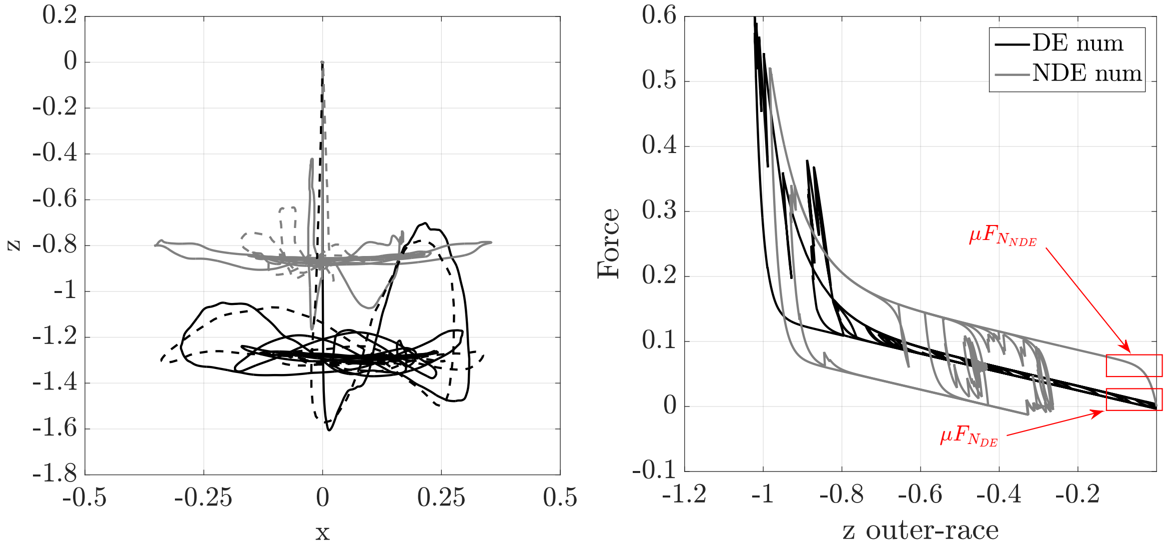

(c) Orbit - $\mu F_{N_{DE,NDE}}$ (d) Hysteresis loops - $\mu F_{N_{DE,NDE}}$

Figure 3.18: Normalized predicted (solid lines) vs measured (dotted lines) results - Model 3, see Table 3.2 - reduced slipping threshold

dicted drop loads and rebounds heights respectively, computed with the three TDB models. These results provide an overview of the model to correctly represent the transmitted loads and the transient dynamics. It is shown that all the three models with initial parameters provide accurate predictions in terms of drop loads at the DE side. At the NDE side, the discrepancies are larger for all the three models either for loads or rebounds and the model 3 with initial parameters gave the closest results. Considering the heights of the first rebound, the model 1 seems to be the most suitable considering both the DE and the NDE side.

Considering the previous comparisons and Tables 3.3 and 3.4, it is reasonable to conclude that the simple contact law is sufficiently representative for the requirements of this research

Table 3.3: Normalized predicted vs measured maximal drop loads in vertical direction and the relative deviations

	Measures	Model 1	Model 2	Model 3	Model 3 (modified)
DE	0.48	0.48 / 0%	0.48 / 0%	0.49 / 2%	0.6 / 25%
NDE	0.15	0.49 / +226%	0.46 / +206%	0.31 / +106%	0.52 / +246%

Table 3.4: Normalized predicted vs measured heights of the first vertical rebound and the relative deviations

	Measures	Model 1	Model 2	Model 3	Model 3 (modified)
DE	0.8	0.62 / -23%	0.72 / -10%	0.24 / -70%	0.9 / +13%
NDE	0.31	0.72 / +132%	1.02 / +229%	0.23 / -25%	0.74 / 138%

project; the model 1 is selected. The predicted orbits comparisons between the contact law and the four Dof model using the Kelvin-Voigt model have shown that the contribution of rotor inner race and outer race housing interactions can be considered negligible in this case. Finally, the behaviour of the ribbon damper showed different characteristics when subjected to harmonic or transient excitations.

Rotor drop at rest permits selecting and validating the TDB model in lateral direction. To validate the rotational modelling, predictions and measures of the lateral dynamics of a spinning rotor during drop are compared.

3.3.3 Rotational validation - drop at 6 500 rpm

The rotor runs at 6 500 rpm and has been balanced previously; the unbalance was estimated to obtain close measured rotor orbits and is assumed to be mainly located at the coupling location.

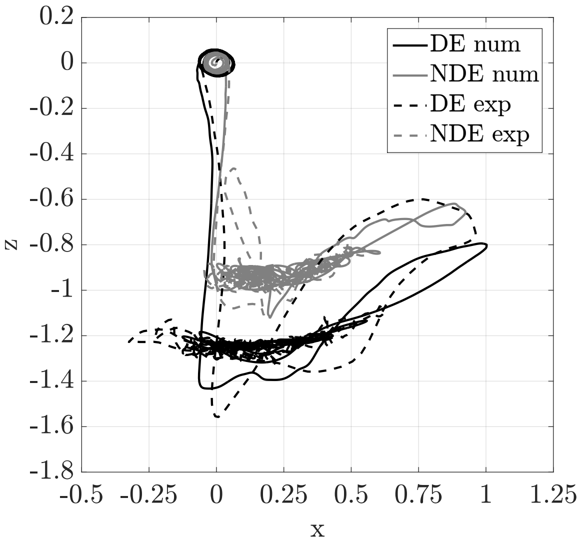

Figure 3.19: Normalized predicted (solid lines) vs measured (dotted lines) orbits - drop at 6 500 rpm

The validated contact law provides the nonlinear restoring forces. The drop occurs around 0.2 s and the friction forces drive the TDBs until they reach the rotor rotational speed. Figure 3.19 shows the normalized measured and predicted orbits. The transient drop dynamics characterized by rebounds quickly cease and the rotor stabilizes at the bottom of its TDBs. No dangerous behaviour is developed. Qualitatively, predicted and measured results are close.

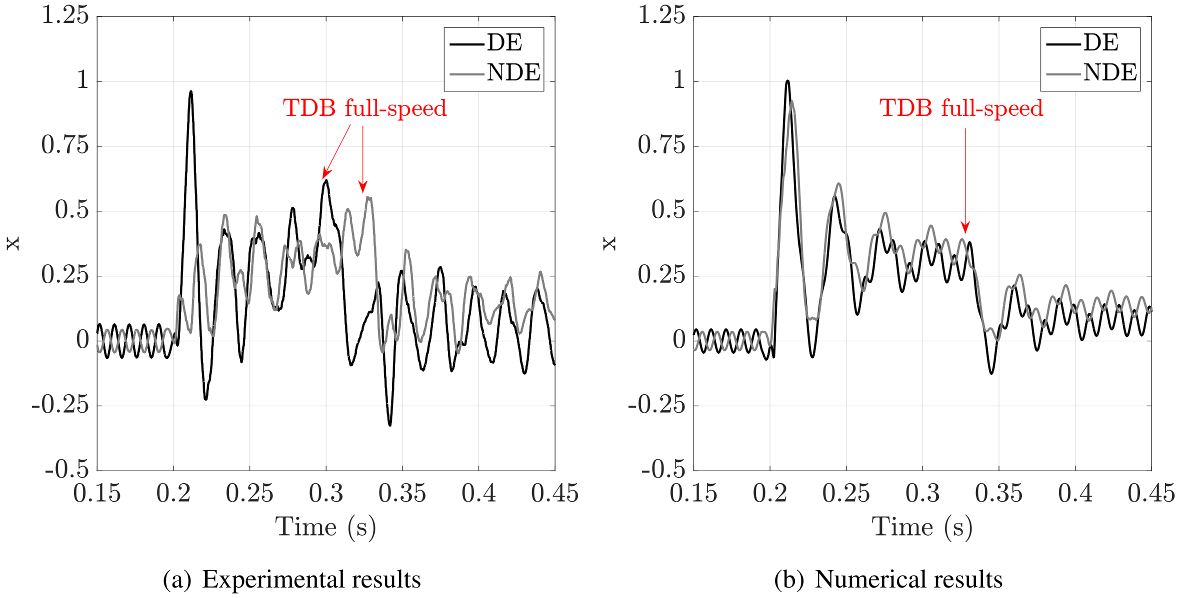

(a) Experimental results

(b) Numerical results

Figure 3.20: Normalized measured (a) and predicted (b) horizontal rotor displacements - drop at 6 500 rpm

Horizontal displacements are presented in Figure 3.20 showing that the global dynamic behaviour is reproduced. It is worth mentioning that the first horizontal motion of the rotor just after the drop is described well at the DE side. The most important information for the purpose of that subsection lies in the change of dynamics, occurring close to 0.3 s and visible in both the predictions and measures. The rotor is recentred in the bottom of its TDBs; this corresponds to the moment where the TDBs reach the rotor rotational speed, as shown in Figure 3.21(a). At this moment, the tangential friction forces become close to zero since the relative speed is nil. The DE touchdown bearing seems to reach full speed earlier.

Table 3.5 provides the measured vs predicted times for the TDBs to reach the rotor rotational speed. It is shown that the predictions provided by the model are satisfactory. These results show the ability of the rotational modelling to describe correctly the spin-up of TDBs. The observed phenomenon echoes with the works of Kärkkäinen *et al.* [113] and Helfert *et al.* [139]; the assumptions concerning rolling without slipping kinematic conditions seems to be valid.

The remaining discrepancies of orbits plots, see Figure 3.19, may be attributable to rotating effects since rotor drop predictions at rest gave relatively good results. Gyroscopic effects cannot be the explanation since the rotor has no large discs; gyroscopic effects are weak. The

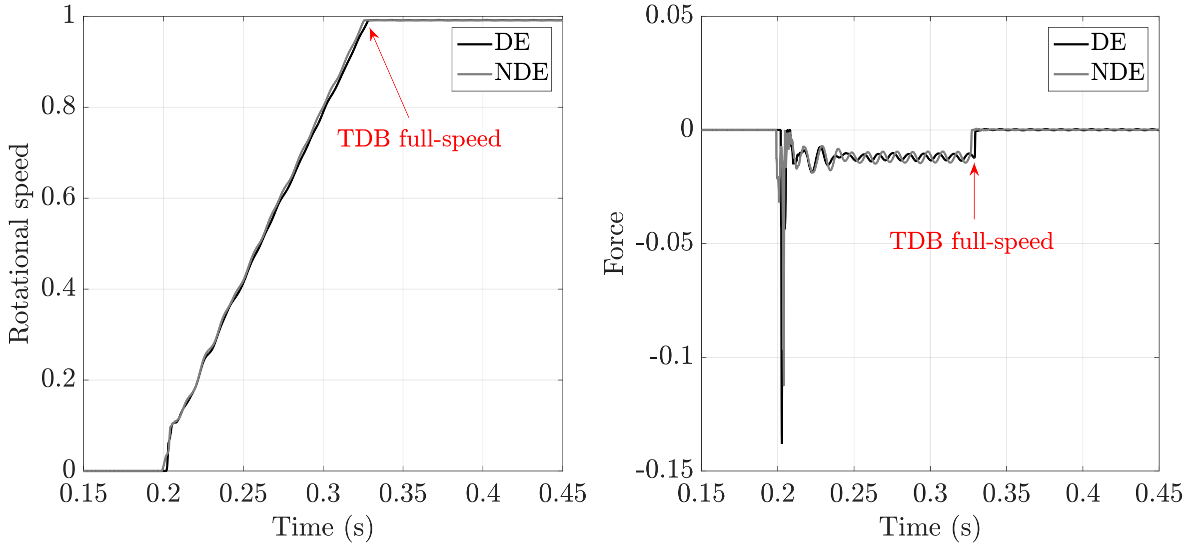

(a) TDB rotational speed (b) Tangential contact loads

Figure 3.21: Normalized predicted TDB rotational speed (a) and tangential contact loads (b) - drop at 6 500 rpm

Table 3.5: Predicted vs measured TDB times to reach full-speed and the relative deviations

	Measures	**Model**
DE	0.11s	0.125s / +14%
NDE	0.129s	0.126s / -3%

sliding friction could be an explanation since it is a crucial parameter of drop dynamics. However, the value of the friction coefficient was set to 0.2 which is the order of magnitude for dynamic friction. In Figure 3.19, the first rebound in the x-direction is driven mostly by friction effects. At the DE side, the latter reaches almost the normalized value of one for both the predictions and the measurements; the friction coefficient may not be the main cause of discrepancies here.

It is well-known that the mass unbalance (amplitude, phase and distribution) can lead to completely different rotor transient behaviours during drops. A numerical assessment is carried out to analyse the effect of the phase on the transient drop dynamics. For an identical mass unbalance located at the coupling, the associated phase angle at the moment of drop is modified from 0° to 270°. The influence in terms of rotor orbit is plotted in Figure 3.22. It is shown that depending on the phase angle, the rebound paths are different.

It is then reasonable to assume that the reason for these discrepancies lies from the difficulty to represent accurately the unbalance distribution.

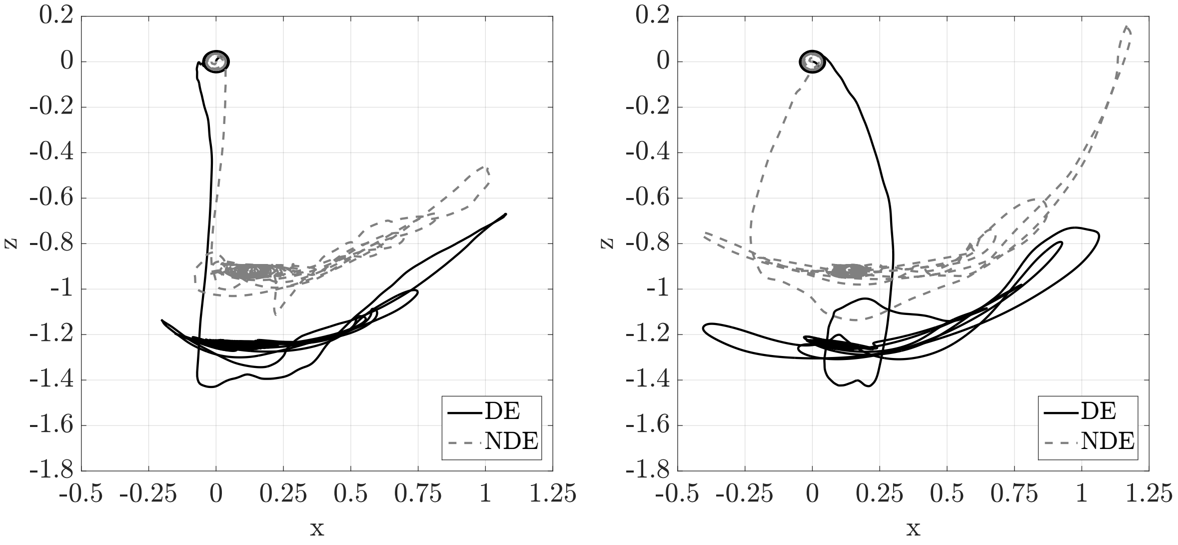

(a) Unbalance phase angle : 0°

(b) Unbalance phase angle : 90°

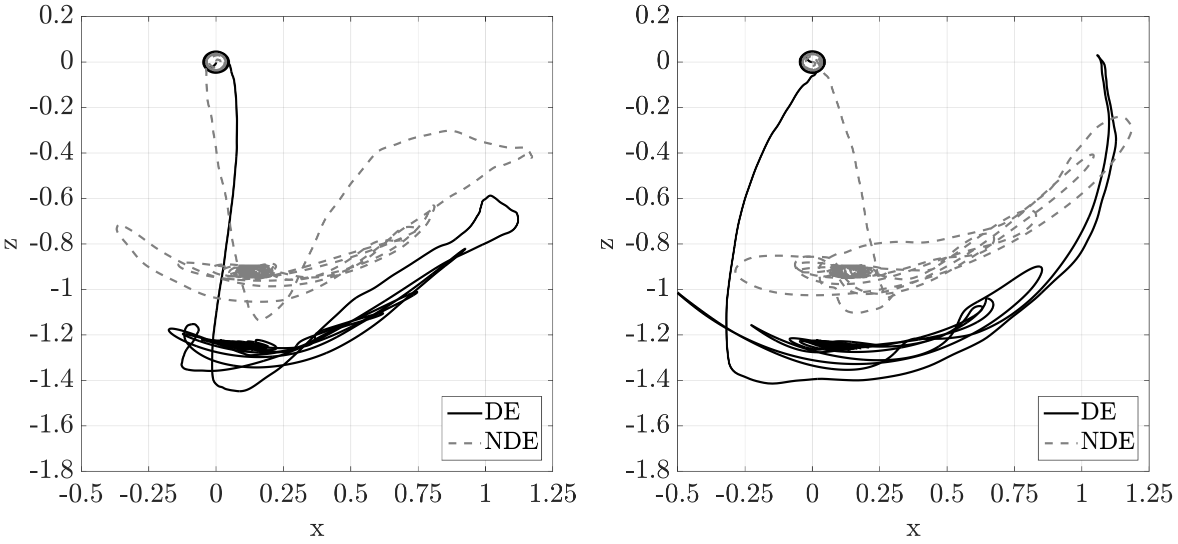

(c) Unbalance phase angle : 180°

(d) Unbalance phase angle : 270°

Figure 3.22: Normalized predicted orbits for different unbalance phase angle

3.4 Conclusions

This chapter gives insights into the modelling of rotor drop. A particular effort was done concerning the degree of detail required for the TDB model to represent with sufficient accuracy the measured rotor displacements. For the need of this study, a sufficiently representative model is required. The experimental validation shows that the contact law gives satisfactory results, in terms of loads and overall dynamics, and is simple to implement. It is able to correctly predict the drop dynamics for a standstill and spinning rotor. Predictions and tests show that the friction-driven TDBs reach the rotor full speed almost at the same time. Further investigations were done on the ribbon damper which is a key component for rotor stability. The generalized Dahl model was able to reproduce well the observed dry friction phenomena in the case of harmonic forcing. Using the developed model based on harmonic test may overestimate the damping in the system in the drop case. It is shown that reducing the slipping threshold parameter gave satisfactory results. The ribbon may behave differently when subjected to shock and further research should be carried out in this field. Developing a slipping threshold dependent on the rotor impact velocity would be an interesting improvement of the model.

Chapter 4

On-board rotor-AMB system dynamics

The aim of this chapter is to validate the developed on-board rotor-AMB system model. The academic test rig, comprising a rigid shaft, is mounted on a 6-axis shaker and subject to different types of excitation, each of them being representative of real operating conditions. The predicted and measured rotordynamics subjected to a combination of base motion, mass unbalance, gravity and potential TDB contacts loads are assessed. The PID controller is tuned for conventional rotordynamics purposes and not specifically to sustain base motion or TDB contact loads. The numerical model combines the different models presented throughout the previous chapters. In each of the tested cases, the capability of the rotor-AMB system to remain stable is assessed numerically and experimentally. The sliding friction effects, the nonlinear features of magnetic forces and the contact loads are of particular interest.

Contents

The aim of this chapter is to validate the complete numerical model, but also to provide an answer to the initial problem of this PhD which is: *what would be the dynamic behaviour of a rotor supported by AMB, controlled by conventional control strategy (PID), subjected to conventional rotordynamics loads (gravity and unbalance) but also to external base motion and contact nonlinearities ?*. The same kind of study was carried out by Hawkins [52], however, no experimental validations were conducted. Thereafter, the approach is numerical and experimental.

Industrial turbomachinery is usually not designed to operate during critical conditions, involving large rotor displacements. When the latter exceed a certain threshold, an emergency shut-down procedure is launched and the machine is progressively stopped; the rotor runs-down, often followed by an AMB shut-down. Here, this threshold is not considered and the system is allowed to operate even when rotor-TDB contact occurs. It is then possible to analyse how the rotor-AMB system reacts and how far it is able to handle these events. In particular, it is important to answer to the following questions:

- Does the controller able to destabilise the rotor rather than stabilises it during rotor-TDB contact?
- Does the friction forces able to drive the rotor backward whirl during rotor-TDB contact?
- Does the TDB contact loads exceed its capacity?

To carry out this study, an academic rotor-AMB system is used. The rotor is designed to have the dynamic characteristics of industrial turbomachinery, the target of this investigation. Most importantly, the validation of the model could be extended for industrial designs.

A 6-axis shaker, unique in the French public research, is employed to perform harmonic and impulse base motion tests which represent earthquakes and shocks (induced for example by large waves), respectively. These events could occur while turbomachinery operates.

The complete numerical model that takes into account base motions, AMBs, unbalance and gyroscopic effects, gravity and contact with TDBs is schemed in Figure 4.1.

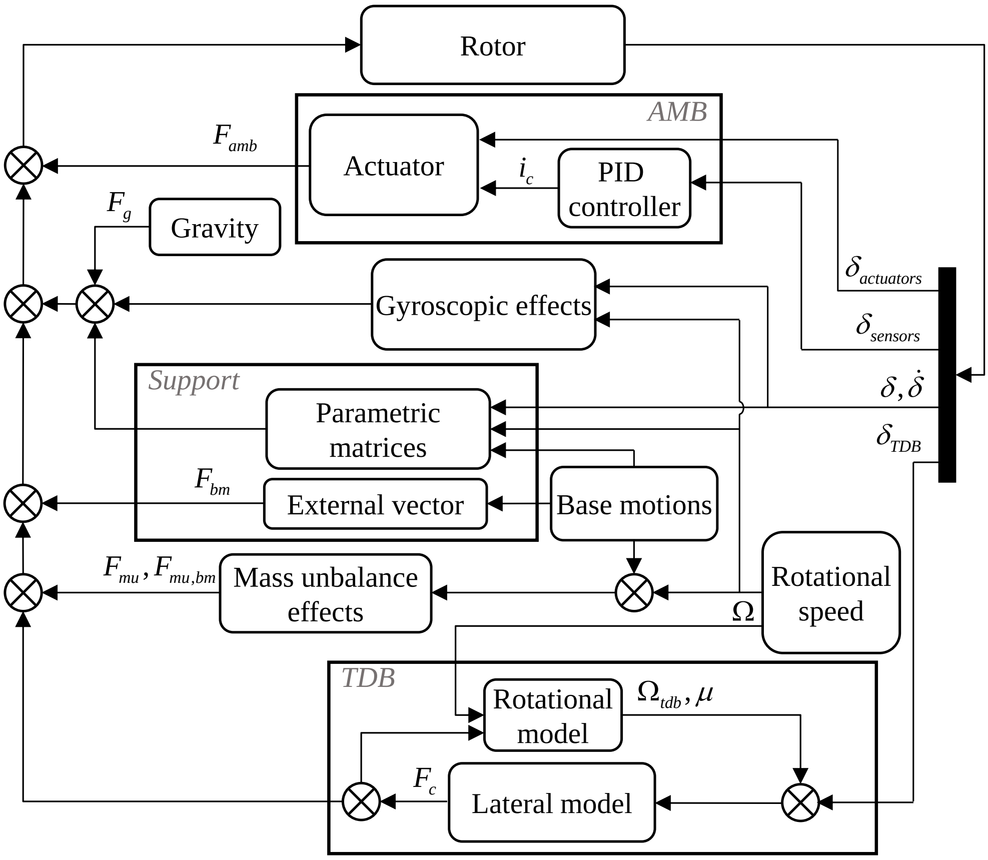

Figure 4.1: Numerical model scheme

4.1 Academic scale test rig

The test bench, see Figure 4.2, was manufactured by SKF® . This rig was used previously by Defoy [137] and Defoy *et al.* [184, 185]. It is made of a steel disc-shaft system mounted on two AMBs equipped with TDBs. It is on-board on the 6-axis shaker.

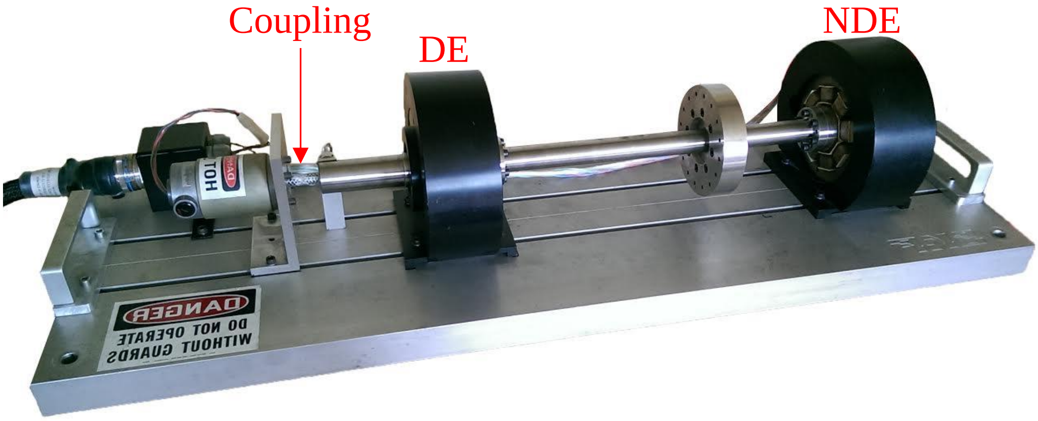

Figure 4.2: Academic scale test rig

4.1.1 Rotor

In the present study, the rotor is designed to obtain the dynamic behaviour of high speed turbomachinery with a rigid shaft in the operating speed range and low gyroscopic effects. The rotor,

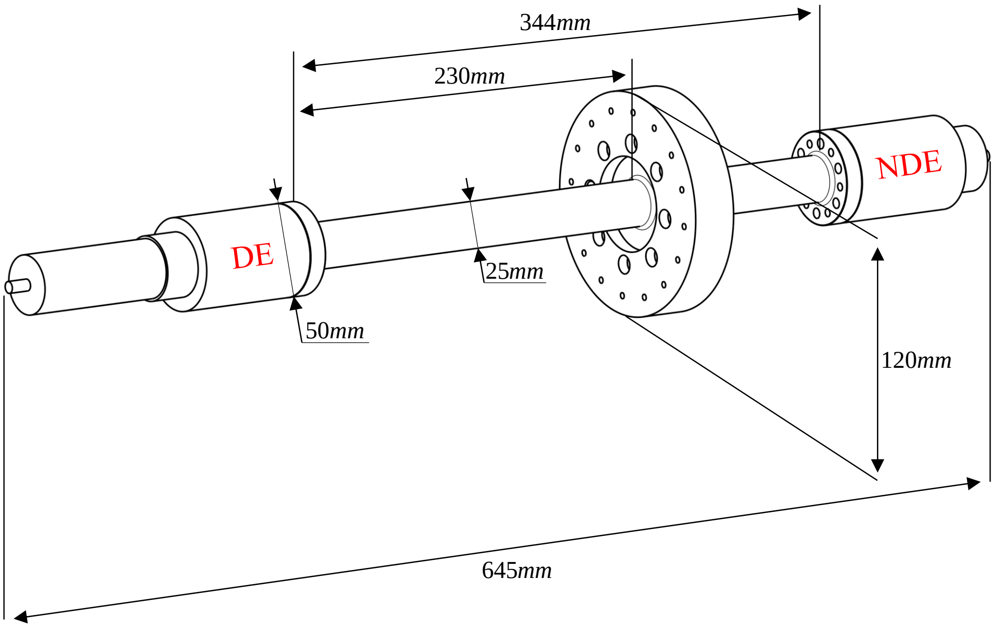

Figure 4.3: Academic shaft

schemed in Figure 4.3, is made of standard steel, its mass is 6.5 kg and its length is 645 mm. It is composed of three parts bolted together; a central part (diameter: 25 mm; length: 344 mm) with a disc, 120 mm in diameter and 25 mm in thickness, placed at two-thirds of the bearing span from the DE side, and two shaft ends (50 mm of main diameter). The steel lamination stacks are fitted on each of these two shaft ends. The rotor FE mesh, sketched in Figure 4.4, comprises 41 Timoshenko beam elements according to the on-board theory presented in Chapter 2. The first three bending modes of the rotor at rest (no base motion, no rotational speed) are plotted in Figure 4.4. The calculation of the natural frequencies, given in Table 4.1, was performed with a direct stiffness equals to $8 \times 10^5 N.m^{-1}$ and representative of the magnetic bearing characteristics under PID control.

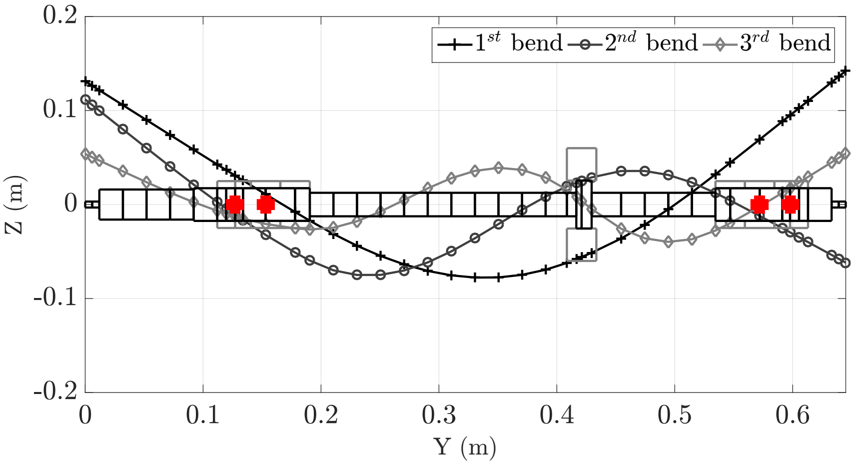

Figure 4.4: Academic rotor FE model and the first three FE in-plane mode shapes

Table 4.1: Rotor natural frequencies

Modes	0 rpm (Hz)	15 000 rpm (Backward) (Hz)	15 000 rpm (Forward) (Hz)
Rigid 1	75	75	75
Rigid 2	92	89	94
1	203	194	213
2	581	563	598
3	1 142	1 036	1 260
4	2 103	2 088	2 119

The rotor was driven by a 500 W electric motor with a maximum speed of 12 600 rpm controlled by a dedicated PI controller. The latter was not considered in the model and the rotational speed of the rotor was set constant. The torque transmission is provided through a flexible coupling. The operating speed range is from 0 to 9 500 rpm (160 Hz), which includes the first two rigid modes, as shown in Table 4.1. The rotational speed was recorded by using a tachometer placed close to the motor. Vibration nodes located between the sensor and the actuator (the red points in Figure 4.4) are present at the NDE side for both the third and the fourth modes. This FE model permits numerical tuning of the AMB controller.

4.1.2 Active magnetic bearings

The rotor test rig is equipped with two identical radial AMBs called NDE and DE bearings. No thrust bearing is present and the flexible coupling sustains the axial loads. Each radial bearing has a maximum static load capacity of 210 N. The action lines are positioned in the configuration “load between axes”; the angle between the vertical axis and an action line is 45°. They are powered in differential driving mode with a bias current of 1 A. Currents are provided in the range of [0-3]A using PWM amplifiers. The AMB characteristics are gathered in Table 4.2.

Table 4.2: AMB characteristics

α	$\mu_0\left(T.m.A^{-1}\right)$	$S\left(m^2\right)$	N	$g_0\,(mm)$	$\mu_r\left(T.m.A^{-1}\right)$	$L\,(mm)$
$\frac{\pi}{8}$	$4\pi\times10^{-7}$	233×10^{-6}	138	0.432	5000	114

The current k_i and negative k_x stiffness are given in Table 4.3.

Table 4.3: Magnetic stiffness

Current stiffness $k_i\left(N.A^{-1}\right)$	**Negative stiffness** $k_x\left(N.m^{-1}\right)$
-104.8	2.18×10^5

The considered frequency bandwidth is [0-2]kHz. Each AMB has two action lines and each line has its own augmented PID controller (SISO system). The related transfer functions, identical for each action line of the AMBs, are given in Figure 4.5(a) for the DE and NDE sides.

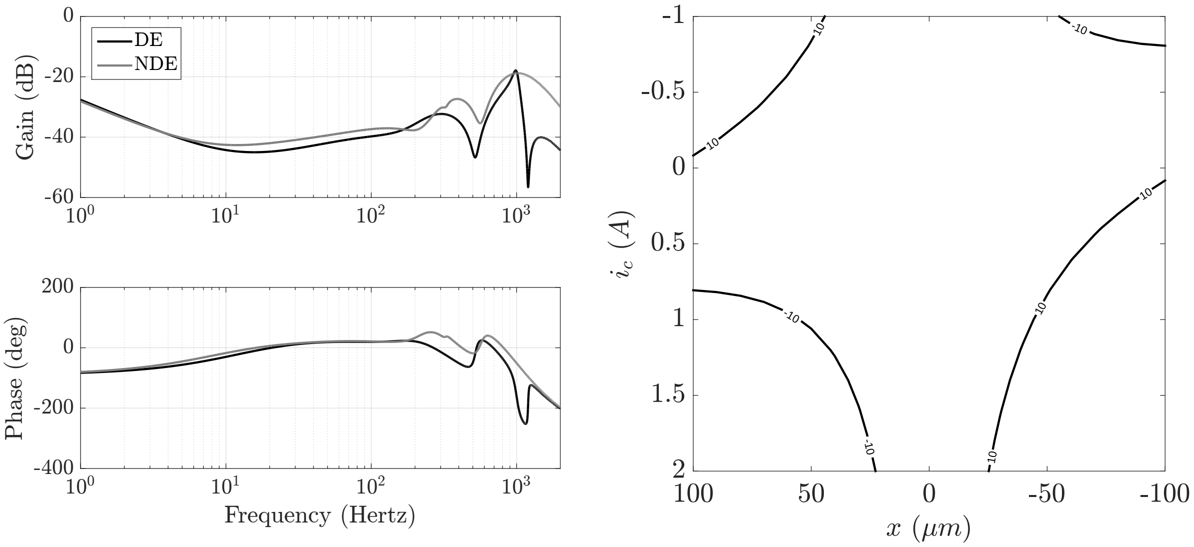

(a) Transfer functions

(b) Linearity limit

Figure 4.5: AMB transfer functions (a) and magnetic force linearity limit (b)

They provide output control currents (A) for given rotor displacements (μm) and are tuned for conventional rotordynamics purposes; they are not optimised to face base motion or contact nonlinearities. The vibration nodes present on the third and fourth bending modes were considered for the tuning of the controller. Two proximity probes (variable reluctance) were integrated in the housing of each bearing and were non-collocated with actuators. The linearity of magnetic forces is assessed using the surface plot recalled in Figure 4.5(b), previously described in Chapter 2.

4.1.3 Touchdown bearings

At both DE and NDE housings are mounted two TDBs, cageless single row deep groove ball bearings (no contact angle and then no axial preload) in a typical radial arrangement. Their characteristics are provided in Table 4.4.

Table 4.4: SKF TDB properties

d_m (mm)	α_c (°)	D (mm)	Z	C_s (N)	J_{eq} (kg.m)
45.5	0	4.7	23	8 200	1.4×10^{-5}

They are composed of nitrogen steel races and 23 ceramic balls having a diameter D of 4.7 mm. The pitch diameter d_m equals 45.5 mm and the length of the TDB is 10 mm. The previously validated TDB contact law provides the nonlinear restoring forces when rotor displacement exceeds TDB clearance. The estimated ball bearing force-deflection relationship is determined using the previous analytical method and is plotted in Figure 4.6(a). The load capacity C_s has been estimated to be 8 200 N.

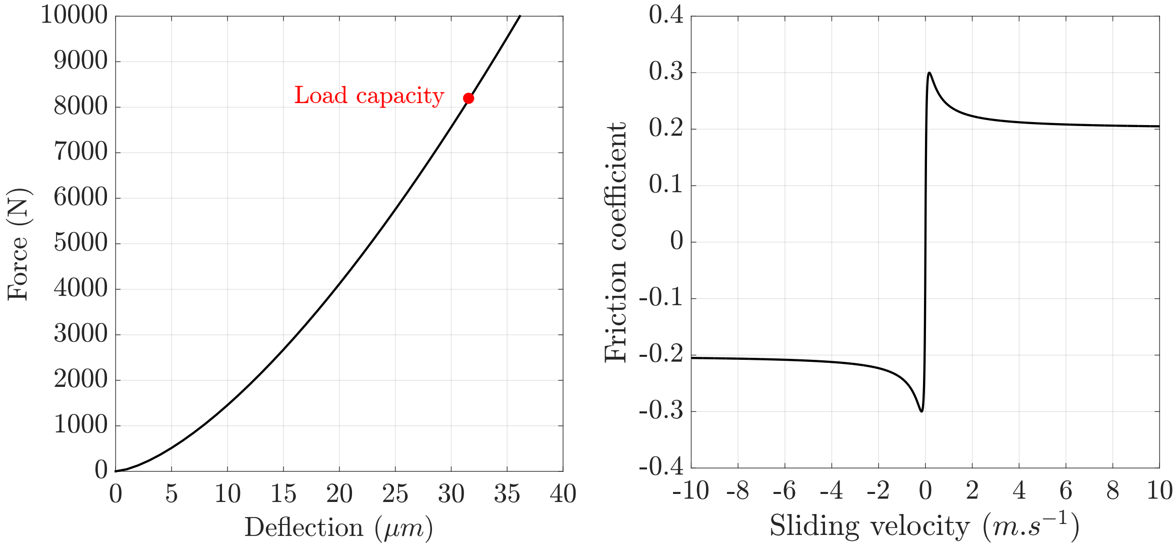

(a) Force-deflection relationship

(b) Sliding friction coefficient

Figure 4.6: TDB force-deflection relationship (a) and sliding friction coefficient (b)

Depending on the amplitude of the rotor-TDB penetration, the ball bearing restoring force is nonlinear. In the case of backward whirl, a linear formulation may underestimate the transmitted loads, as shown by Jarroux *et al.* [169]. The outer race is separated from the housing by a ribbon damper, which has stiffness k_{rd}, damping c_{rd} and dynamic crushing capacity δ_{rd}, estimated and reported in Table 4.5.

Table 4.5: SKF ribbon properties

k_{rd} $(N.m^{-1})$	c_{rd} $(Ns.m^{-1})$	δ_{rd} (μm)
3×10^6	1×10^3	20

Here, the sliding friction force, see Figure 4.6(b), is generated using the Stribeck model given in equation (2.93) in contrast with the previous rotor drop tests. The latter may be more convenient when the rotor-TDB relative speed is close to zero. This may be the case in the following tests. The rotational dynamics are considered by the equivalent inertia J_{eq} and an internal resistance torque. The rotational damping is used to apply breaking on the bearing when no more external loads are present. The value of this damping was assessed experimentally. The 0.1 mm TDB clearance is provided by the manufacturer. An experimental identification of these clearances and misalignments was carried out for each action line. The results of this procedure are plotted in Figure 4.7 and the associated numerical values are gathered in Table 4.6. The red crosses represent the measured positions where the rotor enters in contact with the TDBs. The misalignments are not negligible and the values of the TDB clearances are not exactly as specified.

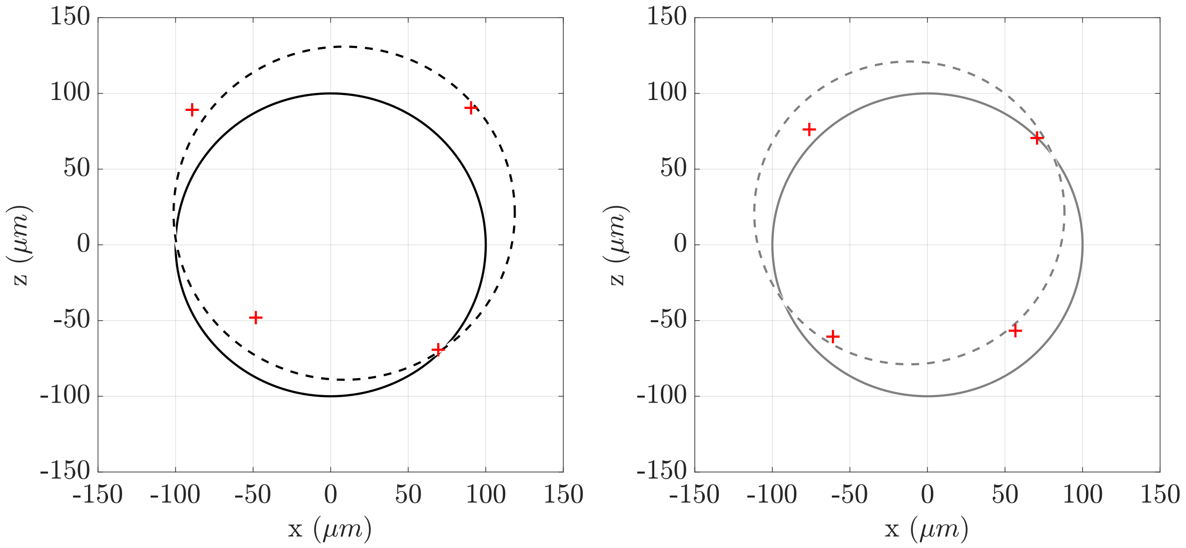

(a) DE side

(b) NDE side

Figure 4.7: Initial (solid line) vs readjusted (dotted line) TDB clearances including misalignments

Table 4.6: Initial vs readjusted TDB clearance - misalignments

	Misalignments (μm)				**TDB clearance** (μm)	
	DE x	DE z	NDE x	NDE z	DE	NDE
Initial	0	0	0	0	100	100
Readjusted	8	20	-11	21	108	98

4.1.4 Shaker and measurements

To perform base motion tests, a 6-axis hydraulic shaker, commonly called Cube™, provided by TEAM Corporation® was available. The Cube™, see Figure 4.8, is a fully integrated system. It has 6 real-time pilots able to apply various combinations of solicitations along and around the 3 axes (translations and rotations) to a maximum mass of 450 kg in a range [0-250]Hz, knowing that the complete rotor test rig weights about 40 kg. A maximum acceleration of 10 G, ± 50 mm in translation and ± 4°in rotation can be generated.

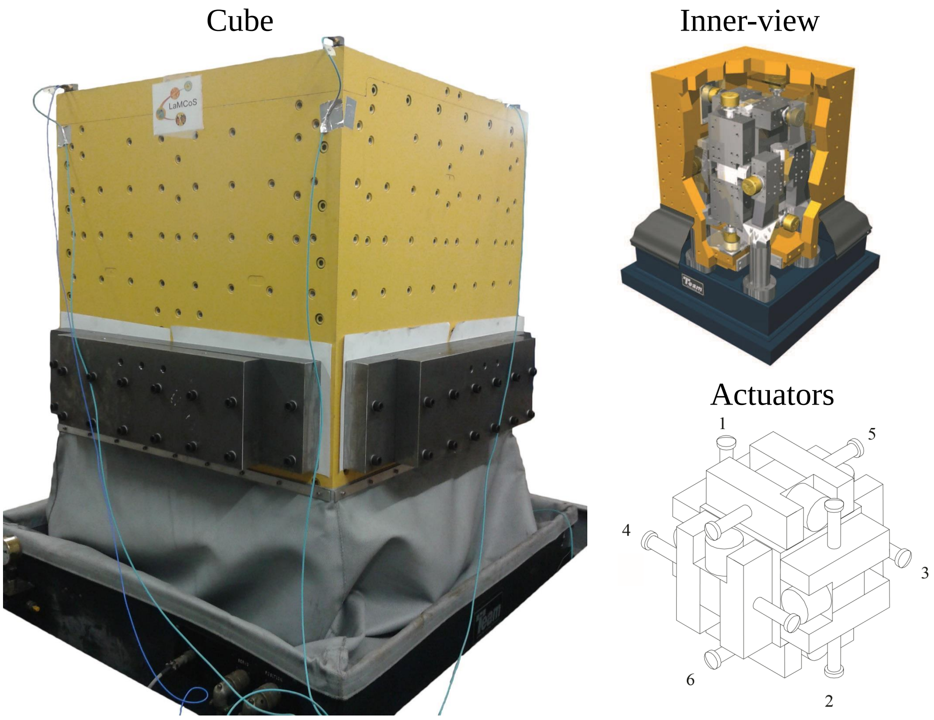
Cube

Inner-view

Actuators

Figure 4.8: The Cube™

Inside the shaker, six servo hydraulic actuators generate motions of the cube, as shown in Figure 4.8. Each numbered actuator consists of two pistons with high performance servo valves. In standard control configuration, the six hydraulic cylinders act together to generate multi-directional base motions. To achieve single Dof translation or rotation, two actuators of a pair must be combined. To execute a single Dof translational motion, two actuators must receive the same driving signal while for rotational motion, the signal must have an opposite sign. Obviously, translation and rotation combinations can be generated. The transmission of load to the shaker table is provided by piston heads on which hydrostatic bearings are attached.

This type of technology avoids direct metal-metal contact, almost avoiding wear. It offers a very high stiffness and transmissibility. A fundamental limitation is the so-called "oil column resonance" that depends on the volume of oil trapped between the actuator piston and the servo-valve. To increase this frequency, the oil trapped volume should be reduced. This is why servo valves are located at actuator pistons halves. To isolate the surrounding building structure, the shaker had to be fixed on a reaction mass. A 40 tons steel-reinforced concrete reaction mass mounted on air isolators was employed. The hydraulic power is provided by two hydraulic pumps generating pressurized oil up to 200 bars in a closed loop circuit. High speed servo valves permit rapid oil injection and high frequency piston motion. The academic test rig was mounted on the shaker by means of mounting clips as shown in Figure 4.9.

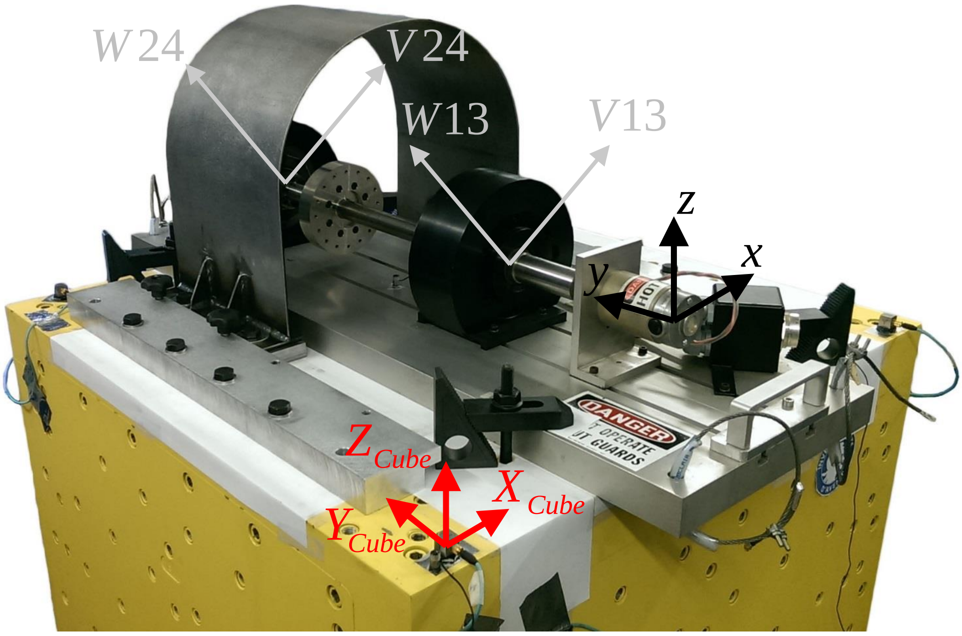

Figure 4.9: Rotor rig - Cube™ assembly - measuring sensors

The data acquisition system of the shaker was used. Base accelerations were recorded in the three directions (Xcube, Ycube, Zcube) using four tri-axial accelerometers fixed on the shaker, see Figure 4.9. The displacement and current sensors for each action line (V13, W13, V24, W24) were accessible via BNC connectors provided by the output panel. The rotational speed was recorded by means of a tachometer. The sampling frequency was set to 24 756 Hz. Before performing base motion tests, the system identification was realized.

4.2 System identification

Mass unbalance responses and drop at rest were first realised to identify the system and assess the numerical model for simple test cases.

4.2.1 Mass unbalance response

The rotor response considering a 17 g.mm mass unbalance located at 0° of the tachometer TDC (top dead centre) is shown in Figure 4.10.

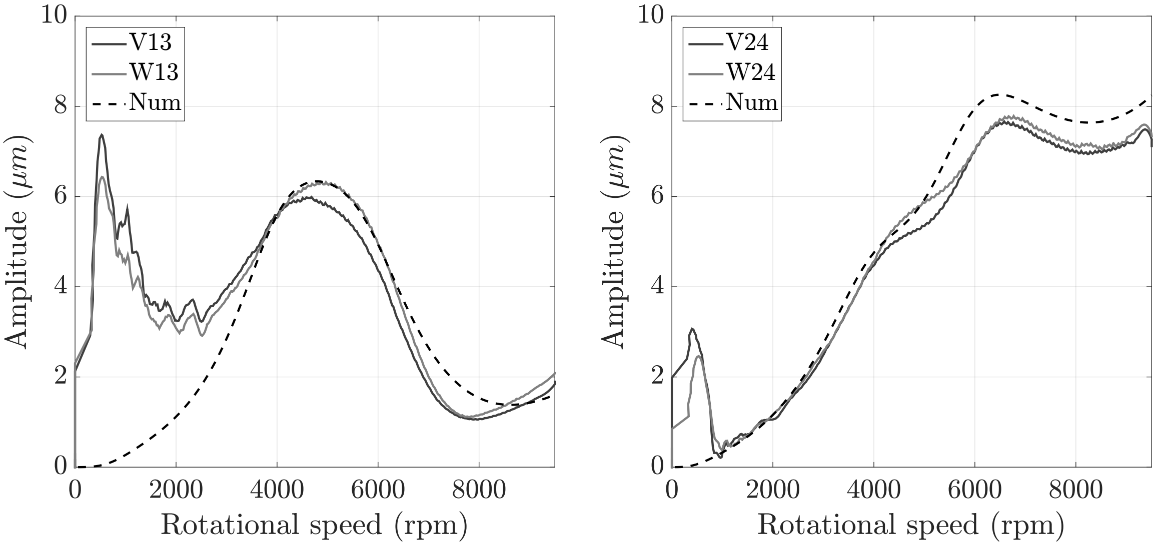

(a) Unbalance response - DE

(b) Unbalance response - NDE

Figure 4.10: Predicted (dotted lines) vs measured (solid lines) mass unbalance responses

The rotational speed was progressively increased with a rate of 50 rpm per seconds up to 9 500 rpm. AMBs are considered linear for these simulations since rotor displacements are expected to be small. In Figure 4.10, the evolution of the synchronous response is plotted. Trends are identical in terms of vibration amplitudes and frequency position of the rigid modes. The large vibration amplitudes revealed at low speed, particularly visible at DE side, are due to the electrical motor. Between 0 and 2 500 rpm, the motor was not able to produce a purely constant rotational speed. Therefore, the following tests were performed above 3 000 rpm.

4.2.2 Rotor drop at rest

The rotor is at rest and initially levitated by the AMBs. At 1 s, the AMBs are shut-down. The results of the measured and predicted drop responses are provided in Figure 4.11. The transient behaviour seems to be accurately described and the rotor displacements are comparable. The numerical model seems to bring less damping during the first rebounds. The cylindrical mode of the coupled rotor-TDB system sets-up around 1.04 s just after the transient rebounds, see Figure 4.11. The drop loads in normal direction are reported in Figure 4.12. The maximal loads are found at DE side with almost 370 N which is far from the static load capacity of the TDBs. The peaks appearing during the first rebounds are related to the complete crushing of the ribbon damper. It is worth mentioning that when the rotor stabilizes at the bottom of its TDBs, the contact loads at both DE and NDE tends to 30 N, which equals to the half of the rotor weight.

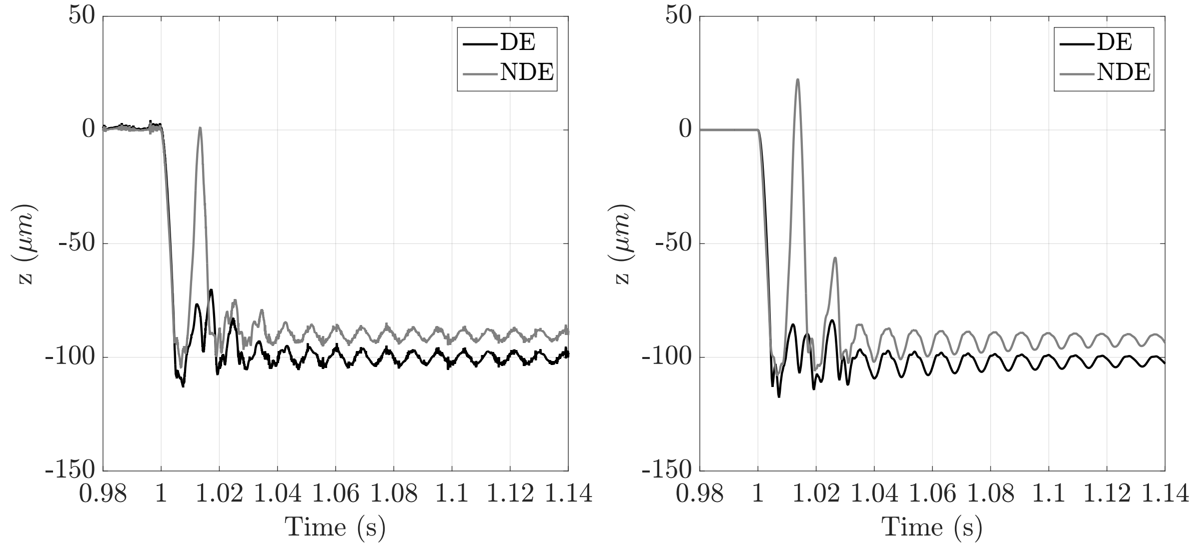

(a) Experimental results

(b) Numerical results

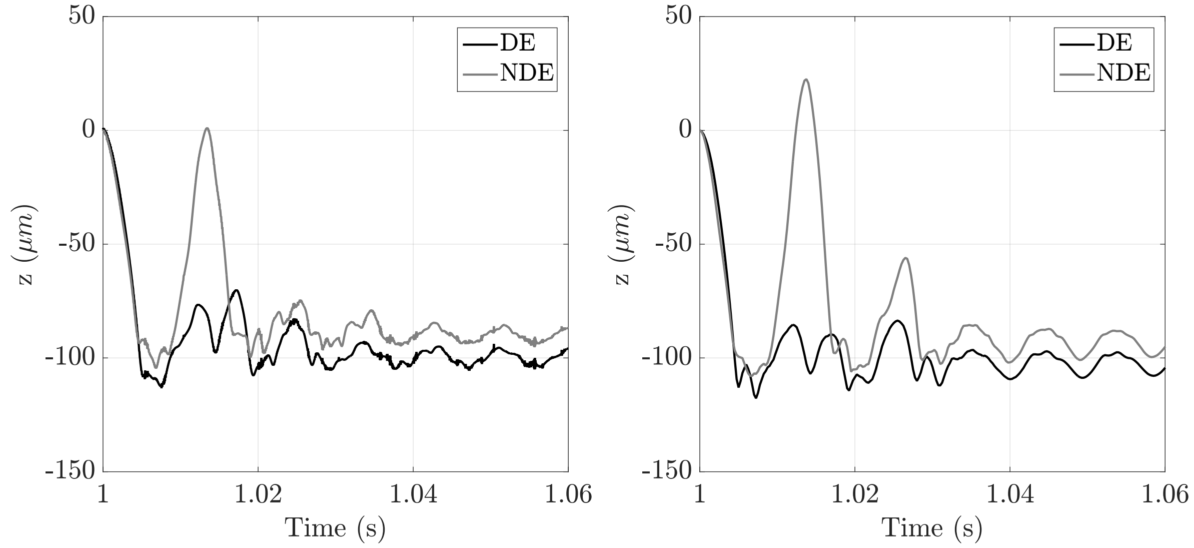

(c) Experimental results - zoom

(d) Numerical results - zoom

Figure 4.11: Measured (a,c) vs predicted (b,d) vertical rotor displacements - drop at rest

These preliminary tests were conducted to assess the numerical model ability to reproduce unbalance response and drop dynamics at rest. Considering the unbalance response, vibration amplitudes and the position of rigid modes are described well. The large vibrations found at the DE side, between 0 and 2 500 rpm, could comes from the electrical motor controller, which was initially tuned for the shaft used by Defoy [137] that had a lower rotational inertia. In future research, the PI controller could be adapted to the considered design. Considering the rotor drop at rest, the numerical model gives similar results and the estimation of the TDB and ribbon properties can be considered satisfactory. The remaining small discrepancies may be attributable to the nonlinear behaviour of the ribbon as explained in the previous chapter. The larger damping generated in experiences visible during the first rebounds could be related to a

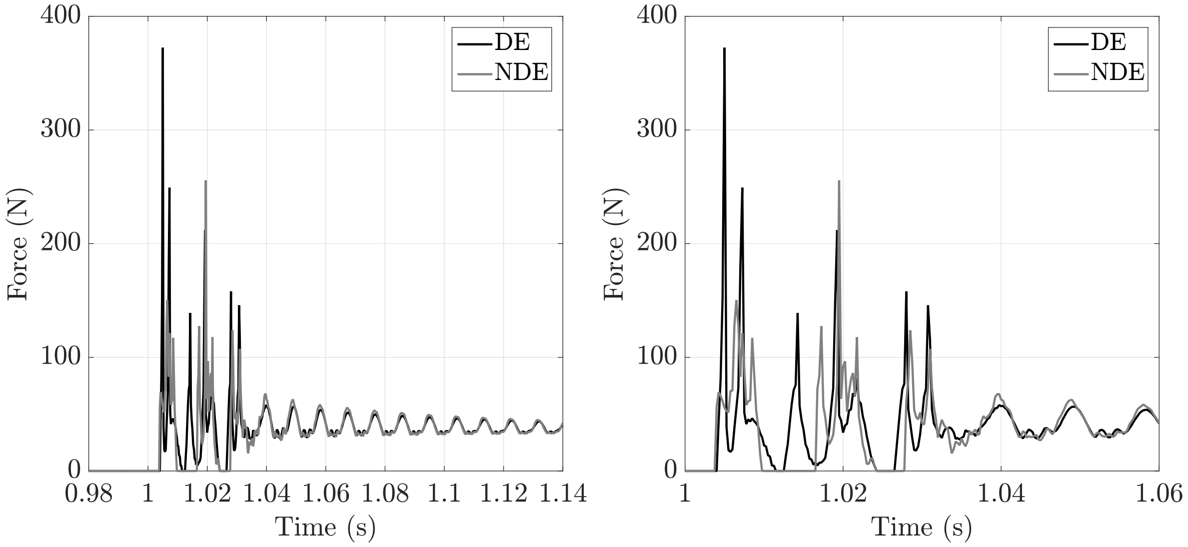

(a) Numerical results (b) Numerical results - zoom

Figure 4.12: Predicted normal contact loads - drop at rest

slip state of the ribbon bumps. Once the transient passed, these bumps may remain in the stuck position, generating low damping. In the following subsections, the dynamics of the academic rotor-AMB system subjected to different kinds of base motions are investigated.

4.3 Test configurations

The tests were carried out in vertical translation of the Cube™, "Zcube" in Figure 4.9, by using harmonic and impulse excitations. The Table 4.7 summarizes the performed tests.

Table 4.7: Test matrix

	Frequency (Hz)	**Acceleration (G)**	**Rotational speed (rpm)**	**Duration (s)**
Harmonic	20	0.1 to 1.1	Standstill	5
Harmonic	20	0.1 to 1.1	3 000 to 9 500	$\sim$ 100
Impulse	50	0.5 to 3.1	9 500	$\sim$ 40

For all the configurations tested, the same level of mass unbalance was applied; 32 g.mm at 0° with respect to the tachometer TDC. The security alarm usually shut-down the rotor-AMB system when rotor displacement exceeds the absolute value of 75 μm. This threshold was set to 200 μm to permit nonlinear contact analysis.

4.3.1 Harmonic tests

Considering harmonic tests, the support motion is a 20 Hz sine translation ranging from 0.1 to 1.1 G. The chosen frequency ω and amplitude are representative of energetic earthquake bandwidth, as explained by Matsushita *et al.* [7] or large industrial supports structural response. It also corresponds to the smallest dynamic stiffness of the studied academic rotor-AMB system; it represents the best frequency range to exhibit TDB contact phenomena. Two cases are studied: standstill and spinning levitated rotors. The first permits the system assessment for cases where no unbalance nor gyroscopic forces are present. The linearity of the magnetic restoring forces as well as the capacity of the controller to maintain the rotor in contact situations can be discussed. The shaker quickly reaches the acceleration instruction and 5 s of signals are recorded. Figure 4.13 shows an example of the measured acceleration level for the 0.3 G case.

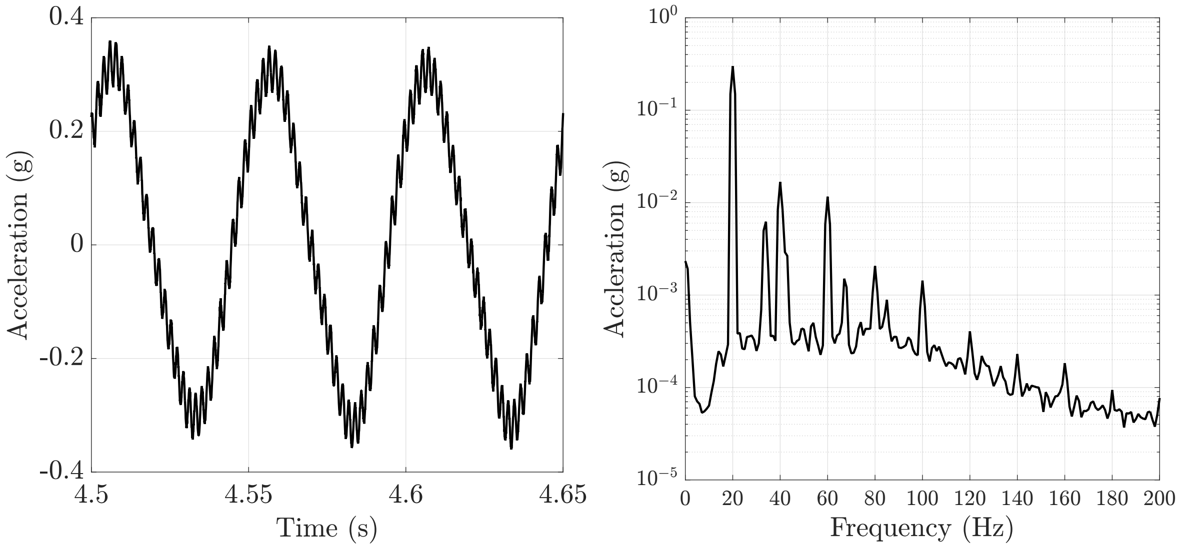

(a) 3 periods

(b) Spectral content

Figure 4.13: Measured base acceleration (Zcube) in time (a) and frequency (b) domain - 0.3 G at 20 Hz - non-rotating shaft

A zoom in the range [4.5-4.65]s is provided as well as the spectral content. The signal is not purely sinusoidal; the second and third harmonics of the fundamental base motion frequency are present. During operations, the shaker generates unavoidable operating frequencies; a 35 Hz component and its second harmonic as well as a 513 Hz component, which is due to the opening and closing of the high pressure valves providing the injection of oil in hydraulic actuators. Then, three rotational speeds Ω, covering the operating speed range, were tested; 3 000, 6 000 and 9 500 rpm. The TDB friction effects and dry whip instabilities are of particular interest. In order to smoothly trigger rotor-TDB contact, the acceleration level targeted by the shaker is set-up progressively enabling reduced overshoot. The procedure lasted almost 30 s. Once reached, the shaker motion was maintained for approximately 40 s to catch potential onset of nonlinear dynamic regimes. Figure 4.14 shows an example of the measured acceleration level for the 1.1 G case.

As for the 0.3 G case, the signal is not purely sinusoidal and the same shaker operating frequencies are present. After 40 s, the shaker stop is also recorded to analyse the controller

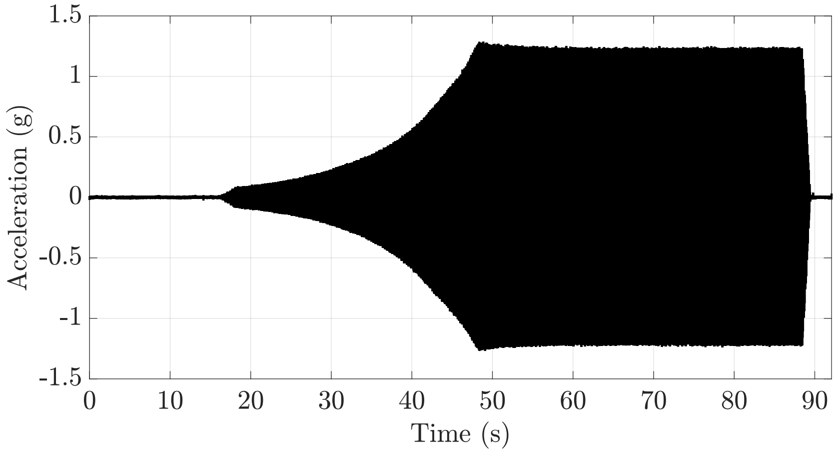

Figure 4.14: Measured base acceleration (Zcube) - 1.1g at 20 Hz - rotating shaft

capacity to recentre the rotor.

4.3.2 Impulse tests

Impulse tests were also realised. It is well-known that the onset conditions of contact can lead to complete different rotor dynamic behaviours. Lingener [77] or Bartha [9] were particularly interested in applying shock on the rotor triggering quasi-instantaneously dry whirl. Here, the impulse comes from the base.

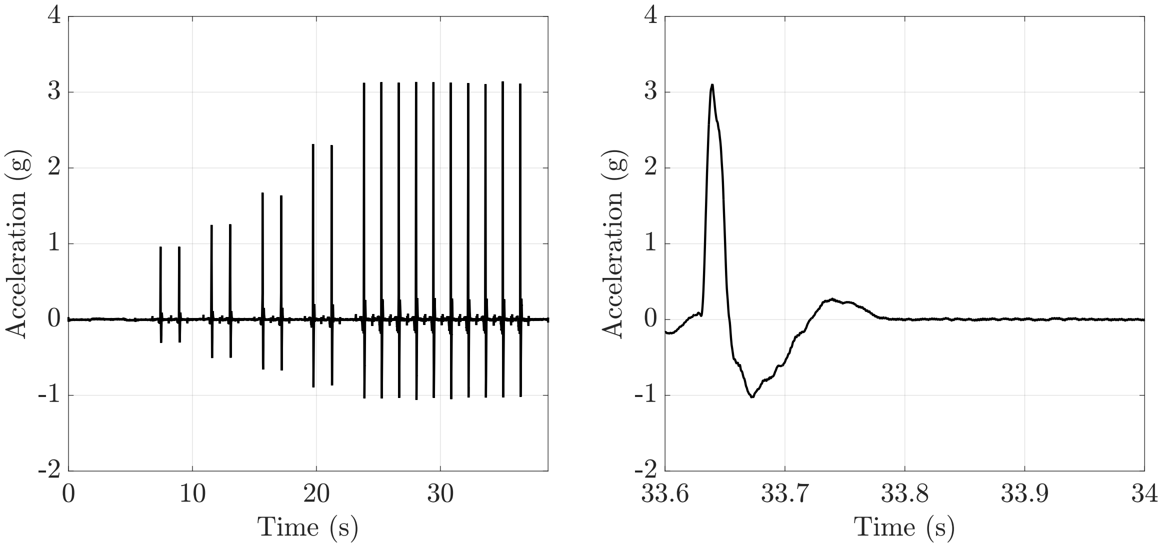

(a) Complete shock test

(b) Zoom on one shock

Figure 4.15: Measured repeated shocks of the base (Zcube) - 3.1 G at 50 Hz

The shock lasted 0.02 s (50 Hz) and the instruction ranges from 0.5 to 3.5 G. Once the acceleration instruction reached, ten shocks were repeated each second. It is noteworthy that these instructions were never fully reached; 3.5 G required gave 3.1 G measured. In what follows, the level of acceleration will refer to the one measured on the shaker for more consistency. In what follows, impulse frequency refers to the impulse duration rather than repeatability. This test are representative of the effects of large waves crashing on the hull of a boat (FPSO for example). The instruction was achieved after several shocks and once reached, ten successive impulses were generated by the shaker. Only full speed tests are detailed here. Figure 4.15 shows the base acceleration for the 3.1 G impulse test.

4.4 Numerical and experimental investigations - harmonic tests

In the following subsections, the numerical and experimental investigations considering harmonic tests are performed. Measured and predicted results are presented. The accelerations recorded on the shaker are injected in the numerical model.

4.4.1 Linear behaviour and stability

This subsection is devoted to the analysis of the linear behaviour of the system. The 0.3 G case enables assessment of the AMB linearity considering a standstill rotor: almost the half of the TDB clearance is consumed without exhibiting any contact nonlinearities.

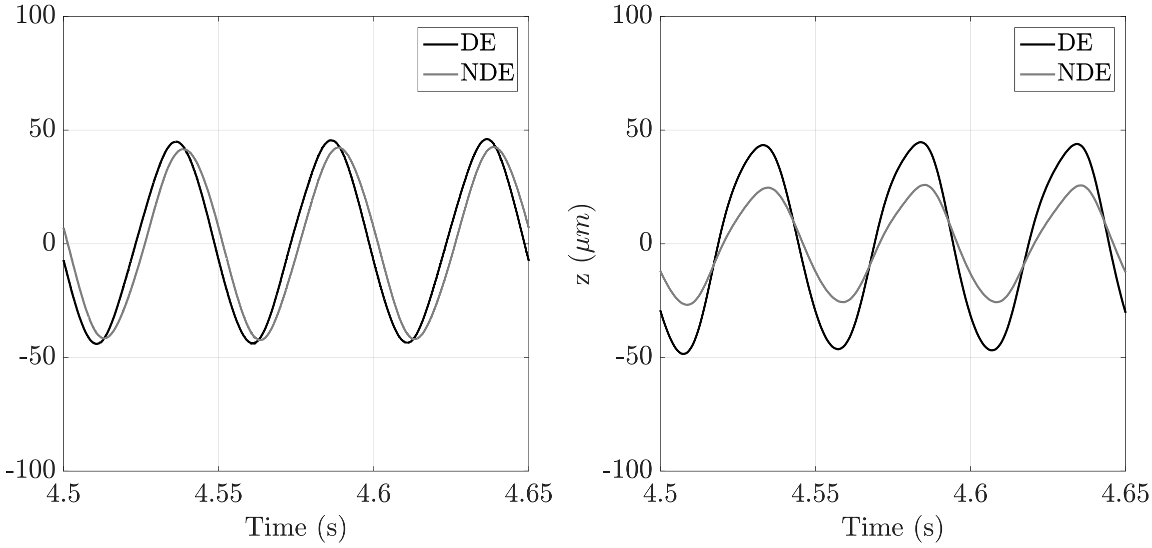

(a) Experimental results

(b) Numerical results

Figure 4.16: Measured (a) vs predicted (b) vertical rotor displacements - 0.3 G at 20 Hz

The measured and predicted rotor vertical displacements at both DE and NDE subjected to a 0.3 G base acceleration considering a standstill rotor are plotted in Figure 4.16. As the signal between [0-5]s is harmonic, a zoom on the range [4.5-4.65]s provides an insight on three periods. The predicted rotor vertical displacements are close to measures in terms of amplitude

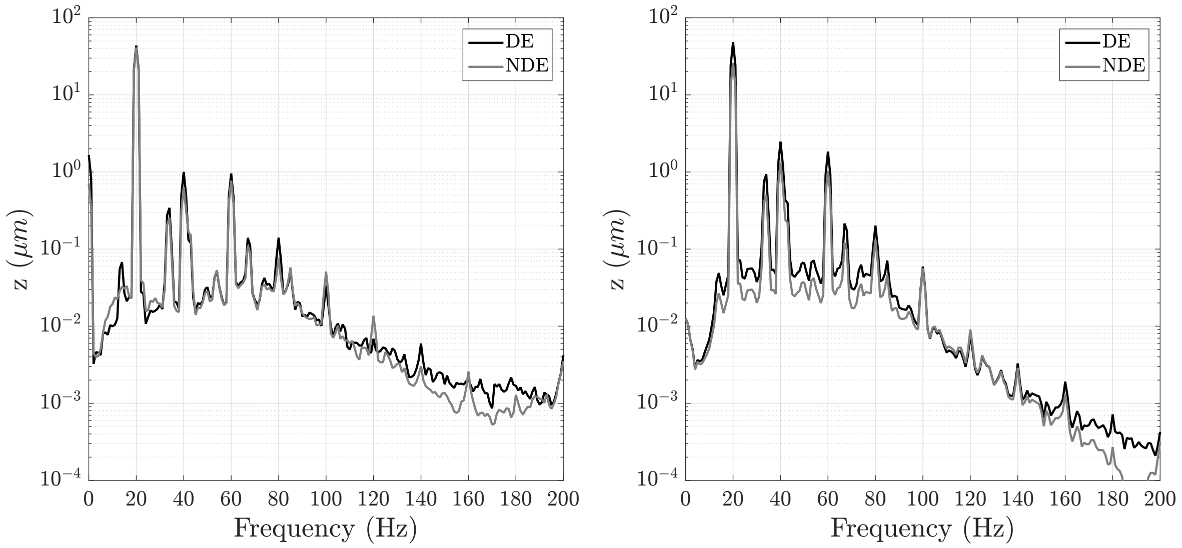

(a) Experimental results (b) Numerical results

Figure 4.17: Measured (a) vs predicted (b) spectral contents of the vertical rotor displacements - 0.3 G at 20 Hz

at DE side. The predicted and measured spectral contents of the vertical rotor displacements are close, as shown in Figure 4.17. No particular instabilities are generated by the shaker operating frequencies. The top currents for each action line are reported in Figure 4.18. The latter are small and far from amplifier saturation. The predicted static and control currents are close to those measured.

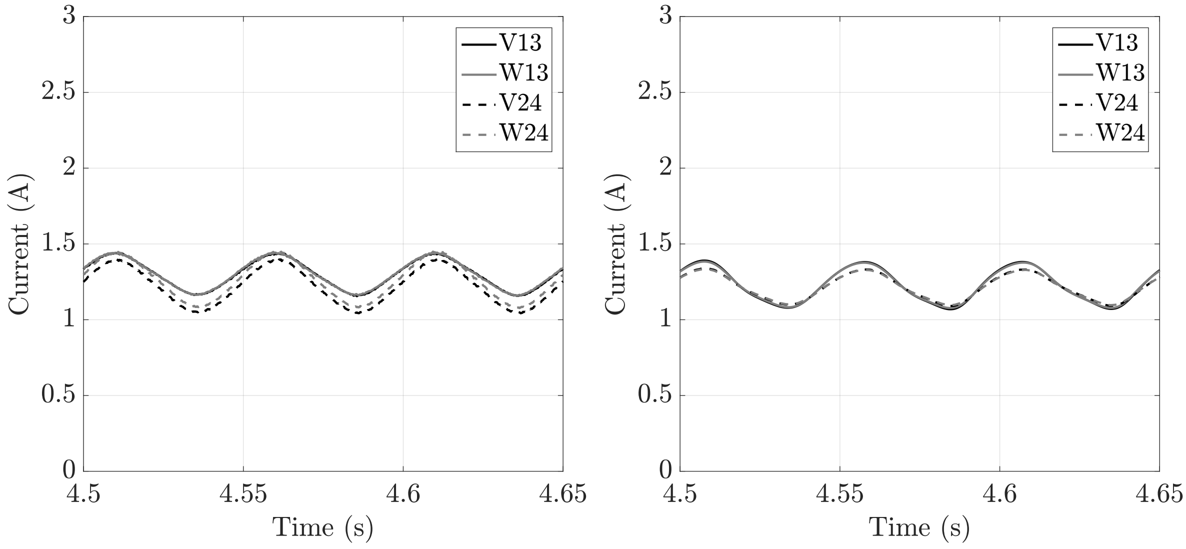

(a) Experimental results (b) Numerical results

Figure 4.18: Measured (a) vs predicted (b) top currents - 0.3 G at 20 Hz

The magnetic force linearity is assessed using the relative deviation surface described in Chapter 2. The results for the 0.3 G case are plotted in Figure 4.19.

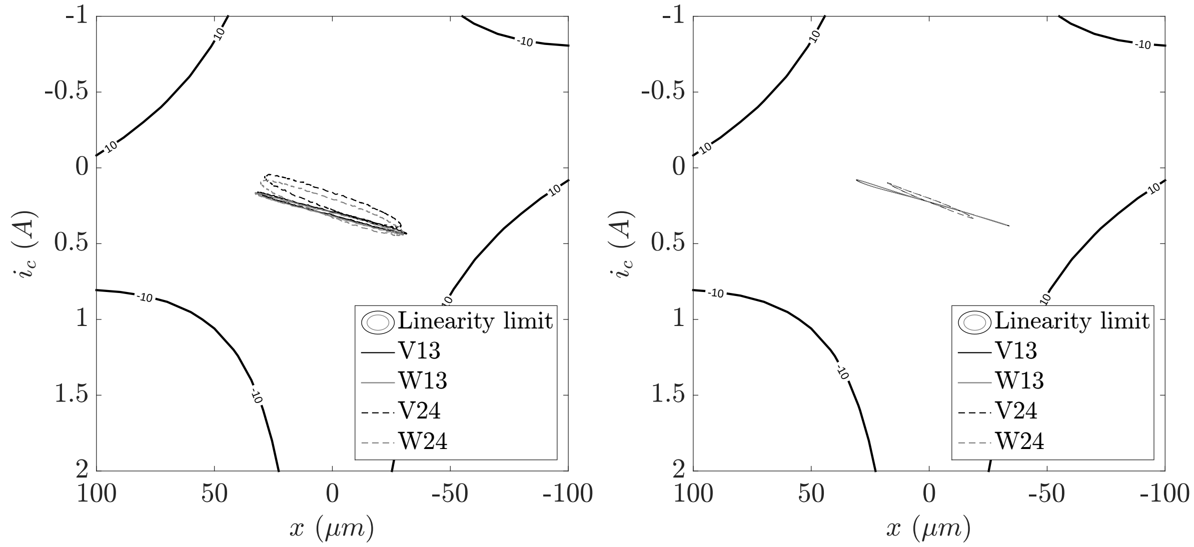

(a) Experimental results

(b) Numerical results

Figure 4.19: Measured (a) vs predicted (b) linearity limit - 0.3 G at 20 Hz

The magnetic restoring forces remain in their linear range for both experimental and numerical results. The control current i_c is related to the applied magnetic force; these figures are close to force-deflection curves and hysteresis loops can be distinguished.

Two remarks can be made:

- The slopes are identical for both the measured and predicted control currents vs displacements plots revealing a good estimation of the magnetic “stiffnesses”.

- The inner surfaces of each loop are larger in experimental results, especially at the NDE side which may indicate a different damping generated by AMBs.

To sum-up, the numerical model is able to reproduce the overall dynamics of the system. The AMBs remain stable and in a linear range considering small base acceleration level. No particular sensibility to the shaker operating frequencies was exhibited. The discrepancies in terms of rotor displacements, current amplitude and phase, visible especially at the NDE side, are expected to be due to some differences between the numerical and the experimental AMB transfer functions.

Figure 4.20 and Table 4.8 present the maximal predicted and measured rotor vertical displacements and the maximal predicted contact loads for the different acceleration level tested at both DE and NDE sides. It is shown that the DE predictions are close to those measured, while some discrepancies are found at the NDE side. The TDB contacts appear between 0.5 and 0.7 G.

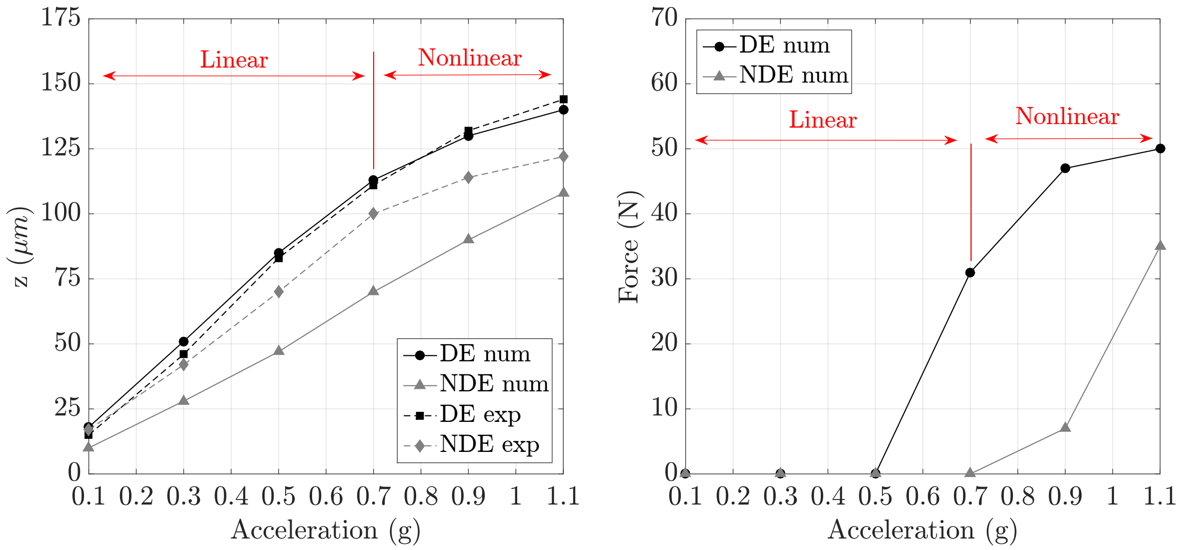

(a) Max rotor displacements (b) Max normal contact loads

Figure 4.20: Measured and predicted maximal vertical rotor displacements (a) and predicted maximal contact loads (b) vs support acceleration - harmonic test

Table 4.8: Predicted vs measured maximal rotor displacements in vertical direction and the relative deviations

			0.1 G	**0.3 G**	**0.5 G**	**0.7 G**	**0.9 G**	**1.1 G**
Max displ (μm)	**DE**	Exp	15	46	83	111	132	144
		Num	18	51	85	113	130	140
		Dev.	20%	11%	2%	2%	-2%	-3%
	NDE	Exp	17	42	70	100	114	122
		Num	10	28	47	70	90	108
		Dev.	-41%	-33%	-33%	-30%	-21%	-11%
Max load (N)	**DE**	Num	0	0	0	31	47	50
	NDE	Num	0	0	0	0	7	35

4.4.2 Nonlinear behaviour and stability

This subsection is devoted to the analysis of the contact effects on the AMB stability and the linearity of magnetic forces is assessed. To achieve clarity, a standstill rotor was considered since no mass unbalance forces are generated. The 1.1 G case is investigated to analyse clearly visible contact effects. The predicted and measured vertical displacements for a standstill rotor subjected to a 1.1 G base acceleration are plotted in Figure 4.21.

The model seems to be able to predict accurately the rotor displacements. The dotted lines represent the estimated TDB clearances, the effects of contact are clearly visible for both the numerical and experimental results. The rotor vertical motions are flattened at both DE and NDE sides. The effects of contact are less visible on the predicted rotor displacements at NDE side. Small oscillations appear when the rotor contacts the bottom of the TDBs and may corre-

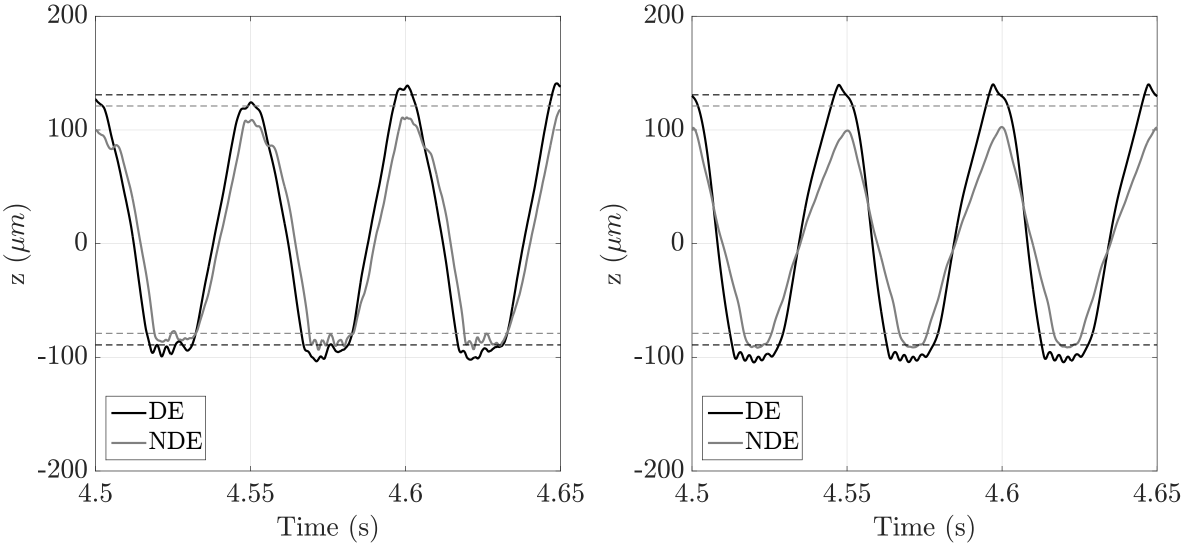

(a) Experimental results

(b) Numerical results

Figure 4.21: Measured (a) vs predicted (b) vertical rotor displacements (solid lines) and TDB clearances (dotted lines) - 1.1 G at 20 Hz

spond to the contribution of the coupled rotor-TDB modes. The predicted rotor deflections are plotted in Figure 4.22. The red points represent the position of the nodes while black and grey circles are the TDBs at DE and NDE respectively. A non-contacting and a contacting case, corresponding to the time 4.508 s and 4.522 s in Figure 4.21, are presented; the rotor bends during contact and the minimal displacement reaches -125 μm while it reaches -100 μm at TDB level.

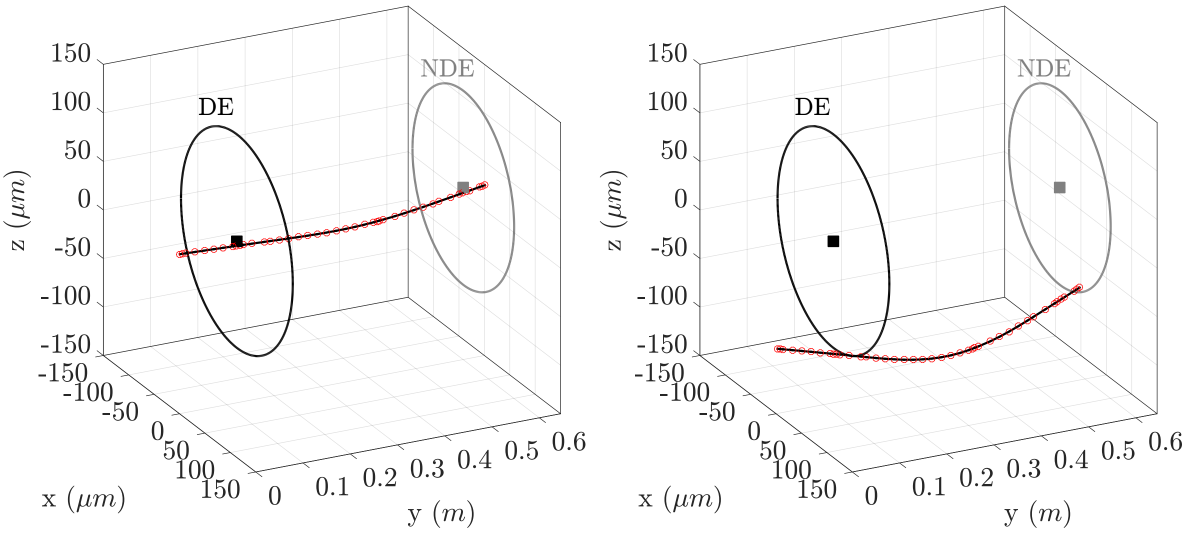

(a) Without contact - 4.508 s

(b) With contact - 4.522 s

Figure 4.22: Predicted rotor deformed shapes with (a) and without (b) contact - 1.1 G at 20 Hz

The predicted and measured spectral contents are plotted in logarithmic scale in Figure 4.23. The rotor response is multiharmonic due to the nonlinear contact effects. Both the exper-

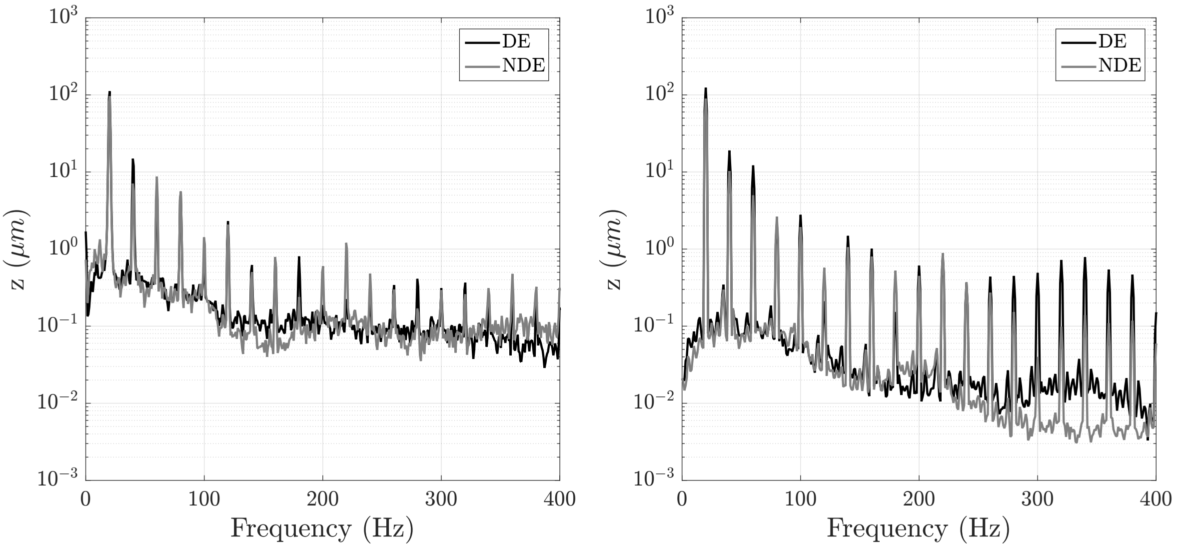

(a) Experimental results (b) Numerical results

Figure 4.23: Measured (a) vs predicted (b) spectral content of the vertical rotor displacements - 1.1 G at 20 Hz

imental and numerical results are close and exhibit superharmonics of the 20 Hz fundamental frequency. Although the coupled rotor-TDB modes were not considered for the design of the PID controller, the AMBs remain stable and the predicted vs measured top currents are given in Figure 4.24. The effects of contact are clearly visible on the generated currents. Predictions are close to measurements especially at the DE side.

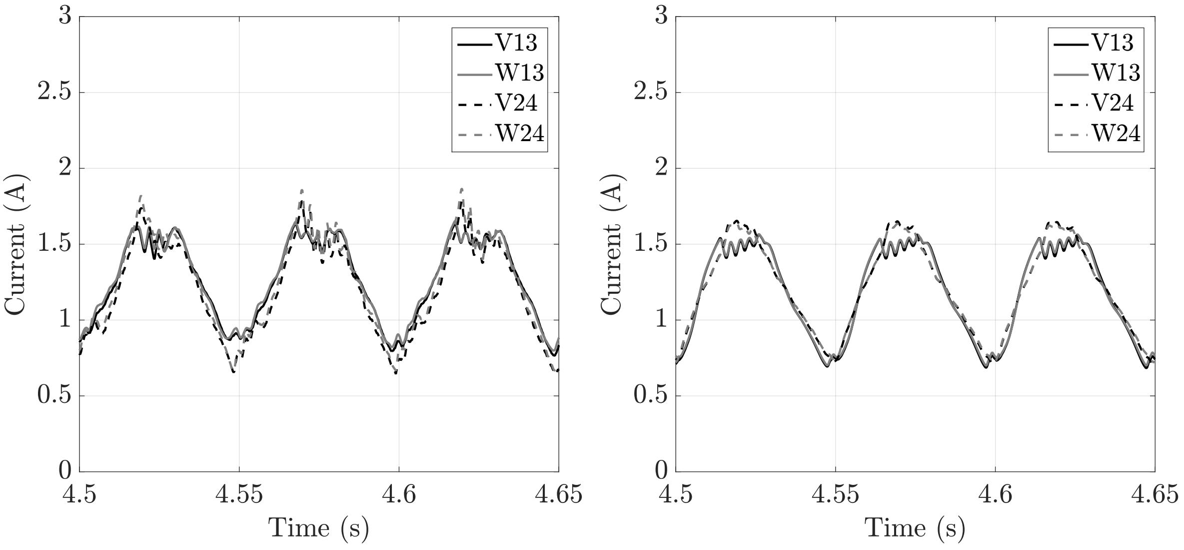

(a) Experimental results (b) Numerical results

Figure 4.24: Measured (a) vs predicted (b) top currents - 1.1 G at 20 Hz

When the rotor exceeds the TDB clearance, loads are shared between AMBs and TDBs. The predicted normal contact loads are given in Figure 4.25; they are small in comparison with those generated during a rotor drop at rest, see Figure 4.12; the base motion effects are mainly counteract by magnetic forces. Moreover, the ribbon damper is not fully crushed; the ball bearing, comprising a much higher stiffness, is lightly loaded. The oscillations due to the excitation of the coupled rotor-TDB modes are visible on the contact loads.

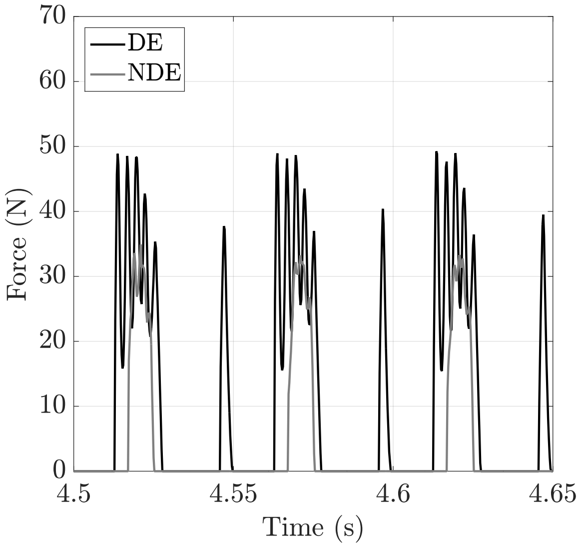

Figure 4.25: Predicted normal contact loads - 1.1 G at 20 Hz

The linearity limit of magnetic forces is assessed using the relative deviation surface. The results for the 1.1 G case are plotted in Figure 4.26.

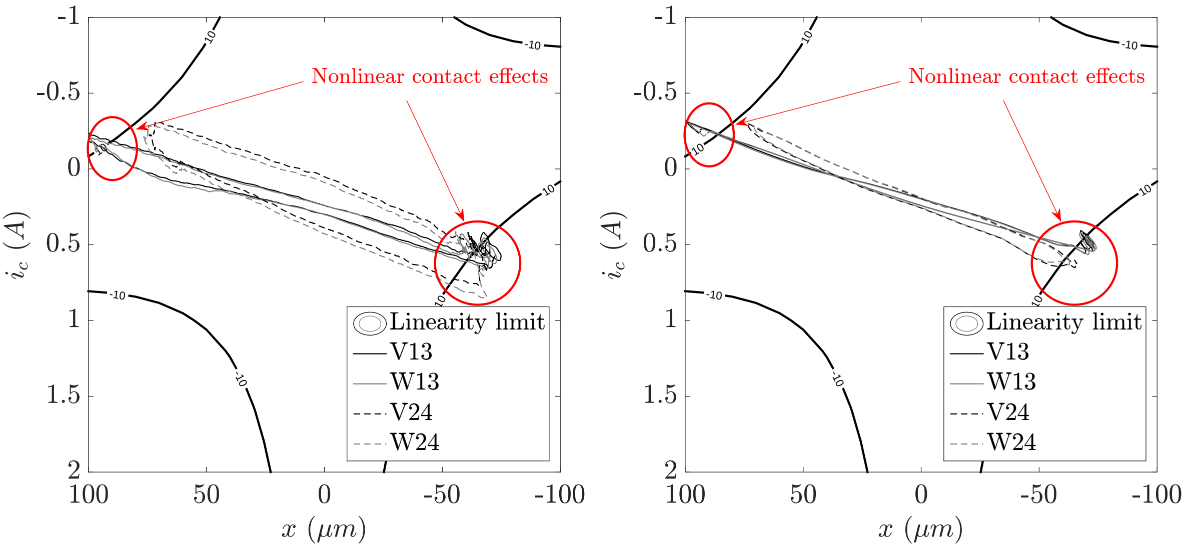

(a) Experimental results

(b) Numerical results

Figure 4.26: Measured (a) vs predicted (b) linearity limit - 1.1 G at 20 Hz

The linearity limit of the magnetic force seems to be reached; nonlinear effects are clearly visible in Figures 4.26(a) and 4.26(b) at each extremities and these effects are due to rotor-TDB contact; the magnetic linearity limit is almost reached when the rotor contacts the TDBs; the limit of 10% is slightly exceeded, meaning that the nonlinearity is weak.

To sum-up, the numerical model is able to reproduce the observed phenomena. The PID controller remained stable during these nonlinear contact events and was able to maintain the rotor in levitation. The external base motion effects are shared between the AMBs and TDBs almost preventing the appearance of magnetic nonlinearities (restoring force and amplifier saturation). Three comments can be done according to these observations:

- Considering the academic test rig used in this research project, the TDB-to-AMB clearance ratio is close to 0.25 preventing the rotor from large displacements and magnetic nonlinearities. Considering industrial turbomachinery designs, this ratio is usually close to 0.5; stronger nonlinearities may be exhibited in this case.
- For excitations in the direction of action lines, typically 45° with respect to the vertical axis, stronger magnetic nonlinearities may be generated.
- The coupled rotor-TDB modes are excited during contact while the related frequencies are not considered in the PID design. However, the rotor-AMB system remained stable. An explanation on that particular point could be that the ribbon generates enough damping to avoid controller instabilities. Moreover, the contact loads remain quite small for the considered acceleration level and are alternative (two contacts per period).

For all of the following tested cases, amplifier saturation was never observed. For the sake of consistency, the nonlinear magnetic restoring force are used since the linearity limit previously fixed at 10% was slightly exceeded.

4.4.3 Sliding friction effects

This subsection is devoted to the analysis of the tangential friction force effects induced by the contact on the rotor-AMB system response. The 1.1 G test cases enable the friction effects to be analysed since all the rotational speeds (3 000, 6 000, 9 500 rpm) were tested for this acceleration level. The 6 000 rpm case is further presented in this subsection. First, the results are analysed for the whole test duration then, a zoom on three periods provides better insights into the involved phenomena. Figure 4.27 shows the predicted and measured rotor displacements in vertical direction for a shaft rotating at 6 000 rpm and subjected to a progressively increased acceleration of the shaker up to 1.1 G. The base motion starts close to 10 s and contact is generated close to 35 s. The measured vertical responses seem to be described qualitatively well by the numerical model. The controller manages the unbalance forces combined with base motions and TDB contacts. Once the shaker stops, the rotor quickly recovers its centred position in both predictions and measures.

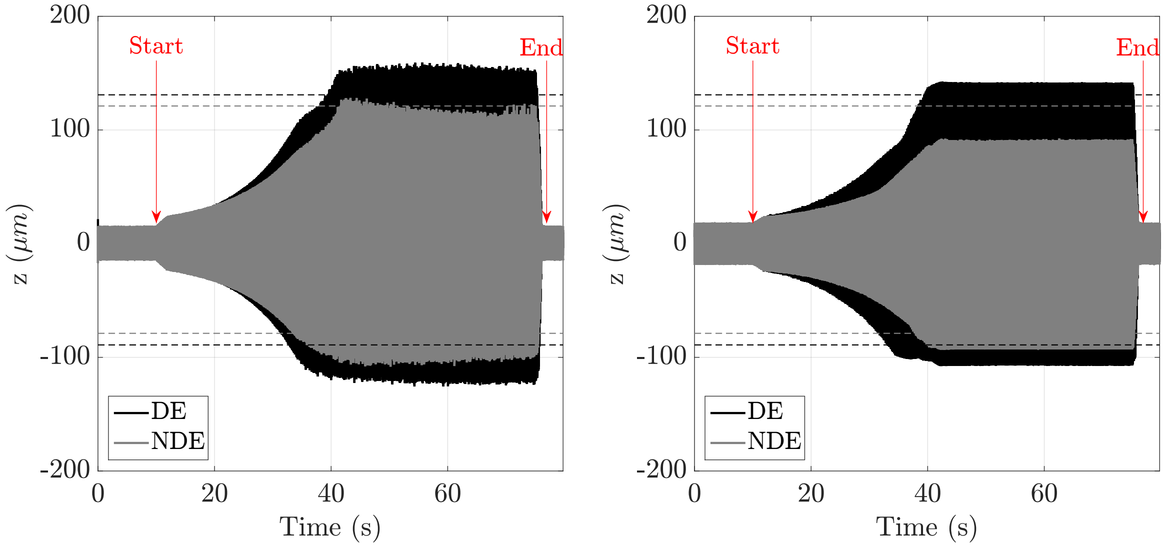

(a) Experimental results

(b) Numerical results

Figure 4.27: Measured (a) vs predicted (b) vertical rotor displacements (solid lines) and TDB clearances (dotted lines) - 6 000 rpm and 1.1 G at 20 Hz

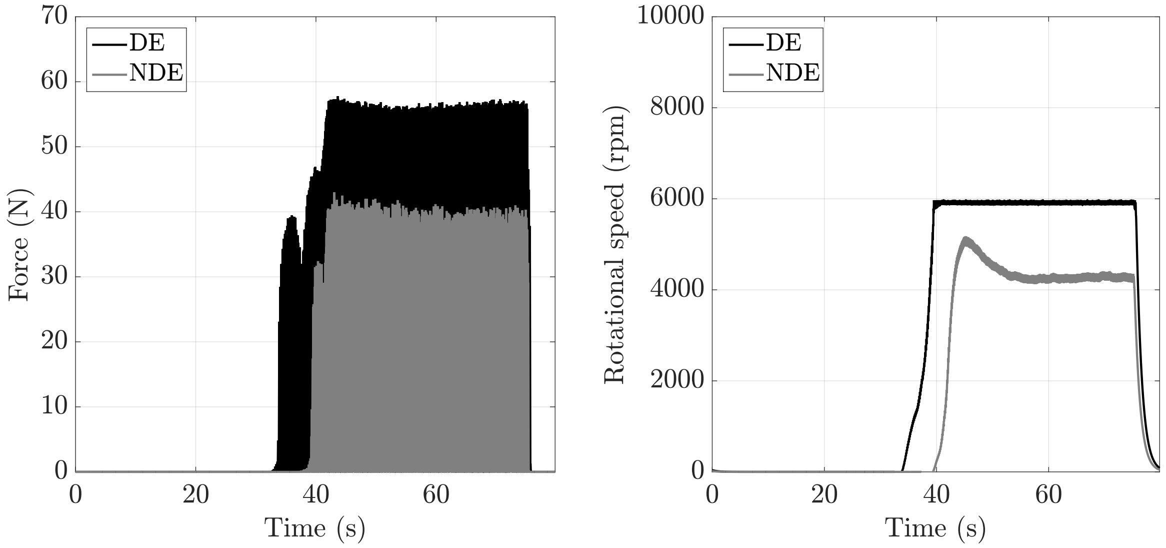

(a) Normal contact loads

(b) TDB rotational speed

Figure 4.28: Predicted normal contact loads (a) and predicted TDB rotational speeds (b) - 6 000 rpm and 1.1 G at 20 Hz

The contact loads are given in Figure 4.28(a). Vertical amplitudes are quite identical compared with the non-rotating case. The differences are due to the mass unbalance responses at each bearings generated for the related rotational speed. TDBs are driven in rotations by the friction contact with the rotor and results are given in Figure 4.28(b). The predicted contact loads at NDE side seem not to be sufficient to drive the TDBs to full speed on this side.

Figures 4.29 and 4.30 provide a zoom in the range [60.7-60.85]s on the predicted and measured vertical and horizontal rotor displacements respectively: the results are close in both these

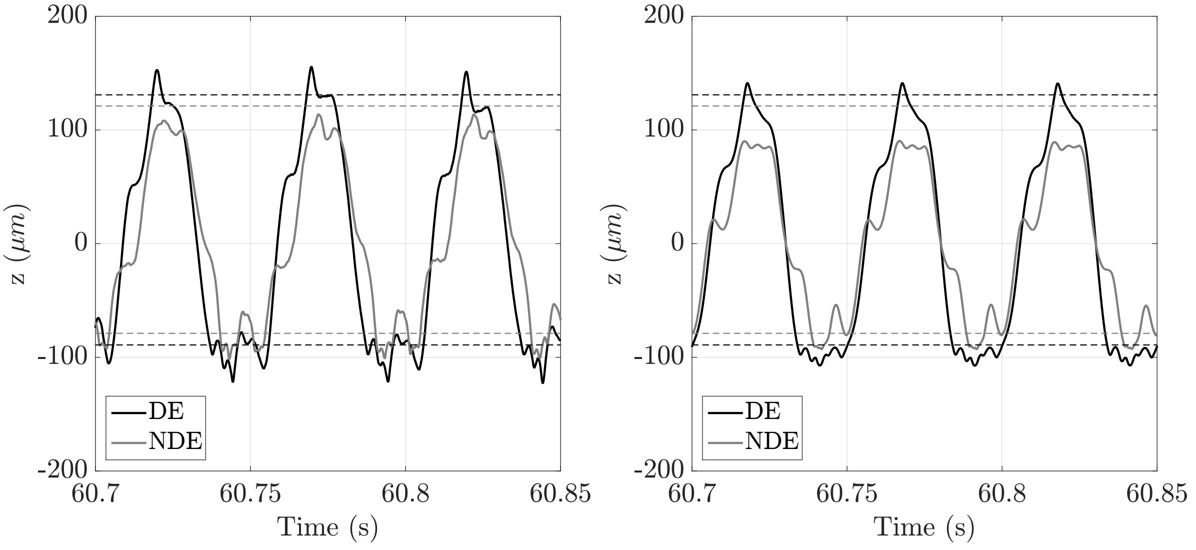

(a) Experimental results

(b) Numerical results

Figure 4.29: Measured (a) vs predicted (b) vertical rotor displacements (solid lines) and TDB clearances (dotted lines) - 6 000 rpm and 1.1 G at 20 Hz

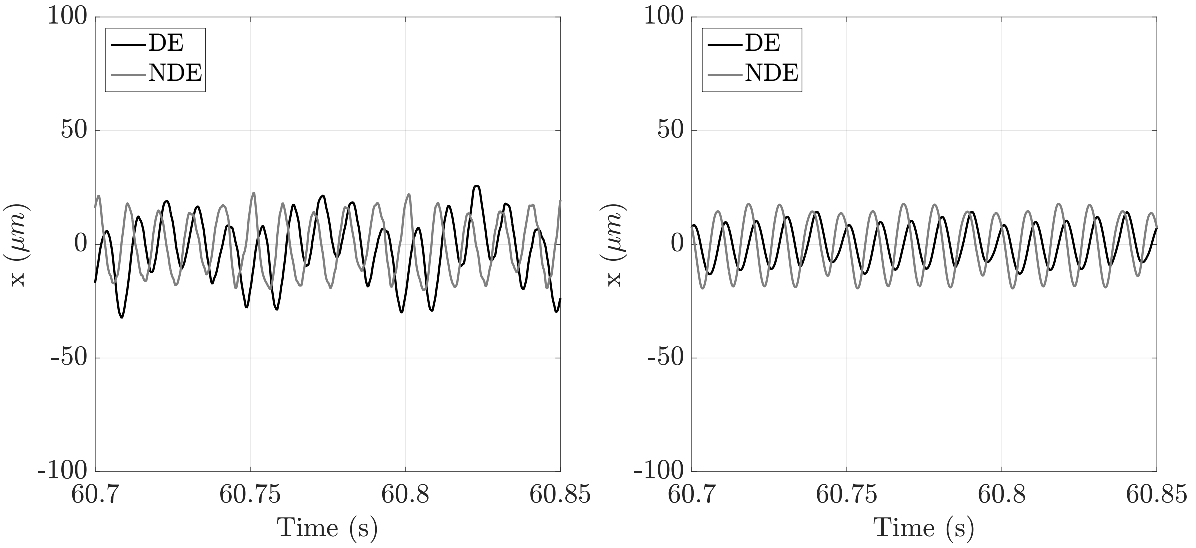

(a) Experimental results

(b) Numerical results

Figure 4.30: Measured (a) vs predicted (b) horizontal rotor displacements (solid lines) and TDB clearances (dotted lines) - 6 000 rpm and 1.1 G at 20 Hz

directions. It seems that friction effects are weak due to small contact forces. The effects of contacts are visible in x-direction and a nonlinear periodicity is set-up. The TDB spin speed is a good indicator to estimate the sliding friction effects, but no measure of the TDB spin speed was available.

Figure 4.31 shows the predicted TDB speed at DE and NDE sides and the evolution of the friction coefficient in the range [60.7-60.85]s. The tangential contact load effects are clearly visible; when the rotor touches the TDB, a severe rotational speed increase is observed inducing

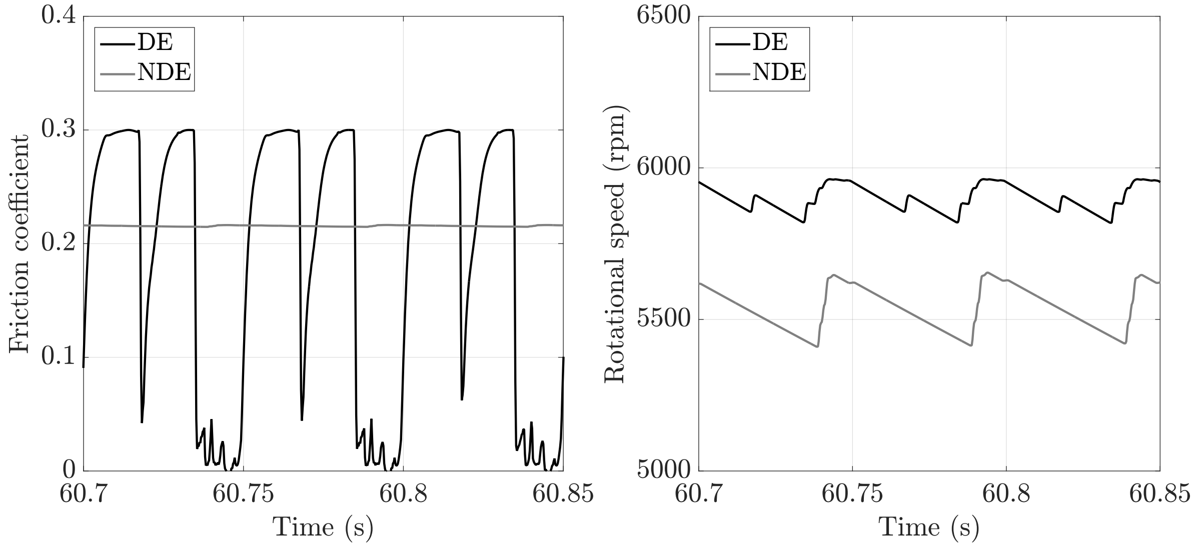

(a) Evolution of the friction coefficient

(b) TDB rotational speed

Figure 4.31: Predicted friction coefficient (a) and TDB rotational speeds (b) - 6 000 rpm and 1.1 G at 20 Hz

a rapid decrease of the friction coefficient, especially at DE side. The NDE TDB does not reach the rotor full speed since contact is generated only one time per period (bottom contact) inversely to the DE side, where two contacts per period are generated. The tangential loads are then more able to fully drive the TDB at the DE side. Moreover, it is noteworthy that the dry friction coefficient (0.3) appears between each contact since the relative velocity is very close to zero in contrast with the NDE side where the latter remains close to the dynamic value (0.2).

To sum-up, the predicted and measured rotor displacements are in good agreement. No dry whip instabilities or dangerous friction effects were noticed during these tests. It seems that the effects of sliding friction are weak due to small contact loads but also due to the TDB spin-up. During contact, the friction coefficient is strongly reduced at DE side. The horizontal dynamics generated by the contact is visible in both experimental and numerical results and is due to radial contact effects and misalignments. These observations were found for all the rotor speeds tested. The AMBs remain stable and the rotor was quickly recentred after the shaker stops.

4.4.4 On-board rotor nonlinear features

This subsection provides insights into on-board rotor features. Especially, the combined effects of mass unbalance and base motion loads for a linear case (0.3 G) and a nonlinear case (1.1 G); with or without contact, respectively. Different tested speeds are employed. Orbit plots are used in this subsection and the last ten periods according to the base motion frequency are provided. The predicted and measured orbits of the rotor subjected to 0.3 G base acceleration are respectively plotted in Figures 4.32, 4.33 and 4.34 running at 3 000, 6 000 and 9 500 rpm.

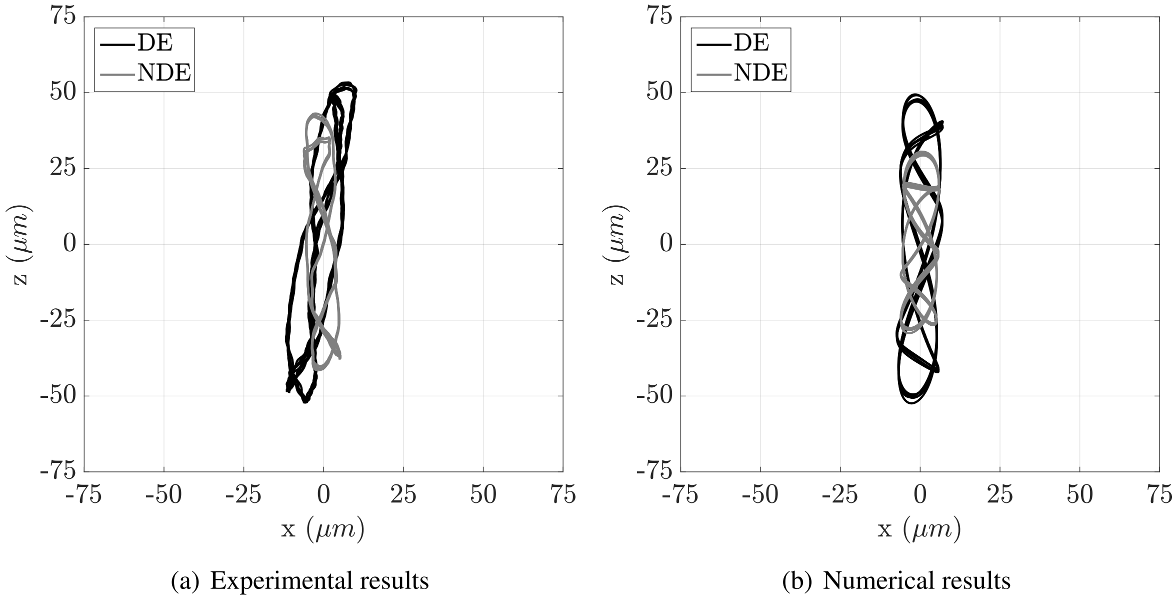

(a) Experimental results (b) Numerical results

Figure 4.32: Measured (a) vs predicted (b) rotor orbits - 3 000 rpm and 0.3 G at 20 Hz

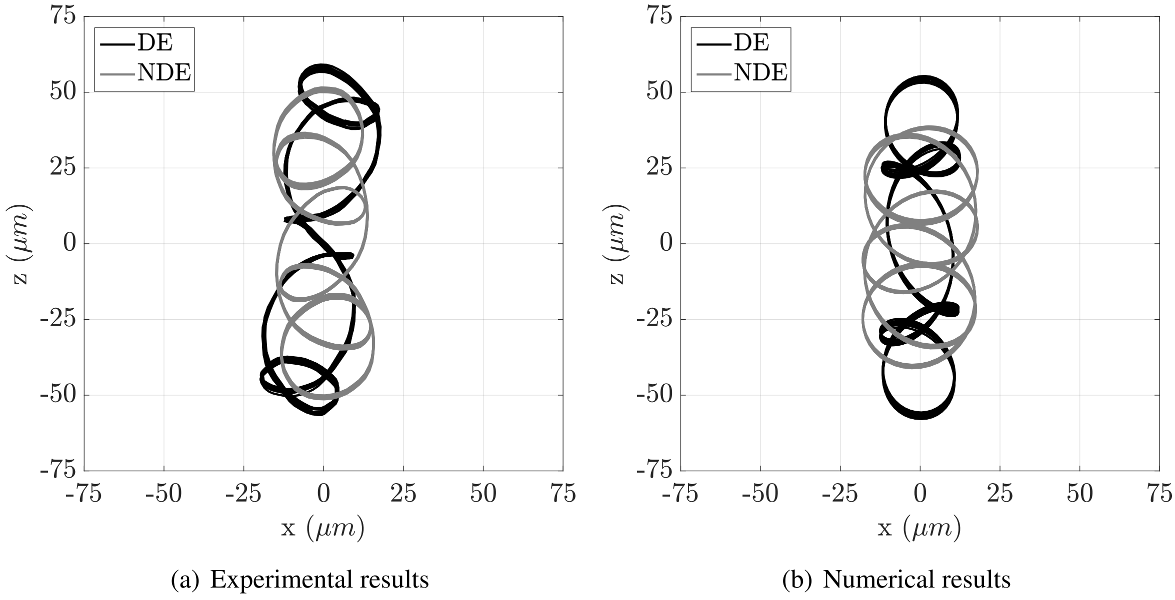

(a) Experimental results (b) Numerical results

Figure 4.33: Measured (a) vs predicted (b) rotor orbits - 6 000 rpm and 0.3 G at 20 Hz

Predicted and measured orbits are close and typical combinations of vertical base motion and unbalance forces are exhibited. As explained by Driot *et al.* [4], when the ratio n between the base frequency ω and the rotational speed Ω is an integer, particular orbits are found. This also true when this ratio n is a rational generating more complicated orbits.

$$\omega = \frac{\beta}{\chi}\Omega = n\Omega \tag{4.1}$$

where β and χ are integers. For the case where Ω equals 3 000 rpm and 6 000 rpm, the ratio n is rational and equals $\frac{2}{5}$ and $\frac{1}{5}$ respectively; orbits are periodic for these two cases. When Ω

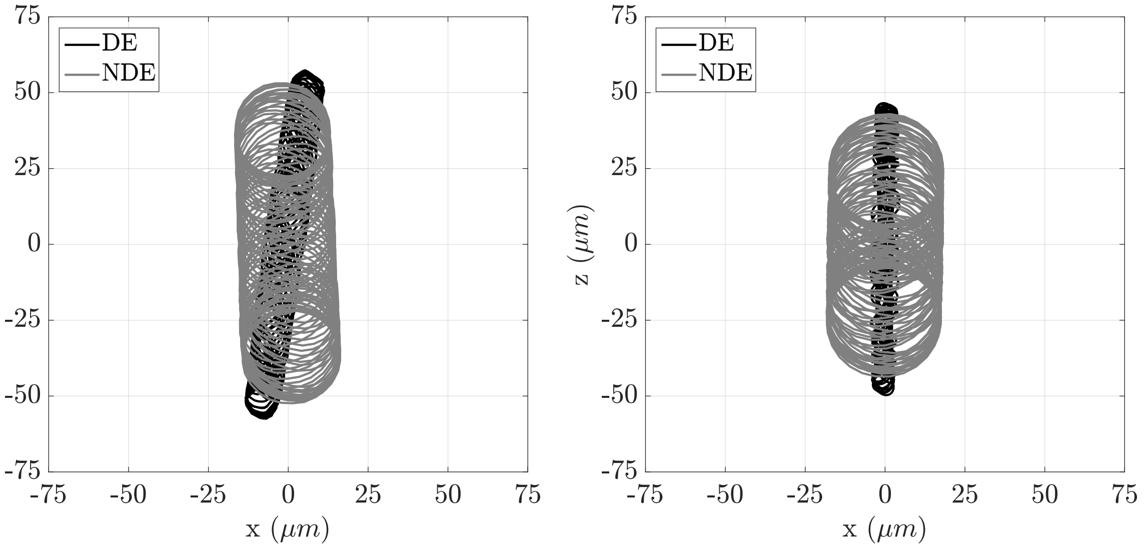

(a) Experimental results

(b) Numerical results

Figure 4.34: Measured (a) vs predicted (b) rotor orbits - 9 500 rpm and 0.3 G at 20 Hz

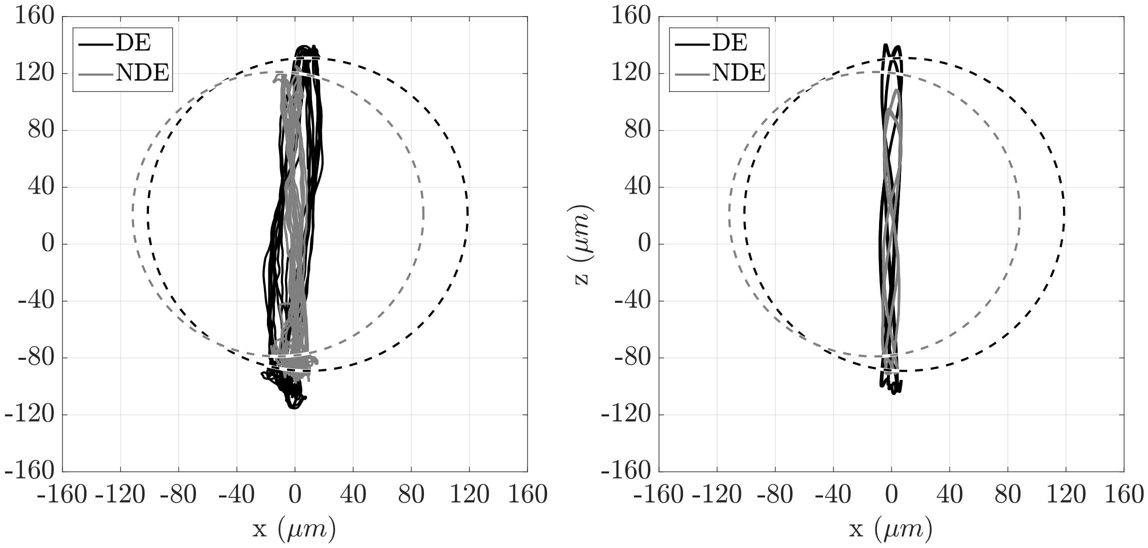

(a) Experimental results

(b) Numerical results

Figure 4.35: Measured (a) vs predicted (b) rotor contacting orbits - 3 000 rpm and 1.1 G at 20 Hz

equals 9 500 rpm, orbits are quasi-periodic since the ratio *n* is ordinary. Table 4.9 summarizes these results.

The predicted and measured orbits of the rotor subjected to 1.1 G base acceleration are respectively plotted in Figures 4.35, 4.36 and 4.37 running at 3 000, 6 000 and 9 500 rpm. Predicted and measured orbits are close and typical combinations of vertical base motion, unbalance and contact forces are exhibited. The periodicity of orbits is conserved with respect to the non-contacting case. Orbit shapes are flattened and the rotor has mainly forward whirl

Table 4.9: Orbits periodicity

	3 000 rpm	**6 000 rpm**	**9 500 rpm**
β	2	1	20
χ	5	5	158
n	rational	rational	ordinary
Orbit	periodic	periodic	quasi-periodic

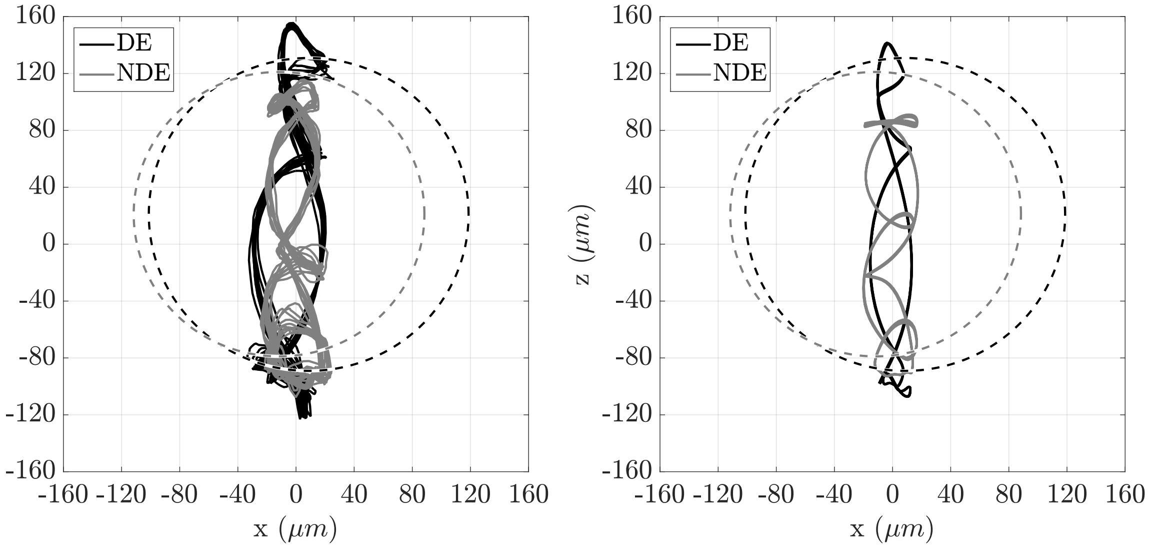

(a) Experimental results (b) Numerical results

Figure 4.36: Measured (a) vs predicted (b) rotor contacting orbits - 6 000 rpm and 1.1 G at 20 Hz

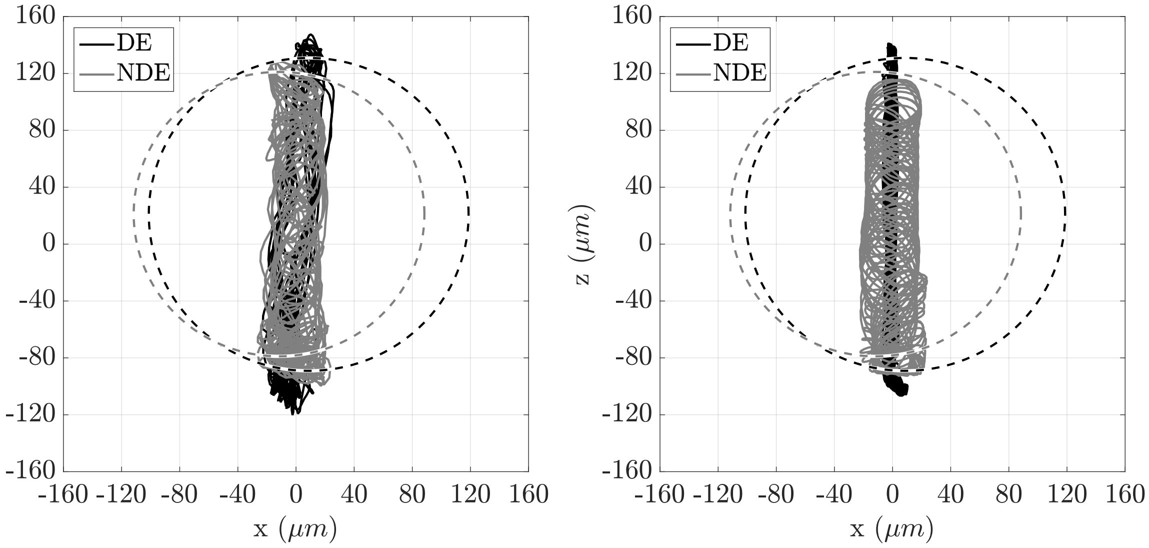

(a) Experimental results (b) Numerical results

Figure 4.37: Measured (a) vs predicted (b) rotor contacting orbits - 9 500 rpm and 1.1 G at 20 Hz

orbits, indicating weak sliding friction effects, as concluded in the previous subsection.

To sum-up, the model is able to correctly describe the combination of base motion and mass unbalance, generating complex orbits. The latter may be periodic or quasi-periodic depending on the base frequency over the rotational speed ratio. Considering acceleration level leading the rotor to contact TDBs, the orbit periodicities are conserved and their shapes are flattened with respect to the non-contacting case. Measured orbits are slightly titled and this may be related to some small discrepancies in the proximity sensor sensitivity.

4.4.5 Spectral content

The analysis of the spectral content gives further informations on the effects of contact. The previous test case, 1.1 G with a 6 000 rpm spinning shaft, is employed. Spectrograms are used to provide the time evolution of the frequency content of the rotor displacements. The NDE side is chosen since the mode shapes generate larger displacements on this bearing. The measured and predicted spectral contents of the rotor displacements in horizontal direction are plotted in Figures 4.38 and 4.39, respectively. The plots are composed of spectrograms and the average spectra (average along the time axis). The predicted and measured results are similar. Experimentally and numerically, the effects of contact are clearly highlighted, close to 30 s. The contact with TDBs excites a wide frequency bandwidth which includes the first three bending modes located close to 200, 580 and 1 140 Hz. Gyroscopic effects split these frequencies into forward and backward whirl modes; this is visible especially for the second and third bending modes. The level of response of these modes is, however, small.

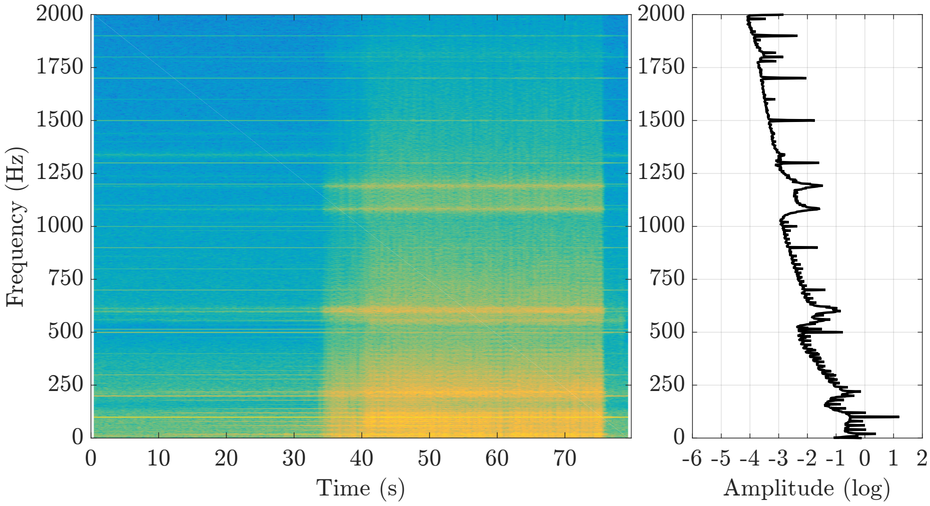

Figure 4.38: Measured NDE spectrogram and average spectrum in horizontal direction - 6 000 rpm and 1.1 G at 20 Hz

To sum-up, the predicted and measured spectral contents are close. The contact excites all the rotor structural modes and generates multi-harmonic responses. The global measured energetic level of vibrations is higher than the predicted one since the acceleration signals are filtered

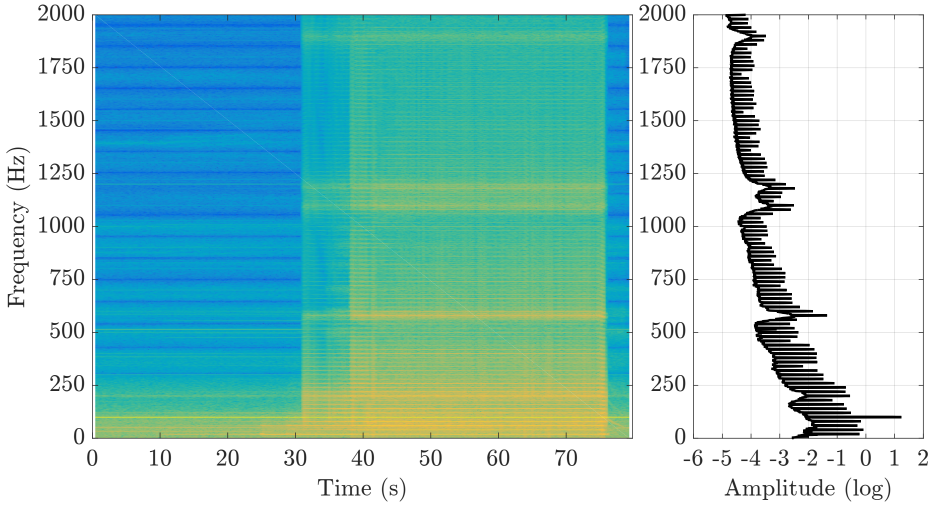

Figure 4.39: Predicted NDE spectrogram and average spectrum in horizontal direction - 6 000 rpm and 1.1 G at 20 Hz

before being implemented in the model. Moreover, the vibrations coming from the foundation are not considered in the numerical model since the support is assumed to be infinitely rigid.

4.5 Numerical and experimental investigations - impulse tests

In the following subsections, the numerical and experimental investigations considering impulse tests are performed. As for the harmonic case, the accelerations recorded on the shaker are implemented in the model.

Figure 4.40 and Table 4.10 provide the predicted and measured maximal rotor displacements (absolute value) and the maximal predicted contact loads for the different accelerations tested. Predictions are close to measurements. From 1 G, the rotor reaches the TDBs and the maximal displacement is flattened. From 1.9 G, a change of slope is observed in Figure 4.40(a) at the DE side: the rotor rebound height is larger, in absolute value, than the displacement related to the maximal acceleration level. This is seen in the following sections. From 1.4 G, the ribbon is fully crushed during contact at the DE side and this is the reason for this change of slope in contact loads, exhibited in Figure 4.40(b). The analysis for a non-contacting and contacting case considering a standstill rotor as well as the spectral content are not provided in this section since the same conclusion can be drawn with respect to harmonic tests.

The 3.1 G case combined with a 9 500 rpm full-speed rotor is further investigated in the next subsections.

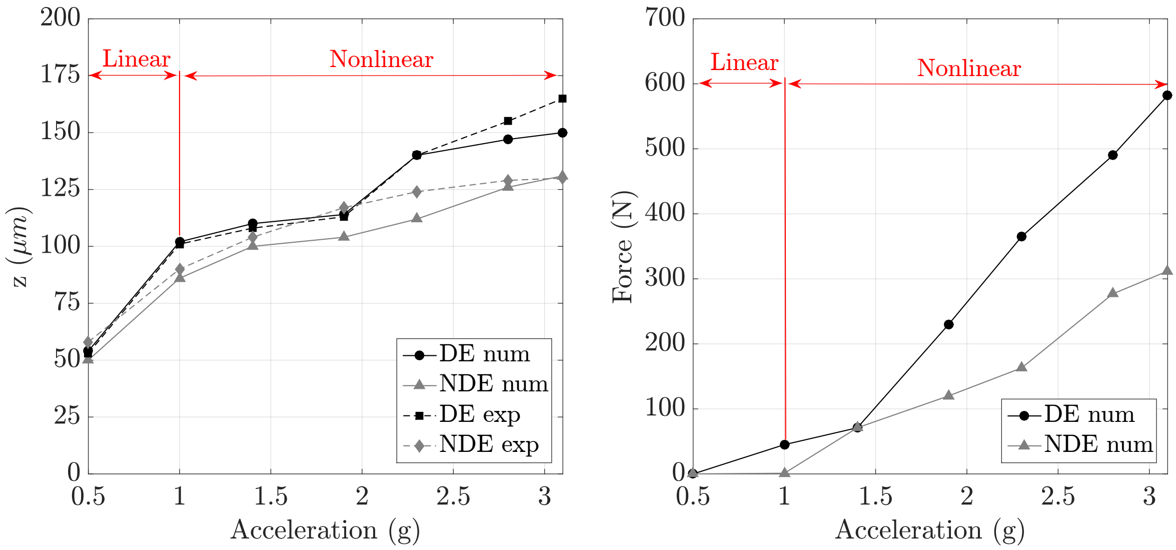

(a) Max rotor displacements (b) Max normal contact loads

Figure 4.40: Measured and predicted maximal vertical rotor displacements (a) and predicted maximal contact loads (b) vs support acceleration - impulse test

Table 4.10: Predicted vs measured maximal rotor displacements in vertical direction and the relative deviations

			0.5 G	**1 G**	**1.4 G**	**1.9 G**	**2.3 G**	**2.8 G**	**3.1 G**
Max displ (μm)	**DE**	Exp	53	101	108	113	140	155	165
		Num	54	102	110	114	140	147	150
		Dev.	2%	1%	2%	1%	0%	-5%	-9%
	NDE	Exp	58	90	104	117	124	129	130
		Num	50	86	100	104	112	126	131
		Dev.	-14%	-4%	-4%	-11%	-10%	-2%	1%
Max load (N)	**DE**	Num	0	45	71	230	365	490	582
	NDE	Num	0	1	71	120	163	277	312

4.5.1 Nonlinear transient behaviour and stability

The predicted and measured vertical rotor displacements are presented in Figure 4.41. Generally speaking, numerical and experimental results are in good agreement. The predicted normal contact loads are given in Figure 4.42(a). The maximum values reach almost 600 N and 320 N at DE and NDE, respectively, and are related to the maximal acceleration level. During contact, the TDBs are driven in rotation and the predicted rotational speeds are plotted in Figure 4.42(b) at both DE and NDE sides. It seems that the latter never reach the rotor full speed. The currents remains in reasonable range (less than 2.2 A) for both measures and predictions up to 3.1 G.

To sum-up, predictions are close to measurements and no dangerous dry whip behaviours are triggered in both experimental and numerical results. The rotor is quickly recentred after each shock without generating established instabilities. The predicted loads are lower than the

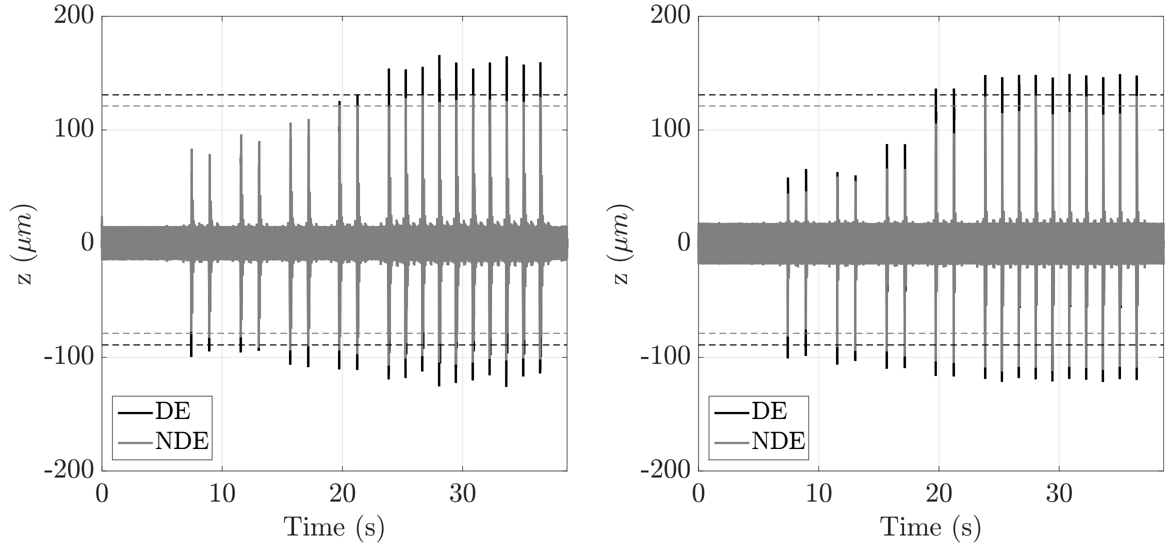

(a) Experimental results

(b) Numerical results

Figure 4.41: Measured (a) vs predicted (b) vertical rotor displacements (solid lines) and TDB clearances (dotted lines) - 9 500 rpm and 3.1 G at 50 Hz

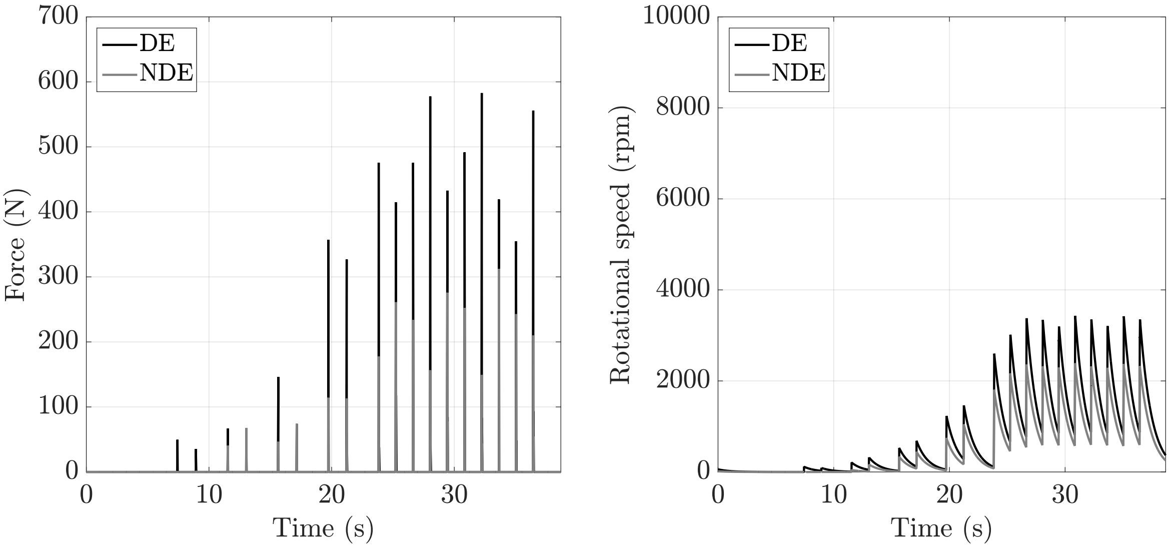

(a) Normal contact loads

(b) TDB rotational speed

Figure 4.42: Predicted normal contact loads (a) and TDB rotational speeds (b) - 9 500 rpm and 3.1 G at 50 Hz

bearing load capacity.

4.5.2 Sliding friction effects

This subsection is devoted to the analysis of the tangential friction force effects. Focus on the rotor response during a single contact gives further insights on nonlinear transient dynamics. Figure 4.43 provides the measured and the predicted rotor displacements during one impulse.

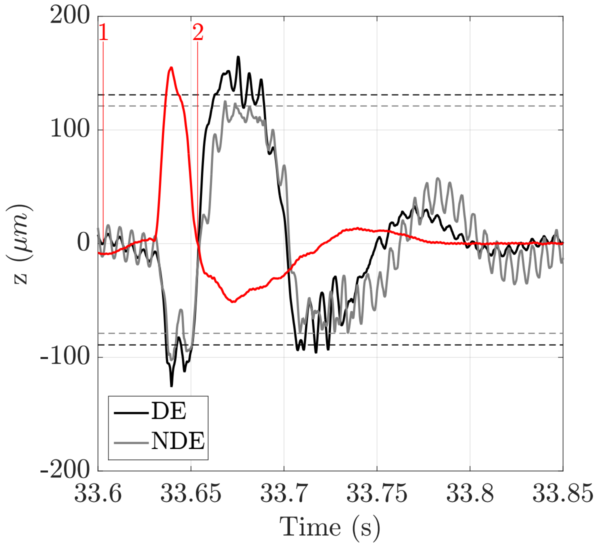

(a) Experimental results

(b) Numerical results

Figure 4.43: Measured (a) vs predicted (b) vertical rotor displacements (solid lines), TDB clearances (dotted lines) and acceleration profile (red lines) - 9 500 rpm and 3.1 G at 50 Hz

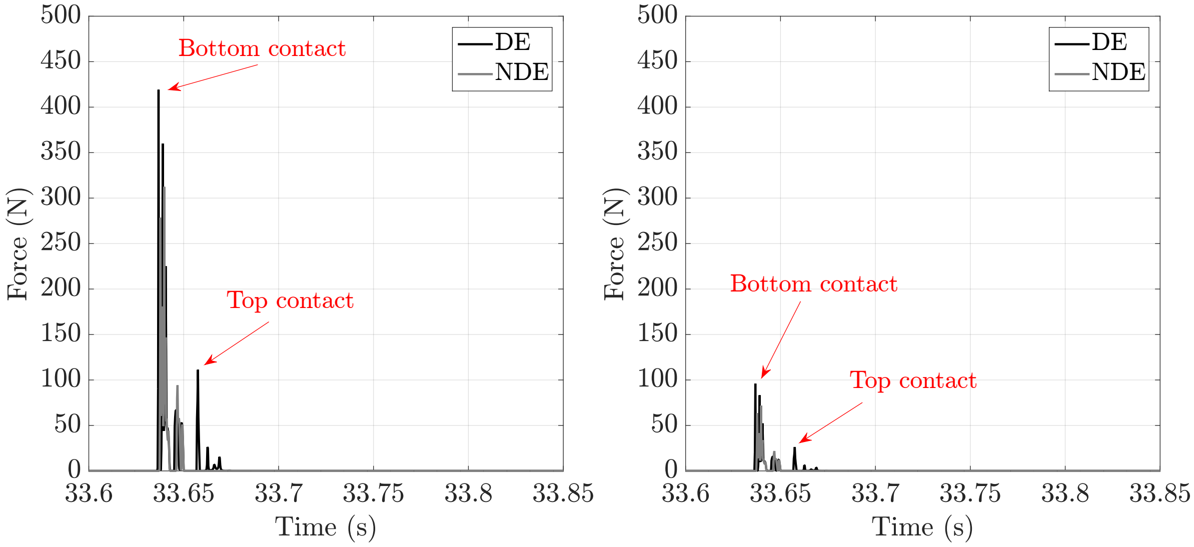

(a) Nomal contact loads

(b) Tangential contact loads

Figure 4.44: Predicted contact loads - 9 500 rpm and 3.1 G at 50 Hz

The acceleration profile is also plotted in red; the related values have no physical meanings, the maximum value being 3.1 G. Numerical and experimental results are close. It is shown that the vertical rotor rebound height, just after the first contact, is larger than the displacement related to the maximal acceleration level. This is observed in Figure 4.40 from 1.9 G, numerically and experimentally; this is due to vertical misalignments. The measured rotor rebounds, in Figure 4.43, show that for one base shock, three successive contacts are generated while two are predicted. Figure 4.44 provides the predicted contact loads at both DE and NDE sides. It is

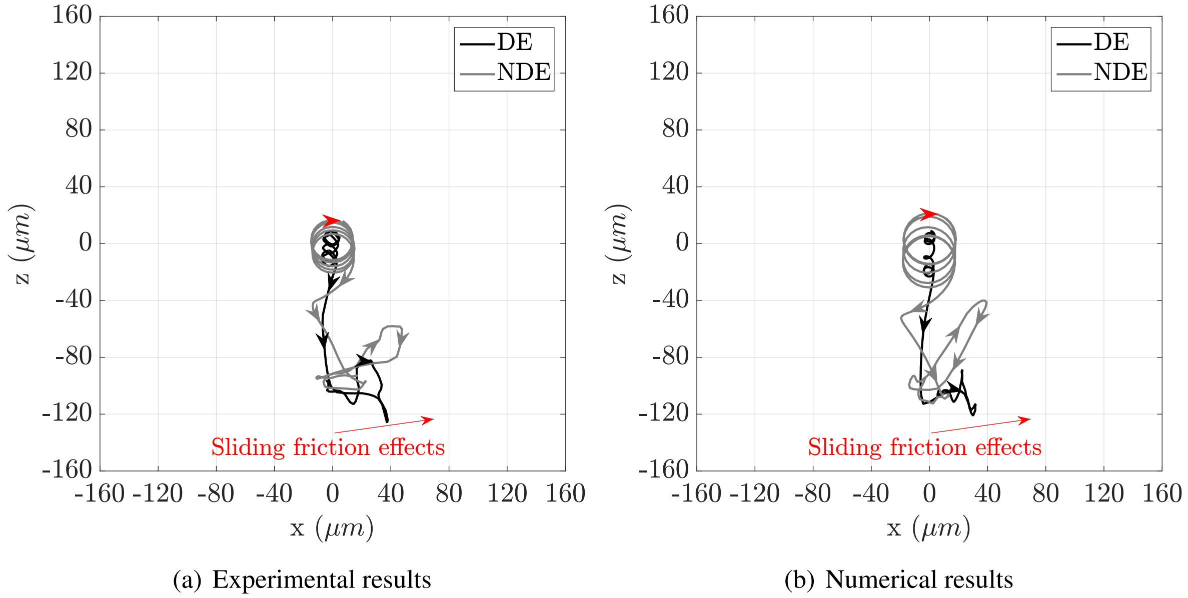

(a) Experimental results

(b) Numerical results

Figure 4.45: Measured (a) vs predicted (b) rotor orbits - 9 500 rpm and 3.1 G at 50 Hz

shown that the maximal force is generated when the acceleration of the support is maximal. The second contact, at the TDBs top, is almost four times smaller. The predicted friction coefficient is not shown since it remained almost constant; even if the TDBs are driven in rotation during contacts, they are far to reach the rotor full-speed as previously shown in Figure 4.42(b). The friction coefficient is then the dynamic one, close to 0.2. The effect of sliding friction are analysed throughout the duration of the first contact, located at the bottom of the TDBs. The related range in time domain are set between the instants 1 and 2, in Figure 4.43. The predicted and measured orbits on that particular range are given in Figure 4.45. The initial forward whirl orbit, indicated by the red arrow, is induced by the mass unbalance forces. As observed in the time domain, the first contact is described well by the numerical model, at both DE and NDE sides, in terms of height and direction of rebound. The grey and black arrows indicate the instantaneous rotor whirl direction for the DE and NDE sides, respectively. Sliding friction effects are clearly visible in Figure 4.45 since orbit has backward whirl during the contact.

To sum-up, the model gives satisfactory results. As shown by the measured and the predictions, the sliding friction effects drive the rotor in backward whirl. These effects are visible due to relatively large contact loads and since the TDBs do not reach the rotor rotational speed. This was not observed during harmonic excitations. No established dry whip behaviours are, however, triggered.

4.6 Further investigations

4.6.1 Numerical assessment

The last sections have shown that the model gives close predictions considering harmonic and impulse tests; it can be considered reliable. The aim of this section is to perform a numerical assessment considering a particular case. As explained previously, the emergency shut-down procedure is usually launched when the rotor displacement exceeds a designed threshold in industrial turbomachinery. This procedure consists in a rotor coast-down followed by a deactivation of AMBs. Assuming this procedure ends while base motions still continue, the rotor could be subjected to support motions and contact nonlinearities while no more AMB restoring forces are present to counteract it. The rotor at the bottom of its TDBs, without any AMB restoring forces, is subjected to a 1.1 G at 20 Hz base motion in vertical direction. The predicted rotor vertical displacements and the normal contact loads are presented in Figures 4.46 and 4.47, in the range [4.5-4.65]s. The maximal normal load reaches almost 1 500 N, which is 30 times higher than the maximal loads (50 N) considering the case where AMBs still operate, see Figure 4.25. According to the estimated load capacity, these loads are not high enough to destroy the ball bearings. The predicted orbits are given in Figure 4.48. No particular paths are found and the rotor behaviour can be considered chaotic.

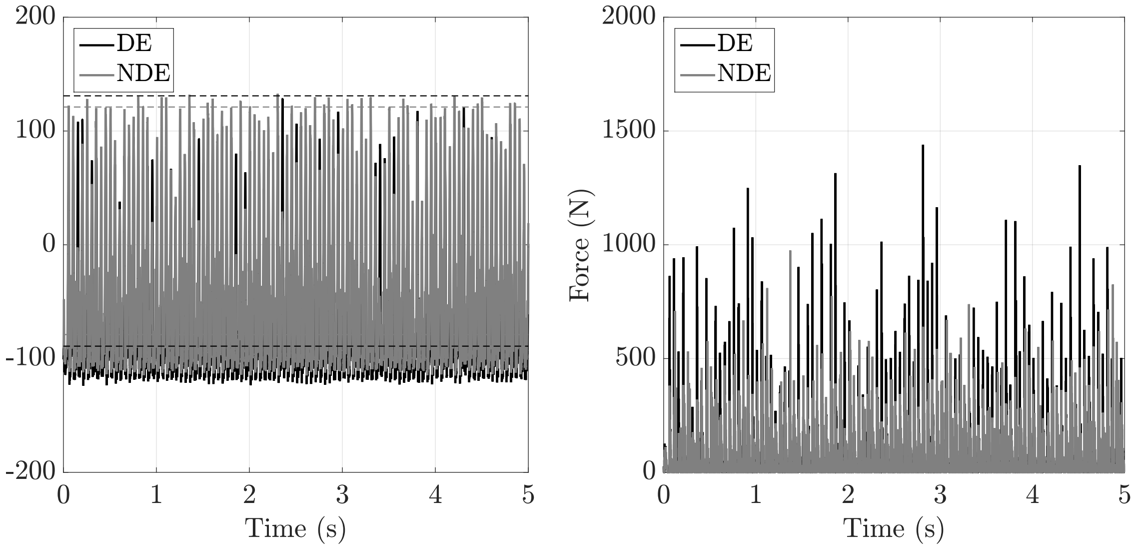

(a) Vertical rotor displacements

(b) Normal contact loads

Figure 4.46: Predicted rotor vertical displacement (a) and loads (b) and TDB clearances (dotted lines) - 1.1 G at 20 Hz

It is clear that the AMBs reduce significantly the TDBs loads when severe base motion occurs. An interesting shut-down procedure could be the following one: when strong base motions occur, leading the rotor to exceed a designed threshold, the rotational speed is stopped, but the AMBs keep operating.

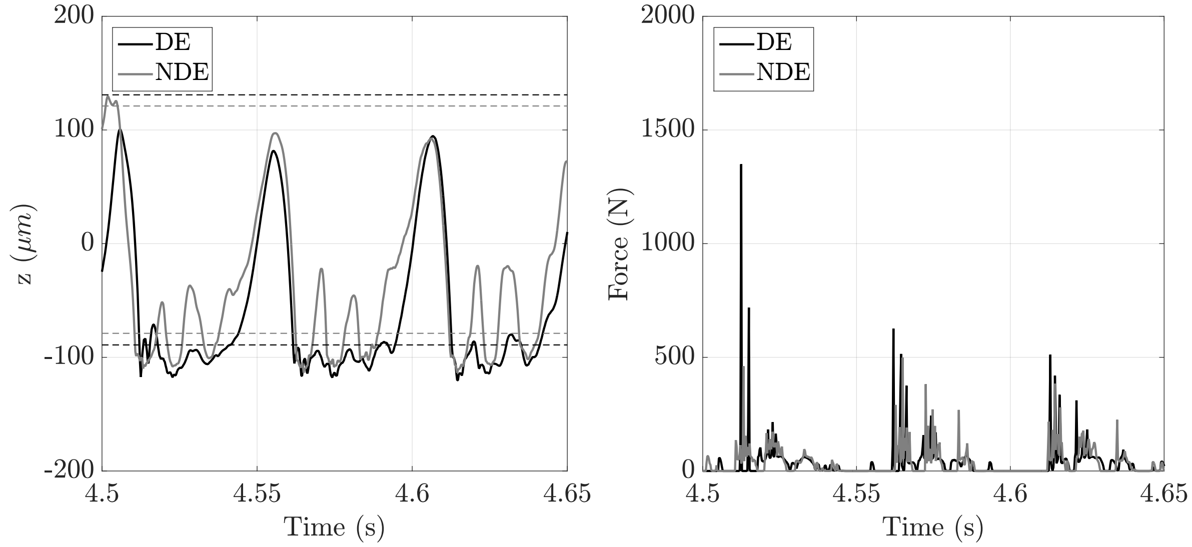

(a) Vertical rotor displacements

(b) Normal contact loads

Figure 4.47: Predicted rotor vertical displacement (a) and loads (b) and TDB clearances (dotted lines) - 1.1 G at 20 Hz

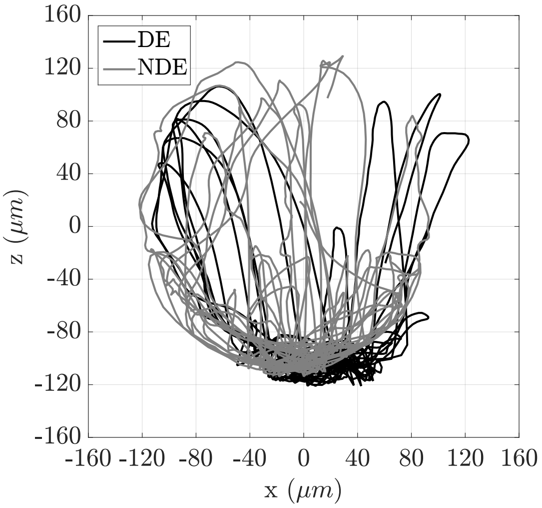

Figure 4.48: Predicted rotor orbits - 1.1 G at 20 Hz

4.6.2 Fleeting events

This subsection deals with particular events observed during impulse tests. It is shown, in Figure 4.49, that the second measured rotor rebound, located at the top of TDBs, seemed more violent than the predicted one.

The orbit responses between the instants 1 and 3, represented in Figure 4.49, are given in Figure 4.50. A measured “fleeting event” appears, changing the orbit in backward whirl.

A zoom on the second contact, defined by the red rectangles in Figure 4.50, is provided in Figure 4.51. The predicted and measured coil currents permit the computation of the estimated applied magnetic forces, given at each time step by the red and purple arrows for the DE and

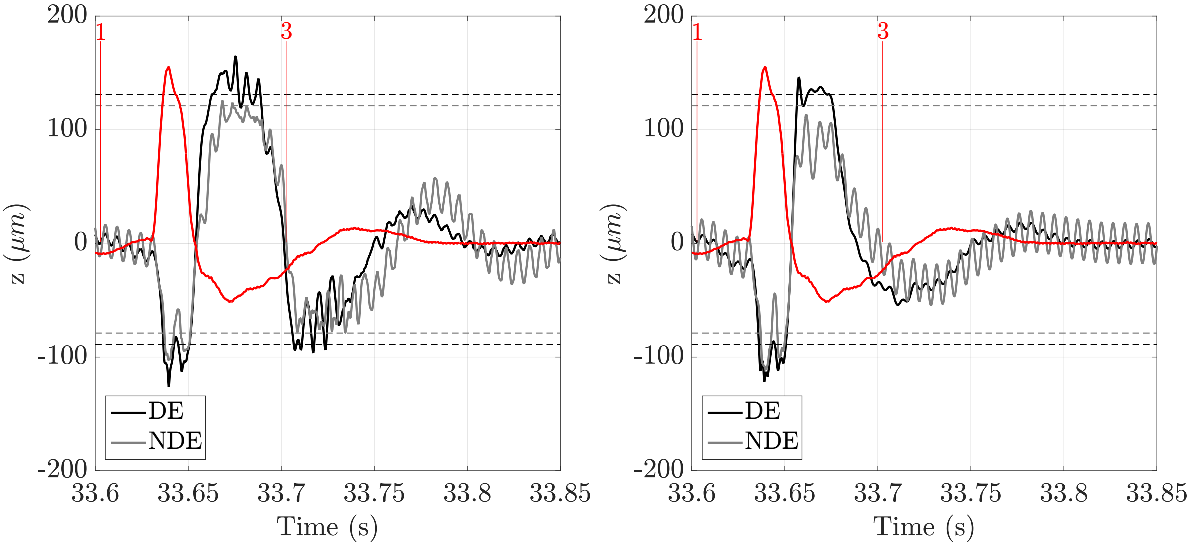

(a) Experimental results

(b) Numerical results

Figure 4.49: Measured (a) vs predicted (b) vertical rotor displacements (solid lines), TDB clearances (dotted lines) and acceleration profile (red lines) - 9 500 rpm and 3.1 G at 50 Hz

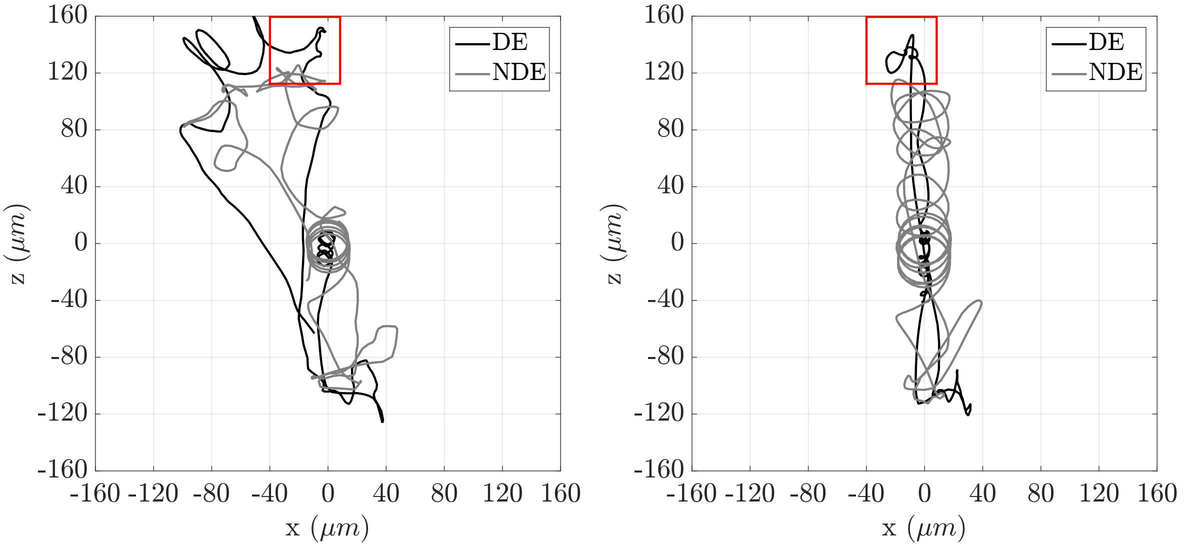

(a) Experimental results

(b) Numerical results

Figure 4.50: Measured (a) vs predicted (b) rotor orbits - 9 500 rpm and 3.1 G at 50 Hz

NDE AMBs respectively. The rotor instantaneous whirl is represented by the black arrows, numbered in chronological order. The measured magnetic forces at DE side push the rotor in backward direction between the arrows 3 and 4, but not in the predictions. This could be due to negative damping provided by the experimental AMB transfer function or to the controller delay to apply the instruction. Obviously, tangential forces induced by friction contributes also to this backward whirl motion. However, the predicted contact loads, especially the tangential ones, are small during the top contact, as shown in Figure 4.52.

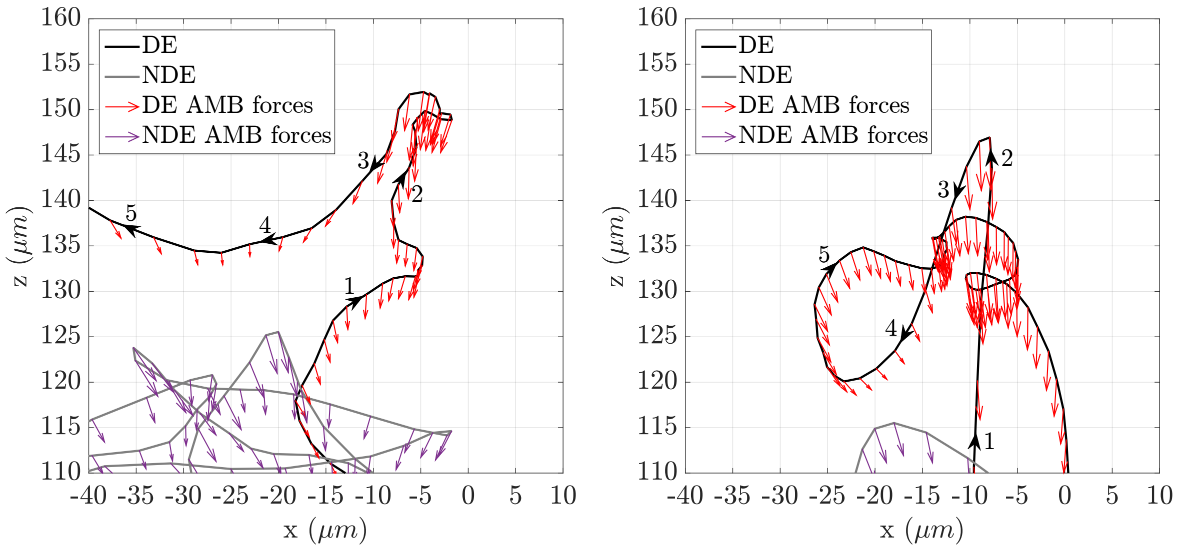

(a) Experimental results - zoom

(b) Numerical results - zoom

Figure 4.51: Measured (a) vs predicted (b) rotor orbits and AMB forces - 9 500 rpm and 3.1 G at 50 Hz

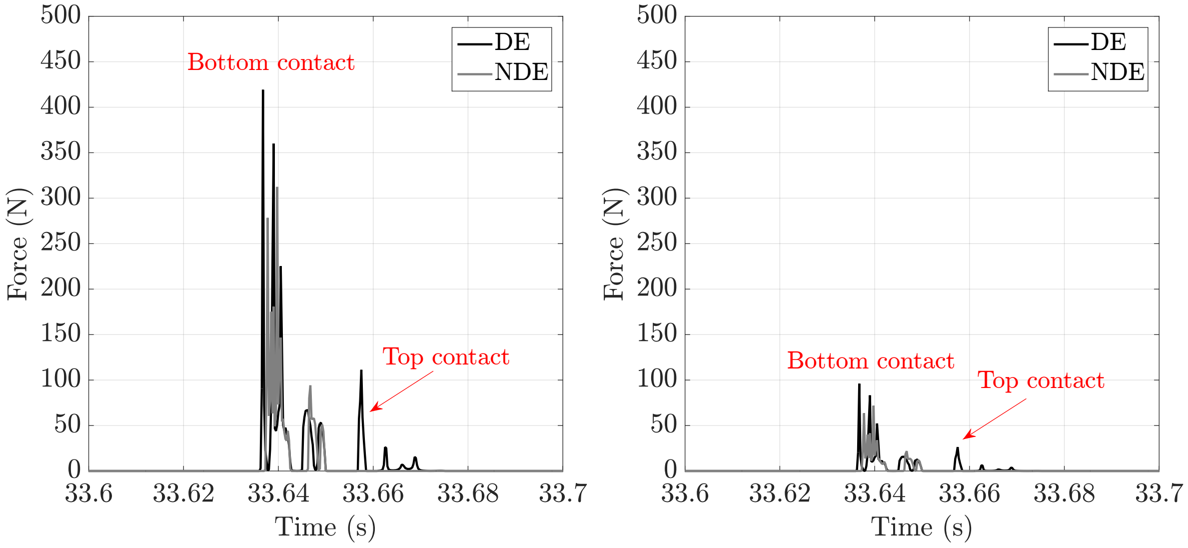

(a) Nomal contact loads

(b) Tangential contact loads

Figure 4.52: Predicted contact loads - 9 500 rpm and 3.1 G at 50 Hz

To sum-up, it is shown that some fleeting instabilities can be exhibited while rotor-TDB contact occur. This is thought to be related to a fleeting AMB instability: the time delay generated by the controller to produce an instruction or some discrepancies between the experimental and the numerical AMB transfer functions. However, just after this event, the rotor is quickly recentred by the AMBs and no established instabilities are triggered.

4.7 Conclusions

4.7.1 Outcomes

The model was able to reproduce the overall dynamics and the observed phenomena considering an academic on-board rotor-AMB system subjected to harmonic or impulse base excitations and TDB contact nonlinearities. The predicted rotor displacements and control currents are found to be close to measurements. This numerical validation provides confidence considering the prediction of the dynamic behaviour of on-board industrial turbomachinery. Moreover, the dynamic properties of the shaft as well as the base motions tested are representative of real operating conditions.

The numerical simulation uses the different components presented in this work. The PID controller is tuned for conventional rotordynamics as it is done in most of the actual turbomachinery supported by AMBs. First, the model was assessed for conventional mass unbalance response and rotor drop at rest; the predictions were found in agreement with the measures. The estimated TDB parameters were considered valid. Then, the numerical and experimental investigations for harmonic and impulse tests in vertical direction were conducted. The configuration tests were chosen to be representative of real turbomachines operating conditions.

Considering harmonic tests with small base accelerations (no TDB contact), the controller was able to sustain the combined base motion effects and unbalance forces which give periodic or quasi-periodic orbits depending on the ratio of the base motion frequency over the rotational speed. This was well reproduced by the model. Generally speaking, TDB contact generates the rotor displacements flattening and rich frequency responses comprising many superharmonics of the fundamental base motion frequency. Linear modes of the rotor-AMB system are excited since contacts act, to some extent, like modal tests. The restoring magnetic forces generated by actuators remain in an acceptable linear range. No amplifier saturations were noticed. The nonlinear rotor-TDB coupled modes are excited throughout the duration of each contact. Even if the PID controller was tuned without considering these particular frequencies, the rotor-AMB controller remains globally stable in both numerical and experimental tests. No AMB nonlinearities are exhibited whether amplifier saturation or magnetic force nonlinearity in both predictions and measures. This is mainly due to the fact that TDB contacts prevent actuator nonlinearities emergences. This could be due to the fact that the TDB over AMB clearances ratio is close to 0.25 which is smaller than industrial values, closer to 0.5. In these cases, the nonlinearities of actuator forces could be more relevant. Considering a rotating shaft, no dry whip instabilities are triggered in both experimental and numerical results, considering both harmonic and impulse tests. It seems that the TDBs are driven in rotation reaching the rotor rotational speed during harmonic tests; therefore, tangential friction effects are limited. Moreover, the acceleration level did not generate large contact loads. Considering impulse tests, the effects are more visible. On the one hand, because the acceleration levels tested were higher and on the other hand, because the TDBs are not driven in rotation up to the rotor speed. The sliding friction was then higher than for harmonic cases. During impulse tests, some fleeting instabilities were recorded experimentally. The latter were never established and the rotor was always quickly recentred. These instabilities are most likely to be triggered by AMBs.

4.7.2 Discussion

It is well-known that nonlinear rotordynamics are sensitive to contact parameters such as clearance, misalignments, contact damping and stiffness, sliding friction, etc. On the other hand, the rotor-AMB system is also sensitive to the electromagnetic forces provided by the controller. The combination of both these phenomena is complex and several discrepancies were noticed when comparing predicted and measured results:

- A difference between the numerical and the experimental AMB transfer function was noticed. This was revealed by smaller displacements and different sensitivity to harmonics. An identification procedure was carried-out and it was shown that the experimental AMB transfer function was not exactly the implemented one. The amplifier is supposed to be the most probable source of discrepancies. Due to a lack of time, the modification has not been implemented yet in the numerical model. The fleeting events observed during impulse tests could be also a cause of these differences.

- The measured rotor-TDB clearance was not exactly the provided one. Several assumptions can explain these differences; manufacturing issues, the unknown TDB internal clearance and uncertainties of the ribbon. Even if the rotor was initially centred with respect to TDBs, the measured clearances and misalignments change after each contact, due probably to the nonlinear behaviour of the ribbon.

- Measured orbits at both DE and NDE sides are not perfectly vertical and are tilted in opposite direction. This could be due to sensors sensitivity discrepancies. This could also explain the difficulty to obtain the exact clearances and misalignments.

Chapter 5

General conclusions

5.1 Summary and results

Turbomachinery supported by AMBs are being increasingly employed in industry for their many advantages. Most of them are on-board machines; assuming their support fixed may be a strong assumption. The effect of external environment should be considered for reliable rotordynamics and loads predictions. With the objective of continually improving designs and operability of machines, this thesis contributes to the improvement of knowledge concerning the dynamic behaviour of turbomachinery when subjected to external events. The problematic is recalled. The aim was to determine *what would be the dynamic behaviour of a rotor supported by AMBs, controlled by conventional control strategy (PID), subjected to conventional rotordynamics loads (gravity and unbalance) but also to external base motion and contact non-linearities ?*

To answer this question, the problematic of on-board rotors, active magnetic bearings and touchdown bearings are first analysed individually and then combined.

The on-board FE rotor model is based on the efficient Lagrangian approach integrating the three translations and rotations of the supporting rigid base. Any kind of base motions (harmonic, impulse, etc.) can be implemented and the rotor rotational speed is variable. The energetic formulation of each element composing the rotor is modified according to the foundation motions. External force vectors and matrices with parametric coefficients are added to the conventional equations of motion of Timoshenko beam elements for lateral analysis. A major advantage of this method lies in the fact that any type of bearing can be used.

AMBs provide active restoring forces modulated according to a specific frequency range by a dedicated augmented PID controller. The proportional gain provides the minimum stiffness to the system. The integral term centres the rotor while the derivative gain generates damping on the operating speed range. Several filters are added to ensure high frequency stability and avoid spillover effects. When the rotor displacement exceeds the TDB clearance, contact occurs. A large part of the work concerns the description and modelling of the different elements composing the TDBs and its mechanical link to stator. Among the different TDB types, the ball bearing is exclusively studied. A classical analytical law is employed to describe the bearing force deflection relationship and gave successful results. An equivalent rotational inertia is established for the TDB spin-up based on kinematic rolling-without-slipping conditions. The dynamic properties of the mechanical joint located between the TDB outer race and the stator housing, called ribbon damper, has a major role.

This device was experimentally tested and generates dry friction damping when subjected to harmonic excitation. The generalized Dahl model is a nonlinear first-order differential equation adapted to fairly reproduce the observed phenomenon under harmonic forcing.

The experimental validation of the TDB model is carried out using an industrial scale test rig. The idea was to obtain a sufficiently detailed model able to provide the observed phenomena. Numerical and experimental investigations during drop events at rest and at 6 500 rpm were performed. The general outcomes, that may be valid for any kind of turbomachinery design, can be listed as follows:

- A simple TDB bilinear contact law seemed to be enough precise to adequately describe the whole rotor drop dynamics and loads.
- The TDB spin-up time was correctly estimated using a single equation of motion. The rolling-without-slipping kinematic condition seemed to be valid.
- The ribbon damper may have a different behaviour when subjected to transient loads rather than harmonic excitations.

Then, experimental and numerical investigations were carried out considering an academic on-board rotor-AMB system subjected to support motions. The rotor has the dynamic characteristics of real turbomachinery and the implemented PID controller was not specifically tuned to sustain base motion or TDB contacts. The latter was mounted on a 6-axis shaker and was subjected to 20 Hz harmonic up to 1.1 G and 50 Hz impulse tests up to 3.1 G in vertical direction, representative of earthquakes and wave shocks, respectively.

The general outcomes, that may be valid for any kind of turbomachinery design, can be listed as follows:

- When support motions exceed the AMBs dynamic capacity, loads are shared with TDBs; keeping AMBs operating may limit TDB loads while base motion occur.
- The nonlinear coupled rotor-TDB modes are excited throughout the duration of contact.
- The TDB spin-up reduce the sliding friction effects during harmonic tests; they are more visible during impulse tests.
- The combination of base motion effects and mass unbalance forces generates complex orbits related to the base motion frequency over the rotational speed ratio.

The outcomes, at least valid for our tests, can be listed as follows:

- The PID controller was able to sustain conventional, base motion and nonlinear loads without exhibiting established instabilities.
- No amplifier saturation nor strong magnetic nonlinearities were exhibited; this is mainly due to the fact that TDB over AMB clearance ratio is 0.25 in the tested rotor-AMB system, thus preventing these AMB nonlinearities.
- Predicted contact loads for all tested cases were far from the TDB maximal load capacity.

Generally speaking, the predictions produce reliable results. The validation of the developed numerical model with an academic rotor permits being confident on its capacity to reproduce the observed phenomena with industrial turbomachinery design. From an industrial point of view, it is still difficult to carry out base motion tests on real and heavy industrial machines due to mass issues. The model could then help to design on-board industrial turbomachinery facing their external environments.

5.2 Future work

First of all, the design of conventional PID could be enhanced by considering at least the first rotor-TDB coupled mode. Providing damping on this frequency could prevent the observed controller fleeting instabilities. The time delay produced by the controller to deliver an instruction could also be considered in the numerical model. Several control strategies could be employed to limit the effect of base motion and contact, separately. First, the effect of the support could be reduced by implementing a feedforward control loop using support acceleration as input, as done by Matsushita *et al.* [7]. In the case where contacts occur, the fuzzy control strategy using polar quantities, developed by Defoy *et al.* [186], could be enhanced to treat contact problems. Indeed, the effect of contacts are clearly visible on normal displacement while the rotor whirling velocity gives useful informations on the tangential friction effects; increasing the tangential damping could probably limit the effects of friction. Considering rotations of the support (pitching or yawing), it could be interesting to determine the effect of a simple PID controller on the instability zones due to inherent parametric excitations. The developed ribbon damper model based on harmonic excitation tests gave fairly accurate results. However, its behaviour during the drop rebounds seemed to be different. We think that the slipping threshold decreases when subjected to transient loads, reducing instantaneously the damping brought into the system. It could then be interesting to improve the developed dry friction model by implementing a slipping threshold dependent on the outer race velocity. Impact tests should then be carried out on the ribbon to analyse the evolution of the slipping threshold according to the impact velocity. Discrete models, like those of Le lez *et al.* [25, 26], could be adapted to model the outer race stator housing interactions. The validation of the rotational modelling could be done by measuring the TDB rotational speed of a test bench. In parallel, simulation using rolling elements multi-Dof could be performed to analyse how far this simple equation of motion is valid.

Bibliography

[1] A. Berlioz, R. Dufour, and S. C. Sinha. Bifurcation in a nonlinear autoparametric system using experimental and numerical investigations. *Nonlinear Dynamics*, 23(2):175–187, 2000.

[2] M. Duchemin, A. Berlioz, and G. Ferraris. Dynamic behavior and stability of a rotor under base excitation. *Journal of Vibration and Acoustics*, 128(5):576–585, 2006. 10.1115/1.2202159.

[3] M. Duchemin. *Contribution à l'étude du comportement dynamique d'un rotor embarqué*. PhD thesis, INSA Lyon, 2003.

[4] N. Driot, C. H. Lamarque, and A. Berlioz. Theoretical and experimental analysis of a base-excited rotor. *Journal of Computational and Nonlinear Dynamics*, 1:257–263, 2006.

[5] M. Dakel, S. Baguet, and R. Dufour. Nonlinear dynamics of a support-excited flexible rotor with hydrodynamic journal bearings. *Journal of Sound and Vibration*, 333(10):2774–2799, 2014.

[6] A. S. Lee, B. O. Kim, and Y. C. Kim. A finite element transient response analysis method of a rotor-bearing system to base shock excitations using the state-space newmark scheme and comparisons with experiments. *Journal of Sound and Vibration*, 297(3-5):595–615, 2006.

[7] O. Matsushita, T. Imashima, Y. Hisanaga, and Hiroki Okubo. Aseismic vibration control of flexible rotors using active magnetic bearing. *Journal of Vibration and Acoustics*, 124(1):49–57, 2001. 10.1115/1.1423633.

[8] J. C. Wilkes, D. W. Childs, B. J. Dyck, and S. G. Phillips. The numerical and experimental characteristics of multimode dry-friction whip and whirl. *Journal of Engineering for Gas Turbines and Power*, 132(5):052503–052503–9, 2010. 10.1115/1.3204658.

[9] A. R. Bartha. *Dry friction backward whirl of rotors*. Phd thesis, ETH Zürich, 2000.

[10] Y. S. Choi. Investigation on the whirling motion of full annular rotor rub. *Journal of Sound and Vibration*, 258(1):191–198, 2002.

[11] D. E. Bently, J. J. Yu, P. Goldman, and M. Agnes. Full annular rub in mechanical seals, part i: Experimental results. *International Journal of Rotating Machinery*, 2002.

[12] D. E. Bently, P. Goldman, and J. J. Yu. Full annular rub in mechanical seals, part ii: Analytical study. *International Journal of Rotating Machinery*, 2002.

[13] J. J. Yu, P. Goldman, D. E. Bently, and A. Muzynska. Rotor/seal experimental and analytical study on full annular rub. *Journal of Engineering for Gas Turbines and Power*, 124(2):340–350, 2002. 10.1115/1.1416691.

[14] G. Von Groll and D. J. Ewins. A mechanism of low subharmonic response in rotor/stator contact - measurements and simulations. *Journal of Vibration and Acoustics*, 124(3):350–358, 2002. 10.1115/1.1467648.

[15] M. O. T. Cole and P. S. Keogh. Asynchronous periodic contact modes for rotor vibration within an annular clearance. *Proceedings of the Institution of Mechanical Engineers, Part C: Journal of Mechanical Engineering Science*, 217(10):1101–1115, 2003.

[16] G. Yang, Z. Shi, X. Liu, and J. Zhao. Research and experiment of auxiliary bearings with no lubrication for helium blower of htr-10. In *14th International Symposium on Magnetic Bearings*, pages 104–108, 2014.

[17] J. Schmied and J. C. Pradetto. Behaviour of a one ton rotor being dropped into auxiliary bearings. In *3rd International Symposium on Magnetic Bearing*, pages 145–156, 1992.

[18] M. T. Caprio, B. T. Murphy, and J. D. Herbst. Spin commissioning and drop tests of a 130 kw-hr composite flywheel. In *9th International Symposium on Magnetic Bearing*, 2004.

[19] Peter Siebkea and Hermann Golbachb. A novel rolling element back-up bearing for a 9 t rotor application. In *14th International Symposium on Magnetic Bearings*, 2014.

[20] O. Halminen, A. Kärkkäinen, J. Sopanen, and A. Mikkola. Active magnetic bearing-supported rotor with misaligned cageless backup bearings: A dropdown event simulation model. *Mechanical Systems and Signal Processing*, 50-51(0):692–705, 2015.

[21] H. Xie, G. T. Flowers, L. Feng, and C. Lawrence. Steady-state dynamic behavior of a flexible rotor with auxiliary support from a clearance bearing. *Journal of Vibration and Acoustics*, 121(1):78–83, 1999. 10.1115/1.2893951.

[22] G. Sun. *Auxiliary bearing design guides in Active Magnetic Bearing system.* VDM, 2003.

[23] G. Sun, A. B. Palazzolo, A. Provenza, and G. Montague. Detailed ball bearing model for magnetic suspension auxiliary service. *Journal of Sound and Vibration*, 269(3-5):933–963, 2004.

[24] G. Gilardi and I. Sharf. Literature survey of contact dynamics modelling. *Mechanism and Machine Theory*, pages 1213–1239, 2002.

[25] S. Le Lez, M. Arghir, and J. Frene. A new bump-type foil bearing structure analytical model. *Journal of Engineering for Gas Turbines and Power*, 129(4):1047–1057, 2007. 10.1115/1.2747638.

[26] S. Le Lez, M. Arghir, and J. Frêne. Nonlinear numerical prediction of gas foil bearing stability and unbalanced response. *Journal of Engineering for Gas Turbines and Power*, 131(1):012503–012503–12, 2008. 10.1115/1.2967481.

[27] B. Al Sayed, E. Chatelet, S. Baguet, and G. Jacquet-Richardet. Dissipated energy and boundary condition effects associated to dry friction on the dynamics of vibrating structures. *Mechanism and Machine Theory*, 46(4):479–491, 2011.

[28] M. Lalanne, P. Berthier, and J. Der Hagopian. *Mechanical Vibrations for Engineers*. Wiley, 1984.

[29] E. E. Swanson, C. D. Powell, and S. Weissman. A practical review of rotating machinery critical speeds and modes. *Journal of Sound and Vibration*, 2005.

[30] M. Lalanne and G. Ferraris. *Rotordynamics Prediction in Engineering*. Wiley, 1998.

[31] G. Genta. *Dynamics of rotating systems*. Springer, 2005.

[32] S. Doughty. Response of single degree of freedom mechanisms to base excitation. *Mechanism and Machine Theory*, 36(7):833–842, 2001.

[33] S. Edwards, A. W. Lees, and M. I. Friswell. Experimental identification of excitation and support parameters of a flexible rotor-bearings-foundation system from a single rundown. *Journal of Sound and Vibration*, 232(5):963–992, 2000.

[34] P. Bonello and M. J. Brennan. Modelling the dynamic behaviour of a supercritical rotor on a flexible foundation using the mechanical impedance technique. *Journal of Sound and Vibration*, 239(3):445–466, 2001.

[35] N. Feng and E. J. Hahn. Identification of the modal parameters of a flexibly supported rigid casing. *Journal of Engineering for Gas Turbines and Power*, 125(1):184–192, 2002. 10.1115/1.1519265.

[36] K. L. Cavalca, P. F. Cavalcante, and E. P. Okabe. An investigation on the influence of the supporting structure on the dynamics of the rotor system. *Mechanical Systems and Signal Processing*, 19(1):157–174, 2005.

[37] A. W. Lees, J. K. Sinha, and M. I. Friswell. Model-based identification of rotating machines. *Mechanical Systems and Signal Processing*, 23(6):1884–1893, 2009.

[38] M. Dakel. *Stabilité et dynamique non linéaire de rotors embarqués*. PhD thesis, INSA Lyon, 2014.

[39] M. Dakel, S. Baguet, and R. Dufour. Steady-state dynamic behavior of an on-board rotor under combined base motions. *Journal of Vibration and Control*, 20(15):2254–2287, 2014.

[40] Q. Han and F. Chu. Parametric instability of flexible rotor-bearing system under time-periodic base angular motions. *Applied Mathematical Modelling*, 39(15):4511–4522, 2015.

[41] R. Bouziani and N. Ouelaa. Simulation of the dynamic behavior of a rotor subject to base motion under variable rotational speed. *Mechanics & Industry*, 2017.

[42] F. M. A. El-Saeidy and F. Sticher. Dynamics of a rigid rotor linear/nonlinear bearings system subject to rotating unbalance and base excitations. *Journal of Vibration and Control*, 16(3):403–438, 2010.

[43] B. Samali, K. Kim, and J. Yang. Random vibration of rotating machines under earthquake excitations. *Journal of Engineering Mechanics*, 112(6):550–565, 1986.

[44] M. Ghafory-Ashtiany and M. P. Singh. Structural response for six correlated earthquake components. *Earthquake Engineering & Structural Dynamics*, 14(1):103–119, 1986.

[45] L. E. Suarez, M. P. Singh, and M. S. Rohanimanesh. Seismic response of rotating machines. *Earthquake Engineering & Structural Dynamics*, 21(1):21–36, 1992.

[46] Y. Hori and T. Kato. Earthquake-induced instability of a rotor supported by oil film bearings. *Journal of Vibration and Acoustics*, 112(2):160–165, 1990. 10.1115/1.2930108.

[47] Y. Murai, K. Watanabe, and Y. Kanemitsu. Seismic test on turbo-molecular pumps levitated by active magnetic bearing. In G. Schweitzer, editor, *Magnetic Bearings: Proceedings of the First International Symposium, ETH Zurich, Switzerland, June 6-8, 1988*, pages 303–310, Berlin, Heidelberg, 1989. Springer Berlin Heidelberg.

[48] L. A. Hawkins, B. Murphy, J. Zierer, and R. Hayes. Shock and vibration testing of an amb supported energy storage flywheel. *JSME International Journal Series C Mechanical Systems, Machine Elements and Manufacturing*, 46(2):429–435, 2003.

[49] G. Leilei, L. Wan, and Y. Suyuan. Theoretical investigation on dynamic behavior of amb-rotor system subject to base motion disturbances. In *12th International Symposium on Magnetic Bearings*, pages 82–90, 2010.

[50] L. A. Hawkins, R. K. Khatri, and K. B. Nambiar. Test results and analytical predictions for mil-std-167 vibration testing of a direct drive compressor supported on magnetic bearings. *Journal of Engineering for Gas Turbines and Power*, 137(5):052507–052507–8, 2015. 10.1115/1.4028684.

[51] M. E. Kasarda, J. Clements, A. L. Wicks, C. D. Hall, and R. G. Kirk. Effect of sinusoidal base motion on a magnetic bearing. In *Proceedings of the 2000. IEEE International Conference on Control Applications. Conference Proceedings (Cat. No.00CH37162)*, pages 144–149, 2000.

[52] L. A. Hawkins. Shock analysis for a homopolar, permanent magnet bias magnetic bearing system. In *ASME Turbo Expo 1997: Power for Land, Sea and Air*, number 78712, page V004T14A040, 1997. 10.1115/97-GT-230.

[53] Y. Suzuki. Acceleration feedforward control for active magnetic bearing systems excited by ground motion. *IEE Proceedings - Control Theory and Applications*, 145(2):113–118, 1998.

[54] S. Marx and C. Nataraj. Suppression of base excitation of rotors on magnetic bearings. *International Journal of Rotating Machinery*, 2007:10, 2007.

[55] M. S. Kang and W. H. Yoon. Acceleration feedforward control in active magnetic bearing system subject to base motion by filtered-x lms algorithm. *IEEE Transactions on Control Systems Technology*, 14(1):134–140, 2006.

[56] H. S. Kim, H. Y. Kim, C. W. Lee, and T. H. Kang. Stabilization of active magnetic bearing system subject to base motion. In *ASME 2003 International Design Engineering Technical Conferences and Computers and Information in Engineering Conference*, number 37033, pages 2007–2013, 2003. 10.1115/DETC2003/VIB-48546.

[57] M. S. Kang, J. Lyou, and J. K. Lee. Sliding mode control for an active magnetic bearing system subject to base motion. *Mechatronics*, 20(1):171–178, 2010.

[58] M. O. T. Cole, P. S. Keogh, and C. R. Burrows. Vibration control of a flexible rotor/magnetic bearing system subject to direct forcing and base motion disturbances. *Proceedings of the Institution of Mechanical Engineers, Part C: Journal of Mechanical Engineering Science*, 212(7):535–546, 1998.

[59] P. S. Keogh, M. Necip, S. Clifford, R. Burrows, and S. Prabhakar. Wavelet based adaptation of h-infinity control in flexible rotor/magnetic bearing systems. In *7th IFToMM International Conference on Rotor Dynamics*, Vienna, Austria, September 2006.

[60] Y. Maruyama, T. Mizuno, M. Takasaki, Y. Ishino, H. Kameno, and A. Kubo. Study on control system for active magnetic bearing considering motions of stator. *Journal of System Design and Dynamics*, 3(6):954–965, 2009.

[61] A. S. Das, J. K. Dutt, and K. Ray. Active vibration control of unbalanced flexible rotor-shaft systems parametrically excited due to base motion. *Applied Mathematical Modelling*, 34(9):2353–2369, 2010.

[62] J. M. T. Thompson and R. Ghaffari. Chaos after period-doubling bifurcations in the resonance of an impact oscillator. *Physics Letters A*, 91(1):5–8, 1982.

[63] S. W. Shaw and P. J. Holmes. A periodically forced piecewise linear oscillator. *Journal of Sound and Vibration*, 90(1):129–155, 1983.

[64] I. A. Mahfouz and F. Badrakhan. Chaotic behaviour of some piecewise-linear systems part i: Systems with set-up spring or with unsymmetric elasticity. *Journal of Sound and Vibration*, 143(2):255–288, 1990.

[65] I. A. Mahfouz and F. Badrakhan. Chaotic behaviour of some piecewise-linear systems, part ii: Systems with clearance. *Journal of Sound and Vibration*, 143(2):289–328, 1990.

[66] S. Natsiavas. Periodic response and stability of oscillators with symmetric trilinear restoring force. *Journal of Sound and Vibration*, 134(2):315–331, 1989.

[67] Y. S. Choi and S. T. Noah. Forced periodic vibration of unsymmetric piecewise-linear systems. *Journal of Sound and Vibration*, 121(1):117–126, 1988.

[68] A. Narimani, M. E. Golnaraghi, and G. Nakhaie Jazar. Frequency response of a piecewise linear vibration isolator. *Journal of Vibration and Control*, 10(12):1775–1794, 2004. 10.1177/1077546304044795.

[69] S. Deshpande, S. Mehta, and G. N. Jazar. Optimization of secondary suspension of piecewise linear vibration isolation systems. *International Journal of Mechanical Sciences*, 48(4):341–377, 2006.

[70] J. Jiang and H. Ulbrich. The physical reason and the analytical condition for the onset of dry whip in rotor-to-stator contact systems. *Journal of Vibration and Acoustics*, 127(6):594–603, 2004.

[71] J. Jiang. The analytical solution and the existence condition of dry friction backward whirl in rotor-to-stator contact systems. *Journal of Vibration and Acoustics*, 129(2):260–264, 2006. 10.1115/1.2345677.

[72] J. Jiang. Determination of the global responses characteristics of a piecewise smooth dynamical system with contact. *Nonlinear Dynamics*, 57(3):351–361, 2009.

[73] Z. Shang, J. Jiang, and L. Hong. The global responses characteristics of a rotor/stator rubbing system with dry friction effects. *Journal of Sound and Vibration*, 330(10):2150–2160, 2011.

[74] G. Jacquet-Richardet, M. Torkhani, P. Cartraud, F. Thouverez, T. Nouri-Baranger, M. Herran, C. Gibert, S. Baguet, P. Almeida, and L. Peletan. Rotor to stator contacts in turbomachines. review and application. *Mechanical Systems and Signal Processing*, 40(2):401–420, November 2013.

[75] O. Alber and R. Markert. Rotor-stator contact – overview of current research. *MATEC Web of Conferences*, 16:03001, 2014.

[76] H. F. Black. Interaction of a whirling rotor with a vibrating stator across a clearance annulus. *Journal of Mechanical Engineering Science*, 10, 1968.

[77] A. Lingener. Investigation of reverse whirl of flexible rotor. *Rakenteiden Mekaniikka*, 24:3–21, 1991.

[78] D. W. Childs and A. Bhattacharya. Prediction of dry-friction whirl and whip between a rotor and a stator. *Journal of Vibration and Acoustics*, 129(3):355–362, 2007. 10.1115/1.2731412.

[79] J. Wilkes. *A perspective on the numerical and experimental characteristics of multi mode dry friction whip and whirl*. Msc thesis, Texas A&M University, 2008.

[80] O. Ismeurt. *Contribution à l'étude de l'influence du frottement rotor - stator sur le comportement dynamique des machines tournantes*. Phd thesis, INSA Lyon, 1995.

[81] S. Braut, R. Žigulić, A. Skoblar, G. Štimac, and M. Butković. Dynamic analysis of the rotor-stator contact due to blade loss. In *12th IFToMM International Conference on Rotor Dynamics*, 2007.

[82] C. Duran, L. Manin, M. A. Andrianoely, C. Bordegaray, and R. Dufour. Effect of rotor-stator contact on the mass unbalance response. In *9th IFToMM International Conference on Rotor Dynamics*, Milan, Italy, September 2014.

[83] C. Duran. *Modélisation du comportement dynamique non-linéaire et transitoire de turbomoteur avec multitouches rotor/stator*. Phd thesis, INSA Lyon, 2014.

[84] C. Wang, D. Zhang, Y. Ma, Z. Liang, and J. Hong. Theoretical and experimental investigation on the sudden unbalance and rub-impact in rotor system caused by blade off. *Mechanical Systems and Signal Processing*, 76-77:111 – 135, 2016.

[85] Sunil K. Sinha. Rotordynamic analysis of asymmetric turbofan rotor due to fan blade-loss event with contact-impact rub loads. *Journal of Sound and Vibration*, 332(9):2253 – 2283, 2013.

[86] S. Lahriri, H. I. Weber, I. F. Santos, and H. Hartmann. Rotor-stator contact dynamics using a non-ideal drive - theoretical and experimental aspects. *Journal of Sound and Vibration*, 331(20):4518 – 4536, 2012.

[87] C. A. L. L. Fonseca, R. R. Aguiar, and H. I. Weber. On the non-linear behaviour and orbit patterns of rotor/stator contact with a non-conventional containment bearing. *International Journal of Mechanical Sciences*, 105:117–125, 2016.

[88] A. Muszynska and P. Goldman. Chaotic responses of unbalanced rotor/bearing/stator systems with looseness or rubs. *Chaos, Solitons & Fractals*, 5(9):1683–1704, 1995.

[89] F. Chu and Z. Zhang. Bifurcation and chaos in a rub impact jeffcott rotor system. *Journal of Sound and Vibration*, 210(1):1–18, 1998.

[90] F. Chu and W. Lu. Experimental observation of nonlinear vibrations in a rub-impact rotor system. *Journal of Sound and Vibration*, 283(3-5):621–643, 2005.

[91] S. Popprath and H. Ecker. Nonlinear dynamics of a rotor contacting an elastically suspended stator. *Journal of Sound and Vibration*, 308(3–5):767–784, 2007.

[92] P. Varney and I. Green. Nonlinear phenomena, bifurcations, and routes to chaos in an asymmetrically supported rotor-stator contact system. *Journal of Sound and Vibration*, 336:207 – 226, 2015.

[93] M. A. Abuzaid, M. E. Eleshaky, and M. G. Zedan. Effect of partial rotor-to-stator rub on shaft vibration. *Journal of Mechanical Science and Technology*, 23(1):170–182, 2009.

[94] P. Pennacchi, N. Bachschmid, and E. Tanzi. Light and short arc rubs in rotating machines: Experimental tests and modelling. *Mechanical Systems and Signal Processing*, 23(7):2205 – 2227, 2009.

[95] M. Torkhani, L. May, and P. Voinis. Light, medium and heavy partial rubs during speed transients of rotating machines: Numerical simulation and experimental observation. *Mechanical Systems and Signal Processing*, 29:45 – 66, 2012.

[96] S. Roques, M. Legrand, P. Cartraud, C. Stoisser, and C. Pierre. Modeling of a rotor speed transient response with radial rubbing. *Journal of Sound and Vibration*, 329(5):527 – 546, 2010.

[97] Y. B. Kim and S. T. Noah. Quasi-periodic response and stability analysis for a non-linear jeffcott rotor. *Journal of Sound and Vibration*, 190(2):239 – 253, 1996.

[98] L. Peletan, S. Baguet, M. Torkhani, and G. Jacquet-Richardet. A comparison of stability computational methods for periodic solution of nonlinear problems with application to rotordynamics. *Nonlinear Dynamics*, 72(3):671–682, 2013// 2013.

[99] L. Peletan, S. Baguet, M. Torkhani, and G. Jacquet-Richardet. Quasi-periodic harmonic balance method for rubbing self-induced vibrations in rotor–stator dynamics. *Nonlinear Dynamics*, 78(4):2501–2515, 2014// 2014.

[100] L. Xie, S. Baguet, B. Prabel, and R. Dufour. Numerical tracking of limit points for direct parametric analysis in nonlinear rotordynamics. *Journal of Vibration and Acoustics*, 138(2):021007, 2016.

[101] G. Sun. Rotor drop and following thermal growth simulations using detailed auxiliary bearing and damper models. *Journal of Sound and Vibration*, 289(1-2):334–359, 2006.

[102] L. Hawkins, P. McNullen, and V. Vuong. Development and testing of the backup bearing system for an amb energy storage flywheel. In *ASME Turbo Expo 2007: Power for Land, Sea and Air*, 2007.

[103] D. Ransom, A. Masala, J. Moore, G. Vannini, M. Camatti, and M. Lacour. Development and application of a vertical high speed motor-compressor simulator for rotor drop onto auxialiary bearing. In *Proceedings of the 38th turbomachinery symposium*, 2009.

[104] D. Ransom, A. Masala, J. Moore, G. Vannini, and M. Camatti. Numerical and experimental simulation of a vertical high speed motorcompressor rotor drop onto catcher bearings. *Journal of System Design and Dynamics*, 3(4):596–606, 2009.

[105] J. Wilkes, J. Moore, D. Ransom, and G. Vannini. An improved catcher bearing model and an explanation of the forward whirl / whip phenomenon observed in amb transient drop experiments. *Journal of Engineering for Gas Turbines and Power*, 136:504–515, 2014.

[106] L. A. Hawkins, A. Filatov, S. Imani, and D. Prosser. Test results and analytical predictions for rotor drop testing of an active magnetic bearing expander/generator. *Journal of Engineering for Gas Turbines and Power*, 129(2):522–529, 2006. 10.1115/1.2436549.

[107] T. Ishii and R. G. Kirk. Transient response technique applied to active magnetic bearing machinery during rotor drop. *Journal of Vibration and Acoustics*, 118(2):154–163, 1996.

[108] R. G. Kirk. Evaluation of amb turbomachinery auxiliary bearings. *Journal of Vibration and Acoustics*, 121(2):156–161, 1999. 10.1115/1.2893958.

[109] S. Zeng, J. Q. Zhang, and H. N. Wang. Transient response of active magnetic bearing rotor during rotor drop on backup bearings. *Proceedings of the Institution of Mechanical Engineers, Part C: Journal of Mechanical Engineering Science*, 220(6):785–794, 2006.

[110] S. Zeng. Modelling and experimental study of the transient response of an active magnetic bearing rotor during rotor drop on back-up bearings. *Proceedings of the Institution of Mechanical Engineers, Part I: Journal of Systems and Control Engineering*, 217(6):505–517, 2003.

[111] F. Zhi-chu. Study on catastrophic mechanism for rotor drop transient vibration following magnetic bearing failure. *Applied Mathematics and Mechanics*, 23(11):1319–1325, 2002// 2002.

[112] R. G. Kirk, E. J. Gunter, and W. J. Chen. Rotor drop transient analysis of amb machinery. In *ASME 2005, Proceedings of IDETC/CIE 2005*, 2005.

[113] A. Kärkkäinen, J. Sopanen, and A. Mikkola. Dynamic simulation of a flexible rotor during drop on retainer bearings. *Journal of Sound and Vibration*, 306(3-5):601–617, 2007.

[114] G. Siegl, T. Tzianetopoulou, and J. Denk. Simulation and experimental validation of a 9 ton amb rotor landing in rolling element back-up bearings. *Mechanical Engineering Journal*, 3(1):15–00136–15–00136, 2016.

[115] A. Gelin, J. M. Pugnet, and J. Der Hagopian. Dynamic behavior of flexible rotors with active magnetic bearings on safety auxiliary bearings. In *Proceedings of Third International Conference on Rotordynamics*, pages 503–508, Lyon, France, 1990.

[116] A. Gelin. *Etude théorique et expérimentale des comportements dynamiques permanents et transitoires de rotors sur paliers magnétiques*. Phd thesis, INSA Lyon, 1991.

[117] M. A. Fumagalli. *Modelling and measurement analysis of the contact interaction between a high speed rotor and its stator*. Phd thesis, ETH Zürich, 1997.

[118] A. Kärkkäinen, M. Helfert, B. Aeschlimann, and A. Mikkola. Dynamic analysis of rotor system with misaligned retainer bearings. *Journal of Tribology*, 130(2):021102–021102, 2008. 10.1115/1.2908921.

[119] E. H. Maslen and L. E. Barrett. Rotor whirl in compliant auxiliary bearings. *Journal of Vibration and Control*, 2(2):145–159, 1996. 10.1177/107754639600200202.

[120] X. Wang and S. Noah. Nonlinear dynamics of a magnetically supported rotor on safety auxiliary bearings. *Journal of Vibration and Acoustics*, 120(2):596–606, 1998. 10.1115/1.2893869.

[121] Y. Ishida and T. Inoue. Vibration characteristics of a rotor system in contact with a backup bearing: Cases with various failure patterns of the active magnetic bearing. *Journal of Vibration and Control*, 14(4):571–589, 2008.

[122] M. O. T. Cole, P. S. Keogh, and C. R. Burrows. The dynamic behavior of a rolling element auxiliary bearing following rotor impact. *Journal of Tribology*, 124(2):406–413, 2001. 10.1115/1.1430673.

[123] P. S. Keogh and W. Y. Yong. Thermal assessment of dynamic rotor/auxiliary bearing contact events. *Journal of Tribology*, 129(1):143–152, 2006. 10.1115/1.2401209.

[124] J. G. Lee and A. Palazzolo. Catcher bearing life prediction using a rainflow counting approach. *Journal of Tribology*, 134(3):031101–031101, 2012. 10.1115/1.4006176.

[125] P. S. Keogh. Contact dynamic phenomena in rotating machines: Active/passive considerations. *Mechanical Systems and Signal Processing*, 29:19–33, 2012.

[126] Jr J. L. Lawen and G. T. Flowers. Interaction dynamics between a flexible rotor and an auxiliary clearance bearing. *Journal of Vibration and Acoustics*, 121(2):183–189, 1999. 10.1115/1.2893962.

[127] J. I. Inayat-Hussain. Nonlinear dynamics of a magnetically supported rigid rotor in auxiliary bearings. *Mechanism and Machine Theory*, 45(11):1651 – 1667, 2010.

[128] J. I. Inayat-Hussain. Bifurcations in the response of a rigid rotor supported byÂ load sharing between magnetic and auxiliary bearings. *Meccanica*, 46(6):1341–1351, 2011.

[129] P. S. Keogh and M. O. T. Cole. Rotor vibration with auxiliary bearing contact in magnetic bearing systems part 1: Synchronous dynamics. *Proceedings of the Institution of Mechanical Engineers, Part C: Journal of Mechanical Engineering Science*, 217(4):377–392, 2003.

[130] P. S. Keogh, M. O. T. Cole, M. N. Sahinkaya, and C. R. Burrows. On the control of synchronous vibration in rotor/magnetic bearing systems involving auxiliary bearing contact. *Journal of Engineering for Gas Turbines and Power*, 126(2):366–372, 2004. 10.1115/1.1689362.

[131] P. S. Keogh and M. O. Cole. Contact dynamic response with misalignment in a flexible rotor/magnetic bearing system. *Journal of Engineering for Gas Turbines and Power*, 128(2):362–369, 2006. 10.1115/1.2056530.

[132] M. O. T. Cole. Model-free control of touchdowns involving circular whirl in rotor-magnetic bearing systems. *Journal of System Design and Dynamics*, 3(4):584–595, 2009.

[133] I. S. Cade, M. N. Sahinkaya, C. R. Burrows, and P. S. Keogh. An active auxiliary bearing control strategy to reduce the onset of asynchronous periodic contact modes in rotor/magnetic bearing systems. In *ASME Turbo Expo 2009: Power for Land, Sea and Air*, number 48876, pages 855–865, 2009. 10.1115/GT2009-59659.

[134] J. Jiang, H. Ulbrich, and A. Chavez. Improvement of rotor performance under rubbing conditions through active auxiliary bearings. *International Journal of Non-Linear Mechanics*, 41(8):949 – 957, 2006.

[135] C. Jarroux, J. Mahfoud, R. Dufour, B. Defoy, and T. Alban. On the dynamics of rotating machinery supported by amb during base motion. In *Proceedings of ISMB15*, pages 109–115, Kitakyushu, Japon, August 2016.

[136] G. Schweitzer and E. H. Maslen. *Magnetic Bearings, Theory, Design, and Application to Rotating Machinery*. Springer-Verlag, 2009.

[137] B. Defoy. *Investigation on the Control of Supercritical Centrifugal Compressors supported by Active Magnetic Bearings*. PhD thesis, INSA Lyon, 2012.

[138] T. Collins, A. Masala, R. S. Richter, and Z. Guo. Numerical and experimental results of auxiliary bearings testing on a high speed test rig. In *Proceedings of ISMB14*, Linz, Austria, August 2014.

[139] M. Helfert, M. Ernst, R. Nordmann, and B. Aeschlimann. High-speed video analysis of rotor-retainer-bearing-contacts due to failure of active magnetic bearings. In *10th International Symposium on Magnetic Bearing*, 2006.

[140] A. Palmgren. *Le roulements à billes et à rouleaux*. SKF, 1947.

[141] D. E. Brewe and B. J. Hamrock. Simplified solution for elliptical-contact deformation between two elastic solids. *Journal of Lubrication Technology*, 99(4):485–487, 1977. 10.1115/1.3453245.

[142] B. J. Hamrock and W. J. Anderson. *Rolling-Element Bearings*. Nasa Reference publication, 1105, 1983.

[143] T. A. Harris. *Rolling Bearing Analysis*. John Wiley & Sons, 2001.

[144] J. Sopanen and A. Mikkola. Dynamic model of a deep-groove ball bearing including localized and distributed defects. part 1: Theory. *Proceedings of the Institution of Mechanical Engineers, Part K: Journal of Multi-body Dynamics*, 217(3):201–211, 2003/09/01 2003.

[145] J. Sopanen and A. Mikkola. Dynamic model of a deep-groove ball bearing including localized and distributed defects. part 2: Implementation and results. *Proceedings of the Institution of Mechanical Engineers, Part K: Journal of Multi-body Dynamics*, 217(3):213–223, 2003/09/01 2003.

[146] E. Krämer. *Rolling-element Bearings*, pages 129–141. Springer Berlin Heidelberg, Berlin, Heidelberg, 1993.

[147] P. Guay. Roulements calculs. *Techniques de l'ingénieur Guidage mécanique*, base documentaire : TIB183DUO.(ref. article : bm5371), 2013. fre.

[148] H. Hertz. Ueber die berührung fester elastischer körper. *Journal für die reine und angewandte Mathematik (Crelle's Journal)*, 1882(92):156, 1882.

[149] P. Dietl, J. Wensing, and G. C. V. Nijen. Rolling bearing damping for dynamic analysis of multi-body systems—experimental and theoretical results. *Proceedings of the Institution of Mechanical Engineers, Part K: Journal of Multi-body Dynamics*, 214(1):33–43, 2000.

[150] G. Lundberg and A. Palmgren. *Dynamic capacity of roller bearings*. Generalstabens litografiska anstalts förlag, 1947.

[151] A. Palmgren and inc SKF Industries. *Ball and roller bearing engineering*. SKF Industries, 1959.

[152] C. M. Pereira, A. L. Ramalho, and J. A. Ambrósio. A critical overview of internal and external cylinder contact force models. *Nonlinear Dynamics*, 63(4):681–697, 2011.

[153] S. Lahriri and I. F. Santos. Experimental quantification of contact forces with impact, friction and uncertainty analysis. *Tribology International*, 66(0):93–104, 2013.

[154] S. Lahriri and I. F. Santos. Theoretical modelling, analysis and validation of the shaft motion and dynamic forces during rotor-stator contact. *Journal of Sound and Vibration*, 332(24):6359–6376, 2013. 10.1016/j.jsv.2013.07.008.

[155] S. Lahriri and I. F. Santos. Experimental quantification of dynamic forces and shaft motion in two different types of backup bearings under several contact conditions. *Mechanical Systems and Signal Processing*, 40(1):301–321, 2013.

[156] V. Popov. *Rigorous Treatment of Contact Problems - Hertzian Contact*, chapter 5, pages 55–70. Springer Berlin Heidelberg, 2010.

[157] M. Legrand. *Modèles de prédiction de l'interatction rotor/stator dans un moteur d'avion*. PhD thesis, École Centrales de Nantes, 2005.

[158] M. Legrand, B. Peseux, and C. Pierre. Investigation of structural rotor-stator modal interaction in turbomachinery. In *Sixth European Conference on Structural Dynamics (Eurodyn 2005)*, Paris, France, September 2005.

[159] G. A. H. Abulrub. *Modelling and control of contact in magnetic bearing / flexible rotor systems*. Phd thesis, Bath University, 2006.

[160] M. N. Sahinkaya, A. H. G. Abulrub, and P. S. Keogh. On the modelling of flexible rotor-magnetic bearing systems when in contact with retainer bearings. In *9th International Symposium on Magnetic Bearings*, 2004.

[161] M. N. Sahinkaya, A. H. G. Abulrub, P. S. Keogh, and C. R. Burrows. Multiple sliding and rolling contact dynamics for a flexible rotor/magnetic bearing system. *IEEE/ASME Transactions on Mechatronics*, 12(2):179–189, April 2007.

[162] S. Roques. *Modélisation du comportement dynamique couple rotor-stator d'une turbine en situation accidentelle*. Phd thesis, École Centrales de Nantes, 2007.

[163] H. M. Lankarani and P. E. Nikravesh. Continous contact force models for impact analysis in mutlibody systems. *Non-linear Dynamics*, pages 193–207, 1994.

[164] A. Gummer and B. Sauer. Influence of contact geometry on local friction energy and stiffness of revolute joints. *Journal of Tribology*, 134(2):021402–021402, 2012. 10.1115/1.4006248.

[165] C. S. Liu, K. Zhang, and R. Yang. The fem analysis and approximate model for cylindrical joints with clearances. *Mechanism and Machine Theory*, 42(2):183–197, 2007.

[166] K. H. Hunt and F. R. E. Crossley. Coefficient of restitution interpreted as damping in vibroimpact. *Journal of Applied Mechanics*, 42(2):440–445, 1975. 10.1115/1.3423596.

[167] Y. Zhang and I. Sharf. Validation of nonlinear viscoelastic contact force models for low speed impact. *Journal of Applied Mechanics*, 76(5):051002–051002, 2009. 10.1115/1.3112739.

[168] D. A. Jacobs and K. J. Waldron. Modeling inelastic collisions with the hunt& crossley model using the energetic coefficient of restitution. *Journal of Computational and Nonlinear Dynamics*, 10(2):021001–021001, 2015. 10.1115/1.4028473.

[169] C. Jarroux, R. Dufour, J. Mahfoud, B. Defoy, and T. Alban. Parametric analysis of a rigid rotor drop onto touchdown bearings. In *Colloquium 573 - Coupling and Nonlinear interactions in Rotating Machinery*, 2015.

[170] C. Jarroux, R. Dufour, J. Mahfoud, B. Defoy, T. Alban, and A. Delgado. Non-linear models for rotor-amb system drop. *MATEC Web Conf.*, 83:05005, 2016.

[171] C. Jarroux, R. Dufour, J. Mahfoud, B. Defoy, T. Alban, and A. Delgado. On the drop of a rotor-amb system onto touch-down bearing. In *11th IMechE International Conference on Vibrations in Rotating Machinery (VIRM11)*, pages 671–681, Manchester, United Kingdom, September 2016.

[172] I. Iordanoff, B. Bou-Said, A. Mezianne, and Y. Berthier. Effect of internal friction in the dynamic behavior of aerodynamic foil bearings. *Tribology International*, 41(5):387 – 395, 2008.

[173] B. Bou-Saïd, G. Grau, and I. Iordanoff. On nonlinear rotor dynamic effects of aerodynamic bearings with simple flexible rotors. *Journal of Engineering for Gas Turbines and Power*, 130(1):012503–012503–9, 2007. 10.1115/1.2747262.

[174] F. Balducchi, M. Arghir, and R. Gauthier. Experimental analysis of the unbalance response of rigid rotors supported on aerodynamic foil bearings. *Journal of Vibration and Acoustics*, 137(6):061014–061014, 2015. 10.1115/1.4031409.

[175] L. S. Andrés and T. H. Kim. Forced nonlinear response of gas foil bearing supported rotors. *Tribology International*, 41(8):704–715, 2008.

[176] K. Gjika and R. Dufour. Rigid body and nonlinear mount identification : Application to onboard equipment with hysteretic suspension. *Journal of Vibration and Control*, 5(1):75–94, 1999.

[177] E. Ciğeroğlu and H. N. Ögüven. Nonlinear vibration analysis of bladed disks with dry friction dampers. *Journal of Sound and Vibration*, 295(3-5):1028–1043, 2006.

[178] E. Chatelet, G. Michon, L. Manin, and G. Jacquet. Stick/slip phenomena in dynamics: Choice of contact model. numerical predictions & experiments. *Mechanism and Machine Theory*, 43(10):1211–1224, 2008.

[179] A. Al Majid and R. Dufour. Formulation of a hysteretic restoring force model. application to vibration isolation. *Nonlinear Dynamics*, 27(1):69–85, 2002.

[180] A. Al Majid and R. Dufour. Harmonic response of a structure mounted on an isolator modelled with a hysteretic operator: experiments and prediction. *Journal of Sound and Vibration*, 277(1-2):391–403, 2004.

[181] G. Michon, L. Manin, and R. Dufour. Hysteretic behavior of a belt tensioner: Modeling and experimental investigation. *Journal of Vibration and Control*, 11(9):1147–1158, 2005/09/01 2005.

[182] J. Bastien, G. Michon, L. Manin, and R. Dufour. An analysis of the modified dahl and masing models: Application to a belt tensioner. *Journal of Sound and Vibration*, 302(405):841–864, 2007.

[183] K. Gjika, R. Dufour, and G. Ferraris. Transient response of structures on viscoelastic or elastoplastic mounts: Prediction and experiment. *Journal of Sound and Vibration*, 198(3):361–378, 1996.

[184] B. Defoy, T. Alban, and J. Mahfoud. Experimental assessment of a new fuzzy controller applied to a flexible rotor supported by active magnetic bearings. *Journal of Vibration and Acoustics*, 136(5):051006–051006, 2014. 10.1115/1.4027959.

[185] B. Defoy, T. Alban, and J. Mahfoud. Energy cost assessment of a polar based controller applied to a flexible rotor supported by amb. *Mechanical Engineering Journal*, 2015.

[186] B. Defoy, T. Alban, and J. Mahfoud. Assessment of the effectiveness of a polar fuzzy approach for the control of centrifugal compressors. *Journal of Dynamic Systems, Measurement, and Control*, 136(4):041004–041004, 2014. 10.1115/1.4026468.

Appendix A

On-board rotors

The equations of motion for a on-board rotor-AMB system are:

$$\begin{aligned} M\ddot{\delta} + \left(\Omega C^{g} + \omega^{y} C_{bm}^{\omega^{y}}\right)\dot{\delta} + \big(K^{e} + \dot{\Omega} K^{\dot{\Omega}} + \dot{\omega}^{y} K_{bm}^{\dot{\omega}^{y}} + \Omega\omega^{y} K_{bm}^{\Omega\omega^{y}} + \omega^{x2} K_{bm}^{\omega^{x2}} \\ + \omega^{y2} K_{bm}^{\omega^{y2}} + \omega^{z2} K_{bm}^{\omega^{z2}} + \omega^{x}\omega^{z} K_{bm}^{\omega^{x}\omega^{z}}\big)\delta = F_{mu} + F_{mu,bm} + F_{bm} + F_{amb} + F_{c} + F_{g} \end{aligned} \tag{A.1}$$

In the following, the subscripts *d* and *sh* stand for disc or shaft element, respectively. They can be combined with the subscript *bm* which corresponds to the base motion effects. The elasticity of the shaft is represented by the subscript *e* while the classical gyroscopic effects of disc and shaft elements are represented by *g*. The subscript *re* stands for the rotational effect coming from disc and shaft kinetic energies while *gse* comes from the geometric stiffening effect associated with centrifugal stressing due to base rotations. The latter comes exclusively from the shaft elements. The mass unbalance forces are generated by the rotor rotational speed but also by the base motions which are respectively represented by the subscripts *mu* and mu,bm. The subscripts *c* and *s* are respectively associated with cosine and sine functions. The expressions of the kinetic, strain energies and the virtual work of external forces are not detailed in this work and readers can refer to Dakel *et al.* [5, 39]. In what follows, the different elements of the equations of motion (A.1) are detailed in their elementary expressions.

A.1 The mass unbalance

The vector $\{F_{emu}(t)\}$ is the classical force vector found in conventional rotordynamics studies.

$$\{F_{emu}(t)\} = \{V_{emu}^{c}\}\,\Omega^{2}\cos\Omega t + \{V_{emu}^{s}\}\,\Omega^{2}\sin\Omega t \tag{A.2}$$

with:

$$\left\{V^{c}_{emu}\right\} = m_{mu}r_{mu}\begin{Bmatrix} \sin\eta_{mu} \\ \cos\eta_{mu} \\ 0 \\ 0 \end{Bmatrix} ; \left\{V^{s}_{emu}\right\} = m_{mu}r_{mu}\begin{Bmatrix} \cos\eta_{mu} \\ -\sin\eta_{mu} \\ 0 \\ 0 \end{Bmatrix} \tag{A.3}$$

where η_{mu} is the initial phase angle of the mass unbalance. The vector $\left\{F_{emu,bm}(t)\right\}$ represents the base motion intake in the formulation of the mass unbalance forces.

$$\begin{aligned} \left\{F_{emu,bm}(t)\right\} = &\left(\left\{V^{\dot{\omega}^y,c}_{emu,bm}\right\}\dot{\omega}^y + \left\{V^{\Omega\omega^y,c}_{emu,bm}\right\}\Omega\omega^y + \left\{V^{\omega^{x2},c}_{emu,bm}\right\}\omega^{x2} + \left\{V^{\omega^{y2},c}_{emu,bm}\right\}\omega^{y2} \right. \\ &+ \left\{V^{\omega^{z2},c}_{emu,bm}\right\}\omega^{z2} + \left.\left\{V^{\omega^x\omega^z,c}_{emu,bm}\right\}\omega^x\omega^z\right)\cos\Omega t + \left(\left\{V^{\dot{\omega}^y,s}_{emu,bm}\right\}\dot{\omega}^y + \left\{V^{\Omega\omega^y,s}_{emu,bm}\right\}\Omega\omega^y \right. \\ &+ \left.\left\{V^{\omega^{x2},s}_{emu,bm}\right\}\omega^{x2} + \left\{V^{\omega^{y2},s}_{emu,bm}\right\}\omega^{y2}\left\{V^{\omega^{z2},s}_{emu,bm}\right\}\omega^{z2} + \left\{V^{\omega^x\omega^z,s}_{emu,bm}\right\}\omega^x\omega^z\right)\sin\Omega t \end{aligned} \tag{A.4}$$

with:

$$\left\{V^{\dot{\omega}^y,c}_{emu,bm}\right\} = m_{mu}r_{mu}\begin{Bmatrix} -\cos\eta_{mu} \\ \sin\eta_{mu} \\ 0 \\ 0 \end{Bmatrix} ; \left\{V^{\dot{\omega}^y,s}_{emu,bm}\right\} = m_{mu}r_{mu}\begin{Bmatrix} \sin\eta_{mu} \\ \cos\eta_{mu} \\ 0 \\ 0 \end{Bmatrix} \tag{A.5}$$

$$\left\{V^{\Omega\omega^y,c_1}_{emu,bm}\right\} = 2m_{mu}r_{mu}\begin{Bmatrix} \sin\eta_{mu} \\ \cos\eta_{mu} \\ 0 \\ 0 \end{Bmatrix} ; \left\{V^{\Omega\omega^y,c_1}_{emu,bm}\right\} = 2m_{mu}r_{mu}\begin{Bmatrix} \cos\eta_{mu} \\ -\sin\eta_{mu} \\ 0 \\ 0 \end{Bmatrix} \tag{A.6}$$

$$\left\{V^{\omega^{x2},c}_{emu,bm}\right\} = m_{mu}r_{mu}\begin{Bmatrix} 0 \\ \cos\eta_{mu} \\ 0 \\ 0 \end{Bmatrix} ; \left\{V^{\omega^{x2},s}_{emu,bm}\right\} = m_{mu}r_{mu}\begin{Bmatrix} 0 \\ -\sin\eta_{mu} \\ 0 \\ 0 \end{Bmatrix} \tag{A.7}$$

$$\left\{V^{\omega^{y2},c}_{emu,bm}\right\} = m_{mu}r_{mu}\begin{Bmatrix} \sin\eta_{mu} \\ \cos\eta_{mu} \\ 0 \\ 0 \end{Bmatrix} ; \left\{V^{\omega^{y2},s}_{emu,bm}\right\} = m_{mu}r_{mu}\begin{Bmatrix} \cos\eta_{mu} \\ -\sin\eta_{mu} \\ 0 \\ 0 \end{Bmatrix} \tag{A.8}$$

$$\left\{V^{\omega^{z2},c}_{emu,bm}\right\} = m_{mu}r_{mu}\begin{Bmatrix} \sin\eta_{mu} \\ 0 \\ 0 \\ 0 \end{Bmatrix} ; \left\{V^{\omega^{z2},s}_{emu,bm}\right\} = m_{mu}r_{mu}\begin{Bmatrix} \cos\eta_{mu} \\ 0 \\ 0 \\ 0 \end{Bmatrix} \tag{A.9}$$

$$\left\{V_{emu,bm}^{\omega^x\omega^z,c}\right\} = m_{mu}r_{mu}\begin{Bmatrix} -\cos\eta_{mu} \\ -\sin\eta_{mu} \\ 0 \\ 0 \end{Bmatrix};\left\{V_{emu,bm}^{\omega^x\omega^z,s}\right\} = m_{mu}r_{mu}\begin{Bmatrix} \sin\eta_{mu} \\ -\cos\eta_{mu} \\ 0 \\ 0 \end{Bmatrix} \tag{A.10}$$

A.2 Disc matrices and external force vectors

The disc finite element *ed* is modelled by a node n_i and has four degrees of freedom, two translations $u_{ed}^{n_i}$, $w_{ed}^{n_i}$ and two rotations $\theta_{ed}^{n_i}$, $\varphi_{ed}^{n_i}$. The nodal displacement vector $\left\{\delta_{ed}^{n}\right\}$ is written as:

$$\left\{\delta_{ed}^{n}\right\} = \left\langle u_{ed}^{n_i}, w_{ed}^{n_i}, \theta_{ed}^{n_i}, \varphi_{ed}^{n_i}\right\rangle^T \tag{A.11}$$

Using the expression of the kinetic energy of the disc, the equations of motion are obtained thanks to the Lagrange's equations 2.2:

$$\left[M_{ed}\left(t\right)\right]\left\{\ddot{\delta}_{ed}^{n}\right\} + \left[C_{ed}\left(t\right)\right]\left\{\dot{\delta}_{ed}^{n}\right\} + \left[K_{ed}\left(t\right)\right]\left\{\delta_{ed}^{n}\right\} - \left\{F_{ed}\left(t\right)\right\} \tag{A.12}$$

with:

$$\left[M_{ed}\left(t\right)\right] = \left[M_{ed}^{tr}\right] + \left[M_{ed}^{ro}\right] \tag{A.13}$$

$$\left[C_{ed}\left(t\right)\right] = \left[C_{ed}^{g}\right]\Omega + \left[C_{ed,bm}^{re,\omega^y}\right]\omega^y \tag{A.14}$$

$$\begin{aligned}\left[K_{ed}\left(t\right)\right] = {} & \left[K_{ed}^{\dot{\Omega}}\right]\dot{\Omega} + \left[K_{ed,bm}^{re,\dot{\omega}^y}\right]\dot{\omega}^y + \left[K_{ed,bm}^{re,\Omega\omega^y}\right]\Omega\omega^y + \left[K_{ed,bm}^{re,\omega^{x2}}\right]\omega^{x2} \\ & + \left[K_{ed,bm}^{re,\omega^{y2}}\right]\omega^{y2} + \left[K_{ed,bm}^{re,\omega^{z2}}\right]\omega^{z2} + \left[K_{ed,bm}^{re,\omega^x\omega^z}\right]\omega^x\omega^z\end{aligned} \tag{A.15}$$

$$\begin{aligned}&\left\{F_{ed}\left(t\right)\right\} = -\left\{V_{ed,bm}^{u}\right\}\left(\ddot{x}_0 + 2\dot{z}_0\omega^y - 2\dot{y}_0\omega^z + z_0\left(\dot{\omega}^y + \omega^x\omega^z\right) - y_0\left(\dot{\omega}^z - \omega^x\omega^y\right)\right. \\ &\left. -x_0\left(\omega^{y2} + \omega^{z2}\right)\right) \\ &- \left\{V_{ed,bm}^{w}\right\}\left(\ddot{z}_0 + 2\dot{y}_0\omega^x - 2\dot{x}_0\omega^y + y_0\left(\dot{\omega}^x + \omega^y\omega^z\right) - x_0\left(\dot{\omega}^y - \omega^x\omega^z\right) - z_0\left(\omega^{x2} + \omega^{y2}\right)\right) \\ &- \left\{V_{ed,bm}^{yw}\right\}\left(\dot{\omega}^x + \omega^y\omega^z\right) + \left\{V_{ed,bm}^{yu}\right\}\left(\dot{\omega}^z - \omega^x\omega^y\right) - \left\{V_{ed,bm}^{\theta}\right\}\left(\dot{\omega}^x + \omega^y\omega^z\right) \\ &- \left\{V_{ed,bm}^{\varphi}\right\}\left(\dot{\omega}^z - \omega^x\omega^y\right) - \left\{V_{ed,bm}^{y\varphi}\right\}\left(\Omega\omega^x + \omega^x\omega^y\right) + \left\{V_{ed,bm}^{y\theta}\right\}\left(\Omega\omega^z + \omega^y\omega^z\right)\end{aligned} \tag{A.16}$$

where the related matrices and external force vectors are detailed from equation A.17 to A.28.

$$\left[M_{ed}^{tr}\right]=\begin{bmatrix} m_d & 0 & 0 & 0\\ 0 & m_d & 0 & 0\\ 0 & 0 & 0 & 0\\ 0 & 0 & 0 & 0 \end{bmatrix} \tag{A.17}$$

$$\left[M_{ed}^{ro}\right]=\begin{bmatrix} 0 & 0 & 0 & 0\\ 0 & 0 & 0 & 0\\ 0 & 0 & I_{m_d}^{x} & 0\\ 0 & 0 & 0 & I_{m_d}^{x} \end{bmatrix} \tag{A.18}$$

$$\left[C_{ed}^{g}\right]=\begin{bmatrix} 0 & 0 & 0 & 0\\ 0 & 0 & 0 & 0\\ 0 & 0 & 0 & -I_{m_d}^{y}\\ 0 & 0 & I_{m_d}^{y} & 0 \end{bmatrix} \tag{A.19}$$

$$\left[C_{ed,bm}^{re,\omega^y}\right]=\begin{bmatrix} 0 & 2m_d & 0 & 0\\ -2m_d & 0 & 0 & 0\\ 0 & 0 & 0 & -\left(I_{m_d}^{y}-2I_{m_d}^{x}\right)\\ 0 & 0 & I_{m_d}^{y}-2I_{m_d}^{x} & 0 \end{bmatrix} \tag{A.20}$$

$$\left[K_{ed}^{\dot{\Omega}}\right]=\begin{bmatrix} 0 & 0 & 0 & 0\\ 0 & 0 & 0 & 0\\ 0 & 0 & 0 & 0\\ 0 & 0 & I_{m_d}^{y} & 0 \end{bmatrix} \tag{A.21}$$

$$\left[K_{ed,bm}^{re,\dot{\omega}^y}\right]=\begin{bmatrix} 0 & m_d & 0 & 0\\ -m_d & 0 & 0 & 0\\ 0 & 0 & 0 & I_{m_d}^{x}\\ 0 & 0 & I_{m_d}^{y}-I_{m_d}^{x} & 0 \end{bmatrix} \tag{A.22}$$

$$\left[K_{ed,bm}^{re,\Omega\omega^y}\right]=\begin{bmatrix} 0 & 0 & 0 & 0\\ 0 & 0 & 0 & 0\\ 0 & 0 & I_{m_d}^{y} & 0\\ 0 & 0 & 0 & I_{m_d}^{y} \end{bmatrix} \tag{A.23}$$

$$\left[K_{ed,bm}^{re,\omega^{x2}}\right]=\begin{bmatrix} 0 & 0 & 0 & 0\\ 0 & -m_d & 0 & 0\\ 0 & 0 & 0 & 0\\ 0 & 0 & 0 & -\left(I_{m_d}^{y}-I_{m_d}^{x}\right) \end{bmatrix} \tag{A.24}$$

$$\left[K_{ed,bm}^{re,\omega^{y2}}\right] = \begin{bmatrix} -m_d & 0 & 0 & 0 \\ 0 & -m_d & 0 & 0 \\ 0 & 0 & I_{m_d}^{y} - I_{m_d}^{x} & 0 \\ 0 & 0 & 0 & I_{m_d}^{y} - I_{m_d}^{x} \end{bmatrix} \tag{A.25}$$

$$\left[K_{ed,bm}^{re,\omega^{z2}}\right] = \begin{bmatrix} -m_d & 0 & 0 & 0 \\ 0 & 0 & 0 & 0 \\ 0 & 0 & -\left(I_{m_d}^{y} - I_{m_d}^{x}\right) & 0 \\ 0 & 0 & 0 & 0 \end{bmatrix} \tag{A.26}$$

$$\left[K_{ed,bm}^{re,\omega^{x}\omega^{z}}\right] = \begin{bmatrix} 0 & m_d & 0 & 0 \\ m_d & 0 & 0 & 0 \\ 0 & 0 & 0 & I_{m_d}^{y} - I_{m_d}^{x} \\ 0 & 0 & I_{m_d}^{y} - I_{m_d}^{x} & 0 \end{bmatrix} \tag{A.27}$$

$$\begin{gathered} \left\{V_{ed,bm}^{u}\right\} = \begin{Bmatrix} m_d \\ 0 \\ 0 \\ 0 \end{Bmatrix} ; \left\{V_{ed,bm}^{w}\right\} = \begin{Bmatrix} 0 \\ m_d \\ 0 \\ 0 \end{Bmatrix} ; \left\{V_{ed,bm}^{yw}\right\} = y_d \begin{Bmatrix} 0 \\ m_d \\ 0 \\ 0 \end{Bmatrix} ; \left\{V_{ed,bm}^{yu}\right\} = y_d \begin{Bmatrix} m_d \\ 0 \\ 0 \\ 0 \end{Bmatrix} \\ \left\{V_{ed,bm}^{\theta}\right\} = \begin{Bmatrix} 0 \\ 0 \\ I_{m_d}^{x} \\ 0 \end{Bmatrix} ; \left\{V_{ed,bm}^{\varphi}\right\} = \begin{Bmatrix} 0 \\ 0 \\ 0 \\ I_{m_d}^{x} \end{Bmatrix} ; \left\{V_{ed,bm}^{y\varphi}\right\} = \begin{Bmatrix} 0 \\ 0 \\ 0 \\ I_{m_d}^{y} \end{Bmatrix} ; \left\{V_{ed,bm}^{y\theta}\right\} = \begin{Bmatrix} 0 \\ 0 \\ I_{m_d}^{y} \\ 0 \end{Bmatrix} \end{gathered} \tag{A.28}$$

A.3 Shaft matrices and external force vectors

The shaft is modelled with Timoshenko beam elements with two nodes and four Dof per node, made of circular and constant sections. The nodal displacement vector $\left\{\delta_{esh_i}^{n}\right\}$ of the shaft finite element esh_i associated with the nodes (n_i, n_{i+1}) and expressed in the reference frame R:

$$\left\{\delta_{esh_i}^{n}\right\} = \left\langle u_{esh_i}^{n_i}, w_{esh_i}^{n_i}, \theta_{esh_i}^{n_i}, \varphi_{esh_i}^{n_i}, u_{esh_i}^{n_{i+1}}, w_{esh_i}^{n_{i+1}}, \theta_{esh_i}^{n_{i+1}}, \varphi_{esh_i}^{n_{i+1}} \right\rangle_R^T \tag{A.29}$$

The displacement vector $\left\{\delta_{esh_i}^{n}\right\}$ is separated depending on the direction of bending:

$$\left\{\delta_{esh_i}^{n,u}\right\} = \left\langle u_{esh_i}^{n_i}, \varphi_{esh_i}^{n_i}, u_{esh_i}^{n_{i+1}}, \varphi_{esh_i}^{n_{i+1}} \right\rangle_R^T \tag{A.30}$$

$$\left\{\delta_{esh_i}^{n,w}\right\} = \left\langle w_{esh_i}^{n_i}, \theta_{esh_i}^{n_i}, w_{esh_i}^{n_{i+1}}, \theta_{esh_i}^{n_{i+1}} \right\rangle_R^T \tag{A.31}$$

The nodal shape functions permit expressing the bending displacements u_{esh_i} and w_{esh_i} and the bending rotations θ_{esh_i} et φ_{esh_i} as a function of the nodal displacement vectors:

$$\begin{cases} u_{esh_i}\left(y_{esh_i}\right) = \left\langle F^u_{esh_i}\left(y_{esh_i}\right)\right\rangle \left\{\delta^{n,u}_{esh_i}\right\} \\ w_{esh_i}\left(y_{esh_i}\right) = \left\langle F^w_{esh_i}\left(y_{esh_i}\right)\right\rangle \left\{\delta^{n,w}_{esh_i}\right\} \\ \theta_{esh_i}\left(y_{esh_i}\right) = \dfrac{\partial w_{esh_i}\left(y_{esh_i}\right)}{\partial y_{esh_i}} = \left\langle \dfrac{dF^w_{esh_i}\left(y_{esh_i}\right)}{dy}\right\rangle \left\{\delta^{n,w}_{esh_i}\right\} \\ \varphi_{esh_i}\left(y_{esh_i}\right) = -\dfrac{\partial u_{esh_i}\left(y_{esh_i}\right)}{\partial y_{esh_i}} = -\left\langle \dfrac{dF^u_{esh_i}\left(y_{esh_i}\right)}{dy}\right\rangle \left\{\delta^{n,u}_{esh_i}\right\} \end{cases} \tag{A.32}$$

where $F^u_{esh_i}\left(y_{esh_i}\right)$ and $F^w_{esh_i}\left(y_{esh_i}\right)$ are the shape function vectors, written as:

$$\begin{cases} \left\langle F^u_{esh_i}\left(y_{esh_i}\right)\right\rangle = \left\langle N_1\left(y_{esh_i}\right) \quad 0 \quad 0 \quad N_2\left(y_{esh_i}\right) \quad N_3\left(y_{esh_i}\right) \quad 0 \quad 0 \quad N_4\left(y_{esh_i}\right)\right\rangle \\ \left\langle F^w_{esh_i}\left(y_{esh_i}\right)\right\rangle = \left\langle 0 \quad N_1\left(y_{esh_i}\right) \quad -N_2\left(y_{esh_i}\right) \quad 0 \quad 0 \quad N_3\left(y_{esh_i}\right) \quad -N_4\left(y_{esh_i}\right) \quad 0\right\rangle \end{cases} \tag{A.33}$$

$$\begin{cases} N_1\left(y_{esh_i}\right) = 1 - \dfrac{3y^2_{esh_i}}{l^2_{esh_i}} + \dfrac{2y^3_{esh_i}}{l^3_{esh_i}} \\ N_2\left(y_{esh_i}\right) = -y_{esh_i} + \dfrac{2y^2_{esh_i}}{l_{esh_i}} - \dfrac{y^3_{esh_i}}{l^2_{esh_i}} \\ N_3\left(y_{esh_i}\right) = \dfrac{3y^2_{esh_i}}{l^2_{esh_i}} - \dfrac{2y^3_{esh_i}}{l^3_{esh_i}} \\ N_4\left(y_{esh_i}\right) = \dfrac{y^2_{esh_i}}{l_{esh_i}} - \dfrac{y^3_{esh_i}}{l^2_{esh_i}} \end{cases} \tag{A.34}$$

Matrices and elementary vectors are obtained by substituting the expressions of displacements and slopes in kinetic and strain energies. After the integration along the length l_{esh_i}, Lagrange's equations are applied to obtain the equations of motion:

$$\begin{aligned} &\frac{d}{dt}\left(\frac{\partial T_{esh_i}}{\partial\left\{\dot{\delta}^n_{esh_i}\right\}}\right) - \left(\frac{\partial T_{esh_i}}{\partial\left\{\delta^n_{esh_i}\right\}}\right) \\ &= \left[M_{esh_i}(t)\right]\left\{\ddot{\delta}^n_{esh_i}\right\} + \left[C_{esh_i}(t)\right]\left\{\dot{\delta}^n_{esh_i}\right\} + \left[K_{esh_i}(t)\right]\left\{\delta^n_{esh_i}\right\} - \left\{F_{esh_i}(t)\right\} \end{aligned} \tag{A.35}$$

with:

$$\left[M_{esh_i}(t)\right] = \left[M^{tr}_{esh_i}\right] + \left[M^{ro}_{esh_i}\right] \tag{A.36}$$

$$\left[C_{esh_i}(t)\right] = \left[C^g_{esh_i}\right]\Omega + \left[C^{re,\omega^y}_{esh_i,bm}\right]\omega^y \tag{A.37}$$

$$\left[K_{esh_i}(t)\right] = \left[K^{e}_{esh_i}\right] + \left[K^{\dot{\Omega}}_{esh_i}\right]\dot{\Omega} + \left[K^{re,\dot{\omega}^y}_{esh_i,bm}\right]\dot{\omega}^y + \left[K^{re,\Omega\omega^y}_{esh_i,bm}\right]\Omega\omega^y + \left(\left[K^{re,\omega^{x2}}_{esh_i,bm}\right] + \left[K^{gse,\omega^{x2}}_{esh_i,bm}\right]\right)\omega^{x2}$$
$$+ \left[K^{re,\omega^{y2}}_{esh_i,bm}\right]\omega^{y2} + \left(\left[K^{re,\omega^{z2}}_{esh_i,bm}\right] + \left[K^{gse,\omega^{z2}}_{esh_i,bm}\right]\right)\omega^{z2} + \left[K^{re,\omega^x\omega^z}_{esh_i,bm}\right]\omega^x\omega^z \tag{A.38}$$

$$\left[M^{tr}_{esh_i}\right] = \rho_{esh_i}S_{esh_i}\left[M_{esh_i,1}\right] \tag{A.39}$$

$$\left[M^{ro}_{esh_i}\right] = \rho_{esh_i}I^{x}_{S_{esh_i}}\left[M_{esh_i,2}\right] \tag{A.40}$$

$$\left[C^{g}_{esh_i}\right] = 2\rho_{esh_i}I^{x}_{S_{esh_i}}\left[M_{esh_i,5}\right] \tag{A.41}$$

$$\left[C^{re,\omega^y}_{esh_i,bm}\right] = 2\rho_{esh_i}S_{esh_i}\left[M_{esh_i,6}\right] \tag{A.42}$$

$$\left[K^{e}_{esh_i}\right] = E_{esh_i}I^{x}_{S_{esh_i}}\left[M_{esh_i,7}\right] \tag{A.43}$$

$$\left[K^{\dot{\Omega}}_{esh_i}\right] = \rho_{esh_i}I^{x}_{S_{esh_i}}\left[M_{esh_i,5}\right] - \rho_{esh_i}I^{x}_{S_{esh_i}}\left[M_{esh_i,4}\right] \tag{A.44}$$

$$\left[K^{re,\dot{\omega}^y}_{esh_i,bm}\right] = \rho_{esh_i}S_{esh_i}\left[M_{esh_i,6}\right] - \rho_{esh_i}I^{x}_{S_{esh_i}}\left[M_{esh_i,4}\right] \tag{A.45}$$

$$\left[K^{re,\Omega\omega^y}_{esh_i,bm}\right] = 2\rho_{esh_i}I^{x}_{S_{esh_i}}\left[M_{esh_i,2}\right] \tag{A.46}$$

$$\left[K^{re,\omega^{x2}}_{esh_i,bm}\right] = \rho_{esh_i}S_{esh_i}\left[M_{esh_i,10}\right] + \rho_{esh_i}I^{x}_{S_{esh_i}}\left[M_{esh_i,11}\right] \tag{A.47}$$

$$\left[K^{re,\omega^{y2}}_{esh_i,bm}\right] = -\left(\rho_{esh_i}S_{esh_i}\left[M_{esh_i,1}\right] - \rho_{esh_i}I^{x}_{S_{ea_i}}\left[M_{esh_i,2}\right]\right) \tag{A.48}$$

$$\left[K^{re,\omega^{z2}}_{esh_i,bm}\right] = \rho_{esh_i}S_{esh_i}\left[M_{esh_i,12}\right] + \rho_{esh_i}I^{x}_{S_{ea_i}}\left[M_{esh_i,13}\right] \tag{A.49}$$

$$\left[K^{re,\omega^x\omega^z}_{esh_i,bm}\right] = \rho_{esh_i}S_{esh_i}\left[M_{esh_i,14}\right] - \rho_{esh_i}I^{x}_{S_{ea_i}}\left[M_{esh_i,4}\right] \tag{A.50}$$

$$\left[K^{gse,\omega^{x2}}_{esh_i,bm}\right] = \left[K^{gse,\omega^{z2}}_{esh_i,bm}\right] = \frac{\rho_{esh_i}S_{esh_i}\left(l^{2}_{esh_i} - y^{n_i2}_{sh}\right)}{2}\left[M_{esh_i,15}\right] \tag{A.51}$$

$$\begin{aligned}
\left\{F_{esh_i}(t)\right\} = & -\rho_{esh_i} S_{esh_i} \left\{V_{esh_i,1}\right\} \left(\ddot{x}_0 + 2\dot{z}_0 \omega^y - 2\dot{y}_0 \omega^z + z_0 \left(\dot{\omega}^y + \omega^x \omega^z\right) - y_0 \left(\dot{\omega}^z - \omega^x \omega^y\right)\right. \\
& \left. -x_0 \left(\omega^{y2} + \omega^{z2}\right)\right) \\
& - \rho_{esh_i} S_{esh_i} \left\{V_{esh_i,2}\right\} \left(\ddot{z}_0 + 2\dot{y}_0 \omega^x - 2\dot{x}_0 \omega^y + y_0 \left(\dot{\omega}^x + \omega^y \omega^z\right) - x_0 \left(\dot{\omega}^y - \omega^x \omega^z\right) - z_0 \left(\omega^{x2} + \omega^{y2}\right)\right) \\
& - \rho_{esh_i} S_{esh_i} \left\{V_{esh_i,3}\right\} \left(\dot{\omega}^x + \omega^y \omega^z\right) + \rho_{esh_i} S_{esh_i} \left\{V_{esh_i,4}\right\} \left(\dot{\omega}^z - \omega^x \omega^y\right) \\
& - \rho_{esh_i} I^x_{S_{esh_i}} \left\{V_{esh_i,5}\right\} \left(\dot{\omega}^x - 2\Omega \omega^z - \omega^y \omega^z\right) + I^x_{S_{esh_i}} \left\{V_{esh_i,6}\right\} \left(\dot{\omega}^z + 2\Omega \omega^z + \omega^x \omega^y\right)
\end{aligned} \tag{A.52}$$

where the related matrices and external force vectors are detailed from equation A.53 to A.70.

$$\left[M_{esh_i,2}\right] = \frac{1}{30 l_{esh_i}} \begin{bmatrix}
36 & 0 & 0 & -3l_{esh_i} & -36 & 0 & 0 & -3l_{esh_i} \\
 & 36 & 3l_{esh_i} & 0 & 0 & -36 & 3l_{esh_i} & 0 \\
 & & 4l_{esh_i}^2 & 0 & 0 & -3l_{esh_i} & -l_{esh_i}^2 & 0 \\
 & & & 4l_{esh_i}^2 & 3l_{esh_i} & 0 & 0 & -l_{esh_i}^2 \\
 & & & & 36 & 0 & 0 & 3l_{esh_i} \\
S & & & & & 36 & -3l_{esh_i} & 0 \\
Y & & & & & & 4l_{esh_i}^2 & 0 \\
M & & & & & & & 4l_{esh_i}^2
\end{bmatrix} \tag{A.53}$$

$$\left[M_{esh_i,3}\right] = \frac{1}{30 l_{esh_i}} \begin{bmatrix}
-36 & 0 & 0 & 3l_{esh_i} & 36 & 0 & 0 & 3l_{esh_i} \\
 & 36 & 3l_{esh_i} & 0 & 0 & -36 & 3l_{esh_i} & 0 \\
 & & 4l_{esh_i}^2 & 0 & 0 & -3l_{esh_i} & -l_{esh_i}^2 & 0 \\
 & & & -4l_{esh_i}^2 & -3l_{esh_i} & 0 & 0 & l_{esh_i}^2 \\
 & & & & -36 & 0 & 0 & -3l_{esh_i} \\
S & & & & & 36 & -3l_{esh_i} & 0 \\
Y & & & & & & 4l_{esh_i}^2 & 0 \\
M & & & & & & & -4l_{esh_i}^2
\end{bmatrix} \tag{A.54}$$

$$\left[M_{esh_i,4}\right] = \frac{1}{30 l_{esh_i}} \begin{bmatrix} 0 & 36 & 3l_{esh_i} & 0 & 0 & -36 & 3l_{esh_i} & 0 \\ & 0 & 0 & -3l_{esh_i} & -36 & 0 & 0 & -3l_{esh_i} \\ & & 0 & -4l_{esh_i}^2 & -3l_{esh_i} & 0 & 0 & l_{esh_i}^2 \\ & & & 0 & 0 & 3l_{esh_i} & l_{esh_i}^2 & 0 \\ & & & & 0 & 36 & -3l_{esh_i} & 0 \\ S & & & & & 0 & 0 & 3l_{esh_i} \\ Y & & & & & & 0 & -4l_{esh_i}^2 \\ M & & & & & & & 0 \end{bmatrix} \tag{A.55}$$

$$\left[M_{esh_i,5}\right] = \frac{1}{30 l_{esh_i}} \begin{bmatrix} 0 & -36 & -3l_{esh_i} & 0 & 0 & 36 & -3l_{esh_i} & 0 \\ A & 0 & 0 & -3l_{esh_i} & -36 & 0 & 0 & -3l_{esh_i} \\ N & & 0 & -4l_{esh_i}^2 & -3l_{esh_i} & 0 & 0 & l_{esh_i}^2 \\ T & & & 0 & 0 & -3l_{esh_i} & -l_{esh_i}^2 & 0 \\ I & & & & 0 & -36 & 3l_{esh_i} & 0 \\ S & & & & & 0 & 0 & 3l_{esh_i} \\ Y & & & & & & 0 & -4l_{esh_i}^2 \\ M & & & & & & & 0 \end{bmatrix} \tag{A.56}$$

$$\left[M_{esh_i,6}\right] = \frac{l_{esh_i}}{420} \begin{bmatrix} 0 & 156 & 22l_{esh_i} & 0 & 0 & 54 & -13l_{esh_i} & 0 \\ A & 0 & 0 & 22l_{esh_i} & -54 & 0 & 0 & -13l_{esh_i} \\ N & & 0 & 4l_{esh_i}^2 & -13l_{esh_i} & 0 & 0 & -3l_{esh_i}^2 \\ T & & & 0 & 0 & -13l_{esh_i} & 3l_{esh_i}^2 & 0 \\ I & & & & 0 & 156 & -22l_{esh_i} & 0 \\ S & & & & & 0 & 0 & -22l_{esh_i} \\ Y & & & & & & 0 & 4l_{esh_i}^2 \\ M & & & & & & & 0 \end{bmatrix} \tag{A.57}$$

$$\left[M_{esh_i,7}\right]=\frac{1}{\left(1+\lambda\right)l^3_{esh_i}}\begin{bmatrix} 12 & 0 & 0 & -6l_{esh_i} & -12 & 0 & 0 & -6l_{esh_i} \\ & 12 & 6l_{esh_i} & 0 & 0 & -12 & 6l_{esh_i} & 0 \\ & & \left(4+\lambda\right)l^2_{esh_i} & 0 & 0 & -6l_{esh_i} & \left(2-\lambda\right)l^2_{esh_i} & 0 \\ & & & \left(4+\lambda\right)l^2_{esh_i} & 6l_{esh_i} & 0 & 0 & \left(2-\lambda\right)l^2_{esh_i} \\ & & & & 12 & 0 & 0 & 6l_{esh_i} \\ S & & & & & 12 & -6l_{esh_i} & 0 \\ Y & & & & & & \left(4+\lambda\right)l^2_{esh_i} & 0 \\ M & & & & & & & \left(4+\lambda\right)l^2_{esh_i} \end{bmatrix} \tag{A.58}$$

where $\lambda=\frac{12E_{esh_i}I^x_{S_{esh_i}}}{G_{esh_i}kS_{esh_i}l^2_{esh_i}}$

$$\left[M_{esh_i,8}\right]=\frac{1}{l^3_{esh_i}}\begin{bmatrix} -12 & 0 & 0 & 6l_{esh_i} & 12 & 0 & 0 & 6l_{esh_i} \\ & 12 & 6l_{esh_i} & 0 & 0 & -12 & 6l_{esh_i} & 0 \\ & & 4l^2_{esh_i} & 0 & 0 & -6l_{esh_i} & 2l^2_{esh_i} & 0 \\ & & & -4l^2_{esh_i} & -6l_{esh_i} & 0 & 0 & -2l^2_{esh_i} \\ & & & & -12 & 0 & 0 & -6l_{esh_i} \\ S & & & & & 12 & -6l_{esh_i} & 0 \\ Y & & & & & & 4l^2_{esh_i} & 0 \\ M & & & & & & & -4l^2_{esh_i} \end{bmatrix} \tag{A.59}$$

$$\left[M_{esh_i,9}\right]=\frac{1}{l^3_{esh_i}}\begin{bmatrix} 0 & 12 & 6l_{esh_i} & 0 & 0 & -12 & 6l_{esh_i} & 0 \\ & 0 & 0 & -6l_{esh_i} & -12 & 0 & 0 & -6l_{esh_i} \\ & & 0 & -4l^2_{esh_i} & -6l_{esh_i} & 0 & 0 & -2l^2_{esh_i} \\ & & & 0 & 0 & 6l_{esh_i} & -2l^2_{esh_i} & 0 \\ & & & & 0 & 12 & -6l_{esh_i} & 0 \\ S & & & & & 0 & 0 & 6l_{esh_i} \\ Y & & & & & & 0 & -4l^2_{esh_i} \\ M & & & & & & & 0 \end{bmatrix} \tag{A.60}$$

$$\left[M_{esh_i,10}\right] = \frac{l_{esh_i}}{420}\begin{bmatrix} 0 & 0 & 0 & 0 & 0 & 0 & 0 & 0 \\ & -156 & -22l_{esh_i} & 0 & 0 & -54 & 13l_{esh_i} & 0 \\ & & -4l_{esh_i}^2 & 0 & 0 & -13l_{esh_i} & 3l_{esh_i}^2 & 0 \\ & & & 0 & 0 & 0 & 0 & 0 \\ & & & & 0 & 0 & 0 & 0 \\ S & & & & & -156 & 22l_{esh_i} & 0 \\ Y & & & & & & -4l_{esh_i}^2 & 0 \\ M & & & & & & & 0 \end{bmatrix} \tag{A.61}$$

$$\left[M_{esh_i,11}\right] = \frac{1}{30l_{esh_i}}\begin{bmatrix} -36 & 0 & 0 & 3l_{esh_i} & 36 & 0 & 0 & 3l_{esh_i} \\ & 0 & 0 & 0 & 0 & 0 & 0 & 0 \\ & & 0 & 0 & 0 & 0 & 0 & 0 \\ & & & -4l_{esh_i}^2 & -3l_{esh_i} & 0 & 0 & l_{esh_i}^2 \\ & & & & -36 & 0 & 0 & -3l_{esh_i} \\ S & & & & & 0 & 0 & 0 \\ Y & & & & & & 0 & 0 \\ M & & & & & & & 0 \end{bmatrix} \tag{A.62}$$

$$\left[M_{esh_i,12}\right] = \frac{l_{esh_i}}{420}\begin{bmatrix} -156 & 0 & 0 & 22l_{esh_i} & -54 & 0 & 0 & -13l_{esh_i} \\ & 0 & 0 & 0 & 0 & 0 & 0 & 0 \\ & & 0 & 0 & 0 & 0 & 0 & 0 \\ & & & -4l_{esh_i}^2 & 13l_{esh_i} & 0 & 0 & 3l_{esh_i}^2 \\ & & & & -156 & 0 & 0 & -22l_{esh_i} \\ S & & & & & 0 & 0 & 0 \\ Y & & & & & & 0 & 0 \\ M & & & & & & & -4l_{esh_i}^2 \end{bmatrix} \tag{A.63}$$

$$\left[M_{esh_i,13}\right] = \frac{1}{30l_{esh_i}}\begin{bmatrix} 0 & 0 & 0 & 0 & 0 & 0 & 0 & 0 \\ & -36 & -3l_{esh_i} & 0 & 0 & 36 & -3l_{esh_i} & 0 \\ & & -4l_{esh_i}^2 & 0 & 0 & 3l_{esh_i} & l_{esh_i}^2 & 0 \\ & & & 0 & 0 & 0 & 0 & 0 \\ & & & & 0 & 0 & 0 & 0 \\ S & & & & & -36 & 3l_{esh_i} & 0 \\ Y & & & & & & -4l_{esh_i}^2 & 0 \\ M & & & & & & & 0 \end{bmatrix} \tag{A.64}$$

$$\left[M_{esh_i,14}\right] = \frac{l_{esh_i}}{420}\begin{bmatrix} 0 & 156 & 22l_{esh_i} & 0 & 0 & 54 & -13l_{esh_i} & 0 \\ & 0 & 0 & -22l_{esh_i} & 54 & 0 & 0 & 13l_{esh_i} \\ & & 0 & -4l_{esh_i}^2 & 13l_{esh_i} & 0 & 0 & 3l_{esh_i}^2 \\ & & & 0 & 0 & -13l_{esh_i} & 3l_{esh_i}^2 & 0 \\ & & & & 0 & 156 & -22l_{esh_i} & 0 \\ S & & & & & 0 & 0 & 22l_{esh_i} \\ Y & & & & & & 0 & -4l_{esh_i}^2 \\ M & & & & & & & 0 \end{bmatrix} \tag{A.65}$$

$$\left[M_{esh_i,15}\right] = \frac{1}{30l_{esh_i}}\begin{bmatrix} 36 & 0 & 0 & -3l_{esh_i} & -36 & 0 & 0 & -3l_{esh_i} \\ & 36 & 3l_{esh_i} & 0 & 0 & -36 & 3l_{esh_i} & 0 \\ & & 4l_{esh_i}^2 & 0 & 0 & -3l_{esh_i} & -l_{esh_i}^2 & 0 \\ & & & 4l_{esh_i}^2 & 3l_{esh_i} & 0 & 0 & -l_{esh_i}^2 \\ & & & & 36 & 0 & 0 & 3l_{esh_i} \\ S & & & & & 36 & -3l_{esh_i} & 0 \\ Y & & & & & & 4l_{esh_i}^2 & 0 \\ M & & & & & & & 4l_{esh_i}^2 \end{bmatrix} \tag{A.66}$$

$$\left[M_{esh_i,16}\right] = \frac{1}{30l_{esh_i}}\begin{bmatrix} 36 & 0 & 0 & -6l_{esh_i} & -36 & 0 & 0 & 0 \\ & 36 & 6l_{esh_i} & 0 & 0 & -36 & 0 & 0 \\ & & 2l_{esh_i}^2 & 0 & 0 & -6l_{esh_i} & -l_{esh_i}^2 & 0 \\ & & & 2l_{esh_i}^2 & 6l_{esh_i} & 0 & 0 & -l_{esh_i}^2 \\ & & & & 36 & 0 & 0 & 0 \\ S & & & & & 36 & 0 & 0 \\ Y & & & & & & 6l_{esh_i}^2 & 0 \\ M & & & & & & & 6l_{esh_i}^2 \end{bmatrix} \tag{A.67}$$

$$\left[M_{esh_i,17}\right] = \frac{1}{30l_{esh_i}}\begin{bmatrix} 72 & 0 & 0 & -15l_{esh_i} & -72 & 0 & 0 & 6l_{esh_i} \\ & 72 & 15l_{esh_i} & 0 & 0 & -72 & -6l_{esh_i} & 0 \\ & & 4l_{esh_i}^2 & 0 & 0 & -15l_{esh_i} & -3l_{esh_i}^2 & 0 \\ & & & 4l_{esh_i}^2 & 15l_{esh_i} & 0 & 0 & -3l_{esh_i}^2 \\ & & & & 72 & 0 & 0 & -6l_{esh_i} \\ S & & & & & 72 & 6l_{esh_i} & 0 \\ Y & & & & & & 18l_{esh_i}^2 & 0 \\ M & & & & & & & 18l_{esh_i}^2 \end{bmatrix} \tag{A.68}$$

$$\left\{V_{esh_i,1}\right\} = \frac{l_{esh_i}}{12}\left\{\begin{array}{c} 6 \\ 0 \\ 0 \\ -l_{esh_i} \\ 6 \\ 0 \\ 0 \\ l_{esh_i} \end{array}\right\}; \left\{V_{esh_i,2}\right\} = \frac{l_{esh_i}}{12}\left\{\begin{array}{c} 0 \\ 6 \\ l_{esh_i} \\ 0 \\ 0 \\ 6 \\ -l_{esh_i} \\ 0 \end{array}\right\}; \left\{V_{esh_i,3}\right\} = \frac{l_{esh_i}^2}{120}\left\{\begin{array}{c} 0 \\ 18 \\ 4l_{esh_i} \\ 0 \\ 0 \\ 42 \\ -6l_{esh_i} \\ 0 \end{array}\right\} \tag{A.69}$$

$$\left\{V_{esh_i,4}\right\} = \frac{l_{esh_i}^2}{120}\left\{\begin{array}{c} 18 \\ 0 \\ 0 \\ -4l_{esh_i} \\ 42 \\ 0 \\ 0 \\ 6l_{esh_i} \end{array}\right\}; \left\{V_{esh_i,5}\right\} = \frac{1}{2}\left\{\begin{array}{c} 0 \\ -2 \\ 0 \\ 0 \\ 0 \\ 2 \\ 0 \\ 0 \end{array}\right\}; \left\{V_{esh_i,6}\right\} = \frac{1}{2}\left\{\begin{array}{c} 2 \\ 0 \\ 0 \\ 0 \\ -2 \\ 0 \\ 0 \\ 0 \end{array}\right\} \tag{A.70}$$

FOLIO ADMINISTRATIF

THESE DE L'UNIVERSITE DE LYON OPEREE AU SEIN DE L'INSA LYON

NOM : JARROUX DATE de SOUTENANCE : 19/07/2017

Prénoms : Clément, Maximilien

TITRE : Nonlinear transient dynamics of on-board rotors supported by Active Magnetic Bearings

NATURE : Doctorat Numéro d'ordre : 2017LYSEI069

Ecole doctorale : MEGA

Spécialité : Génie Mécanique

RESUME :

De manière générale, les turbomachines sont des machines tournantes permettant la conversion des différents types d'énergie. Ces dernières sont composées d'une partie mécanique en rotation, appelée rotor, interagissant avec un fluide. La rotation a donc un rôle clé pour ces machines et la liaison entre les parties fixes et les parties tournantes, appelée palier, est primordiale pour un fonctionnement fiable et optimal.

Les turbomachines supportées par des paliers magnétiques actifs (PMAs) sont de plus en plus utilisées par les industriels notamment grâce à l'absence de contact direct entre parties fixes et parties tournantes, permettant un gain d'énergie et une réduction des émissions de CO2. La plupart du temps, ces machines sont « embarquées » et reposent sur des supports mobiles. Les mouvements générés par ces supports doivent être considérés dans la prévision du comportement dynamique des turbomachines afin d'améliorer les designs en conséquence. Cette thèse est une contribution à l'étude des turbomachines supportées par des PMAs sujettes à de fortes sollicitations extérieures.

L'approche est numérique et expérimentale. L'utilisation d'un banc d'essais académique composé d'un système rotor-PMA, aux propriétés d'une turbomachine industrielle, a permis de tester les modèles développés pour des cas de sollicitations extérieures de type séisme et choc, générées grâce à l'excitateur 6-axes de l'equipex PHARE. Il est montré que le modèle permet la bonne prévision du comportement réel de la machine. Cet outil pourra donc être utilisé pour des designs de type industriel.

MOTS-CLÉS : Contact rotor-stator, Paliers atterrisseurs, Rotor embarqués, Paliers magnétiques actifs, Dynamique des rotors, Dynamique non-linéaire

Laboratoire (s) de recherche : LaMCoS

Directeur de thèse: Jarir Mahfoud, Régis Dufour

Président de jury : Isabelle Trébinjac

Composition du jury : Jarir Mahfoud, Régis Dufour, Patrick S. Keogh, Mihaï Arghir, Hannes Bleuler, Isabelle Trébinjac